Understanding the Properties of Obscured Radio AGN and Faint Submillimeter Galaxies at $z \sim 2$

Pallavi Patil
Mumbai, India

B.S. Physics, IISER-Pune, 2014
M.S. Astronomy, IISER-Pune, 2014
M.S. Astronomy, University of Virginia, 2016

A Dissertation Presented to the Graduate
Faculty of the University of Virginia
in Candidacy for the Degree of
Doctor of Philosophy

Department of Astronomy

University of Virginia

December 2020

Committee Members:

Prof. Mark Whittle
Dr. Carol Lonsdale
Prof. Aaron Evans
Dr. Eric Murphy
Dr. Mark Lacy
Prof. David Nichols

Abstract

Cosmic noon marks the period in cosmic history when galaxies were in their most active state, with intense star-formation and maximum black-hole fueling. In order to fully understand the evolution of galaxies, it is essential to study both active galaxies and star-forming galaxies during this period, which in redshift spans $1 < z < 3$. The work I present in this thesis, in four main chapters, targets these two classes of galaxies and identifies a number of important processes that drive change in galaxies across this epoch. Chapter 1 provides a brief outline of the context of the work presented in this thesis.

In Chapter 2, I present new sub-arcsecond-resolution Karl G. Jansky Very Large Array (VLA) imaging at 10 GHz of 155 ultra-luminous ($L_{\rm bol} \sim 10^{11.7-14.2}$ $L_{\odot}$) optically obscured quasars with redshifts $z \sim 0.4 - 3$. The sample was selected to have extremely red mid-infrared (MIR)-optical color ratios based on data from Wide-Field Infrared Survey Explorer (WISE) along with a detection of bright, unresolved radio emission from the NRAO VLA Sky Survey (NVSS) or Faint Images of the Radio Sky at Twenty-Centimeters (FIRST) Survey. Our high-resolution VLA observations have revealed that the majority of the sources in the sample (93 out of 155) are compact with angular scales $< 0.2''$ (≤ 1.7 kpc at $z \sim 2$). The radio luminosity, linear extent, and lobe pressure of these sources are similar to those of young radio AGN, but their space density is considerably lower. Application of a simple adiabatic lobe expan-

sion model suggests a range of properties from more compact to more extended lobes of relatively young ages ($\lesssim 10^3 - 10^6$ years), relatively high ambient ISM density ($\sim 10^{-4} - 10$ cm^{-3}), and relatively modest lobe expansion speeds ($\sim 0.003c - 0.1c$). Folding together the rarity of the sources and their young dynamical age, I estimate that perhaps 20% of our class of AGN evolve through compact phases (such as Gigahertz Peaked Spectrum, GPS, and Compact Steep Spectrum, CSS, sources) to become large scale FR-I/II radio sources. This work has been published in Patil, P., et al. 2020, ApJ, 896, 18.

In Chapter 3, I present broadband radio spectra of the entire sample, constructed from our 10 GHz observations and archival radio data. About 57% of the sample exhibits peaked or curved radio spectra suggesting low-frequency absorption. At least 30% of the sample belongs to the class of peaked spectrum sources such as CSS, GPS, and High-Frequency Peakers (HFP). The sample also has, on average, steeper high-frequency radio spectra than classic optically thin synchrotron sources. A comparison of the magnetic energy density and the MIR photon energy density suggests that the spectral steepening could arise from inverse Compton scattering off the intense MIR photon field. Extrapolating the high-frequency spectra into the submm cannot produce our measured ALMA fluxes, which must therefore originate from another component, most likely cold dust. Returning to the peaked sources, assuming synchrotron self-absorption dominates, I derive source sizes and magnetic field strengths for the emitting regions, finding compact sources (a few to 10s of parsecs) with relatively strong magnetic fields ($10 - 100$ mG), consistent with very young radio sources. While the MIR properties of the sample are quite different from almost all other classes of AGN, I was unable to find any statistically meaningful correlations between the radio spectral properties and the MIR properties. This work will be published in Patil et al. 2021, in prep.

Chapter 4 aims to identify an important new class of submm galaxies (SMGs) with fluxes below the more well-known bright SMGs. These are thought to dominate the extragalactic background submm light but have remained undetected in most previous submm surveys. I present a catalog of 26 faint SMGs in the deep X-ray XMM-LSS field identified serendipitously within archival Band 6 and 7 ALMA observations, cross-matched with other deep multi-band surveys of this field. Of the 26 SMGs in our sample, 15 are identified here for the first time. To further characterize these galaxies, I provide 13-band photometry for the entire catalog using the "*Tractor*" deblending package and calculate photometric redshifts (median $z \sim 2.66$) and rest-frame colors. I find that our faint SMGs have bluer colors than bright SMGs, and the UVJ color-color plot places them on the main sequence of star-forming galaxies. Our results help broaden our understanding of the important population of SMGs and endorse the importance of archival ALMA data in the serendipitous identification of new populations. This work has been published in Patil et al. 2019, ApJ, 871, 109.

In Chapter 5, I summarize ongoing projects that target sub-samples of the primary sample of young radio AGN. In the first, I used multi-frequency multi-resolution imaging from the VLA, VLBA, and e-MERLIN to study 12 compact sources. In the second, I used multi-frequency VLA observations to study 20 well-resolved sources. In each my aim is to understand the physical nature and evolutionary stage of the radio source and relate these to the host properties. In the third, I used ALMA to study the molecular gas content of three sources. The fourth is a pilot NuTSAR study of a single deeply obscured source in hard X-rays to identify the intrinsic AGN emission. Finally, I discuss the next generation Very Large Array (ngVLA) and its role in studying the life-cycles of $z \sim 2$ radio AGN and their broader connection to galaxy evolution. This work has been published in Patil et al. 2018, ASPC, 517, 595.

In the final chapter, I summarize the results presented in my dissertation.

Acknowledgements

I would owe many, many thanks to my advisors Prof. Mark Whittle, Dr. Kristina Nyland, Dr. Mark Lacy, and Dr. Carol Lonsdale, for their constant guidance and enthusiasm throughout my graduate school years. Mark, your dedication, support, and expertise has helped me navigate graduate school and academia with ease. Your insightful feedback pushed me to sharpen my thinking and brought my work to a higher level. I appreciate your encouragement and endless patience when we go on many research endeavors (or "fishing expeditions"). I am also grateful to you and Mary for helping me settle into Charlottesville and hosting me many times over the years. Thank you for making the department more welcoming and friendly for me.

I am indebted to Kristina Nyland for her continual support. Kristina, you have been a wonderful mentor, and I cannot express enough how much I owe this thesis to you. I want to thank you for encouraging my research and allowing me to grow as a research scientist. I am grateful for all you have done for me; editing my research material even at the last hour, sharing your scripts, paying for my many, many meals, and the list goes on. Your passion for Astronomy is contagious. You are a true inspiration, and I am incredibly fortunate to have you as my mentor. I look forward to working together on fascinating and equally strange AGN for the years to come.

I would like to express my gratitude to Dr. Mark Lacy for his belief in my work and abilities. Mark, you are the coolest scientist I have met. I am grateful for your support, expertise, and magical powers to always find funding for me. Finally, I would like to thank Dr. Carol Lonsdale, without whom my Ph.D. would not have been possible. Carol, thank you for introducing me to this project. I appreciate you helping me if I needed anything and being available from anywhere in the world. I wish we could have spent more time together in Charlottesville, but I am happy for you to start the next chapter in life. Thank you for planning my research project in advance that really launched my career.

I would also like to thank all my wonderful collaborators that I made during my time here. Especially, Prof. Colin Lonsdale, thank you for hosting me at Haystack Observatory and helping me even in a hectic schedule. I would like to express sincere thanks to my thesis committee - Prof. Aaron Evans, Dr. Eric Murphy, and Prof. David Nichols - who have carefully read through my thesis. I take this opportunity to thank them for their encouragement and insightful comments. Also, I would like to thank my undergraduate advisor, Dr. Ramana Athreya, who got me interested in radio astronomy.

Nobody has been more important to me in the pursuit of this project than my family members. I want to thank my parents, whose love and guidance are with me in whatever I pursue. Mummy, I wish you were with us today. Pappa, I would not have been here without your unconditional support and tireless efforts. You made this world a better place with your devotion to your patients and social work. I would like to thank my sister, Komal, for teaching me how to strive and follow your passion, no matter how hard life gets. I am amazed at her creativity and, most notably, her ability to stand up for her belief against all odds. The rest of my extended Patil family (the "Family - original" group on WhatsApp), thank you for always being so supportive throughout my life.

Many thanks to the UVA Astronomy department and NRAO for always caring and supporting students. I also want to thank Whitney, Barbara, and Jackie for helping me through all the administrative work. I appreciate all the efforts you put to keep the department running. I must acknowledge the NRAO summer research program and Reber Fellowship for funding me over many summers and the last years of my Ph.D. My research would not be possible with all the computing resources and facilities provided by NRAO. I am grateful to the NRAO staff, Jim Braatz, and JJ, for all your help.

Graduate school has been quite challenging. I would not have made it so far if it were not for the fantastic friends that I made in Charlottesville. All of my Chamiyas, Mitra, Surabhi, Ritika, and Shweta, I love you all. I enjoyed all our crazy talks, laughs, and trips together. All of my Farrish people, Mrugen, Prateek, Preetha, Rajveer, Roshan, Sriram, Srashti (you are still part of UVa), Vishal, and Vishaal, you made my life at UVa so much fun. They are the only ones who believe I will find aliens one day (at least Mrugen does). Thank you for making Charlottesville a home away from home. It will be a special place all because of you. Also, I would like to thank my dear friend, William, the first American I met, for helping me countless times and driving all of Chamiyas through these strange lands. Scar, thank you for being the most adorable pet. And many thanks to UVa grad students Allison, Kristen, Jake T, Loreto, Matt, Mengyao, Poon, Yiqing, Yu, Xiaoshan, and astrowomen for making the department so much fun for me.

Last but the most important person I would like to thank is Abhiraj. Thank you for sticking up with me through these stressful times and always having my back. I really admire all you have done for me, from cooking delicious food, editing my slides to just about anything that I demand/ask. Your patience and ability to help everyone is commendable, and I am grateful to have you in my life. I look forward to our journey together.

Table of Contents

List of Figures

List of Tables

List of Acronyms

ADAF Advection-Dominated Accretion Flow

AGN Active Galactic Nucleus

AIPS Astronomical Image Processing Software

ALMA Atacama Large Millimeter Array

APEX Atacama Pathfinder Experiment

ASKAP Australian Square Kilometer Array Pathfinder

ASTE Atacama Submillimeter Telescope Experiment

BAL Broad Absorption Line

BH Black Hole

BLAGN Broad-Line Active Galactic Nucleus

BLR Broad-Line Region

BLRG Broad-Line Radio Galaxy

BRATS Broadband Radio Astronomy ToolS

CASA Common Astronomy Software Applications

CDM Cold Dark Matter

CENSORS Combined EIS–NVSS Survey Of Radio Sources

CFHT Canada-France-Hawaii Telescope

CFHTLS CFHT Legacy Survey

CGM Circumgalactic Medium

CIB Cosmic Infrared Background

CMB Cosmic Microwave Background

CO Carbon Monoxide

COBE Cosmic Background Explorer

CPL Curved Power Law

CSO Compact Symmetric Objects

CSS Compact Steep Spectrum

CT Compton Thick

DDF Deep Drilling Fields

DSFG Dusty Star-forming Galaxy

DOG Dust Obscured Galaxy

DSS Digitized Sky Survey

EAZY Easy and Accurate z_{phot} from Yale

EBL Extragalactic Background Light

EFFA External Free Free Absorption

EIS ESO Imaging Survey

ESO European Southern Observatory

FFA Free Free Absorption

FIR Far InfraRed

FIRE Folded-port InfraRed Eschellette

FIRST Faint Images of the Radio Sky at Twenty-Centimeters

FR-I/II Fanaroff-Riley Type I/II

FSRQ Flat-Spectrum Radio Quasar

FWHM Full Width at Half Maximum

GBT Green Bank Telescope

GLEAM Galactic and Extra-galactic Murchinson Widefield Array

GMRT Giant Meterwave Radio Telescope

GMT Giant Magellan Telescope

GPS Gigahertz Peaked Spectrum

HEG High-Excitation Galaxy

HERG High-Excitation Radio Galaxy

HFP High-Frequency Peakers

Hot DOG Hot Dust Obscured Galaxy

HSC Hyper Suprime-Cam Subaru Strategic Program

ICM Intra-Cluster Medium

IFRS Infrared-Faint Radio Sources

IGM Intergalactic Medium

IR InfraRed

IRAS Infra-Red Astronomical Satellite

ISM Interstellar Medium

ISO Infrared Space Observatory

JCMT James Clerk Maxwell Telescope

JWST James Webb Space Telescope

LABOCA Large Apex Bolometer Camera

LAS Largest Angular Scale

LBA Long Baseline Array

LBG Lyman Break Galaxy

LBT Large Binocular Telescope

LEG Low-Excitation Galaxy

LERG Low-Excitation Radio Galaxy

LIRG Luminous InfraRed Galaxy

LLS Largest Linear Size

LOFAR Low-Frequency Array

MAMBO Max Planck Millimeter Bolometer

MBH Massive Black Hole

NASA National Aeronautics and Space Administration

NAT Narrow-Angle Tail

NED NASA Extragalactic Database

ngvla ngVLANext-Generation Very Large Array

nglobo ngLOBONext-Generation LOw-Band Observatory

NLR Narrow-Line Region

NRAO National Radio Astronomy Observatory

NRL Naval Research Laboratory

NVSS NRAO VLA Sky Survey

PL Power Law

PSF Point Spread Function

QSO Quasi-Stellar Object/Quasar

RFI Radio Frequency Interference

RL Radio Loud

RLF Radio Luminosity Function

RM Rotation Measure

RMS Root-Mean-Square

RQ Radio Quiet

SB StarBurst

SBA Short Baseline Array

SCUBA Submillimeter Common-User Bolometer Array

SDSS Sloan Digital Sky Survey

SED Spectral Energy Distribution

SERVS Spitzer Extragalactic Representative Volume Survey

SF Star Formation

SFG Star-forming Galaxy

SFR Star-Formation Rate

SFRD Star-Formation Rate Density

SFRG Submillimeter Faint Radio Galaxy

SKA Square Kilometer Array

SMBH SuperMassive Black Hole

SMG Submillimeter Galaxy

SNR Signal-to-Noise Ratio

SSA Synchrotron Self Absorption

TMT Thirty Meter Telescope

UDS UKIDSS-Ultra Deep Survey

ULIRG Ultra-Luminous Infrared Galaxy

USS Ultra Steep Spectrum

VLA Very Large Array

VLBA Very Large Baseline Array

VLBI Very Long Baseline Interferometry

WAT Wide-angle Tail

WISE Wide-Field Infrared Explorer

XMM-LSS XMM Large Scale Structure

Chapter 1

Introduction

It is almost 100 years since Hubble published his famous redshift-distance relation (Hubble, 1929), with its implication of cosmic expansion and an origin in a "Big Bang". Over those 100 years, and in particularly over the past 40 years, there has been remarkable progress in our understanding not only of the earliest times, but also of the more complex arc of cosmic history that starts with infant galaxies and arrives at today's wonderfully varied population of galaxies. While the overall story of galaxy evolution is perhaps now relatively secure, there are still many areas of uncertainty and many steps along the way that need to be understood. Within this overall framework, my dissertation aims to zero in on some of those "steps along the way" and identify some important properties and processes that occur early in the lives of galaxies.

1.1 Epoch of Cosmic High Noon

The epoch of cosmic noon is a phase after the Big Bang, defined by the significant growth of galaxies and black-holes. This epoch happened when the universe was 2-7 billion years old – when the "size" of the universe (its scale factor) was between a quarter and half its current size, equivalently a redshift range of 1 to 3. Galaxies were

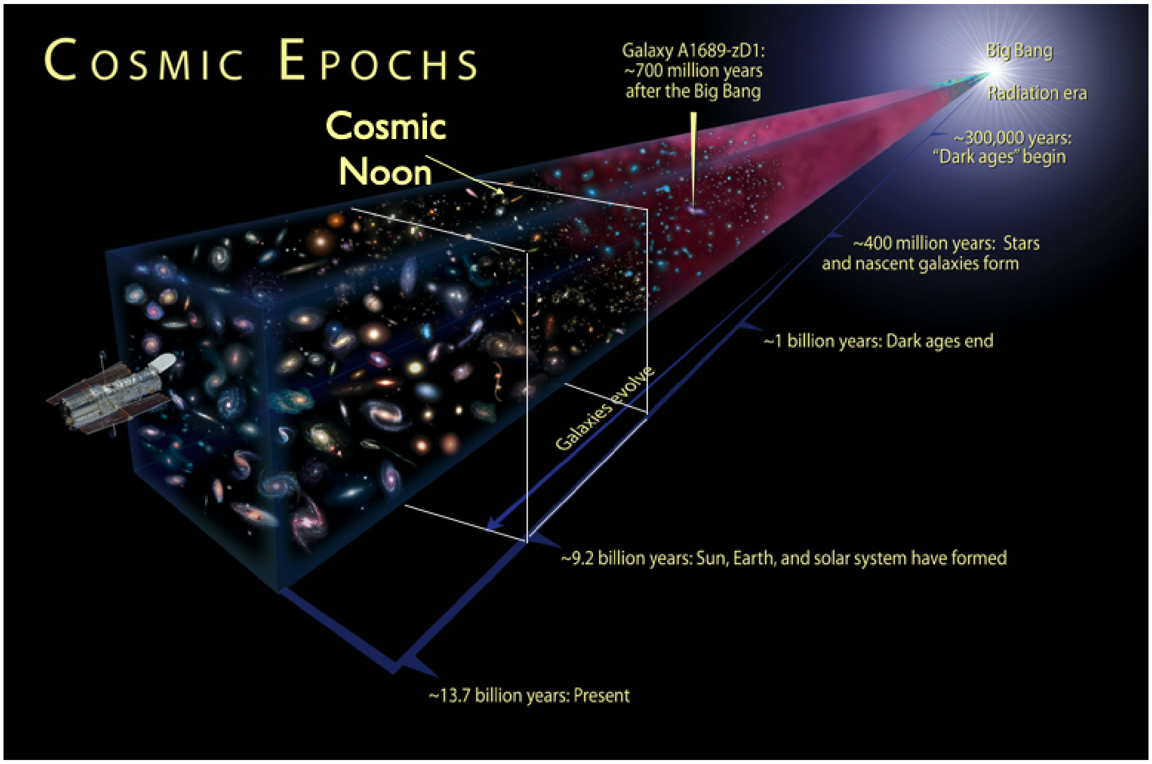

Figure 1.1: History of the Universe. Figure Courtesy NASA/STSCI.

undergoing drastic transformations via mergers and were forming stars at maximum rate. Active galactic nucleus (AGN) activity, which is the accretion of gas onto a black hole (BH) lying in the center of its host galaxy, also reached its peak around a similar time, suggesting a link between the evolution of galaxies and black-holes.

Three key observational results provide strong support to the supermassive black-hole (SMBH)[1]-galaxy co-evolution. There is a close similarity between the evolution of the global star-formation rate (SFR; tracing the buildup of galaxies) and AGN activity (tracing the growth of SMBH) over most of the cosmic time (Madau & Dickinson, 2014, and references therein). The average SFR density and space density of SMBH growth increased sharply from the earliest epochs to $z \sim 2$, reaching a broad

[1]The BHs in the centers of galaxies are $10^6 - 10^{10} M_{\odot}$, compared to $\sim 10 M_{\odot}$ for BHs created at the endpoint of massive star evolution, and hence are termed supermassive black-holes

peak at $z \approx 1.9$, before declining quickly from $z \approx 1$ to today (Shankar et al., 2009). As shown in figure 1.2, the cosmic evolution of SF and SMBH growth are strikingly similar. Another important piece evidence comes from the correlation of SMBH mass with bulge mass (e.g., McLure & Dunlop, 2002) and bulge velocity dispersion (e.g., Gebhardt et al., 2000; Gültekin et al., 2009) of the host galaxy in the local universe (see Kormendy & Ho, 2013, for a comprehensive review). This empirical relationship seems to hold across several dex in mass and provides strong evidence interlinking the SMBH-host galaxy growth at least locally. While the observational results in the local Universe are well constrained, the situation at higher redshifts is less clear.

The galaxy-SMBH co-evolution seems plausible, but the differences of nine dex in the spatial scales of the SMBH and the bulge make it difficult to understand how such a connection might arise (Alexander & Hickox, 2012). Many galaxy formation models and simulations introduce a suite of regulatory processes, dependant on common cold-gas supply and proceeding via secular or interacting events (e.g., major-mergers). One popular framework is AGN feedback, in which actively accreting SMBH (AGN) inject large amounts of energy and momentum into the surrounding regions, quenching star formation and purging the host of its interstellar medium (ISM; Croton et al. 2006; Fabian 2012. One apparent success of the theory of AGN feedback has been to account for the observed properties of massive quiescent galaxies in the nearby Universe (e.g., Dubois et al., 2016). There is a growing support from observations, theory, and numerical simulations (e.g., Kauffmann & Haehnelt, 2000; Sijacki et al., 2015) for AGN feedback but its importance at different epochs and in different environments is not well understood.

Re-framing these processes in terms of the evolution of a single object: a major-merger is followed by a nuclear starburst and triggering of AGN accretion (Sanders et al., 1988; Hopkins & Hernquist, 2006; Treister et al., 2012). The most powerful of these AGN reach bolometric luminosities $L_{AGN} \gtrsim 10^{45}$ erg s^{-1} and are called quasars. The early growth of these AGN is expected to be highly obscured by the presence of large amounts of gas and dust, fueling the SMBH (e.g., Sanders et al., 1988; Fabian, 1999; Di Matteo et al., 2005; Hopkins et al., 2008; Treister et al., 2009), followed by a blowout phase in which energy release from SMBH accretion purges the gas from the nuclear regions to expose the central luminous AGN, making it visible. Quasars and major-mergers are uncommon in the nearby Universe but they were much more common in the past during the epoch of cosmic noon. The study of the obscured SMBH growth phase is an important component in our overall understanding of how AGN feedback and SMBH-galaxy co-evolution occur. However, it remains difficult to study because of its obscured character, its short duration, and its occurrence at high redshift (e.g., Blecha et al., 2018). The main focus of this thesis is to find $z \sim 2$ obscured quasars that can be used as laboratories to investigate the early phases of AGN feedback. I will explain the background and our sample further in the upcoming sections.

To gain further insights into galaxy evolution during this critical period, we also need to study star-formation during cosmic noon. Star-forming galaxies (SFGs) at cosmic noon had larger molecular gas content, and higher SFR and SMBH growth than today. Like star-forming galaxies at $z \sim 0$, most of $z \sim 2$ SFGs define a “main sequence” between SFR and stellar mass (e.g., Speagle et al., 2014; Förster Schreiber & Wuyts, 2020). A minority of massive galaxies with intense SFR lie above this relation. These galaxies are probably merger-driven and are likely to host AGN. The most luminous of these massive galaxies were first discovered in the submm-bands and were called Submillimeter Galaxies (SMGs; Blain et al. 2002). In Chapter 4 of this thesis I present a sample belonging to a recently discovered class of galaxy, called Faint SMGs. These sources are less luminous than bright SMGs and form a bridge between regular SFGs and massive SMGs in the main-sequence.

Tracing the $z \sim 2$ star-formation and obscured quasar activity via radio and millimeter observations is the central theme of my thesis. In the quasar study, I will focus on a sub-population of obscured quasars that also emit bipolar jets. Shocks associated with these jets accelerate charged particles to very high energy resulting in the emission in the radio bands, making radio a tool of choice for this study. On the star-formation side, most star-formation during cosmic noon is expected to take place in the presence of large amounts of dust and thus obscuring most of the optical/ultra-violet emission (Casey et al., 2015). Therefore, it is necessary to probe these galaxies at longer wavelengths such as millimeter-submillimeter (mm-submm) and radio. The radio telescope and ground-based submm/mm telescopes both generate their images using the principles of interferometry. Section 1.7 provides an introduction to radio astronomy, imaging techniques, and telescopes used in this thesis.

1.2 Studying Star-Formation at $z \sim 2$

As we have learned in the previous section, comprehensive multi-wavelength studies of galaxies across cosmic time have shown a consistent picture of the history of the Universe, in which about 50% of the stellar mass formed during the peak epoch of star formation, $z \sim 1-3$ (Figure 1.2; Madau & Dickinson, 2014). One of the star-formation tracers is far-infrared (FIR) emission coming from dust surrounding massive O/B stars. The UV radiation from the O/B stars is absorbed by the dust, warming it to $T_{dust} \sim 15-60$K), and thus the dust emits thermally in the FIR/submm. It was realized soon after the launch of IR telescopes that the majority of the star formation at high-redshift was enshrouded in the dust and therefore missed by optical/UV surveys (e.g., Hauser et al., 1998). Many ground-based telescopes such as the James Clerk Maxwell Telescope (JCMT; Robson et al. 2017), the Atacama Pathfinder EX-

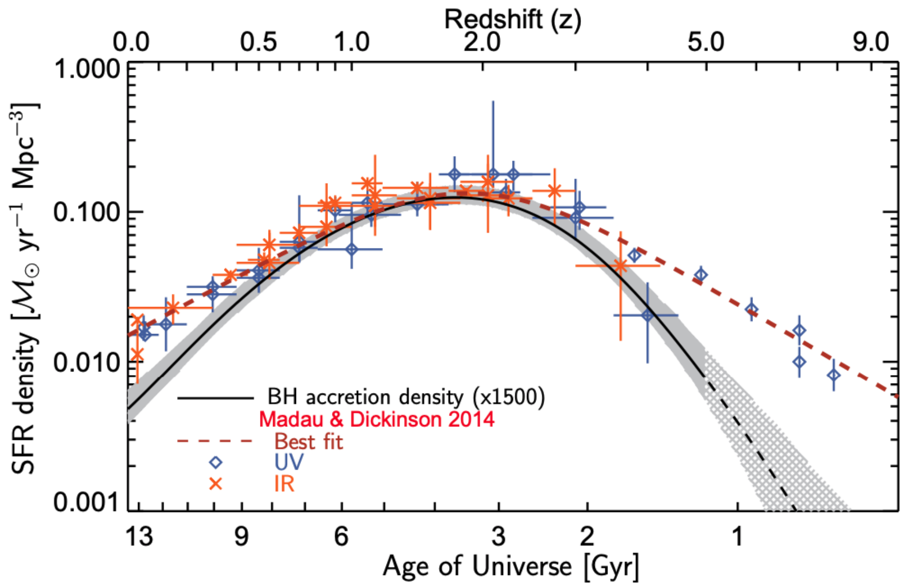

Figure 1.2: From Aird et al. (2015). The figure shows the total star-formation-rate density and SMBH accretion density across cosmic time. The SMBH accretion and star formation rates evolve in a similar manner over most of the cosmic time, with both peaking around $z \sim 2$.

periment (APEX; Güsten et al. 2006), as well as space telescopes such as Spitzer and Herschel have unveiled a large population of dusty star-forming galaxies at higher redshifts (Casey et al., 2014).

The existence of bright submm/FIR sources was first indicated by the cosmic infrared background (CIB) and optical/UV background, which are the total of all radiation emitted in a particular wavelength range by all populations throughout all of cosmic time (Cooray, 2016). Single-dish submm instruments such as Submillimeter Common-User Bolometer Array (SCUBA) on JCMT were the first to resolve the CIB into a distant, submm-bright but optically faint population called Submillimeter galaxies (SMGs; Blain et al. 2002; Casey et al. 2014; Hodge & da Cunha 2020). Follow-up studies revealed that SMGs are numerous at high redshift with a peak around $z \sim 2.5$ (Chapman et al., 2003), massive and dusty, with extreme SFRs

($> 100\,M_{\odot}\ \mathrm{yr}^{-1}$) contributing to $\sim$20% of the global SFR density at $z = 2 - 4$ (e.g., Michałowski et al., 2010). These are thought to be progenitors of today's massive elliptical galaxies (Simpson et al., 2014), caught in a starburst phase driven by gas-rich mergers followed by triggering of luminous, obscured AGN (Hopkins & Hernquist, 2006; Narayanan et al., 2015).

SMGs are more generally called Dusty Star-forming Galaxies (DSFGs), and were initially the only ones studied due to limited sensitivity and resolution of the early sub-millimeter telescopes. The advent of the Atacama Large Millimeter Array (ALMA) operating in the mm-submm bands has transformed our understanding of star-formation and the molecular gas and dust content of galaxies at high-redshift (see review by Hodge & da Cunha, 2020). The ALMA's sub-arcsecond resolution has allowed to accurately pinpoint the multi-wavelength counterparts and enabled resolved studies of the bright SMG population (e.g., Casey et al., 2014).

ALMA has pushed the continuum detection limit to sub-mJy levels unveiling a new population that dominates the CIB at submm/mm wavelengths (e.g., Hatsukade et al., 2013). These sources, also referred to as Faint SMGs, are less luminous than classical SMGs with more normal SFRs, and they form the bulk of the normal SFGs at high-redshifts. Searches for faint SMGs have followed two methods— deep blank-field surveys (e.g., Dunlop et al. 2017; González-López et al. 2017; Franco et al. 2018; Yamaguchi et al. 2019), and mining of archival data that was taken for other scientific goals leading to serendipitous detections (e.g., Oteo et al., 2016; Fujimoto et al., 2016; Zavala et al., 2018; Liu et al., 2019, and this thesis). Due to ALMA's small field-of-view, deep large-scale surveys are time-consuming and costly and have resulted in the detection of only a handful of sources. Thus, ALMA's ever-increasing publicly available archive data provides an alternative cost-effective method to find new faint SMGs that can be followed up using deep optical/NIR multi-wavelength surveys

(González-López et al., 2020). The emerging picture is that there is a continuum in galaxy properties with faint SMGs having moderate stellar mass ($\sim 10^{10} - 10^{11}\,M_{\odot}$) and dust mass ($\sim 10^{8} - 10^{9}\,M_{\odot}$) with moderate SFRs ($\sim 10 - 100\,M_{\odot}\mathrm{yr}^{-1}$) (Hodge & da Cunha, 2020). Chapter 4 presents a sample of faint SMGs identified via an ALMA archival search in the XMM field and presents properties of their optical/NIR counterparts.

1.3 Active Galactic Nucleus

The Active Galactic Nucleus (AGN) phenomenon occurs due to accretion of surrounding material by a SMBH residing in the nucleus of its host galaxy. We now know that most galaxies harbor an SMBH in their centers (Kormendy & Ho, 2013). Although most SMBHs in today's galaxies have little or no accretion, there is strong evidence that SMBHs are powering today's active galaxies (hosts of AGN; e.g., Miyoshi et al. 1995; Ghez et al. 2008), and that these were both more numerous and more active in the early universe (e.g., Shankar et al., 2009). These black holes have masses in the range of a few million to a few billion solar masses ($M_{BH} \approx 10^{6} - 10^{10} M_{\odot}$, where $M_{\odot}$ is the mass of the sun). The SMBH feeds on the surrounding material through an accretion process during which the in falling material loses its angular momentum and radiates a significant fraction of its gravitational binding energy. As a result, enormous amounts of mechanical and radiative energies are released via narrow bipolar jets of high-velocity gas, strong wide-angle winds, and intense electromagnetic radiation. This phenomenon is often very luminous with prominent observable features that make AGN distinguishable from inactive or normal galaxies.

Early studies of AGN date back to 1943, when Carl Seyfert found broad emission lines in the nuclei of six spiral nebulae (Seyfert, 1943). However, this study went unnoticed for almost twenty years except for the work by Baade & Minkowski (1954), which found similarities between emission lines of the Seyfert galaxies and a radio source Cygnus A. During the 1950s, many radio galaxies were discovered, and it was realized that some galaxies were unusually active and showed energetic phenomena. The field gained momentum when Minkowski (1960) identified the first quasar[2], 3C295 at a redshift of $z = 0.46$, followed with subsequent discoveries of even more distant quasars (Schmidt, 1963; Burbidge & Burbidge, 1969). The hypothesis soon followed that quasars were accreting SMBH in galaxy nuclei (e.g., Salpeter, 1964; Lynden-Bell, 1969) and this idea was quickly and widely accepted. Since then, tremendous efforts have been put to investigate the nature of AGN across all wavelengths. From a rare and exotic phenomenon, AGN are now believed to be a ubiquitous and a key player in galaxy formation and evolution. The history of the discovery and early understanding of AGN is an interesting episode in the history of science, and is nicely captured in the reviews by, for example, Shields (1999); D'Onofrio et al. (2012); Kellermann (2015), and Kellermann et al. (2020).

1.3.1 The Architecture of AGN and its Unique Electromagnetic Signature

The defining characteristics of AGNs are 1) stronger emission than normal or inactive galaxies 2) unique emission signatures across the entire electromagnetic spectrum. The very high luminosity makes them detectable even at very high redshifts (e.g., Mortlock et al., 2011; Wang et al., 2017). Furthermore, distinguishable emission features allow for efficient AGN identifications in large surveys (See review by Padovani et al., 2017). The techniques developed over the past five decades have not only identified many classes of AGN (next section) but also have probed deeper into

[2]Quasar, also known as Quasi-stellar object is a type of AGN that has extreme luminosity and strong emission lines, appearing in images like a star rather than a galaxy. See Section 1.3.2 for more details.

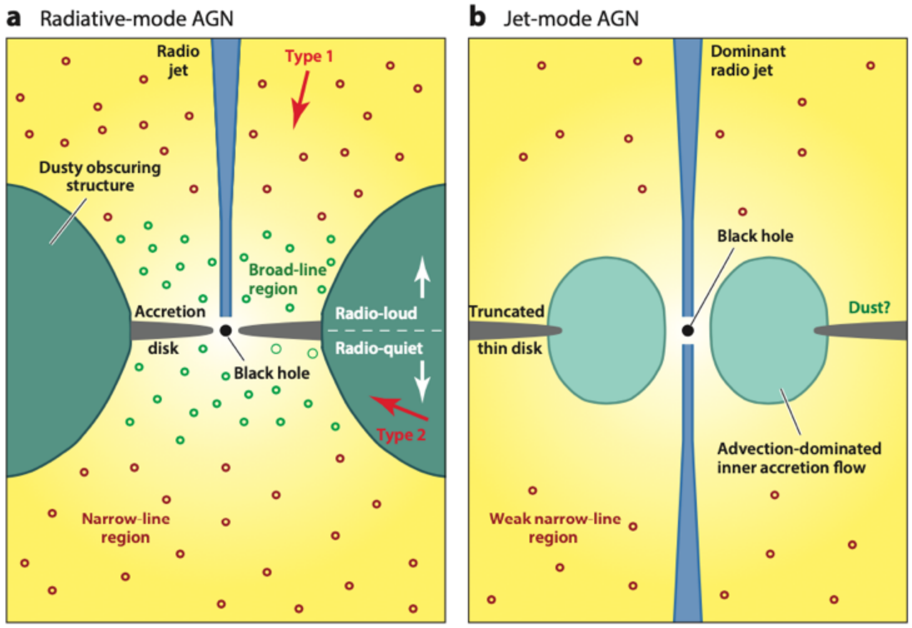

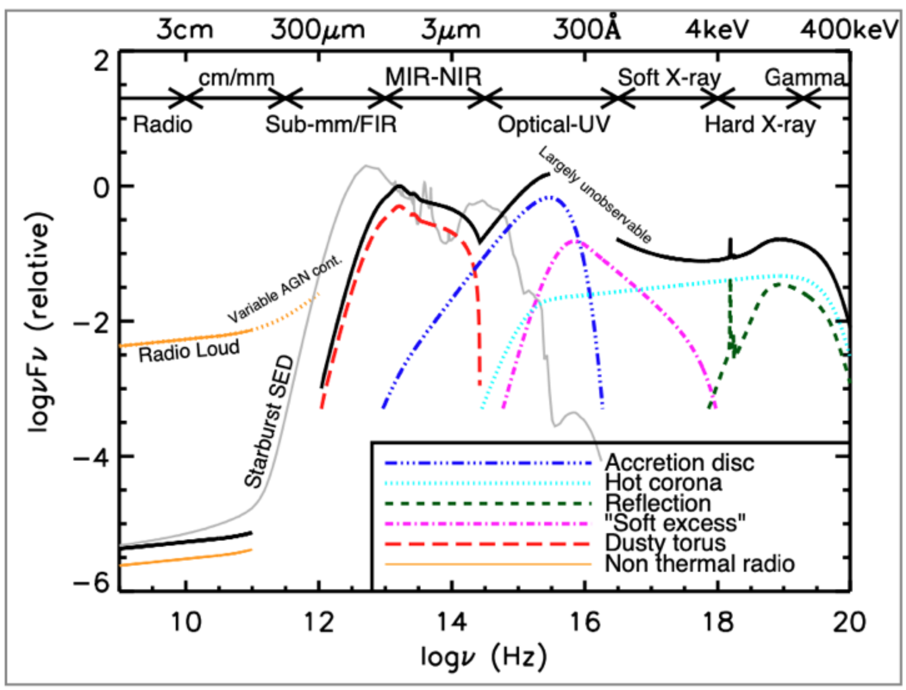

Figure 1.3: **Top**: Schematic representation of the structure of the central engine for two types of AGN; radiative-mode and jet-mode. The figure is taken from Heckman & Best (2014). **Bottom**: A composite SED of a typical AGN across the entire electromagnetic spectrum (black). Colored lines highlight the contribution from different components of AGN. The gray line is the SED of a pure star-forming galaxy. The figure is taken from Harrison (2014)

the central engine to understand its physical structure. Here I describe the currently accepted AGN model and the features seen in their spectral energy distributions (SEDs).

Basic Anatomy of AGN

There are several physical processes and components associated with AGN, although not every AGN appears to be the same. Depending on the central engine's physical properties and the host galaxy environment, there can be variation in the appearance of different components and their relative contributions to the broadband emission. I provide a short overview with an emphasis on the AGN classes relevant to this work.

Black Hole: The black holes in the centers of galaxies have masses ranging from $M_{BH} \approx 10^6 - 10^9 M_\odot$ (Kormendy & Ho, 2013; McConnell & Ma, 2013; Baron & Ménard, 2019). The mass and spin are the two key properties of a black hole. The mass determines the total energy output, and the spin, although still debated, determines the accretion efficiency. It may play a role in producing relativistic jets and AGN winds (Narayan & McClintock, 2012; Blandford et al., 2019). The top panel in Figure 1.3 shows a schematic diagram for the components of AGN, divided into two classes based on their accretion mode (Heckman & Best, 2014). The radiative-mode AGN, which is the focus of the presented work, has a high accretion rate and liberates most of its energy as radiation. It is also called radiatively-efficient due to higher Eddington ratios ($\lambda_{Edd} \gtrsim 0.1$). The AGN with low-power accretion is called 'jet-mode' or 'radiatively-inefficient' AGN as it has ($\lambda_{Edd} \leq 0.1$). In these AGN much of the energy emerges as bipolar jets.

Accretion Disk: In a standard accretion disk model, the disk is formed by gas close to the black hole circulating in approximately Keplerian orbits (Shakura, 1972, 1973; Pringle, 1981). The gas in the disk loses angular momentum via viscous forces of magnetic origin, finally reaching the last stable orbit, after which it rapidly spirals inward across the event horizon and into the black hole. Since the last stable orbit is in the relativistic regime, the energy liberated as the gas moves through the accretion disk can be $\sim 5 - 40\%$ of the rest mass which is remarkably efficient compared to almost all other forms of energy production (Kerr, 1963). The hot accretion disk emits locally like a blackbody and when summed over the whole disk can generate a prominent peak in the UV-band (called 'big blue bump'; dashed-dotted blue line in Figure 1.3). The geometry of the disk changes at lower accretion efficiencies (e.g., Yuan & Narayan, 2014). For example, jet-mode AGN do not have a simple thin disk but instead have a geometrically thick structure, called an Advection-Dominated Accretion Flow (ADAFs; e.g., Narayan & Yi 1995). Sometimes the inner structure is associated with an outer truncated thin disk.

Corona: The hot corona surrounding the accretion disk is optically thin and produces X-ray via Compton up-scattering of the UV-optical photons (Cyan line in Figure 1.3b). These X-rays can reflect from the accretion disk giving rise to a reflection component in hard X-rays[3](Green line; George & Fabian 1991).

Broad-Line Region (BLR): The UV and X-ray radiation coming from the accretion disk and corona photoionize the surrounding dense ($\sim 10^{10}$ cm^{-3}), high velocity ($10^3 - 10^4$ km s^{-1}) gas, which is still under the gravitational influence of the SMBH. This results in very broad emission lines (linewidths > 1000 km s^{-1}) in the optical and NIR bands. This emission defines the BLR. The high density of the gas means that only permitted (not forbidden) lines come from this region.

Narrow-Line Region (NLR): The radiation escaping from the polar regions

[3]X-ray regime of EM spectrum is broadly divided into two energy categories–'Soft' X-rays are from $0.5 - 10$ kev while 'Hard' X-rays are from $10 - 100$ kev.

also photoionizes a relatively lower density gas ($\sim 10^6 - 10^2$ cm^{-3}) residing beyond the BLR. The emission from this region includes both permitted and forbidden lines with narrower widths (a few hundred km s^{-1}). Hence, this region is called the NLR.

Torus: About one or two parsecs away from the central SMBH, the physical conditions are favorable enough for the existence of dust and molecular gas. This region of dusty molecular gas structure is called the torus that absorbs the incoming radiation from the accretion disk and emits thermal radiation peaking in MIR ($\lambda_{peak} \sim 1 - 10\mu$m). Although, as the name suggests, the geometry of this obscuring material is considered to be a torus, the exact structure is not yet clear, with some studies claiming a uniform dust distribution (e.g., Pier & Krolik, 1992; Fritz et al., 2006), and others finding the torus to be clumpy (e.g., Tristram et al., 2007; Assef et al., 2013).

Relativistic Jets: In about 10% of the luminous AGN, collimated, bipolar jets of relativistic plasma are also launched in the direction perpendicular to accretion disk (Blandford et al., 2019), capable of reaching very large distances up to to a few megaparsecs (e.g., Dabhade et al., 2020). The jets are thought to originate close to the accretion disk and are formed due to spinning black hole and magnetized accretion disk (Blandford & Znajek, 1977). A structured magnetic field around the jet axis accelerates electrons to velocities close to the speed of light (up to $0.2c$). The jet's emission profile is double-humped, one peak in the mm-NIR range, and another in the γ-ray band. The lower energy bump is due to synchrotron emission radiated by relativistic charged particles accelerating in a magnetic field. The origin of high-energy γ-ray emission is debated to be either inverse Compton scattering of ambient photons by relativistic electrons (e.g., Maraschi et al., 1992) or synchrotron emission from protons (Böttcher et al., 2013). In most cases, the emission from the jets is detected only in radio and γ-ray bands. In a minority of AGN population called blazars, the AGN is viewed directly along the jet axis, and the entire jet SED is relativistically boosted, outshining the emission from other AGN components as well as the host (e.g., Ghisellini, 2016). The radio emission from jets is a very well-studied phenomenon and is relevant to this work. I will return to discuss radio AGN in Section 1.4.

1.3.2 AGN Classification and Unification

Given their unusual emission involving a number of spectral features, various techniques have been devised to select large samples of AGN. Unfortunately, one consequence of these varied selection techniques, there has arisen a number of sub-classes, making a 'zoo' of AGN with some overlap between the classes (see the review by Padovani et al. (2017) for a detailed discussion on the AGN demographics). Different wavebands provide a window into various physical processes and AGN components, resulting in different kinds of AGNs. In radio surveys, AGNs are classified based on their morphologies (radio shapes), e.g., Fanaroff-Riley (FR) type I and II radio galaxies (Fanaroff & Riley, 1974) or radio spectrum, e.g., blazars (Giommi et al., 2013). The AGN heated dust in the torus emits in the MIR and is warmer than the dust heated by O/B stars in star-formation regions. This makes an efficient way to search for AGN, e.g., using MIR colors in photometric surveys (e.g., Lacy et al., 2004; Wright et al., 2010), MIR spectroscopic surveys (e.g., Alexander et al., 2008), and fitting MIR-FIR SEDs with AGN components (e.g., Sajina et al., 2012). However, as the Earth's atmosphere absorbs much of the MIR emission, these surveys are only possible with high-altitude or orbiting facilities, e.g., *SOFIA, Spitzer, WISE* (Lutz, 2014). Optical-UV-NIR surveys have used a number of criteria — optical-UV colors that reveal emission from the accretion disk (e.g., Richards et al., 2001), and emission line diagnostics the reveal the Broad and Narrow Line Regions (e.g., Baldwin et al., 1981; Kewley et al., 2006). The AGN classes identified via optical-UV surveys include Type 1 and 2 AGN, Seyfert 1/2 galaxies, Broad-line and Narrow-line AGN, and Radio galaxies (BLAGN, BLRG, NLAGN, and NLRG), and others (Padovani et al., 2017). Lastly, the X-ray band[4] provides one of the most reliable and complete ways to select AGN as they are among the brightest astrophysical objects in X-rays, and a number of X-ray surveys have provided uniform samples (e.g., Luo et al., 2017). However, heavily obscured AGN, meaning those in which the accretion disk is hidden by the dusty torus or larger scale dust distribution, are missing in X-rays surveys due to high column densities (Hickox & Alexander, 2018). This class of AGN is used in this thesis to study a population caught in a transient state in their lives, and we will revisit this topic in Section 1.6.

Although the number of AGN classes seems to indicate a large variation in their physical properties, the reality is much simpler, with a dependency on only a few parameters. In the 1980s, the "Unification Model" was the first attempt to explain the AGN diversity. This model suggests that many classes of AGN are intrinsically similar, and their observational differences are due to differences in the observer's viewing angle with respect to the dusty torus and relativistic jets (Antonucci, 1993; Urry & Padovani, 1995). Figure 1.4 shows an example of how different populations are connected but differ in the presence or absence of certain observed features due to the observer's orientation. When viewed through the torus, the dust obscures the central accretion disk and BLR, resulting in a Type 2 AGN or NLRG, whereas the BLR and accretion disk become visible when viewed at modest angles adding broad emission lines and blue continuum to the spectrum, making a Type 1 AGN or BLRG. When an AGN with jets is viewed directly down the jet, or close to it, we see the

[4]Like the MIR and FIR, X-rays can only be observed from orbiting satellites, e.g., *Chandra, XMM-Newton, and NuSTAR.*

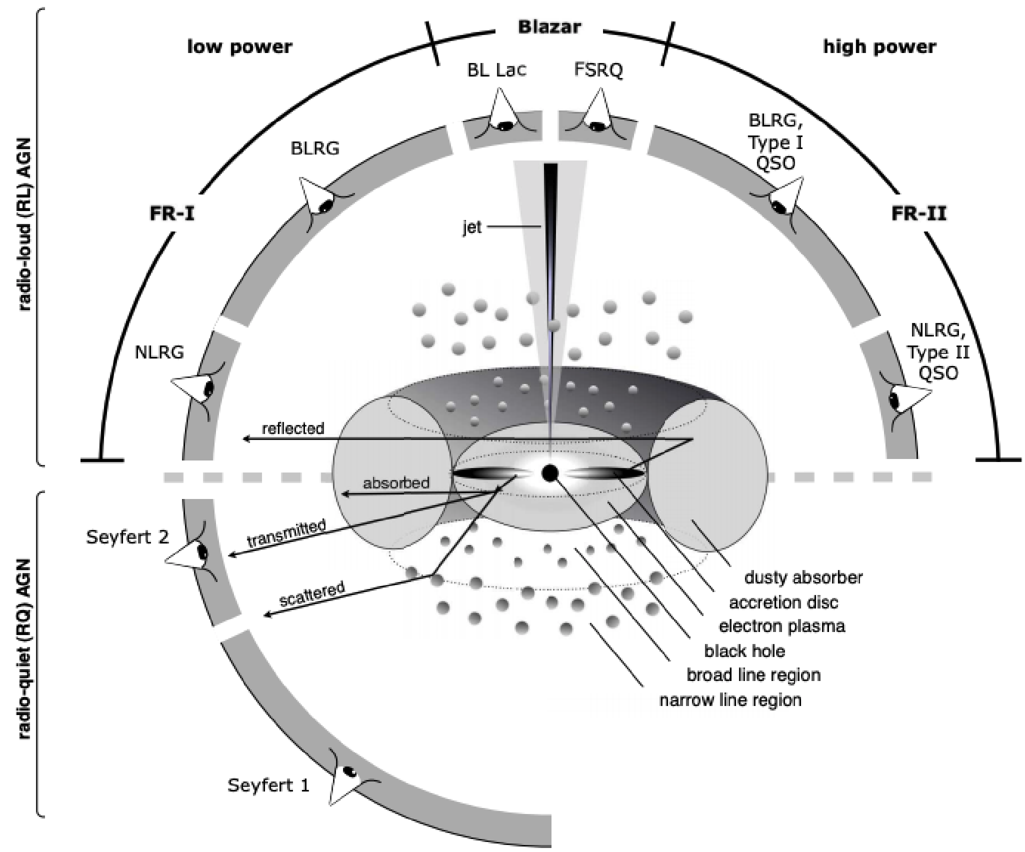

Figure 1.4: Figure from Beckmann & Shrader (2012) A schematic view of the AGN unification scheme. The type of AGN we observe is dependent on our line of sight to the AGN, the presence or absence of jets, and the power of the accreting black hole. Note that the jets are emitted in both directions. They are represented as one-sided here to incorporate both jetted and non-jetted AGN in one picture.

Doppler boosted emission from the jet, making it a blazar or Flat-Spectrum Radio Quasar (FSRQ).

Although this "strong" Unification model could explain the connections between Seyferts 1 and 2, NLRGs and BLRGs, and FSRQs-HEGs, it became clear that this model alone cannot explain the full diversity of AGN classes, and some other parameters besides viewing angle are also important (Netzer, 2015). As summarized in Padovani et al. (2017), I list the parameters here— 1) orientation angle, 2) the structure of emission flow divides AGN into radiative-mode and jet-mode AGN (Heckman & Best, 2014), 3) the presence or absence of a powerful relativistic jets giving jetted and not-jetted AGN (Padovani, 2016; Hardcastle & Croston, 2020), 4) the stage of development of AGN, e.g., compact radio AGN such as Gigahertz Peaked Spectrum (GPS) sources (O'Dea & Saikia, 2020) are recently triggered as opposed to old, large scale FRI/II radio galaxies. A further consideration is the host galaxy and its environment which seem to correlate with the AGN class, for example, jet-mode AGNs are found in massive elliptical galaxies while radiative-mode AGN are hosted by Spirals and Star-forming Galaxies (SFGs).

Over the years, we have realized that AGN play a critical role in the evolution of galaxies. Both observational and theoretical studies have enriched our understanding of AGNs and provided new insights into this phenomenon. We now know that BH growth and star formation activity are interlinked (Heckman & Best, 2014), and the activity in both these peaked around the epoch of high cosmic noon (Madau & Dickinson, 2014). AGNs can deposit large amounts of energy and momentum into their host galaxies, suppressing further accretion of gas (a process called "feedback") and affecting the evolution of the host galaxy (Fabian, 2012). Many questions, however, still remain unanswered. The AGN activity is not continuous and the AGN life-cycle is still an area of active research. To probe the feedback processes, thought to be responsible for setting up the co-evolution of SMBH and galaxies, we need more accurate observational constraints as well as improved hydrodynamic simulations. A complete census of AGN activity across a range of hosts and cosmic time is still incomplete due, in part, to the inevitable selection effects and instrumental limits.

The AGN sample presented here belongs to a class of heavily obscured, compact radio AGN. The motivation behind the selection of this sample is to find AGN caught in a brief early phase shortly after triggering. In the following sections, I describe the concepts relevant to the compact radio AGN (Section 1.4), obscured AGN, and their importance in studying the early phases in the life-cycles of AGN (Section 1.5) and our sample selection (Section 1.6).

1.4 Radio AGN

SFGs and AGN are the primary contributors to the radio sky (e.g., Miley, 1980; Condon, 1992). Their radio emission comes from synchrotron radiation from relativistic electrons spiraling in magnetic fields. The relativistic electrons are though to arise from shocks in supernova remnants in SFGs or jets in AGN. Understanding the origin of radio emission can be a difficult task (e.g., Nyland et al., 2016), but SFGs are generally weaker radio sources ($L_{1.4GHz} \lesssim 10^{23}$ W Hz^{-1}) and tend to dominate lower flux samples (Condon et al., 2002; Padovani, 2016). The bright radio sky ($S_{1.4.GHz} \gtrsim 0.1$ mJy) almost entirely consists of radio-emitting AGN and represents about $10\% - 15\%$ of the total AGN population (e.g., Sabater et al., 2019). Here, I outline some basics about Synchrotron emission, the main classes of radio AGN, and the evolutionary cycle of radio AGN, focusing on young radio AGN, which are the primary focus of this thesis.

1.4.1 Synchrotron Emission

Soon after the observations of radio galaxies (Jennison & Das Gupta, 1953; Baade & Minkowski, 1954), it was realized that radio structures stored enormous energies, and that synchrotron radiation was the source of the radio emission (e.g., Burbidge, 1956). The synchrotron process is non-thermal and occurs when relativistic electrons (or positrons) spiral around (i.e. accelerate around) magnetic field lines, and therefore radiate electromagnetic energy. The radio spectrum depends on the distribution of electron energies, which is assumed to have a power-law form: $n(E)dE = kE^{-\delta}dE$.

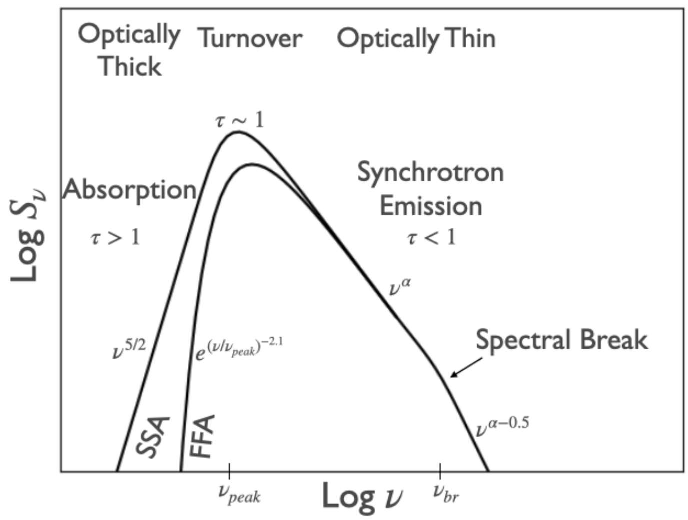

Figure 1.5: A schematic radio spectrum of synchrotron emission. The synchrotron emission follows a power law with a spectral index, α. We show two absorption models, SSA and FFA, making the spectra optically thick below the turnover frequency (ν_{peak}). A spectral break is observed at higher frequencies at ν_{br} due to the aging of high-energy electrons. Under the Continuous Injection model (Kardashev, 1962), the spectral index steepens by 0.5 above ν_{br}.

Here $n(E)$ is the number of electrons per unit volume within energy range E and $E + dE$, k is the normalizing factor, and δ is the power-law index. The emission spectrum can be derived by performing integration over a range of energies and pitch angles. The complete derivation can be found in Rybicki & Lightman (1986); Longair (2011); Beckmann & Shrader (2012), and Condon & Ransom (2016). For observational purposes, the radio emission is usually modeled as a power law, given by

$$S_\nu = S_0 \nu^\alpha \tag{1.1}$$

where S_ν is the flux per Hz observed at a frequency ν. S_0 is the normalizing factor, and α is the spectral index related to the electron energy distribution index as $\alpha = (1 - \delta)/2$. The spectral index is a key parameter that can help distinguish between thermal and non-thermal emission. In the case of optically-thin synchrotron emission, the value of α is -0.5 to -1.0, with a median of -0.7 (Condon et al., 2002). The spectral index from optically thin thermal free-free (Bremsstrahlung) emission in HII regions has a value of -0.2.

Synchrotron emission can be reabsorbed by the same, emitting, population of electrons present in the radiating plasma. This effect is called synchrotron self-absorption and for a given electron density and magnetic field strength, increases towards lower frequencies. Figure 1.5 shows a schematic spectrum with synchrotron emission and self-absorption (SSA). If there is a significant column of ionized thermal gas then free-free absorption (FFA) can occur, again increasing towards lower frequencies. The effects of absorption are seen in some young radio sources, and we will revisit radio spectra and the implications of low-frequency absorption in Chapter 3.

1.4.2 The Dichotomy in Radio AGN

The radio AGNs have been classified by radio morphology, the width of emission lines, and optical galaxy luminosity. Early samples of bright, multi-component radio galaxies were categorized by Fanaroff & Riley (1974) into two types called, Fanaroff-Riley Type I and II. The FRI sources are center-brightened with the brightest regions closer to the center (core), and FRII sources are edge-brightened with hotspots more than halfway from the core (Figure 1.6). Follow-up studies found that the FR morphological distinction is linked to radio luminosity and host galaxy luminosity (Ledlow & Owen, 1995). Fundamentally, the differences are thought to arise from differences in the accretion mode and jet power (e.g., Best & Heckman, 2012; Tadhunter, 2016; Hardcastle, 2018) and the environment into which the jets propagate (e.g., Capetti et al., 2017; Shabala, 2018). More recent radio surveys reaching lower flux limits (e.g., Shimwell et al., 2017; Lacy et al., 2020), have modified our view of the FR population, introducing sources of lower luminosity (e.g., Miraghaei & Best, 2017;

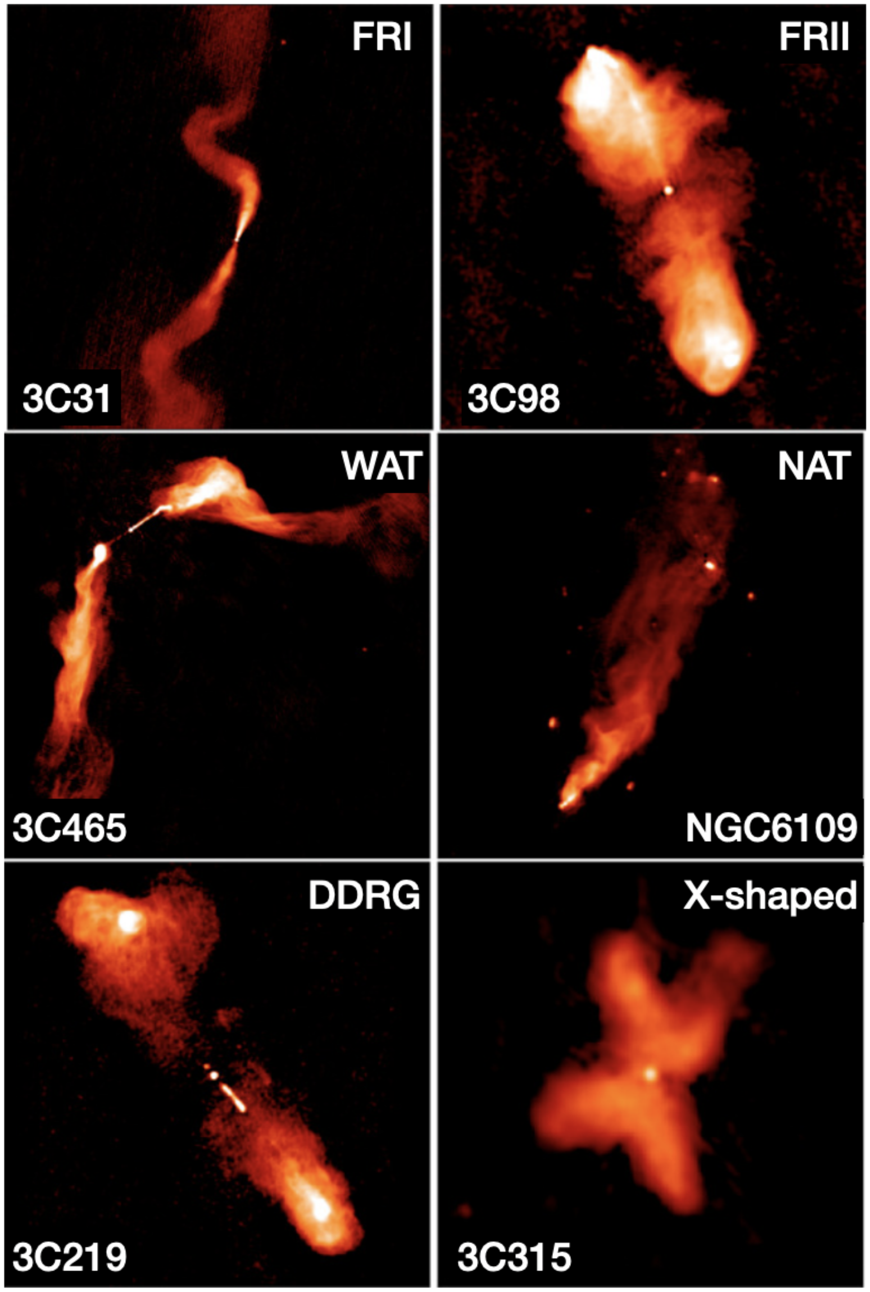

Figure 1.6: Examples of nearby radio AGN exhibiting a variety of morphologies. The top row includes classical FRI (3C31) and FRII (3C98) galaxies. The middle panel includes Wide-angle Tail (WAT) and Narrow-Angle Tail (NAT) sources typically seen in galaxy clusters. The bottom row includes two examples of restarted AGN with a double-double radio galaxy (3C219) and an X-shaped radio galaxy, 3C215. The figure is taken from Hardcastle & Croston (2020)

.

Capetti et al., 2017; Mingo et al., 2019), stressing the importance of environment in jet dynamics (Croston et al., 2018), and including a new FR0 population that lacks extended emission (Baldi et al., 2015). Yet further classes have been introduced based on the appearance of radio emission (Figure 1.6), such as X-shaped, double-double, narrow-angle-tailed, and wide-angle-tailed radio sources, which have been explained by appealing to source evolution and/or the interaction of the jet with the denser environments found in galaxy clusters.

Radio sources are also classified based on their radio spectra as steep ($\alpha < -0.5$) or flat($\alpha > -0.5$). Blazars show very compact, variable, flat spectrum emission and result from our viewpoint directly down, or close to, the jet (Urry & Padovani, 1995). There are two subgroups in the blazar class depending on the emission line optical spectra; FSRQ (with emission lines) and BL Lacs (lacking emission lines). The rest of the radio AGNs tend to have steep radio spectra over most observable frequencies.

Longair & Seldner (1979) first divided the optical emission line spectra of the radio sources from the Third Cambridge Catalog of Radio Sources(3CR). This method has been more generalized and expanded to separate radio and non-radio AGN using equivalent widths of emission lines or the presence of high/low excitation lines (e.g., Baldwin et al., 1981; Laing et al., 1994; Kewley et al., 2006). Quasars, Seyferts, and most FRIs belong to the High-Excitation Galaxies (HEG) or High-Excitation Radio Galaxies (HERG), if jets are present, whereas most FRIs belong to the Low-Excitation (Radio) Galaxies (LEG/LERG) category (e.g., Buttiglione et al., 2010; Gendre et al., 2013; Mingo et al., 2014). As is usually the case, the differences are thought to be related to the accretion mode and power, with HEGs having higher accretion rates, $L/L_{Edd} \gtrsim 0.1$ (e.g., Smolcic, 2016).

Another long-standing classification is Radio Quiet(RQ) and Radio Loud (RL) AGN that depends on radio luminosity (Peacock et al., 1986) or the ratio of radio and optical flux densities (Schmidt, 1970). Deep radio observations have shown that the RL AGN are jet-dominated, whereas RQ AGN can have mix of weak AGN and SF (Kimball et al., 2011; Kellermann et al., 2016). Therefore, as pointed out by Padovani (2016) and Padovani et al. (2017), this terminology can be misleading, and the actual naming should be based on the presence or absence of relativistic jets. Therefore, the term jetted and non-jetted AGN should be adopted as they are better suited to explain the intrinsic properties of AGN. I describe the evolution of jetted AGN and the young radio sources, which is the focus of this thesis.

1.4.3 Life Cycles of Radio AGN

It is now well established that powerful radio activity is intermittent and transient, with its active phase lasting about $10^7 - 10^8$ years (e.g., Shulevski et al., 2015; Jurlin et al., 2020). The life-cycle of a radio source refers to the path from its triggered onset through its large-scale extended FRI/II morphology, and on to its relic phase, and sometimes restarting again. During this life-cycle, the radio source evolves through a wide range of luminosity and morphological stages. This variation is assessed using the luminosity/radio power (P) *vs.* linear Size (D) diagram, also called the 'P-D' diagram (Figure 1.7). A source's location on this diagram provides us clues into its evolutionary stage and its fate (An & Baan, 2012).

What triggers a radio AGN is still an area of active research. The early phases are marked by compact linear sizes when jets are still confined within the host. A number of young radio AGN samples have been identified using various selection techniques (O'Dea 1998; Orienti 2016; O'Dea & Saikia 2020 for review). It is thought that the jet power and ambient medium determine how the compact source expands and whether it can develop into a classical FRI or FRII source. If the AGN activity turns off the source can enter a relic phase in which energy losses aren't replenished and the source

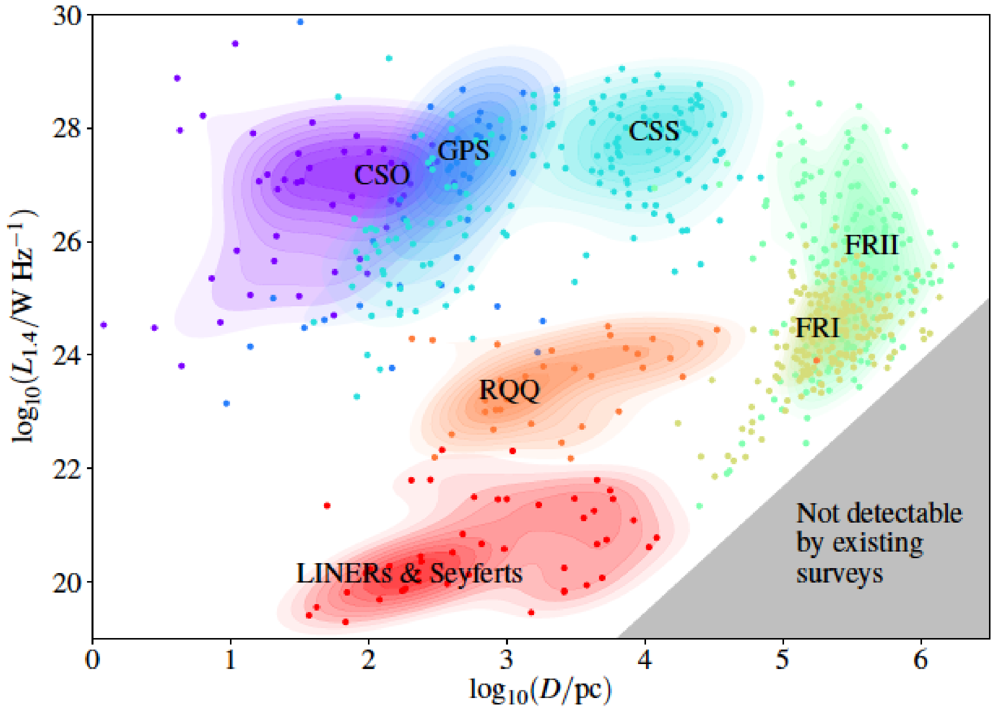

Figure 1.7: Figure taken from Hardcastle & Croston (2020). Radio luminosity *vs.* linear size diagram illustrating the variation in the extent of jet-structures and luminosities.

fades. These relic sources are difficult to identify, although recent advances at lower frequencies are enabling us to look into the remnant stages in more detail (Parma et al., 2007; Murgia et al., 2011; Brienza et al., 2017). A switched-off AGN can restart if the fuel supply is replenished, giving rise to a restarted AGN. Possible examples of these are the double-double radio galaxies (Saikia & Jamrozy, 2009; Mahatma et al., 2019).

A number of evolutionary models have been proposed to account for the wide variety of radio source size, power, spectrum, and morphology. An & Baan (2012) proposed that radio source morphology and spectrum depend on its luminosity, its evolutionary stage, and on the ambient medium. By tracking the pathways followed by different evolutionary scenarios in the P-D diagram, they proposed seven morphological types to explain most of the radio populations we see. Understanding the exact life-cycle of radio AGN is a complex question, and we have just begun to understand a few aspects of it. Current and next-generation large-scale radio surveys with improved sensitivity and resolution will be critical in the investigation of many open issues. The central question addressed in this thesis is the nature of the compact, young radio AGN and the impact of radio jets on the overall evolution of massive galaxies. In the next section, I summarize the properties of compact, young radio AGN.

1.4.4 Compact and Peaked-Spectrum Sources

Unlike the large-scale FRI/II sources, many radio sources in surveys like 3CR were found to be unresolved with an angular size limit of $\sim 1-2''$. Multi-wavelength radio observations revealed that only a minority of these compact sources were blazars and the rest had characteristic convex (peaked) shaped spectra. Gigahertz-Peaked Spectrum (GPS), Compact Steep Spectrum (CSS), and High-Frequency Peakers (HFP) are the powerful ($L_{1.4\mathrm{GHz}} > 10^{25}$ W Hz^{-1}) subgroups of radio loud AGN that are compact with peaked spectra. Their distinction is arbitrarily set based on the observing limitations and the turnover frequency (ν_{peak}). HFPs are the most compact with linear sizes < tens of pc and ν_{peak} of a few GHz. GPS show linear sizes of < 1 kpc and ν_{peak} between 500 MHz and 1 GHz. CSS are more extended with sizes between $1-10$ kpc and turnover frequencies below 500 MHz. Compact Symmetric Objects (CSO; LS < 500 pc) and Medium Symmetric Objects (MSO; 500 pc$\lesssim$LS$\lesssim$10 kpc) are another two categories of compact radio sources selected purely based on their morphologies in high-resolution surveys (Readhead et al., 1996). There is a significant overlap between CSO and GPS/HFPs, but not GPS are CSOs. In this, we will refer to all compact radio AGN as GPS/CSS sources. See reviews by O'Dea (1998);

Orienti (2016), and O'Dea & Saikia (2020) for further details.

These sources are thought to represent early evolutionary stages (ages $< 10^4 - 10^5$ years) in the life-cycle of what will ultimately become FRI/II radio sources (Snellen et al., 2000). I would like to note here that most of our understanding of young, compact radio sources, and therefore the discussion here, is based on high-luminosity samples due to the relatively high sensitivity limits of early radio surveys. More recently, samples have been found that probe lower luminosity sources with some evidence of jets on smaller scales (e.g., Baldi et al., 2015; Keim et al., 2019; Jarvis et al., 2019). However, the nature of these samples and their relation to well-known GPS/CSS are still not clear. As we are interested in understanding the youngest phases in the lives of powerful radio quasars, we will limit our discussion to the classical GPS/CSS sources.

Radio Properties:

The morphology of compact sources can be symmetric with a mini two-lobed structure like that of FRIIs. These sources are also termed CSO/MSO. However, many GPS/CSS show one-sided core-jet structures or even complex asymmetric structures. The reason could be, in part, due to beaming effects and/or jet-interaction with a non-uniform ambient medium.

The convex radio spectrum is the defining property of this population. While optically thin synchrotron generates the underlying power law, at high frequencies this can curve down due to radiative losses of the highest energy electrons, while low frequencies can be absorbed again leading to curvature or even a peak with an inverted spectrum on the low frequency side of the peak (Figure 1.5). There are two possible explanations considered for the absorption process; Synchrotron Self Absorption (SSA) and Free Free Absorption (FFA) from a dense ambient ionized medium. The investigation of the mechanism responsible for the turnover is important as it can constrain certain physical properties or the radio source and its environment. (e.g., Tingay & de Kool, 2003; Tingay et al., 2015; Callingham et al., 2015). This is still a topic of debate with observational support coming for both the interpretations (SSA— Snellen et al. 2000; Artyukh et al. 2008; de Vries et al. 2009; Jeyakumar 2016, and FFA– Bicknell et al. 1997; Tingay et al. 2015; Callingham et al. 2015; Bicknell et al. 2018; Mhaskey et al. 2019). The upcoming and future facilities with more sensitivity and wider spectral coverage may provide the necessary data to constrain the turnover mechanism.

While synchrotron emission is inherently polarized, the observed polarization of CSS/GPS sources depends on a critical size below which sources show weak or no polarization. This phenomenon is known as the Cotton effect (Cotton et al., 2003b). The gas in the NLR region could act as a Faraday screen depolarizing the synchrotron emission. Asymmetric structures seen in high-resolution polarized maps indeed suggest the possibility of a jet-ambient gas interaction in which the ambient medium contributes to the depolarization (Cotton et al., 2003a; Rossetti et al., 2006; Mantovani et al., 2013).

Another key property of GPS/CSS sources is the timescale of their variability. Long term monitoring of compact sources has revealed different results for different subgroups. The GPS/CSS galaxies are not variable on short time-scales with spectra changing only over months or years, likely related to the expansion of the source. In contrast, variability is more common in quasars and is likely to be linked to the beamed emission, which is well-known to be variable on shorter timescales. During flaring events, blazars can also show a peaked spectrum and might therefore contaminate samples of HFP/GPS/CSS (Tinti et al., 2005; Torniainen et al., 2007; Orienti et al., 2010). Ideally, a multi-frequency, multi-epoch program is necessary to reliably identify genuinely young radio sources and model their radio spectra.

Nature of GPS/CSS Sources

There seems to an overabundance of GPS/CSS sources (15%−30%) in flux-limited radio catalogs compared to predictions based on evolutionary models (O'Dea & Baum, 1997; Alexander, 2000). This evidence suggests that not all young sources evolve to become FRI/IIs, and the jet activity can be disrupted due to the dense environment of jet instabilities (Orienti et al., 2010; Czerny et al., 2009). The existence of dying or restarting compact radio sources supports AGN's intermittent nature (e.g., Kunert-Bajraszewska et al., 2010; Orienti et al., 2010; Wołowska et al., 2017). Current observational findings support a few bursts of $10^3 - 10^4$ years separated by $10^4 - 10^6$ years before starting a large-scale activity (Czerny et al., 2009).

Young and Evolving Sources: In the youth scenario, HFP/GPS/CSS are considered to be fundamentally the same class of radio source, but caught at different evolutionary stages (Phillips & Mutel, 1982; Fanti et al., 1995; Snellen et al., 2000). The semi-analytical models predict that CSO/HFPs propagate into the dense medium to become GPS and then CSSs; once jets break out of the host, they can continue to expand in a relatively low-density environment to become FR/IIs (e.g., Begelman, 1999; Snellen et al., 2000; An & Baan, 2012). The observational support for this hypothesis includes the estimation of kinematic ages (Polatidis & Conway, 2003; Gugliucci et al., 2005; An & Baan, 2012; Rastello et al., 2016) and radiative ages (Murgia et al., 1999; Orienti et al., 2010) which are $10 - 10^5$ years compared to a few Myr for FRI/II sources (e.g., Harwood, 2017)

Frustrated Scenario: The youth model alone is not able to explain all of the observed properties of the GPS/CSS sources, e.g., an excess space density of compact sources compared to FRI/II (An & Baan, 2012). The alternate hypothesis is that these sources are older but have been confined on smaller scales by the unusually

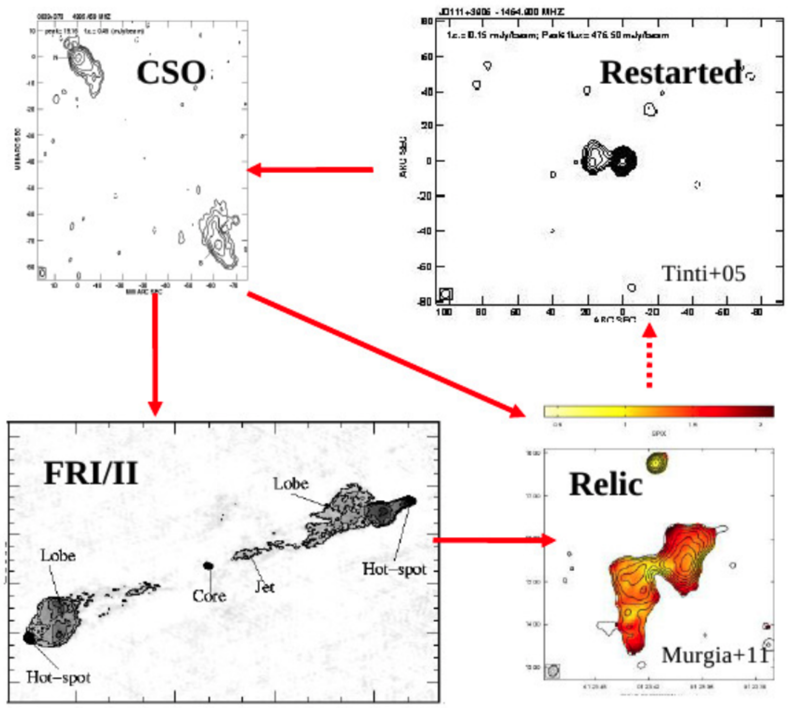

Figure 1.8: From Orienti (2016). The life-cycle of a jetted AGNs. A compact and young source may evolve to become a large-scale FRI/II source or shut down prematurely. Once the AGN activity stops, the source enters the relic phase. The activity may restart, forming a new young radio AGN.

dense nuclear environment of the host (van Breugel et al., 1984; O'Dea et al., 1991). The simulations of jets interacting with a dense ISM has shown that weaker jets are likely to stagnate for an extended period of time, *i.e.* frustrated, whereas powerful jets can move through the host ISM with ease (Bicknell & Sutherland, 2006; Mukherjee et al., 2016, 2018; Bicknell et al., 2018). There is some evidence for frustration in sources with dense ISM, but studies over larger samples are necessary to investigate this hypothesis further (O'Dea & Saikia, 2020).

The similarities between my sample of compact, radio quasars, and GPS/CSS sources are discussed in Chapters 2 and 3.

1.5 AGN Feedback and Obscured AGN

The accretion of SMBHs can release significant energy and momentum via radiation, winds, and radio jets. Through this ejecta, AGNs influence the surrounding interstellar and intergalactic media by purging the gas and dust from the nuclear regions and quenching star-formation, hence regulating the mass buildup of galaxies (Fabian, 2012; Harrison, 2017). This interaction, which is termed AGN feedback, is now routinely used in cosmological simulations to explain the overcooling problem in massive galaxies and the black-hole mass *vs.* bulge velocity dispersion ($M_{BH} - \sigma$) relation (e.g., Kauffmann & Haehnelt, 2000; Croton et al., 2006; Sijacki et al., 2015).

There are two types of AGN feedback that have become popularly discussed in the literature. Feedback associated with radiative-mode accretion (Quasars) is viewed as dominated by radiatively driven winds – hence 'wind-mode' – that have a direct impact on the ISM of the host galaxy. Feedback associated with jet-mode accretion arises when powerful radio jets impact the intra-cluster medium (ICM), creating X-ray bubbles and preventing cooling flows onto the central cluster galaxy. There is now compelling observational evidence in the nearby universe for radio jets regulating the gas cooling and star-formation levels in massive galaxies (McNamara & Nulsen, 2012; Fabian, 2012). On smaller scales, the AGN wind-driven outflows are considered to be the primary driver of feedback (King & Pounds, 2015). A growing number of detections of multi-phase ISM outflows (see Morganti, 2017b, for review) are providing crucial insights into the complex nature of the AGN-ISM interaction.

Radio jets are now well-known to drive feedback on large-scales, for example surrounding central cluster galaxies. However, on smaller scales, the role of radio jets in feedback is less clear, at least observationally. Theoretically, recent hydrodynamic simulations strongly suggest that relativistic jets confined in a dense ISM do indeed lead to its dispersal and heating (Wagner et al., 2012; Mukherjee et al., 2016; Bicknell et al., 2018; Mukherjee et al., 2018). The possible role of radio jet feedback on smaller scales is central to my thesis.

One of the observational challenges in investigating jet-ISM feedback is identifying powerful radio AGNs that are actively interacting with their hosts. Such systems are likely to be present during the peak epoch of cosmic assembly ($z \sim 2$) and are easier to detect in luminous (quasar) systems that contain newly launched, powerful radio jets embedded in large gas and dust reservoirs. Such quasars are expected to be heavily obscured and faint in the optical and X-ray but identifiable based on their red infrared colors and bright, compact radio emission. Therefore, young, luminous $z \sim 2$ radio AGN such as GPS/CSS sources that are also obscured would be ideal candidates to investigate the role and the importance of small, powerful radio jets on the dispersal and compression of the galaxy's ISM and the associated quenching or triggering of star formation. Finding such a sample requires combining various AGN selection techniques and extensive sky coverage as we expect such sources to be rare. This thesis has applied a careful selection to identify such a sample. I provided background on young, compact radio AGN in the previous section. I describe the identification of obscured AGN in the next section and the details of our sample selection in Section 1.6.

1.5.1 Obscured AGN as Tracers of Merger Activity

In obscured AGN the intense optical/UV/X-ray light from the accretion disk is absorbed or scattered by gas and dust surrounding the AGN. As a result, the primary AGN radiation is not seen directly but is only inferred from emission at other wavelengths, for example as MIR-FIR emission from the same dust that absorbed the primary radiation (Hickox & Alexander, 2018, and references therein). A significant

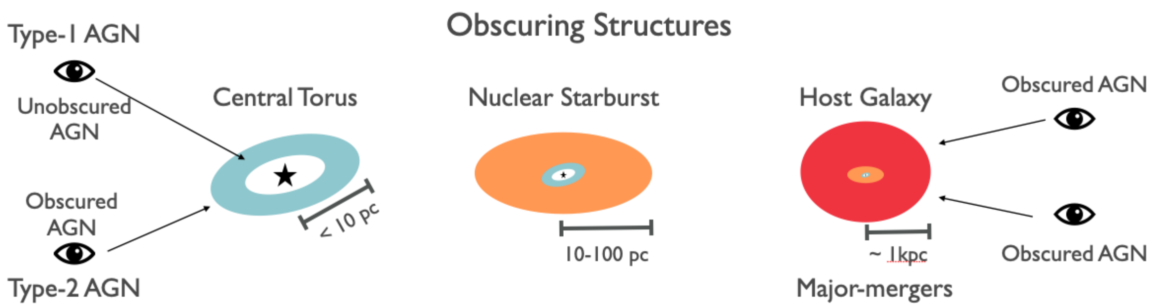

Figure 1.9: A simplified schematic view showing different levels of obscuration. On the smallest scales (< 10 pc), the central torus can block the central engine resulting in an orientation-dependent Type 1 and Type 2 AGN. The central starburst (middle) or merger events (right) can create an obscuring structure on larger scales. In some specific cases, large column densities in galaxy mergers can completely obscure the central AGN.

population of AGN is found to be obscured (e.g., Ueda et al., 2014; Buchner et al., 2015). To characterize the onset of AGN activity, it is important to study complete samples of obscured and unobscured AGN. Figure 1.9 provides a simplified schematic view of thee regimes of obscuration as identified by (Hickox & Alexander, 2018). First, possibly the most common is the central torus (< 10 pc) residing just outside the accretion disk and BLR, giving rise to orientation dependant Type 2 AGN (e.g., QSO2 and Seyfert 2). However, the simplistic unified model of a thick, donut-shaped torus has undergone significant revision over the past few decades and a more recent picture of them is reviewed by Netzer (2015) and Ramos Almeida & Ricci (2017). Second, the dense gas associated with a nuclear ($\sim 10 - 100$ pc) starburst can also obscure an AGN. Some evidence for this is the correlation between AGN luminosity and current star formation (Esquej et al., 2014), but it is difficult to distinguish between the effects of a torus and/or a starburst.

A third regime, which is also important to my thesis, is galaxy-wide ($\lesssim 1$ kpc) obscuration. In a gas-rich major merger, large amounts of cold gas are funneled to the central regions, leading to a starburst followed by a rapidly accreting SMBH (e.g., Hopkins et al., 2008; Alexander & Hickox, 2012). During the early SMBH growth, the AGN will be shrouded in galaxy-scale dust and gas, which is also triggering an intense starburst. This initial phase is thought to be followed by the blowout phase, when AGN feedback disperses the gas via winds, radiation, and/or relativistic jets, to reveal an unobscured (Type 1) quasar. The existence of an important merger-AGN connection is debated with a number of studies providing contradicting results (Villforth et al., 2017a; Farrah et al., 2017; Goulding et al., 2018). It has become clear, however, that at least powerful, obscured AGN tend to be associated with large-scale obscuring structures which are in turn linked to mergers (e.g., Merloni et al., 2014; Chen et al., 2015b; Fan et al., 2016; Ricci et al., 2017a).

Characterizing obscured AGN can therefore provide insights into the role of obscuration in SMBH-galaxy co-evolution and AGN feedback. While heavily obscured systems are challenging to detect at optical and X-ray wavelengths, they are transparent at radio and MIR wavelengths. MIR color diagnostics using telescopes such as Spitzer or WISE can identify the most luminous and heavily obscured AGN, which are believed to represent a transient phase of rapid, massive black hole growth (e.g., Wu et al., 2012a; Assef et al., 2015). My thesis presents a sample that was identified by combining MIR and radio AGN selection. Some fraction of obscured AGN will also have jets, so by selecting obscured quasars associated with compact radio sources, we are in a strong position to observe the impact of jets on the surrounding gas. Recent hydrodynamical simulations also suggest that relativistic jets, when confined on galactic scales, can heat and disperse the dense ISM (e.g., Wagner et al., 2012; Mukherjee et al., 2016, 2018; Bicknell et al., 2018). In the next section, I discuss our sample selection and results published prior to this thesis.

1.5.2 The Era of WISE

Following the opening of the field of extragalactic astronomy in the early seventies (Kleinmann & Low, 1970), the Infrared Astronomical Satellite (IRAS) allowed the selection of a significant sample of nearby MIR-selected AGN (Spinoglio & Malkan, 1989; Wolstencroft et al., 2000). It was soon realized that the bright emission peaking around $3 - 20\mu$m was due to the torus of dust and gas with thick columns (Pier & Krolik, 1992). The advent of Spitzer, launched in 2003 allowed efficient identification of large samples of AGN (Lacy et al., 2004; Lacy & Sajina, 2020). The Wide-Field Infrared Explorer (WISE), launched in 2009, is the latest MIR telescope that has continued the legacy of Spitzer in the study of IR selected AGN (Wright et al., 2010). The WISE mission used a 0.4-m telescope to observe the entire sky in 4 bands 3.5 (W1), 4.6 (W2), 12 (W3), and 22 (W4) μm. Although WISE is less sensitive than Spitzer, WISE's all-sky coverage has found millions of AGN (Assef et al., 2018), including a rare population of heavily obscured and luminous quasars (Lonsdale et al., 2015).

MIR colors can distinguish AGN from other extragalactic populations due to their emission from warm or hot dust heated by the AGN. Many color selection criteria have been developed using Spitzer (e.g., Stern et al., 2005; Mateos et al., 2012) and WISE (e.g., Assef et al., 2013; Mateos et al., 2013) fluxes to identify powerful AGN that are both unobscured and obscured. As shown in the right panel of Figure 1.10, obscured quasars tend to have very red colors in the MIR color-color plane. The reddest colors in the WISE color-color plane come from a rare population representing the most heavily obscured and hyperluminous quasars, e.g., Hot Dust Obscured Galaxies (Hot DOGs; Eisenhardt et al. 2012; Wu et al. 2012a). Their SEDs are dominated by MIR emission from hot dust and have extreme IR and bolometric luminosities (Bridge et al., 2013; Assef et al., 2015; Tsai et al., 2015). Multi-wavelength follow-up studies have revealed the presence of radiative-mode AGN (Assef et al., 2015; Wu et al., 2018; Tsai et al., 2018) embedded in a gas with a very high column density (e.g., Vito et al., 2018), and outflows indicative of strong AGN feedback (e.g., Díaz-Santos et al., 2018; Wu et al., 2018; Jun et al., 2020). The observations support the scenario predicted from simulations that Hot DOGs are in the short-lived, peak-fueling phase of the merger-triggered AGN. This thesis uses similar WISE colors to select a related sample of heavily obscured and luminous quasars, but our sample additionally has a compact radio source, as explained below.

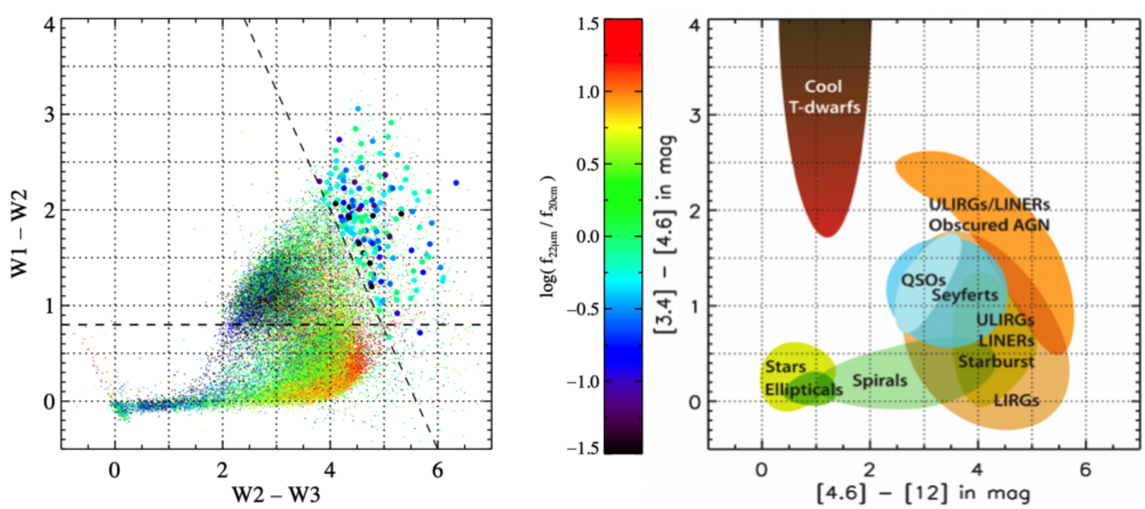

Figure 1.10: The selection method and nature of our parent sample. **Left:**(a) WISE color-color ($3.4 - 4.6 - 12\,\mu$m; in Vega magnitudes) showing the full WISE-NVSS sample of 54,457 sources, color-coded by radio-loudness as shown by the color bar on the right. Our sample of 166 red, obscured, hyper-luminous and radio powerful AGN is shown by large filled circles on the right of the selection line. The black horizontal dashed line shows the AGN color-selection criterion used by Stern et al. (2012): $(W1 - W2)$>0.8. **Right:** (b) From Wright et al. (2010): WISE color-color plane showing the locations of different classes of population. The obscured AGN and Ultra-Luminous Infrared Galaxies (ULIRGs) occupy the reddest parts in both colors.

1.6 A Unique Sample of Dusty, Hyper-luminous Quasars

We have combined the high sensitivity all-sky WISE MIR survey (Wright et al., 2010) at 3.4, 4.6, 12, and 22μm with a radio detection to select a new population of obscured but luminous young radio AGN. We selected the most obscured and luminous ($f_{22\,\mu\mathrm{m}} > 7$ mJy) AGN in the WISE catalog: those with the reddest MIR colors ($[W2-W3]+1.25[W1-W2]-7>0$) and red MIR-optical colors (Figure 1.10). The wide sky coverage allows for the identification of rare, extremely red sources (redder than Spitzer-selected Dust Obscured Galaxies (DOGs), Polletta et al. 2008; Dey et al. 2008 and similar to the radio-quiet Hot DOGs), and not found in earlier, smaller area Spitzer surveys. This sample was cross-matched with unresolved radio sources from teh 21cm NRAO VLA Sky Survey (NVSS; Condon et al. 1998) and Faint Images of the Radio Sky at Twenty-centimeters (FIRST; Becker et al. 1995) surveys. Hence, we will refer to our sample as the 'WISE-NVSS' sample.

Furthermore, visual inspection was performed in two optical surveys; the Sloan Digital Sky Survey (SDSS; York et al. 2000) and the Digitized Sky Survey (DSS), to select only sources with faint or no optical counterparts. This eliminates any artifacts and low redshift objects, guaranteeing the sources are at significant redshift. The final sample had 166 sources, which is sufficiently small for follow-up observations while sufficiently large for statistical analysis. These sources define the parent sample in our investigation of feedback from young radio jets. Details of the sample selection are presented in Lonsdale et al. (2015).

Our sample is very similar to the WISE Hot DOGs in the selection method, MIR luminosity, and SED shape (Figure 1.11). However, it is distinct from these WISE and Spitzer samples in being radio-loud via the NVSS/FIRST cross-match. One aim of our selection is to find sources in a unique evolutionary stage, shortly after the

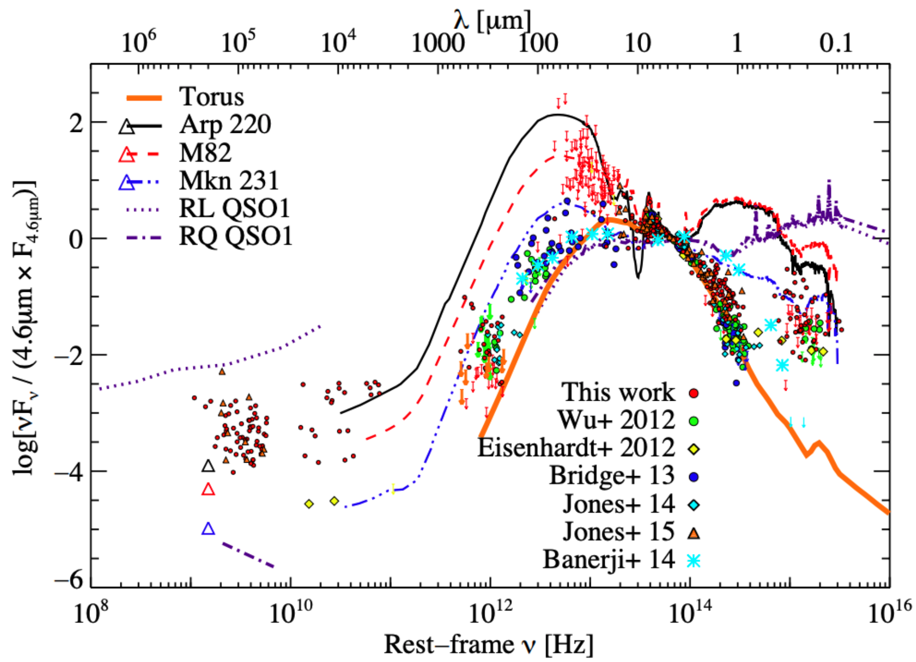

Figure 1.11: The rest-frame SEDs for our red, WISE-NVSS selected sources normalized at 4.6μm (red) compared to WISE radio-quiet Hot DOGs (purple, Eisenhardt et al. 2012; Wu et al. 2012a), Spitzer samples (orange) and starburst-dominated sources (blue), optical AGN (cyan) and radio galaxies (green), compared with AGN and LIRG templates, AGNs from (Shang et al., 2011), and a highly obscured torus. The sources from this work (red) are the reddest, with submm SEDs similar to well-known AGN and the torus templates but significantly redder near MIR-optical.

(re)ignition of the radio AGN, while the host galaxy is still experiencing substantial starburst activity. Therefore, it is important to understand how our sample is different from other Spitzer and WISE mid-IR (MIR) extremely red samples.

1.6.1 Results So Far

The parent sample of 166 sources has been the subject of several follow-up studies, including: a snapshot survey of 49 sources using ALMA Cycle-0 Band-7 led by Dr. Carol Lonsdale; a snapshot survey of 90 sources at C-band using the VLBA led by Prof. Colin Lonsdale; JK band VLT/ISAAC imaging of 31 led by Prof. Andrew Blain; r,g,J,K LBT imaging of 12 sources led by Prof. Mark Whittle; and [OIII] line spectroscopy of 24 sources using FLAMINGOS-2 on Gemini led by Dr. Minjin Kim. An entire sample has also been observed at sub-arcsecond resolution in X-band with the VLA. The primary aim of this follow-up survey was to test and select sources that are truly compact and therefore possibly young. This VLA survey is the subject of this dissertation research and is presented in Chapters 2 and 3. Here, I briefly summarize results from other follow-up surveys.

Optical-NIR Spectroscopy: Optical/NIR spectroscopy was obtained for 71 out of 80 sources attempted using several telescopes (Farris et al. in prep; see Lonsdale et al. 2015 for summary). The redshift range is $0.3 < z < 2.85$, with Type 2 AGN emission line spectra in most cases. Using these redshifts, the mid-IR luminosities reach $\sim 10^{14} L_{\odot}$, which is significantly greater than typical radio galaxies and quasars. Thus, we confirm our sample comprises some of the most luminous AGN known.

FIR and Sub-mm data: ALMA observed 49 southern sources in Band-7(345 GHz/870 μm) during Cycle-0 (Lonsdale et al., 2015). The observations have a resulting resolution of $0.5''-1.2''$, 1.5 min on-source integration time, and an rms noise of $0.3-0.6$ mJy beam^{-1}. ALMA detected 26 of the 49 sources with unresolved emission on $\sim 1''$ scales. The MIR-submm SEDs are AGN-dominated and fits that include a cooler FIR component indicate star formation rates comparable to those of local ULIRGs and Hyper-LIRGs ($L_{FIR} > 10^{12} - 10^{13} L_{\odot}$; SFRs $> 10^2 - 10^3 M_{\odot}$ yr^{-1}, respectively).

[OIII] line spectroscopy: NIR spectra of 24 sources reveal outflows for six objects from their broad [OIII] λ5007Å emission-line profile (Kim et al., 2013), and at least one object has a Broad Absorption Line (BAL) system. Following the method of Shen et al. (2011), the [OIII] 5007 line luminosities indicate SMBH masses of $\sim 10^9 M_{\odot}$. These would be amongst the most massive known SMBHs at $z \sim 2$.

1.6.2 Overarching Goals

After cross-matching WISE and NVSS, we can isolate just the radio-loud AGN. This combined selection yields a very rare sample of very luminous sources, with a surface density of 0.025 per square degree.

Our overarching science goals are to investigate how small ($\sim$5pc to $\sim$20 kpc scales), young ($10^{<2-5}$ yrs), and powerful radio jets interact with the ISM in massive gas-rich mergers near the peak of galaxy and SMBH building, $z \sim 1-3$. This carefully selected sample fills a unique niche: the quasars are caught in a brief and early phase, making them ideal for testing feedback and evolutionary scenarios at this important epoch. Furthermore, the high nuclear obscuration provides an excellent opportunity to study the host galaxies since the quasar light is itself blocked.

1.7 Radio Astronomy

Radio waves lie at one end of the electromagnetic spectrum with the longest wavelengths and lowest energies. The radio band is broad, spanning almost five decades in frequency from $\sim$ 10 MHz – 300 GHz. Radio astronomy focuses on the study of the radio emission coming from celestial objects. The Earth's atmosphere is transparent to radio waves allowing us to build telescopes on the ground. Radio astronomy began in 1932 with a serendipitous detection of the radio emission coming from our Galaxy. Karl G. Jansky, a radio engineer from the Bell Telephone Laboratories, identified that the noisy static in short-wave voice communications came from the Milky Way's center (Jansky, 1933). Since this pioneering work, the field of radio astronomy flourished and made significant contributions to our understanding of the Universe. In a sense, radio observations have provided a parallel view of the Universe, revealing objects and astrophysical phenomena not previously known.

1.7.1 Observational Techniques

Radio observations are conducted using single radio antenna or many connected radio antennas. The antenna has two primary components — a parabolic shaped reflector dish and a receiver. The dish collects incoming radio waves and reflects them to a feed, which sends the signal to the receiver. As the total power received by radio telescopes is minuscule, the receiver amplifies the weak signal and transmits the data to a recorder for further processing and storage. The total power received is expressed as the flux density[5] and is measured in a unit of Jansky (Jy), named in honor of Karl Jansky. The SI conversion is given as

$$1\,\mathrm{Jy} = 10^{-26}\,\mathrm{Wm^{-2}Hz^{-1}} \tag{1.2}$$

The radio dish size is an essential factor as it can determine the sensitivity, resolution and field of view of the observations. The resolution of a radio antenna is given as the full-width half maximum of the antenna's response beam, which in most cases, is an Airy Disk pattern.

$$\theta_{FWHM} = 1.22\frac{\lambda}{D} \tag{1.3}$$

where θ_{FWHM} is the resolution in radians, λ is the observing wavelength, and D is the radio antenna's diameter.

Due to the longer wavelengths of radio, the size of the dish must be larger to achieve a reasonable resolution and the sensitivity to detect faint radio emission. The current single-dish facilities, such as the Green Bank Telescope (GBT) and Arecibo Telescope have $\sim$ 100m antenna diameters providing a resolution of a few arcminutes. To obtain a resolution comparable to ground based optical telescopes ($\sim 1''$),

[5] Flux density S_ν of a source is the total power received per unit frequency per unit detector area.

we would need to build radio antennas with impossibly large apertures. Therefore, an interferometry technique — observing with an array of moderately-sized radio antennas spaced across a large area – was developed to overcome the limitations of the single-dish antennas

Radio Interferometers

Interferometers are the core instrument in radio astronomy. A basic interferometer consists of two equal-sized radio antennas separated by a distance and whose output is correlated in the simplest form. Effectively, this formation will be a radio telescope with a collecting area of $2\pi D^2$ and a resolution of $\sim \lambda/b$, where D is the diameter of the individual dish, and b is a distance between two antennas. In reality, a typical interferometer has many antennas to obtain good sensitivity. Some of the most heavily used radio interferometers are Atacama Large Millimeter Array (ALMA) in Chile; NSF's Karl G. Jansky Very Large Array (VLA) in New Mexico, USA; the Low-Frequency Array (LOFAR) in the Netherlands; MeerKAT in South Africa; the Giant Meterwave Radio Telescope (GMRT) in India; and the Australian Square Kilometer Array Pathfinder (ASKAP) in Australia.

An interferometer acts as a single-dish telescope with a huge partially filled aperture of a size equal to the array's maximum baseline, b_{max}. This aperture is sampled only in places for which a linked element exists. The baselines are vector quantities measured in wavelength units and are projected onto a reference plane called the $uv-$ plane. These projected baselines are called spacings and are evaluated by the following equation,

$$u = b_x/\lambda, \;\; v = b_y/\lambda, \;\; w = b_z/\lambda \tag{1.4}$$

The natural radio signal from any cosmic radio source produces a voltage gain in an interferometer, which is then correlated to produce a complex visibility function,

$V(u, v, w)$. The visibilities are expressed in the $uv-$plane and are the Fourier Transform of the sky brightness distribution. The strength of the signal is dependent on the source time integration and observing bandwidth as each of these factors will increase the sampling of the synthesized aperture. The Earth's rotation changes the projected baselines over time, filling in more points on the $uv-$plane. This Earth rotation aperture synthesis technique was invented by Sir Martin Ryle in the 1960s (Ryle, 1962) and later awarded a Nobel Physics Prize in 1974. Modern telescopes have become quite sophisticated with superior sensitivity and improved receiver technology, providing better positional accuracy, observations over a wide bandwidth that can be divided into narrow frequency channels for spectral line studies. Now, I provide a brief introduction to the radio telescopes used extensively in my dissertation research.

Figure 1.12: The Very Large Array (VLA), an Interferometer in New Mexico, USA. Image courtesy of NRAO.

VLA:

Ever since the VLA became operational in 1980, it has been the most flexible and widely used telescope in the world. The VLA is operated by the National Radio Astronomy Observatory (NRAO) [6] and is located near Socorro, New Mexico (Figure 1.12). It has a Y-shaped array with 27 antennas, each with a diameter of 25 meters. The antennas are mounted on movable tracks providing four different configurations to balance the sensitivity and angular resolution by varying the array density and maximum antenna separations. The VLA cycles through four array configurations, A, B, C, and D, over two years, with A being the most extended configuration (b_{max}=36.4 km), and D being the most compact (b_{max}=1.03 km). The VLA allows for wideband, spectral, subarray observing modes as well as full-polarization mode. The available frequency coverage is uniform over a range from 1 to 50 GHz, divided into eight bands and an additional P-band with a total range from 220−500 MHz. My thesis focuses on this instrument, and I discuss the follow-up snapshot VLA imaging survey of WISE-NVSS quasars in Chapters 2 and 3.

Very Long Baseline Interferometry

Very Long Baseline Interferometry (VLBI) is a general technique that takes interferometry to the next level by connecting radio antennas across very large distances or even across continents, thereby providing a very high resolution. Due to missing shorter baselines, VLBI telescopes have lower sensitivity limits than regular interferometers such as the VLA and are only sensitive to compact, high-surface brightness emission. The Very Large Baseline Array (VLBA) is the NRAO's VLBI facility with ten identical 25-m antennas stationed across the USA. The baselines range from $\sim$ 400

[6] The National Radio Astronomy Observatory is a facility of the National Science Foundation operated under cooperative agreement by Associated Universities, Inc.

km to 8600 km (the longest baseline is between Mauna Kea, Hawaii and St. Croix, Virgin Islands). Although the VLBA has very low surface brightness sensitivity, its excellent angular resolution can probe the AGN's milliarcsecond-level structures. VLBA is also used to obtain precise astrometric measurements with an accuracy of ∼10 microarcseconds. The typical resolution offered is about a few to tens of milliarcseconds. VLBA operates in ten observing bands at frequencies ranging from 0.312 GHz to 90 GHz with a maximum bandwidth of 1 GHz. As our sample is expected to have compact radio emission, a subsample of 90 were observed for quick-look imaging with VLBA (Lonsdale et al., in prep). I will further explain VLBA imaging and some preliminary results in Section 5.1.2.

ALMA

ALMA is the latest breakthrough telescope located at very high altitudes on Chajnantor plateau in Northern Chile. Unlike the previously described telescopes, ALMA operates at millimeter and submillimeter wavelengths with corresponding receiver frequencies in the range 84−950 GHz. It is the most complex and expensive ground-based telescope built through an international collaboration including the NRAO[7]. ALMA is an interferometer with 66 antennas – 12 of 7-m antennas forming a compact array and 54 of 12-m, movable antennas forming a reconfigurable array. Similar to VLA, ALMA cycles through its ten configurations over one year. The most compact configuration has its longest baseline of 0.16 km giving a resolution of $\sim 1''$at 200 GHz and is ideal for studying extended, low-surface brightness emission. The most extended configuration has a maximum baseline of 16 km providing sub-arcsecond resolution in all available bands. ALMA began its operations in late 2011 and has

[7]ALMA is a partnership of ESO (representing its member states), NSF (USA) and NINS (Japan), together with NRC (Canada), MOST and ASIAA (Taiwan), and KASI (Republic of Korea), in cooperation with the Republic of Chile. The Joint ALMA Observatory is operated by ESO, AUI/NRAO and NAOJ.

become the most powerful telescope in millimeter astronomy in just a few years. Through its unique capabilities, ALMA has produced spectacular results about complex chemistry in our solar systems, the formation of planetary systems, the study of gas and dust in distant galaxies. In Chapter 4, I present the serendipitous discovery of a new class of distant galaxies using ALMA.

Next-generation Interferometers

The next-generation facilities are aimed to provide dramatic improvements in the technical capabilities of current generation telescopes and probe the Universe in unprecedented detail. The Square Kilometer Array (SKA) and next-generation Very Large Array (ngVLA) are the two radio interferometers that will provide complementary frequency coverage and open up a new parameter space via ultra-sensitive and high-resolution imaging. In Section 5.4, I will explore the role of ngVLA in improving our understanding of AGNs.

1.8 Thesis Outline

The thesis research focuses on two key populations identified during an epoch when the galaxies were most active. I use radio and submillimeter interferometric observations to study several processes associated with AGNs and star formation that are invisible in the optical but are apparent in the radio. Specifically, the open questions I will address are: (1) What is the nature of radio emission associated with heavily reddened, ultra-luminous quasar hosts at $z \sim 2$? (2) Are these radio sources consistent with a young radio AGN embedded in a dense ISM? (3) What are the multi-wavelength properties of the faint dusty star-forming galaxies?

The structure of the thesis is as follows. Chapters 2 and 3 investigate the radio continuum properties of a sample of heavily obscured, ultra-luminous quasars found in the redshift range $0.8 < z < 3$. Chapter 2 presents sub-arcsecond-resolution 10 GHz VLA imaging to constrain the spatial scales and morphology of the radio emission associated with the quasar (Patil et al., 2020). Chapter 3 uses the 10 GHz snapshot data and other radio archival data to construct, and interpret, the radio spectra of the sample, deriving a number of properties of the sources (Patil et al., 2021 in preparation). Chapter 4 presents a new sample of faint SMGs detected serendipitously in the ALMA archival data (Patil et al., 2019). Chapter 5 describes a number of ongoing observing projects targeting sub-samples from the main sample, and also looks forward to the contribution from the next-generation Very Large Array (ngVLA) to our understanding of young radio AGN and their impact on galaxy evolution (Patil et al., 2018). I provide a summary and concluding remarks in Chapter 6.

Contributions

Chapters 2 and 4 are published as peer-reviewed journal articles. Chapter 3 is in preparation and will be submitted to a journal. Throughout this work, we relied on large, publicly available astronomical surveys. These surveys are made possible by substantial efforts from teams that run and support the facilities and produce final products. We have also used several open-source software packages developed for the astronomical and broader scientific community. Such tools are the backbone of many research projects, including this work. Besides, this thesis has benefited from advice and guidance from many individuals represented as co-authors in the published articles.

The sample presented in Chapters 2 and 3 is selected by Carol Lonsdale. She proposed and gathered the VLA observations that form the basis of these two chapters. Carol and other co-authors in the published article have contributed their expertise and time to shape the direction of this project. Mark Whittle has guided and supported the entire development of the Chapters 2 and 3 through many contributions, feedback, reviews, and suggestions. I performed the complete interferometric data reduction, imaging, and measurement analysis in both chapters. In addition to giving feedback on both chapters, Kristina Nyland analyzed the presence of diffuse radio emission in our sample. Her contribution was particularly important to confirm the compact nature of our radio sources. I performed all of the remaining analyses presented in Chapter 2. Dipanjan Mukherjee provided the analytical framework for the lobe expansion model in Section 2.7.2. Chapter 2 has also benefited from invaluable insights from Mark Lacy, Amy Kimball, Colin Lonsdale, Andrew Blain, Jeremy Harwood, Belinda Wilkes, Lauranne Lanz, and Andreas Efstathiou.

The radio spectra analysis in Chapter 3 also includes commensal VLITE data courtesy of Tracy Clarke and the VLITE team at the NRL. I developed a procedure to perform the data mining, construct radio spectra, and the spectral fitting (Figure 3.1), which is now used in other projects, e.g., Nyland et al. (2020).

Chapter 4 is developed under the guidance of Kristina Nyland and Mark Lacy. Their continued support and feedback have helped shape the main results. The ancillary data is available through SERVS collaboration, led by Mark Lacy. Many of the co-authors are also part of this collaboration and have provided useful comments on the manuscript. I performed the complete analysis from mining the ALMA archive and reducing the data to creating the final catalog. Kristina Nyland performed the forced photometry and provided the 13-band optical-NIR catalog. This data has allowed us to investigate the multi-wavelength properties of the recently discovered population of faint SMGs.

Chapter 2

High-resolution VLA Imaging of Obscured Quasars: Young Radio Jets Caught in a Dense ISM

2.1 Introduction

The active galactic nucleus (AGN) phenomenon, driven by accretion onto supermassive black holes (SMBHs), is believed to play an important role in the evolution of galaxies over cosmic time. There is now compelling evidence interlinking SMBH growth with host galaxy star formation and mass buildup. The primary evidence supporting SMBH-galaxy co-evolution includes the empirical relation found between SMBH mass and the stellar velocity dispersion in galactic bulges (Kormendy & Ho 2013 and references therein) and the similarities in the cosmological evolution of AGN space densities and the star formation rate densities (Heckman & Best 2014; Madau & Dickinson 2014, and references therein).

The energy released by AGN can have an impact on the surrounding interstellar

(ISM) or circumgalactic medium (CGM) via a variety of radiative and mechanical processes. Such interactions, often termed AGN feedback, can shock and/or expel the gas causing suppression or triggering of star formation in the host galaxy. Improving our understanding of SMBH-galaxy co-evolution requires direct observations of AGN feedback in action during the peak epoch of stellar mass assembly and SMBH growth at $1 < z < 3$. However, this phase of galaxy evolution is believed to take place in the presence of thick columns of gas and dust, leading to heavily obscured systems that are challenging to observe at optical and X-ray wavelengths (Hickox & Alexander, 2018).

In dust-obscured systems, emission at optical, UV and X-ray wavelengths from the AGN and/or nuclear starburst is absorbed by dust and re-radiated in the infrared. Mid-infrared (MIR) color diagnostics using infrared satellites such as the *Spitzer Space Telescope* (e.g., Lacy et al., 2004; Stern et al., 2005; Hatziminaoglou et al., 2005; Lacy et al., 2007, 2013; Donley et al., 2012), AKARI (e.g., Oyabu et al., 2011), and *Wide-Field Infrared Survey Explorer* (*WISE*; e.g., Stern et al. 2012; Mateos et al. 2012; Wu et al. 2012b; Assef et al. 2013; Lonsdale et al. 2015) have provided an effective means of identifying both obscured and unobscured AGN populations. Recent studies have suggested that the heavily reddened AGN population represents a transient phase of peak black-hole fueling and stellar mass assembly (e.g., Eisenhardt et al., 2012; Wu et al., 2012a; Jones et al., 2014; Assef et al., 2015; Tsai et al., 2015; Díaz-Santos et al., 2016). The most extreme population of these galaxies, identified based on very red *WISE* colors, are called Hot Dust Obscured Galaxies (Hot DOGs) due to the presence of hot dust and high luminosity MIR emission (Eisenhardt et al., 2012; Wu et al., 2012a; Bridge et al., 2013).

One way to favor obscured AGN emission over obscured star formation is to additionally require a significant radio source. If the radio flux is greater than the

MIR flux, the source is likely to be an AGN (e.g., Ibar et al., 2008). Thus, surveys that combine MIR and radio can identify obscured powerful jetted AGN (e.g., Condon et al. 2002). Ideally, these sources will be similar to the Hot DOGs discussed above – they are AGN caught at an early stage in their evolution – but with the additional possibility of showcasing jet-driven feedback.

Lonsdale et al. (2015) define such a sample, with an additional requirement that the optical counterparts are faint which favors sources at intermediate redshift, $z \sim 1-3$. This sample forms the basis of the present study. As it stands, however, the Lonsdale et al. (2015) sample only made use of relatively low-resolution radio observations. In the current paper, we present high-resolution X-band (8—12 GHz) Karl G. Jansky Very Large Array (VLA) images of this sample, which allow us to place much stronger constraints on the radio source properties. In particular, we wish to establish whether the sources are young, reside in a dense ISM, and may be caught in a state of expansion. In a companion paper (Patil et al. in prep.) we will use multi-frequency observations to explore the radio spectral shapes, using these to further investigate the nature of the radio sources and the nature of the near-nuclear environments.

Section 2.2 summarizes the sample selection and the MIR properties of the sample. The VLA observations and data reduction are described in Section 2.3. We present source measurements and properties in Sections 2.4 and 2.5, respectively. We analyze our sample's radio luminosity function in Section 2.6. Section 2.7 discusses how our sample might fit into an evolutionary framework with the other known classes of compact and extended radio sources. We also use an adiabatic expanding lobe model to derive some important source properties. Section 2.8 summarizes our conclusions. We adopt a ΛCDM cosmology with $H_0 = 67.7$ km s^{-1} Mpc^{-1}, $\Omega_\Lambda = 0.691$ and $\Omega_{\rm M} = 0.307$ (Planck Collaboration et al., 2016).

2.2 Sample Selection

A detailed description of our sample selection is given in Lonsdale et al. (2015). Briefly, point sources from the *WISE* AllSky catalog (Wright et al., 2010) with S/N > 7 in the 12 or 22 μm bands were cross-matched with sources from the National Radio Astronomy Observatory Very Large Array Sky Survey (NVSS; Condon et al. 1998) or, when available, the Faint Images of the Radio Sky at Twenty-centimeters (FIRST; Becker et al. 1995) catalog. An important requirement was that the source be unresolved in NVSS ($\theta_{\rm FWHM} < 45''$) and FIRST ($\theta_{\rm FWHM} < 5''$) catalogs in order to exclude sources dominated by large scale, evolved radio emission. We also required the candidates to have relatively large radio—to—MIR flux ratios, ($q_{22} = \log(f_{22\,\mu{\rm m}}/f_{20\,{\rm cm}}) < 0$) to favor AGN emission as opposed to star formation (Appleton et al., 2004; Ibar et al., 2008).

The selection also includes only objects with very red MIR colors, with a color cut defined by $(W1 - W2) + 1.25(W2 - W3) > 7$ [1] and a flux density cut of 7 mJy at 22 μm. Coupled with the limit on the q_{22} parameter from above, this introduces a 1.4 GHz flux limit of about 7 mJy.

To minimize contamination by the non-AGN population, the sample excludes sources within 10^o of the Galactic plane.

Each source was inspected using the Sloan Digital Sky Survey (SDSS; York et al. 2000) or Digitized Sky Survey (DSS; if not within the SDSS footprint), and only objects that were relative optically faint or undetected were kept. We have not defined any specific optical selection criteria to favor sources within the required redshift interval and to not create a bias against large amounts of scattered optical

[1] We note that this infrared color selection criterion contained an error in Section 2 of Lonsdale et al. (2015). The error was a typo only and did not impact the analysis or any of the figures in Lonsdale et al. (2015). The color cut defined here is the correct version.

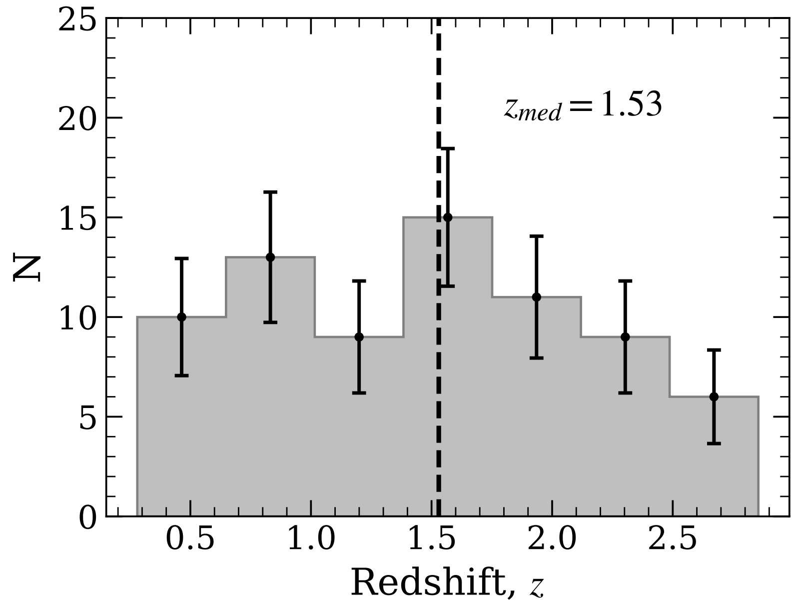

Figure 2.1: Redshift distribution of our sample. We have spectroscopic redshifts available for 71 sources. The black dashed line denotes the median value. The error bar in each redshift bin is the respective binomial uncertainty. The binomial uncertainty is defined as $\sigma_{n_i} = \sqrt{n_i(1 - n_i/N)}$ where n_i is the number of sources in bin i and N is the total number of sources in our sample.

light (Lonsdale et al., 2015). We also relied upon follow-up spectroscopy to refine our sample by redshift. This ensures that the objects are likely to be at intermediate or high redshift, and given the extreme MIR-to-optical color, they are also likely to be heavily obscured. Given the intermediate or high redshift, the bright MIR fluxes then suggest high bolometric luminosity. A total of 167 sources met these selection criteria. We will discuss the completeness of the sample in Section 2.6.

2.2.1 Spectroscopic Redshifts

We obtained spectroscopic redshifts for 71 out of 80 attempted sources using several telescopes (see Lonsdale et al., 2015, for details). The remaining 9 sources were too faint to provide a reliable redshift. Figure 2.1 shows the redshift distribution which is seen to be approximately flat from $0.5 < z < 2$ with a possible decline from

$2 < z < 2.8$. The median value is $z_{\rm med} \sim 1.53$. While the subset of sources targeted for redshift is likely biased to the optically brighter sources, it is unclear whether or not this translates to a bias in redshift – while optically brighter galaxies might be at lower redshift, optically brighter quasars might be at higher resdhift. Taken at face value, our redshift distribution indicates that many of our sources lie in the epoch of peak star-formation and black hole fueling, some are nearer ($z \lesssim 1$) and may be suitable for detailed follow-up observations.

2.2.2 MIR and Submm Properties

870 μm Atacama Large Millimeter/Submillimeter Array (ALMA) imaging of 49 sources (Lonsdale et al., 2015) and 850 μm James Clerk Maxwell Telescope (JCMT)-Submillimetre Common-User Bolometer Array imaging of 30 sources (Jones et al., 2015) yielded 26/49 ALMA and 4/30 JCMT detections. Overall the MIR-submm SEDs of our sample is likely to be dominated in the MIR by AGN heated thermal dust emission. The extremely red optical-WISE colors and bright 22 μm emission revealed that these sources have high IR and bolometric luminosities ($L_{bol} \sim 10^{11.7-14.2} L_\odot$) with a few reaching the Hyper-Luminous Infrared Galaxy (HyLIRG) regime. AGN populations identified using ultra-red WISE color diagnostics are now known to belong to a class of IR-luminous obscured quasars such as Hot DOGs (e.g., Eisenhardt et al., 2012; Wu et al., 2012a; Assef et al., 2015). The MIR signatures and high-ionization lines in the spectra of our sample (Kim et al. 2013, Ferris et al. submitted) are consistent with a population of radiative-mode obscured quasars. We refer our readers to Lonsdale et al. (2015) for more details on the MIR and submm properties of our sample.

2.3 New VLA Data

2.3.1 Observing Strategy

We observed 167 sources from Lonsdale et al. (2015) at X-band (8–12 GHz) with the VLA in the A- and B-arrays through projects 12B-127 and 12A-064, respectively. Due to the complexity of dynamic scheduling for such a large sample, 12 sources were not observed in any array, and 32 were observed in only one array. Therefore, the sample discussed in this paper consists of 155 sources, 26 of which lack imaging with the A-array and 6 of which lack imaging with the B-array. The A-array observations were divided into 13 separate scheduling blocks (SBs), and a total of 129 sources were observed between October and December 2012. The B-array observations were divided into 7 different SBs, and 149 sources were observed from June to August 2012.

Sources closer to each other on the sky were scheduled in groups, with phase calibrators interleaved. However, to maximize observing efficiency, the same calibrator was not always re-observed after each target. This strategy was worth the inherent risk of failing to obtain phase closure for a few targets, because most of the sources were expected to be bright enough for self-calibration.

The observations took place during the Open Shared Risk Observing period when maximum bandwidths were limited to $\sim$2 GHz. Our WIDAR correlator set-up consisted of two basebands with central frequencies 8.6 GHz and 11.4 GHz, respectively. The bandwidth of each baseband was 1024 MHz divided among eight 128 MHz wide spectral windows. The total bandwidth of our observations was 2 GHz. The correlator setup was kept identical for both of the arrays. Our observing strategy aimed to obtain snapshot-imaging of the full sample with about 5 minutes of integration time per source with a theoretical rms noise level of about $\sim 13\ \mu$Jy beam^{-1}.

2.3.2 Calibration and Imaging

We used the Common Astronomy Software Applications package (CASA; McMullin et al. 2007) version 4.7.0 for data editing, calibration, and imaging. The initial step was to remove bad data with the help of the VLA operators log[2] followed by visual inspection of the data in the uv-plane using the task PLOTMS. Hanning smoothing was performed prior to calibration to remove the rigging effect from the Gibbs phenomenon caused by strong Radio Frequency Interference (RFI). The data were calibrated using the CASA VLA calibration pipeline[3] (version 1.3.9).

We then used the pipeline weblog and test images of the targets and phase calibrators to examine the quality of the calibration. If necessary, additional flagging was done, followed by a re-run of the calibration pipeline. We then used the CASA task SPLIT to separate the uv-data for each target into individual datasets for self-calibration and final imaging.

We ran a few rounds of phase-only self-calibration and one round of amplitude and phase calibration to correct artifacts due to residual calibration errors. We used the CASA task CLEAN to produce the final continuum image. Because of the wide bandwidths made available by the new correlator, we formed images using the multi-frequency synthesis mode with two Taylor coefficients (by setting the CLEAN parameter nterms=2) to more accurately model the spectral dependence of the sky. Also, to mitigate the effects of non-coplanar baselines during imaging, we used the W-projection algorithm with 128 w-planes. The full-width half maximum (FWHM) of the synthesized beam of the final images in the A- and B-arrays are typically $\theta_b \sim 0.2''$ and $\sim 0.6''$, respectively.

[2]www.vla.nrao.edu/cgi-bin/oplogs.cgi
[3]www.science.nrao.edu/facilities/vla/data-processing/pipeline

Despite our careful calibration and imaging strategy, a total of 13 targets (11 in A-array and 2 in B-array) suffered from severe phase closure issues. As a result, 110 sources have imaging in both arrays, 8 sources have only A array imaging, and 37 sources have only B array imaging. Thus, the analysis presented in the remainder of this paper is based on 155 sources.

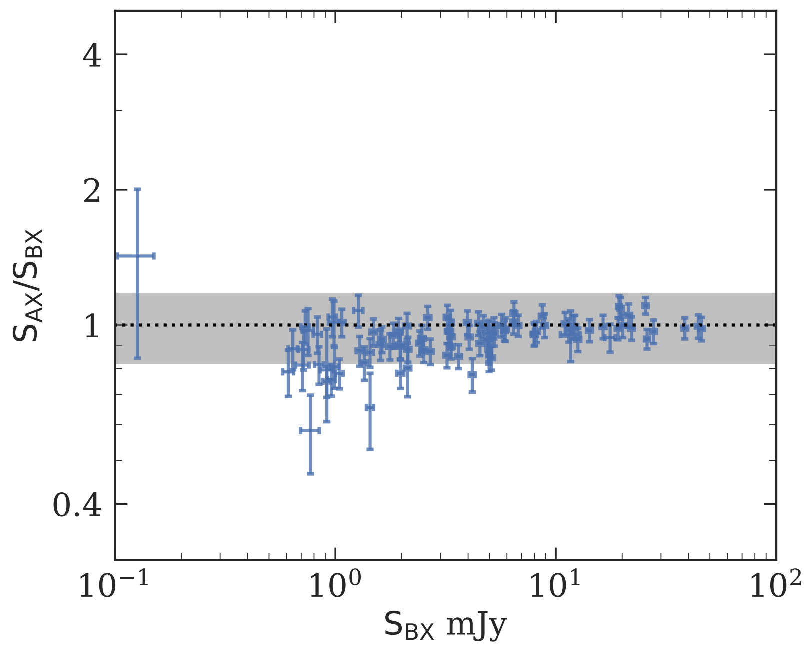

Figure 2.2: The ratio of the total flux measured in A- and B-arrays for 110 sources as a function of the flux measured from the B-array images. The black dotted line shows a ratio of unity. The normalized absolute median deviation of the flux ratios between the A- and B-array observations is 0.18 and is indicated by the gray shaded region.

2.4 Source Measurements

2.4.1 Fluxes

To determine source parameters such as peak flux density, integrated flux, deconvolved shape parameters, and all corresponding uncertainties, we used the JMFIT task available in the 31DEC18 version of the Astronomical Image Processing Software (AIPS). In most cases, the radio sources have either single or multi-component Gaussian-like morphologies, and their flux and shape parameters may be estimated by fitting one or more two-dimensional elliptical Gaussian models. For sources with extended, complex structures, we manually estimated the source parameters using the CASA Viewer [4] The flux measurement uncertainties were calculated by adding the error provided by JMFIT and the 3% VLA calibration error (Perley & Butler, 2013) in quadrature. We provide the clean beam dimensions, peak flux, and total flux from our A- and B-array observations in Table 2.4.

The total flux distributions in A- and B-array observations span the range $0.18-45$ mJy and $0.13-60$ mJy, respectively, with similar medians of ~ 3.3 mJy. Figure 2.2 compares the integrated fluxes of the 110 sources with high-quality flux measurements from both A- and B-arrays. The designation "high-quality" here simply indicates no hint of image artifacts.

We find that, for most of our sample, the total flux measurements from each array are in good agreement. There are 4 sources that lie below the unity line in Figure 2.2 and have less flux recovered in the longer-baseline A-array observations. These sources may have a diffuse emission component that has not been recovered in the A-array data[5]. There is also one outlier in Figure 2.2 with significantly higher flux in the B-array data compared to the A-array, possibly as a result of intrinsic source variability or calibration error.

[4]Following Nyland et al. (2016), we calculate flux measurement uncertainties as $\sqrt{(N \times \sigma)^2 + (0.03 \times S_{tot})^2}$, where N is total number of synthesized beam over 3σ contour emission, σ is the rms noise, and S_{tot} is the integrated flux of the region.

[5]We note that the largest resolvable angular scale (LAS) for the 10 GHz images is $\sim 5.3''$ and $\sim 17''$ for the A- and B-array, respectively. That means that for a given source, the A-array image would be missing flux from any emission present on the intermediate scales between $5.3''$ and $17''$.

2.4.2 Source Angular Sizes

We used the JMFIT task in AIPS to measure the angular sizes of our sources. For resolved sources, JMFIT[6] requires that 1) the integrated flux be larger than the peak flux density and 2) the deconvolved major axis is greater than zero (within the relevant uncertainties). If neither of these criteria were satisfied, the source was classified as unresolved. The source fitting algorithm gives a cautionary message when only one of two criteria is satisfied. We discuss our morphological classification in the next section, including our approach to sources with ambiguous JMFIT results.

Deconvolved source sizes were taken directly from JMFIT. The uncertainties were calculated based on the formalism given by Murphy et al. (2017):

$$\frac{\sigma_\theta}{\sigma_\phi} = \left[1 - \left(\frac{\theta_b}{\phi}\right)^2\right]^{-1/2} \tag{2.1}$$

where σ_θ and σ_ϕ are the rms errors on the deconvolved (θ) and measured (ϕ) source sizes, respectively. The parameter θ_b is the FWHM of the synthesized beam. For the unresolved sources, we consider the maximum deconvolved angular size provided by JMFIT to be an upper limit on the source size. For extended sources with non-Gaussian morphologies, we measured the angular sizes using CASA viewer. Tables 2.5 an 2.6 provide the deconvolved source sizes and morphological classification. For sources with more than one component, separate measurements are given for each component.

[6]We refer our reader to the online documentation of the JMFIT task for more details: http://www.aips.nrao.edu/cgi-bin/ZXHLP2.PL?JMFIT

2.4.3 Morphological Classification

As described in the previous section, the JMFIT task in AIPS uses two basic criteria to determine if a source is formally resolved: the peak/total flux ratio and the deconvolved source size compared to the clean beam size. We use these criteria but modify the first to be more conservative by including a 3% uncertainty in the flux calibration (see Section 2.4.1).

We classify as "unresolved, U" sources that satisfy both criteria, deconvolved sizes consistent with zero in both axes, and peak/total flux ratio of unity within the uncertainties. We classify as "slightly resolved" sources which show finite size along one of the two axes, and a peak/total flux ratio consistent with 1. We classify as "resolved, R" sources that show finite size along both axes and a peak/total flux ratio less than one (within 1 sigma, following Owen (2018)). Sources with more than a single distinct component are classified as double, triple, or multi-component morphologies. Figure 2.3 shows the distribution of morphologies in our sample. We note that the entire analysis is performed separately for the A- and B-array data, and when possible, A-array results are preferred for the morphological classification and further analysis. In summary, we categorize our sample sources into following morphological classes:

1. **Unresolved (UR):** The source is unresolved along both the major and minor axes and the peak/total flux ratio is unity within the 1σ uncertainty.

2. **Slightly resolved (SR):** The source is unresolved along one of the axes and the peak/total flux ratio is unity within the 1σ uncertainty.

3. **Fully resolved (R):** The radio source is resolved along both the axes, and the peak/total flux ratio is < 1.

4. **Double (D):** The source consists of two distinct components, each of which may be unresolved, slightly resolved, or fully resolved.

5. **Triple (T):** The source consists of three distinct components, resembling the core-jet or core-lobe emission seen in large-scale radio galaxies.

6. **Multiple (M):** The source consists of more than three distinct components.

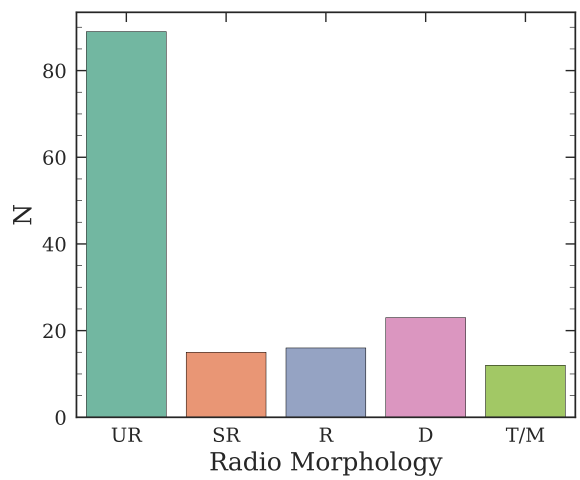

Figure 2.3: The morphological distribution of the 155 sources from our sample. The six morphological classes are: UR: Unresolved, SR: Slightly resolved, R: Resolved, D: Double, T: Triple, and M: Multiple. Where available, A-array images are used, unless they were of poor quality. $55.5 \pm 9.3\%$ of the sources are unresolved, with linear extents ≤ 1.7 kpc at $z \sim 2$.

Figure 2.3 shows the morphological classifications of the 155 sources in our final sample. Expressed as percentages, $55.5 \pm 9.3\%$ are unresolved, $13.5 \pm 4.6\%$ are slightly resolved, $7.7 \pm 3.5\%$ are fully resolved single sources, $14.8 \pm 4.8\%$ are double, $6.4 \pm 3.1\%$ are triple, and $1.3 \pm 1.4\%$ are multi-component sources. Figure 2.4 shows the distribution of angular sizes for each morphological class. There is a wide range of upper limit sizes for the unresolved sources due to the large span of source declinations and the use of both A- and B-array data. Deconvolved sizes are plotted for the slightly

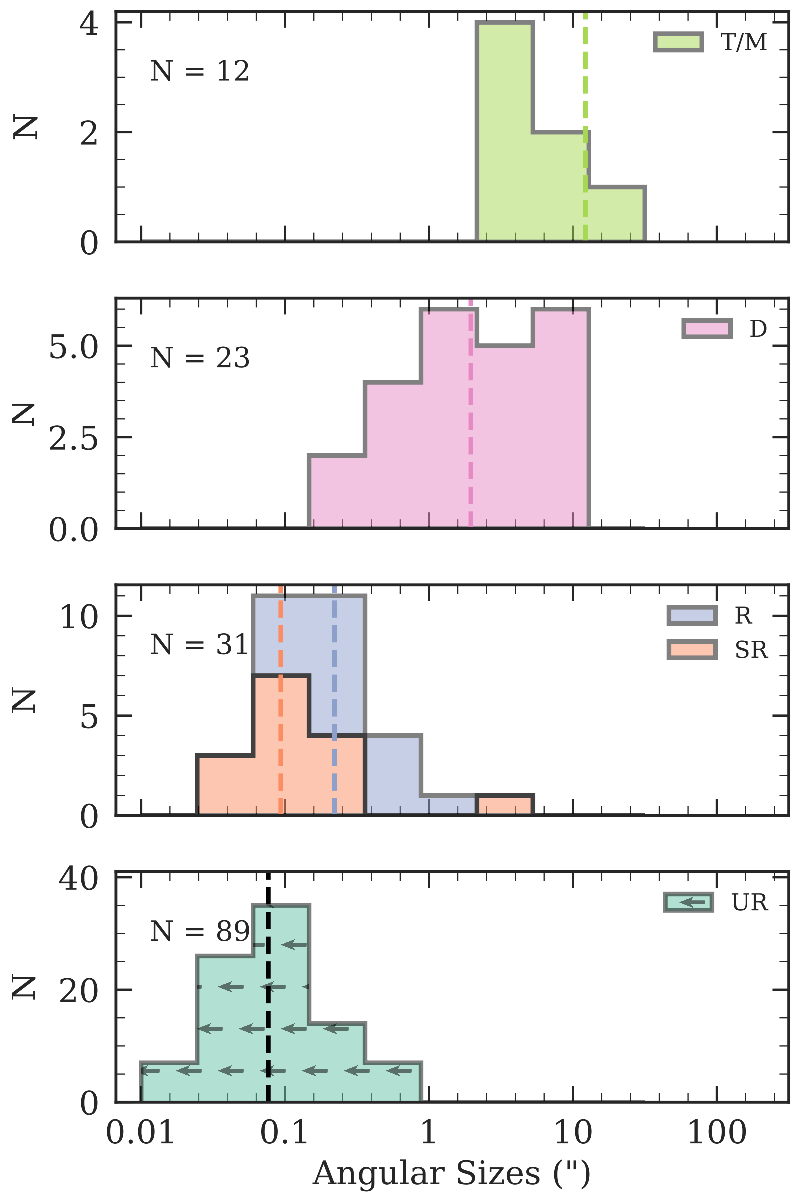

Figure 2.4: The distribution of angular sizes from our new X-band observations broken down by morphological class. The top two panels show the largest angular extents of the double (pink) and triple/multiple (light green) sources. The third panel from the top shows the angular sizes of slightly resolved (orange) and fully resolved (purple) sources. The bottom panel shows the upper limits on the source angular sizes of the unresolved sources (dark green). The dashed line shown in each panel indicates the median angular size for each morphological class.

resolved sources, and outermost peak separation sizes are given for double, triple, and multiple sources.

2.4.4 In-band Spectral Indices

Our VLA X-band observations capture a wide range of frequencies, 8–12 GHz, offering the possibility of measuring "in-band" spectral indices, α (defined as $f_\nu \sim \nu^\alpha$). Although CASA generates a spectral index map with errors, we chose not to use it since its errors are calculated only as uncertainties to a polynomial fit and are less reliable at lower S/N (Cornwell et al., 2005; Rau & Cornwell, 2011). Instead, we have chosen a more classical approach to estimate the in-band spectral index and its uncertainty. By dividing our bandwidth into two halves (centered at $\nu_1 = 8.6$ and $\nu_2 = 11.4$ GHz), we imaged each half separately using identical CLEAN parameters. We smoothed each 11.4 GHz image to match the resolution of the 8.6 GHz image using the task IMSMOOTH. We then re-gridded the smoothed 11.4 GHz image using the corresponding 8.6 GHz image as a template (using the CASA task IMREGRID) to ensure matched coordinate systems in the two images. Finally, we ran JMFIT to obtain source flux and shape measurements of all images.

The in-band spectral index was estimated using the following equation:

$$\alpha_{IB} = \frac{log_{10}(S_{\nu_1}/S_{\nu_2})}{log_{10}(\nu_1/\nu_2)}. \tag{2.2}$$

where ν_1 and ν_2 are 11.4 and 8.6 GHz. Using standard propagation of errors, the uncertainty in the in-band spectral index is:

$$\sigma_{\alpha_{IB}} = \frac{\left[(\sigma_{S_1}/S_{\nu_1})^2 + (\sigma_{S_2}/S_{\nu_2})^2\right]^{1/2}}{log_{10}(\nu_1/\nu_2)}. \tag{2.3}$$

The left panel in Figure 2.5 shows the resulting uncertainty, $\sigma_{\alpha_{IB}}$, plotted against

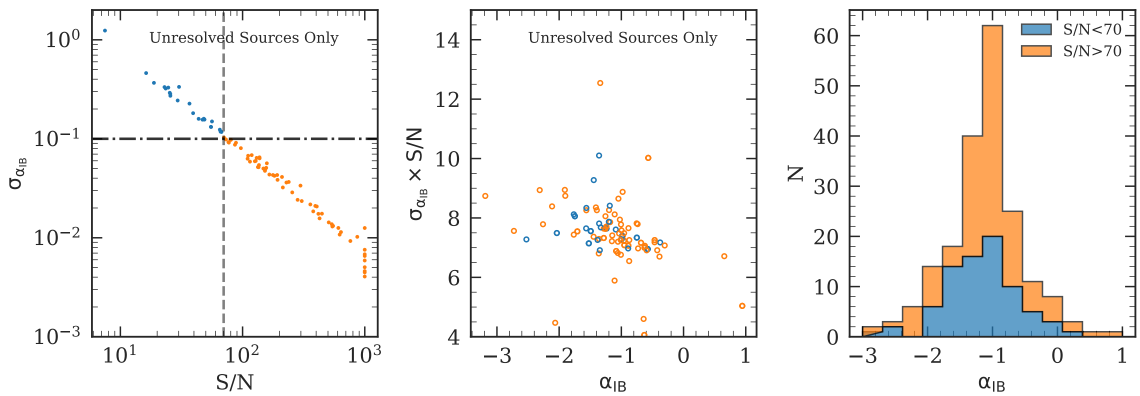

Figure 2.5: Analysis of in-band spectral indices, α_{IB}, and their errors, $\sigma_{\alpha_{IB}}$. **Left**: The relation between $\sigma_{\alpha_{IB}}$ and the average S/N of the 8.6 and 11.4 GHz images, evaluated by simple propagation of errors. A threshold S/N of $\sim$70 (vertical dashed line) ensures $\sigma_{\alpha_{IB}} < 0.1$ (horizontal dashed-dotted line). **Center**: The product $\sigma_{\alpha_{IB}} \times S/N$ from our simple analysis confirms a theoretical analysis by Condon (2015) that predicts a value of $\sim$8. **Right**: The distribution of measured α_{IB} colored according to high S/N (> 70; orange) or low S/N (< 70; blue).

the average S/N of the 8.6 and 11.4 GHz images. As expected, lower S/N yields larger uncertainties in α_{IB} with a threshold of S/N $\gtrsim 70$ for $\sigma_{\alpha_{IB}} \lesssim 0.1$, which we take as a threshold of reliability for the calculated values of α_{IB}.

Condon (2015) gives a theoretical analysis of in-band spectral indices and their uncertainties that broadly confirms our simple approach above. Combining Equations 48 and 49 from Condon (2015) for an in-band spectral index α_{IB} over a bandwidth of 8–12 GHz, we find:

$$\sigma_{\alpha_{IB}} \times S/N = \frac{\sqrt{12}}{\ln(\nu_{max}/\nu_{min})} \;\sim\; 8 \tag{2.4}$$

where, S/N is the signal-to-noise ratio of the source and ν_{max} and ν_{min} are the upper and lower ends of the observing bandwidth. The center panel in Figure 2.5 shows the product $\sigma_{\alpha_{IB}} \times S/N$ for our data, and broadly confirms this result, with values near 7–8 for a range of in-band spectral indices.

The far-right panel of Figure 2.5 shows the distribution of in-band spectral indices with values above/below our S/N threshold color coded as orange/blue. The distribution is strongly peaked near the median value of $\alpha_{IB} = -1.0$, with 80% of the high-quality values within the range -1.7 to -0.5. We will discuss these spectral indices, together with the overall radio SEDs in a companion paper (Patil et al. in prep.). Briefly, the median spectral index is broadly consistent with optically thin synchrotron emission ($\alpha \sim -0.7$ near 1 GHz; e.g., Condon & Ransom 2016), perhaps steepened somewhat via radiative losses as well as inverse Compton scattering from either the Cosmic Microwave Background or local infrared radiation fields. About 5% of our sources might plausibly have a flat spectrum (i.e. $\alpha > -0.5$), consistent with an unresolved synchrotron core. This is also consistent with the absence of evidence for short timescale variability typical of beamed sources, indicated by the good overall agreement between the fluxes measured in our A and B configuration observations. We will address the spectral characteristics and the role of beamed core emission more thoroughly in the SED paper.

2.5 Source Properties

2.5.1 Diffuse Radio Emission?

Our sample was selected to have compact emission in the NVSS and FIRST catalogs. As discussed in Section 2.4, the majority of our sources have compact morphologies in our new high-resolution X-band observations. However, the presence of diffuse, extended emission on scales of a few arcseconds (which could be associated with earlier episodes of AGN activity) cannot be definitively ruled-out on the basis of the X-band data alone due to surface brightness sensitivity limitations.

Table 2.1: List of Radio Continuum Surveys

Survey	ν GHz	θ_{res} $''$	LAS $''$	σ_{rms} mJy/beam	$n_{sources}$
TGSS ADR1	0.15	25	4104	3.5	152
NVSS	1.4	45	970	0.45	155
FIRST	1.4	5	36	0.15	51
VLASS	3	2.5	58	0.12	153
X-band-B	10	0.6	17	0.03	149
X-band-A	10	0.2	5.3	0.03	129

NOTE — Column 1: Name of the radio survey; Column 2: Frequency of the observation in GHz; Column 3: Typical angular resolution of the survey in arcseconds; Column 4: Largest resolvable angular scale in arcseconds; Column 5: 1σ rms noise in mJy/beam; Column 6: Number of our sources observed in each survey

Constraints from Radio Surveys

To check the incidence of such extended emission, we visually inspected images of all of our sources in NVSS and FIRST as well as two additional wide-field radio surveys: The GMRT Sky Survey (TGSS: Intema et al. 2017) and the VLA Sky Survey (VLASS[7]; Lacy et al. 2020). The observing frequency, angular resolution, maximum resolvable scale, and 1σ sensitivity for these surveys is summarized in Table 2.1, along with similar information for our X-band observations. The combination of our new X-band data with lower-resolution radio surveys provides a more complete picture of the radio morphologies of our sources, thus allowing us to constrain the presence of diffuse, extended emission.

[7]We inspected the VLASS Epoch 1 "quicklook" images available at `https://archive-new.nrao.edu/vlass/quicklook/`. We caution readers that these images are preliminary only - higher quality survey products will be publicly available in the future, as discussed in Lacy et al. (2020).

We re-confirmed that all of our sources are indeed compact in NVSS. For the 51/155 sources included in the FIRST survey footprint, we inspected the FIRST images and found 6 sources that appear compact in NVSS but are either resolved into 2 distinct components or extended in FIRST. In all six of these cases, the multiple components identified in FIRST appear to be associated with radio AGN jets/lobes. We provide a further comparison of the NVSS and FIRST properties of our sources in terms of their fluxes in Section 2.6.

TGSS, which provides a factor of two higher angular resolution than NVSS and a much lower frequency of 150 MHz, is more sensitive to steep-spectrum emission from older radio sources. We found a total of 15 sources with clearly resolved, extended emission and 3 sources with multiple components in TGSS. Finally, we examined the 3 GHz VLASS images of our sources, which have two times higher resolution than FIRST. We found 13 extended and 8 multi-component sources.

Ultimately, the TGSS, FIRST, and/or VLASS images revealed extended or multi-component emission in a total of 25/155 unique sources. Of these, 11 sources were not previously classified as being resolved in our X-band observations, thus leading to the re-classification of their morphologies. A summary of the properties of all sources with resolved emission identified in radio survey images is provided in Table 2.2 and image cutouts are shown in Figure 2.6. Thus, we conclude that the majority of our sources are indeed compact, even when observed at lower frequency and at lower resolution. We emphasize that the discovery of extended emission only has an impact on our study by modifying our morphological classification and possibly indicating a prior episode of activity. However, the presence of more extended emission does not affect our primary analysis of the more compact central radio source. It is these sources that we are most interested in because they are likely to be associated with the denser gas responsible for the high dust column and high MIR emission.

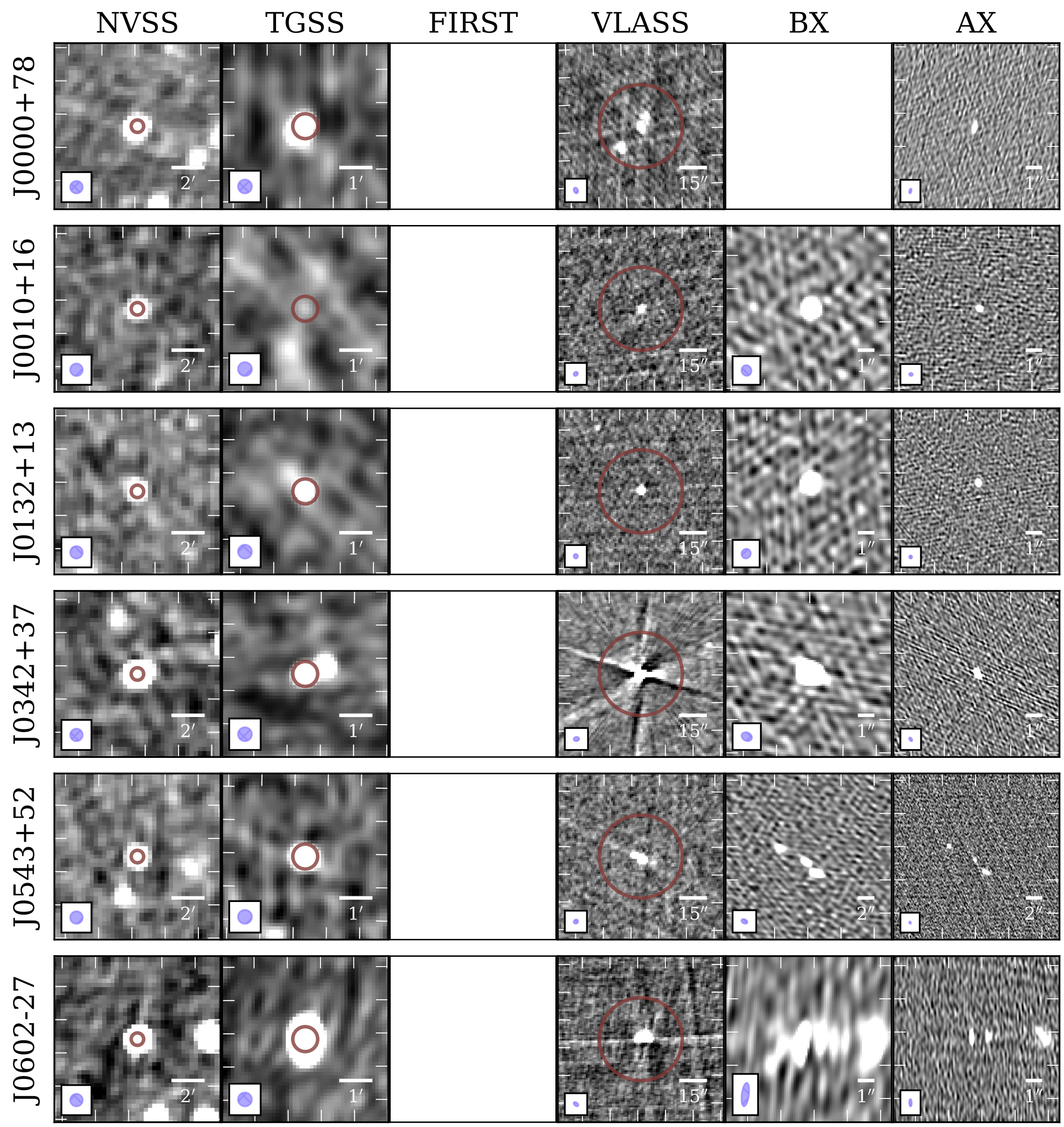

Figure 2.6: Radio continuum cutouts of our sample sources that have extended emission on angular scales greater than a few arcseconds. The source name is shown to the left of the first column and the name of the radio survey is shown above the first row of cutouts. The red circle corresponds to the typical angular resolution of NVSS ($= 45''$). The synthesized beam is shown as a purple ellipse in the lower-left corner. A white solid line on the lower-right denotes the scale bar. The tick mark spacing is equal to the length of the scale bar.

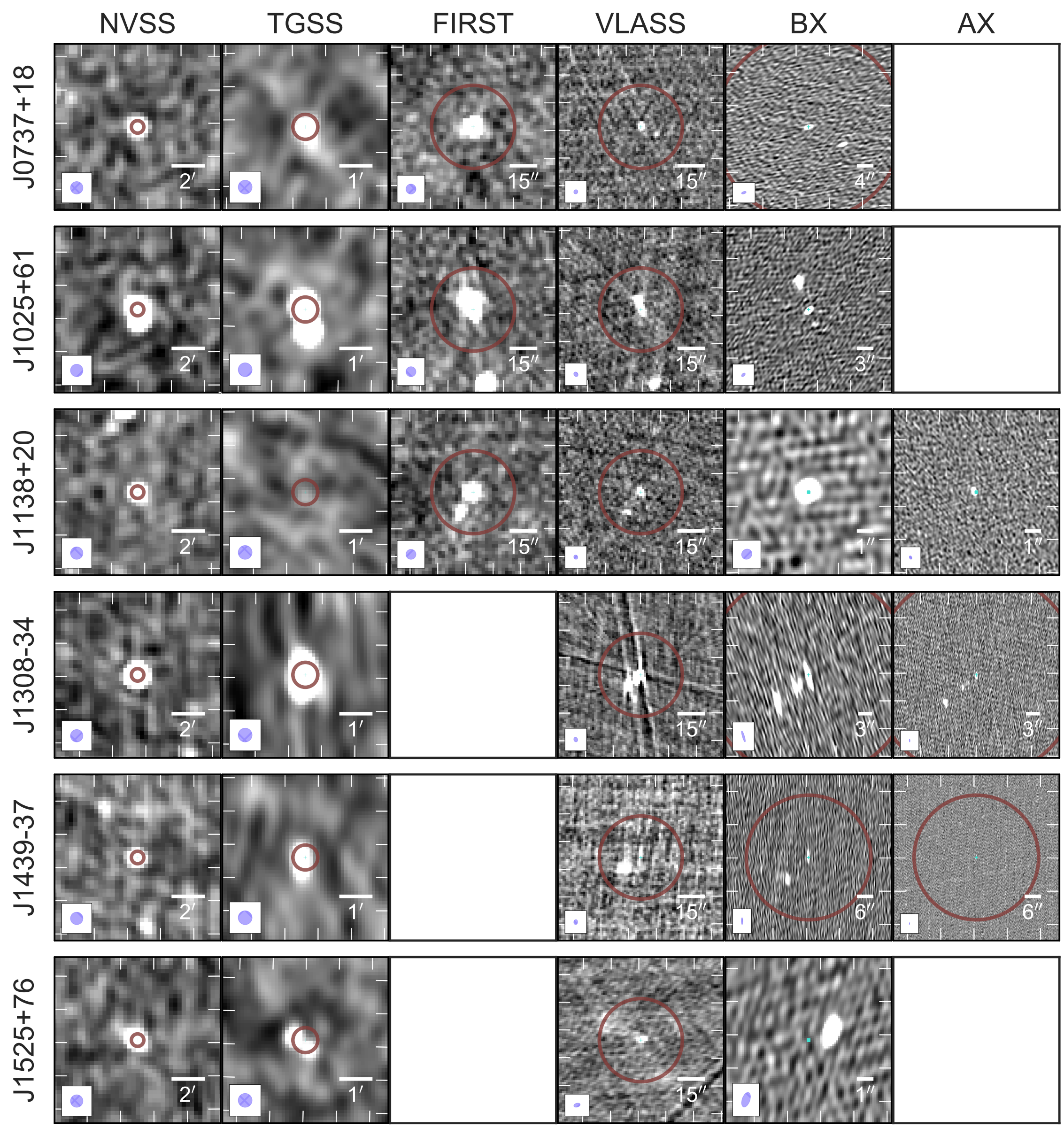

Figure 2.6: *Continued*

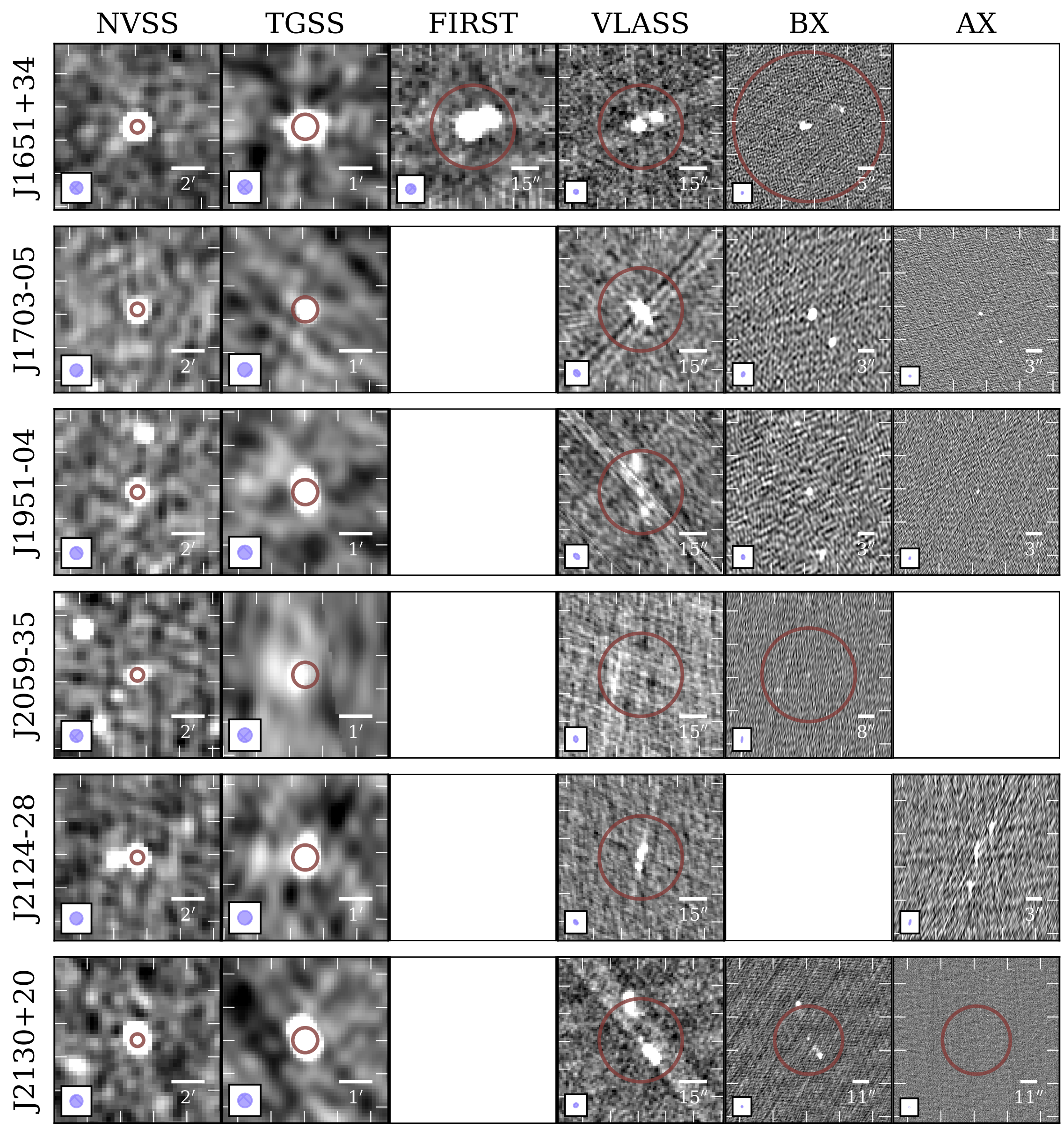

Figure 2.6: *Continued*

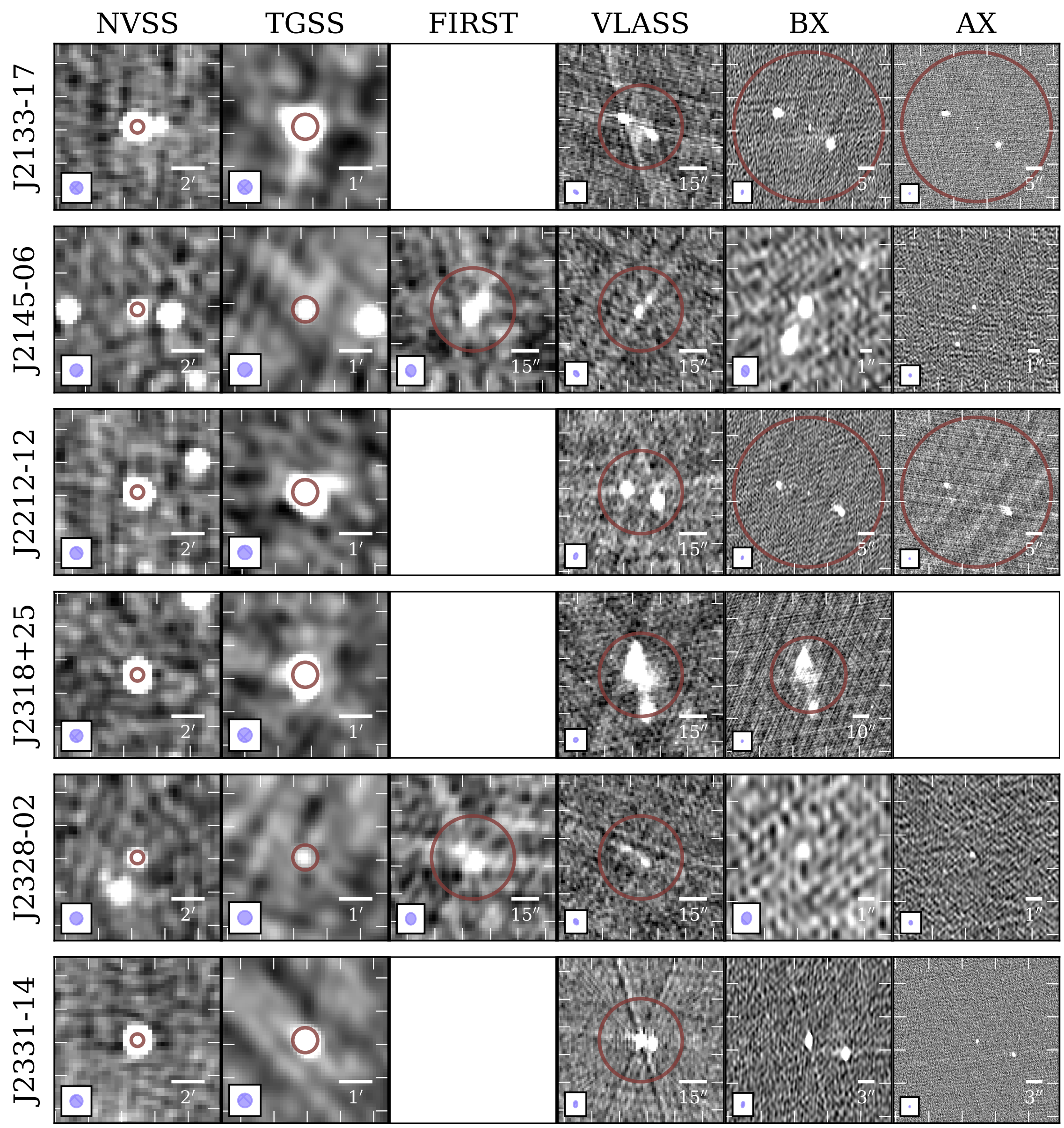

Figure 2.6: *Continued*

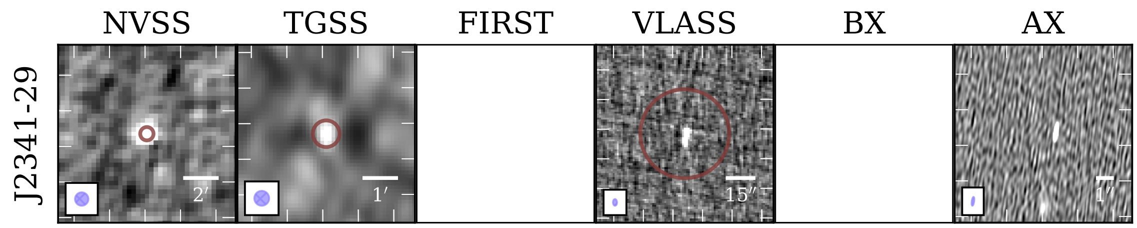

Figure 2.6: *Continued*

Table 2.2: List of Extended Sources

Source	Source Morphology VLA-X	VLASS	FIRST	TGSS	Angular Extent VLA-X ″	VLASS ″	FIRST ″	TGSS ″
(1)	(2)	(3)	(4)	(5)	(6)	7	(8)	(9)
J0000+78	UR	T	···	R	0.04	22.1	···	33.4
J0010+16	UR	UR	···	T	0.07	2.5	···	153.1
J0132+13	SR	UR	···	D	0.07	2.4	···	47.4
J0342+37	UR	UR	···	D	0.04	2.9	···	44.3
J0543+52	T	D	···	UR	5.3	4.5	···	12.0
J0602−27	T	D	···	R	4.4	4.3	···	26.6
J0737+18	D	D	UR	R	9.3	8.9	5.4	29.4
J1025+61	T	T	D	D	46.1	46.8	47.3	47.6
J1138+20	UR	D	D	···	0.02	13.8	14.3	
J1308−34	T	T	···	R	8.9	9.7	···	37.1
J1439−37	D	D	···	R	11.2	15.3	···	48.5
J1525+76	UR	T	···	D	0.11	46.6	···	40.4
J1651+34	M	D	D	R	12.6	12.8	11.9	15.0
J1703−05	D	D	···	R	6.2	7.0	···	13.2
J1951−04	T	T	···	D	24.3	29.5	···	39.9
J2059−35	SR	R	···	D/R	2.4	5.3	···	51.3
J2124−28	M	T	···	R	11.4	11.2	···	30.5
J2130+20	T	T	···	D	39.1	37.1	···	44.8
J2133−17	T	T	···	R	18.8	20.5	···	25.2
J2145−06	D	D	D	UR	3.4	10.4	10.2	25.0
J2212−12	T	T	···	R	20.9	20.0	···	26.8
J2318+25	T	T	···	R	34.7	36.9	···	70.4
J2328−02	SR	D	D	UR	0.13	14.6	12.1	25.0
J2331−14	D	D	···	R	7.2	8.3	···	17.6
J2341−29	UR	D	···	R	0.11	5.7	···	40.6

NOTE — Column 1: Source name. Column 2-6: Source morphologies in our 10 GHz VLA data, VLASS, FIRST, and TGSS, respectively. The morphological classes are as follows: UR: unresolved; SR: slightly or marginally resolved; D: double; T: triple; M: multicomponent sources. The deatiled description of morphological classes is given in Section 2.4.3. Column 6-9: Largest angular extent in arcseconds for the radio emission detected in our 10GHz VLA survey, VLASS, FIRST, and TGSS, respectively. For sources with a single component emission, we provide angular size estimates from their respective source catalogs. For multi-component sources, we provide largest source separation measured manually using CASA task Viewer.

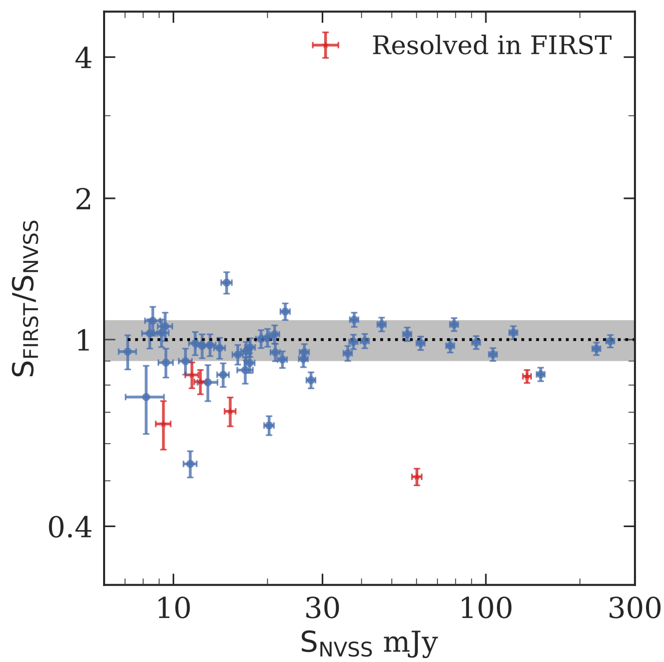

Figure 2.6: The ratio of fluxes measured in FIRST and NVSS as a function of NVSS flux. The black dotted line indicates a ratio of unity. For the majority of our sample, FIRST is able to recover most of the flux measured by NVSS. The gray shaded region shows the normalized median deviation ($\sigma_{\mathrm{nmad}} \sim 0.1$) of the flux ratio. Six sources with resolved morphologies in the FIRST are shown by the red symbols.

NVSS and FIRST Flux Ratios

As a further test for missed emission in our X-band observations, we compare in Figure 2.6 the 1.4 GHz NVSS and FIRST fluxes of our sources. Excluding six sources that are resolved in FIRST but not in NVSS (J1025+61, J1138+20, J1428+11, J1651+34, J2145−06, J2328−2), the fluxes are in good agreement above 30 mJy with slight ($\sim$ 5%) scatter to lower FIRST fluxes for weaker sources, with two outlier sources, J2322−00 and J1717+53, with flux ratios of 0.54 and 0.65 respectively. Neither of these sources shows any extended emission in TGSS, VLASS or FIRST, and since both NVSS and FIRST were corrected for "CLEAN Bias", it cannot explain the offsets. We note that other sources of bias exist for measurements at low S/N (e.g., Hopkins et al. 2015). Variability might explain some of the outliers (Mooley et al., 2016), though we emphasize that Figures 2.2 and 2.6 indicate that the majority of our sources are not likely to be variable on the timescales sampled by our data.

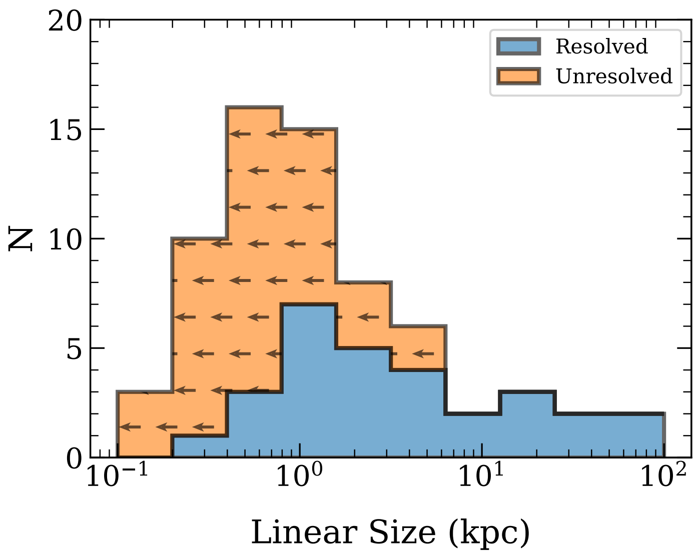

Figure 2.7: Linear sizes for the 71 sources with spectroscopic redshifts. We plot two separate histograms for the two broad morphological categories, resolved and unresolved. The blue histogram shows the largest linear extents for the resolved sources in our sample. The orange histogram with left arrows are the upper limits on the linear extents of unresolved sources and is stacked on top of the blue histogram.

2.5.2 Physical Sizes

Figure 2.7 shows the distribution of physical source sizes, with the sample divided into resolved (including both slightly and fully resolved) and unresolved source morphologies. With the exception of 12 double or triple sources larger than 10 kpc, the rest are smaller than 5 kpc. Roughly 55% of the sources are unresolved with median upper limit near 0.6 kpc. Given that our radio selection only requires sources to be compact on 40″ scales (NVSS, 100% of the sample) or 5″ scales (FIRST, 30% of the sample) we find essentially all our sources are significantly more compact than these size limits, suggesting our joint selection with luminous and red *WISE* MIR emission is preferentially associated with compact radio sources. A further check of whether the MIR selection is associated with compact radio emission is to ask whether an MIR blind radio survey with similar flux threshold and redshift range yields many compact sources.

Such a survey exists. The CENSORS sample of Best et al. (2003) used NVSS to select sources brighter than 7.8 mJy and cross-matched these with the ESO Imaging Survey (EIS). The resulting sample of 150 has similar median redshift and radio luminosity to our sample. However, the median radio source size for the CENSORS sample is $6''$, which is significantly larger than our own median source size of $0.1-0.2''$. Since the redshift distribution and flux cut for the two samples is similar, then we conclude that the smaller source size of our sample is tied to the additional selection criteria of extreme MIR colors and luminosities.

Having established that our radio sources are compact, are there any previously established classes of radio sources that closely resemble our sources? Clearly they are different from the classical Fanaroff-Riley (FR) type I and II (Fanaroff & Riley, 1974) radio sources which are much more extended. Similarly, our sources, with their steep spectral index (Section 2.4.4), are also different from the compact flat spectrum sources. There are four known classes of steep spectrum radio sources that approximately match the angular and physical scales of our sample. These are the GPS (Gigahertz Peaked Spectrum; e.g., Fanti et al. 1990; O'Dea et al. 1991; Snellen et al. 1998; Fanti 2009; Collier et al. 2018), CSS (e.g., Peacock & Wall, 1982; Spencer et al., 1989; Fanti et al., 1990; Sanghera et al., 1995; Fanti et al., 2001), HFPs (High Frequency Peakers e.g., Dallacasa et al. 2000; Stanghellini et al. 2009; Orienti & Dallacasa 2014), and FR0 classes (e.g., Baldi et al. 2015, Sadler et al. 2014). Of these, the FR0 class is significantly less luminous ($< 10^{24}$ W/Hz; Baldi et al. 2018a) and while the available GPS/CSS samples are somewhat more luminous than our sample (see next section), an SED analysis (Patil et al. in prep.) confirms that a significant fraction of our sources have curved or peaked spectra in the GHz range, similar to the GPS/CSS sources. Thus, since our sample seems to share a number of properties with the GPS/CSS sources, we will use these as a point of comparison in the following discussion.

2.5.3 Radio Luminosities

Figure 2.8 presents the 1.4 GHz radio luminosity of our sample, which spans the range $25 \lesssim \log(L_{1.4\,\mathrm{GHz}}/\mathrm{W\ Hz^{-1}}) \lesssim 27.5$, with a median of $\log(L_{1.4\,\mathrm{GHz}}/\mathrm{W\ Hz^{-1}}) \approx 26.3$. We also use Figure 2.8 to compare with other well-known samples of radio AGN to help place our own sample within a wider "zoo" of radio sources.

A representative sample of local ($z < 0.3$) radio AGN was presented by Best & Heckman (2012) who cross-matched NVSS and FIRST sources with SDSS (radio luminosities calculated assuming a spectral index of -0.7). Clearly, our sample is roughly 2 dex more luminous than the local sample, confirming that our sample is much more luminous than the typical local radio AGN.

Next we compare with the well-known low-frequency 3CRR survey, which is complete above $\mathrm{S}_{178\,\mathrm{MHz}} = 10.9$ Jy (Laing et al., 1983). These span a wide range of redshift and luminosity, and broadly divide into large scale FRI and FRII radio sources (Fanaroff & Riley, 1974). Our sample is, on average, 1.4 dex less luminous than the FRIIs and 1.3 dex more luminous than the FRIs, though there is considerable overlap with both these samples.

Turning to radio sources that are, perhaps, better matched to the redshifts and physical scales of our own sources, the right side of Figure 2.8 includes samples of CSS and GPS sources (O'Dea, 1998; Sanghera et al., 1995; Spencer et al., 1989; Fanti et al., 2001) and HFP sources (Dallacasa et al., 2000; Stanghellini et al., 2009). These

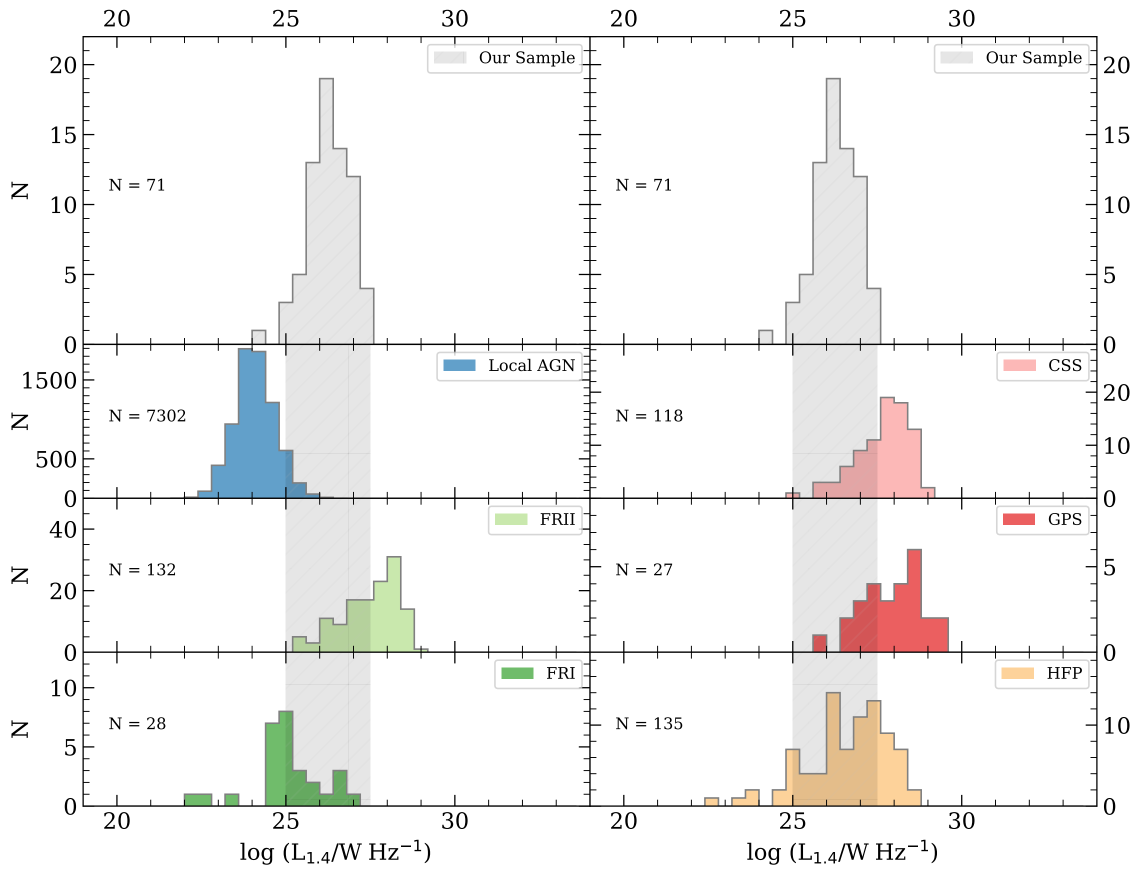

Figure 2.8: Comparison of spectral radio luminosity at 1.4 GHz with other well-studied luminous radio source populations. The top panel shows the distribution of radio luminosities in our sample. The samples plotted in the left-hand panels are local radio AGN ($z < 0.7$), FRI, and FRII galaxies, respectively. The right-hand panels show compact radio AGN; CSS, GPS, and HFP, respectively. The total number of sources in each category is shown in the top left corner of the plot. The range of spectral luminosities for our sample is shown by the gray hatched area. The references for each source population are as follows: SDSS Local Radio-loud AGN: Best & Heckman (2012); FRI and FRII: Laing et al. (1983); CSS and GPS:O'Dea (1998); Sanghera et al. (1995); Spencer et al. (1989); Fanti et al. (2001); HFP: Dallacasa et al. (2000); Stanghellini et al. (2009).

samples show considerable overlap, though the median luminosities of the CSS, GPS, and HFP samples are larger by $\sim$1, 1.8, and 0.5 dex, respectively.

Overall, then, while our sample is significantly more radio luminous than typical radio AGN, it has intermediate luminosity when compared to samples of powerful radio-loud AGN.

2.5.4 Radio Lobe Pressures

An important property of a radio source that affects how it develops is its internal pressure. To first order, the measured pressure likely reflects the pressure of the surrounding medium into which the radio source is expanding. If the radio source is over-pressured relative to the surrounding medium, perhaps being fed by a nuclear jet, then the radio source will expand.

To estimate the internal lobe pressures in our sample sources, we use relations derived from synchrotron theory given in Moffet (1975) and Miley (1980):

$$P_l \approx (7/9)(B_{min}^2/8\pi), \tag{2.5}$$

where P_l is the pressure in the lobe of a radio source in dyne cm^{-2} and B_{min} is the magnetic field in the magnetoionic plasma in Gauss, derived using the common "minimum energy" or "equipartition" assumption that energy is shared approximately equally between the particles and the magnetic field. The equation for this magnetic field strength in Gauss can be written:

$$B_{min} \approx 2.93 \times 10^{-4} \left[\frac{a}{f_{rl}} \frac{(1+z)^{4-\alpha}}{\theta_{rx}\theta_{ry}} \frac{S_\nu}{\nu^\alpha} \frac{X_{0.5}(\alpha)}{\theta_{ry} r_{co}} \right]^{2/7}, \tag{2.6}$$

where the radio source has flux S_ν in Jy with spectral form $S_\nu \propto \nu^\alpha$ and angular size $\theta_{rx}\times$ θ_{ry} arcsec, z is the redshift of the source, and r_{co} is the comoving distance in

Mpc. We choose the filling factor for the relativistic plasma, f_{rl}, and the relative contribution of the ions to the energy, a, to be 1 and 2, respectively. The function $X_{0.5}(\alpha)$ handles integration over the frequency range from ν_l to ν_h, where $\nu_l = 0.01$ GHz and $\nu_h = 100$ GHz, and is defined as:

$$X_q(\alpha) = (\nu_2^{q+\alpha} - \nu_1^{q+\alpha})/(q+\alpha), \tag{2.7}$$

where q is 0.5 in this case and represents the spectral shape function of the synchrotron emission.

Knowledge of the source size is required, since it feeds directly into the estimate of source pressure. For resolved single, double or triple sources we take the measured region sizes directly from JMFIT. For slightly resolved or unresolved sources we take a conservative approach and use the beam major axis as an upper limit to source size. This yields a conservative *lower limit* for the source pressure. Higher resolution Very Long Baseline Array (VLBA) images for a number of the unresolved sources (Patil et al., in prep.) usually reveal yet smaller scale double lobes with yet higher pressures. Thus, our current treatment of the VLA images yields useful, though conservative, lower limits to the radio source pressures in the unresolved sources.

Figure 2.9 shows the distribution of pressures for our sample, with lower limits for the unresolved sources. For the resolved sources, the median pressure is $\log(P_l/(\text{dyne cm}^{-2})) = -8.4$ or ($\log[(P_l/k_B)/(\text{cm}^{-3}\text{K})] = +7.4$). For the lower limits, these values are $\log(P_l/(\text{dyne cm}^{-2})) = -7.1$ or ($\log[(P_l/k_B)/(\text{cm}^{-3}\text{K})] = +8.8$).

To help put our sample in context, we include the typical range of equipartition lobe pressures for a number of other classes of radio AGN. On larger scales, the lobe pressures in FRI (e.g., Worrall & Birkinshaw, 2000; Croston et al., 2008; Croston & Hardcastle, 2014) and FRII (e.g., Croston et al., 2005; Ineson et al., 2017; Harwood

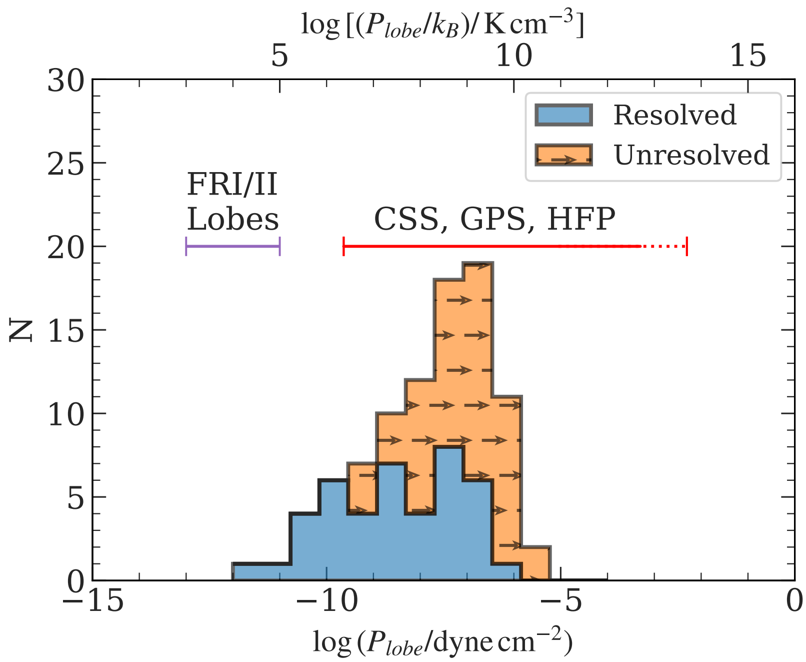

Figure 2.9: The distribution of radio source pressures for our sample, with lower limits for spatially unresolved sources shown as arrows. The orange histogram is stacked on top of the blue histogram. Also shown are typical ranges of source pressures for other classes of radio AGN (see text for references to the data that were used to generate these ranges).

et al., 2016; Vaddi et al., 2019) radio galaxies are roughly 3 dex lower than our sample, almost certainly reflecting the much lower ambient pressures found on larger scales in the circumgalactic environment.

Figure 2.9 also shows the range of equipartition lobe pressures for CSS, GPS, and HFP sources taken directly from various studies (Mutel et al., 1985; Readhead et al., 1996; Orienti & Dallacasa, 2014). There is a considerable overlap between our source pressures and those of the CSS, GPS and HFP samples, possibly indicating a similarity in their properties and stage of development. However, a detailed comparison with these young radio AGN is not straightforward because most measurements for the CSS, GPS and HFP sources come from Very Long Baseline Interferometry (VLBI) observations with ∼milliarcsecond-scale angular resolution capable of identifying much more compact radio structures. Indeed, preliminary analysis of our own VLBA follow up survey shows that many of our unresolved sources also have more compact source components with significantly higher pressures (by $\sim 1-3$ dex, Lonsdale et al. in prep.). In all these comparisons, we have verified that our approach to measuring source pressures reproduces the source pressures given in these other papers.

The compact nature of the radio sources, together with their implied high pressures seem to be a characteristic of the sample, and it is important to understand the origin of these high pressures. Unlike the lobes of extended FRI/FRII radio galaxies, the location of our radio sources deep within the host galaxy means they are embedded within the relatively high-pressure environment of the central ~1 kpc region. If the radio sources are in fact over-pressured relative to the ambient ISM, then that over-pressure may generate an expansion which, when coupled to the small size, may indicate a young source. We will present a more quantitative analysis of the source pressures and ages in Section 2.7.2 when we use a simple model of jet-driven lobe expansion to fit the observed source sizes and pressures.

2.6 Radio Luminosity Function

The radio luminosity function (RLF) measures the number of radio sources per dex of radio continuum luminosity per co-moving Mpc^3 (e.g., Condon et al., 2002). To calculate the RLF for our sample, we use the standard $1/V_{max}$ method (Schmidt, 1968), which sums the space density for each source using a total volume within which that source could have been detected, given our sample selection criteria.

As described in Section 2.2, our sample selection is somewhat complicated and involves a combination of cuts in radio flux and source size as well as infrared fluxes

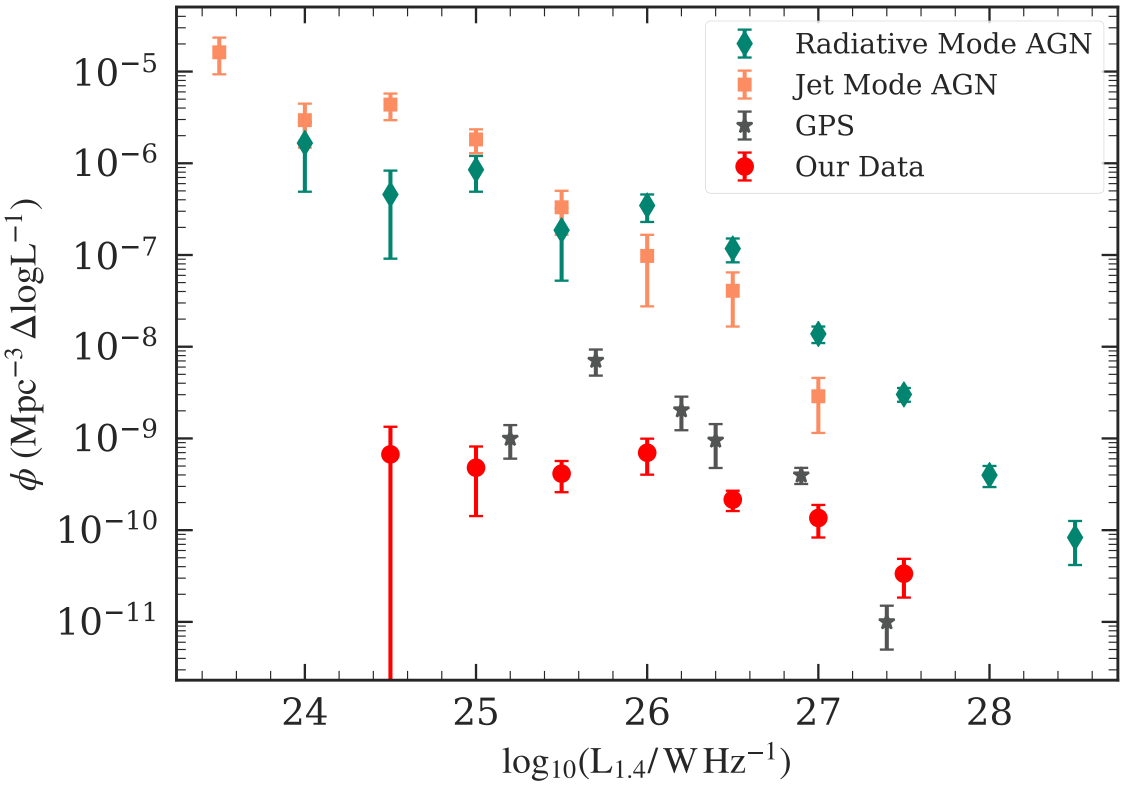

Figure 2.10: Radio luminosity function (RLF) of our sample (red filled circles). For comparison, we have also plotted the RLFs of the populations of radiative- and jet-mode AGN (green diamonds and orange squares, respectively) from Best et al. (2014) as well as young radio AGN (gray asterisk) from the GPS samples presented in Snellen et al. (2000) .

and colors. We therefore defined $V_{max,i}$ for the i^{th} source as:

$$V_{max,i} = \int_{z_{min,i}}^{z_{max,i}} \frac{dV_c}{dz} dz, \tag{2.8}$$

Where V_c is the co-moving volume and $z_{min,i}$ and $z_{max,i}$ are the minimum and maximum redshift limits within which source i would be included in our sample. The full redshift range searched was $z = 0 - 6$, with $\Delta z = 0.01$. To allow for the *WISE* color selection we fitted a second order fit to $\log \nu$ *vs.* $\log F_\nu$ to the four measured *WISE* fluxes and used this SED to establish whether the source passed the color selection at each redshift. We did not include the radio source size criterion ($\theta < 45''$) since our observations indicate that none of our sources would be resolved by NVSS unless they were at a very low redshift ($z < 0.1$) with correspondingly small co-moving volume. In practice, we find that shifting a source to higher redshift usually fails our selection due to becoming too faint in the MIR. Similarly, we find that shifting a source to lower redshift usually fails our selection due to the source becoming too blue in the MIR. Because the color selection is usually affected at lower redshift, where the $1/V_{max}$ factor is small, then the detailed form of the MIR SED does not have a significant impact on the final RLF.

The luminosity function, ϕ, is given by:

$$\phi = \frac{4\pi}{\Omega}\frac{N_{tot}}{N_z}(\Delta \log\ L^{-1})\sum_{i}^{N}\frac{1}{V_{max,i}}, \tag{2.9}$$

where Ω is the solid angle of our survey, which is essentially that of the NVSS since the *WISE* survey is all-sky (a total area of 28,443 sq. deg, Lonsdale et al. 2015) , $\Delta \log\ L^{-1}$ is the width of each luminosity bin (with L measured in units of W Hz^{-1} here), and N is the number of sources in each luminosity bin. Finally, the factor N_{tot}/N_z corrects for the fact that we only measured redshifts for 46% of the total sample. A simple multiplicative factor is adequate since this subset is itself a significant fraction of the total, and is relatively unbiased in redshift. The errors given are simply proportional to $\sqrt{N}$, boosted by N_{tot}/N_z.

Figure 2.10 shows the RLF of our sample, together with the RLFs of samples of high-excitation (radiative mode) and low-excitation (jet mode) radio-loud AGN from Best et al. (2014). As expected given the deliberate selection of a rare class in color space, the RLF of our sample falls $\sim 2-3$ dex below that of the radio AGN from Best et al. (2014). However, this offset is likely to be a lower limit because the radio

AGN sample has lower redshift ($0.5 < z < 1$). Given the well known tendency for the co-moving density of radio sources to increase with redshift (e.g., Best et al., 2014; Pracy et al., 2016; Ceraj et al., 2018), a more detailed comparison at matched redshift would likely find an even greater offset.

How should we interpret the lower space density of our sample compared to the other samples of radio AGN? A straightforward explanation that supports our original motivation for selecting this sample is that the sources are in a short-lived phase (Lonsdale et al., 2015). Two qualities of the sample point to this: (a) they have compact, high-pressure radio sources, which can plausibly be argued are young, (b) they have high bolometric luminosity but are optically faint, suggesting the sample is dominated by obscured quasars with high columns. Within the fairly well-established theory of this class of object they are thought to be in a very young transient stage following a strong fueling event, probably associated with a merger (e.g., Hopkins & Hernquist, 2006).

Another possible explanation for a low RLF is that the high-column material that yields both the red MIR colors and suppressed optical emission has a low covering factor due to a single cloud that happens to fall along our line of sight. However, we think this is unlikely because another characteristic of our sample is that it has high MIR luminosity. First, a simple optically thick blackbody at T$\sim$ 60 K must have a radius of $\sim$ 1 kpc to generate such a high MIR luminosity. Second, the high MIR luminosity suggests a large fraction of the AGN output is reprocessed by high-column absorbing material. Thus the covering factor for the high-column material must be reasonably high.

2.7 Discussion

The overall scientific goal of our multi-wavelength program is to identify heavily obscured quasars at the peak epoch of stellar mass assembly and SMBH growth and investigate their connection to galaxy evolution, possibly via the interaction of a powerful jet with the host's ISM. Our unique selection criteria of extremely red *WISE* colors, along with compact radio and faint optical emission, promises to identify galaxies in a key stage of galaxy growth. In this section, we discuss the implications of our high-resolution radio imaging survey for the early phases of radio source evolution.

2.7.1 Radio Source Evolution

Several models have been proposed to describe the temporal evolution of the observed properties of radio sources, such as luminosity and spectral turnover frequency (e.g., Falle, 1991; Fanti et al., 1995; Readhead et al., 1996; Kaiser & Alexander, 1997; O'Dea & Baum, 1997; Snellen et al., 2000; Kaiser & Best, 2007; Kunert-Bajraszewska et al., 2010; An & Baan, 2012; Maciel & Alexander, 2014). Many of the early models assumed self-similar expansion of radio jets as they move first through dense ISM during their initial growth until they emerge into the IGM and ICM to become large-scale, old sources (Kaiser & Alexander, 1997). Early semi-analytic models found that the radio source luminosity increases as ram-pressure confined lobes expand within the galaxy. The luminosity reaches a maximum when the jets pass the boundary of the ISM, and then it decreases as the lobes expand into the ICM to become FRI/FRII sources.

We now explore the evolutionary stage of our sample and its connection to the FRI/FRII population by plotting our sources on the radio-power *vs.* linear size (PD)

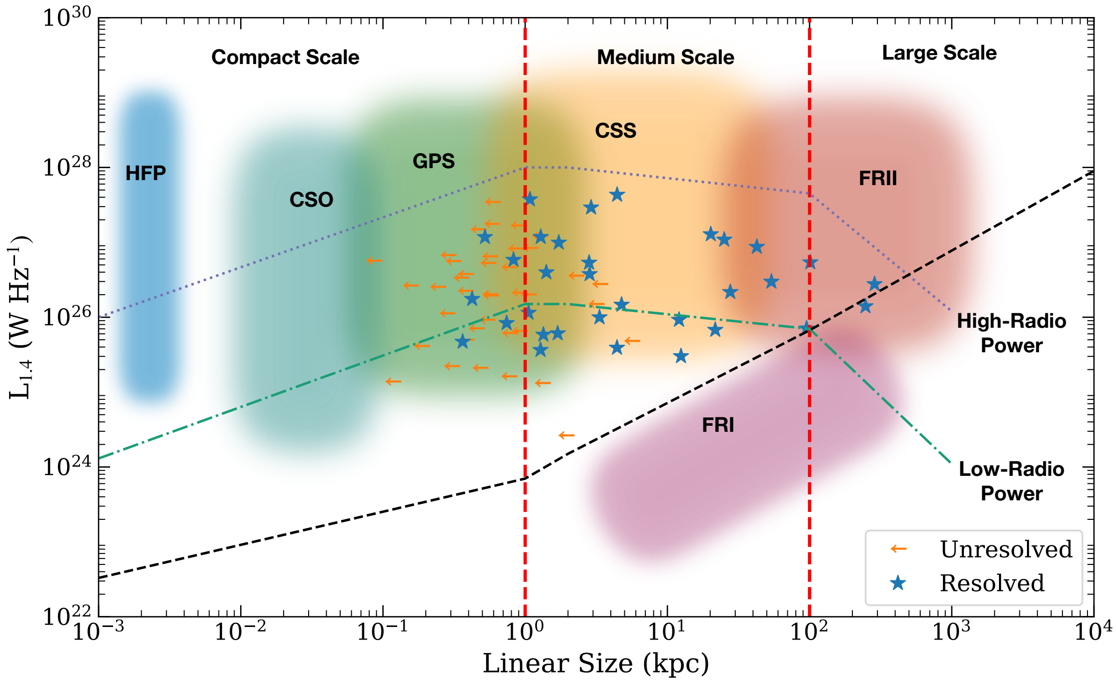

Figure 2.11: 1.4 GHz spectral luminosity *vs*. largest linear source extent. Blue stars represent resolved sources and orange arrows indicate unresolved sources from our sample. The colored boxes represent the parameter space occupied by different radio populations compiled by An & Baan (2012). The purple dotted and green dash-dotted lines are the evolutionary tracks followed by high-(HRP) and low-radio power (LRP) sources, respectively, based on the model given in An & Baan (2012). The vertical red dotted lines divide the entire plane into three broad size scales. The HFP, CSO, and GPS sources are on the compact scales ($<$ 1 kpc), CSS and a minority of FRI/FRII sources fall into the medium scales ($\sim 1 - 100$ kpc), and FRI/II sources are the large scale populations (>100 kpc). The black dashed line is the boundary between the stable and turbulent jet flows.

diagram in Figure 2.11. The range of linear extents of our sources covers multiple classes of medium- and compact-scaled radio sources, including CSS and GPS populations. It is clear from Figure 2.11 and Section 2.5.3 that the radio luminosities of our sample sources lie between those of the classical FRI and FRII populations. We also show the two tracks given by An & Baan (2012) that follow the high radio power (dotted) and low radio power (dash-dotted) sources. Our sources, being intermediate in luminosity, lie between these two tracks in Figure 2.11. The dashed line shows the boundary between stable and unstable jets in the model of An & Baan (2012). The fact that all except one (J2318−25) of our sources lie above this line is consistent with them having stable jets that yield small-scale edge-brightened double or triple morphologies, as indeed we find in the majority of the resolved sources.

Based on the evolutionary models given in An & Baan (2012) and following similar recent analyses (e.g. Jarvis et al. 2019), it seems the position of our sources on the PD diagram relative to the jet instability criterion supports the possibility that they might eventually evolve into classical, FRI/II radio sources. This possibility is reinforced by the fact that our sources are heavily obscured which points to a long term fuel supply that could sustain the SMBH accretion for the $\sim$ 100 Myr time span necessary to create larger radio sources. However, a more careful discussion of possible evolutionary links between the *WISE*-NVSS sources and classical radio galaxies must consider the source ages. This we now attempt using a simple jet-lobe expansion model.

2.7.2 Lobe Expansion Model

There has been considerable work on models of radio source evolution in a variety of contexts, both analytic (e.g., Turner & Shabala, 2015; Hardcastle, 2018) and numerical (e.g., Mukherjee et al., 2016; Perucho, 2018). Our sources may allow a relatively simple approach because the jets enter a dense, near-nuclear environment and are caught early in their development. While this may seem a potentially complex process, detailed simulations of just this situation (e.g., Mukherjee et al., 2016, 2018) suggest that the radio source develops in a quasi-spherical expansion, and in this case, the analytic model of self-similar expansion is approximately correct.

A simple approach assumes purely adiabatic expansion in which case the dynamics of the early phase of jet evolution can be approximated by the presence of a forward shock, a contact discontinuity, and an inner reverse shock.

The mathematical treatment for the expansion of a spherical lobe driven by continuous energy input is given in Weaver et al. (1977). The momentum and energy conservation equations are:

$$\frac{d}{dt}\left(\frac{4}{3}\pi R_l^3 \rho_a V_l\right) = 4\pi R_l^2 p_l \tag{2.10}$$

$$\frac{d}{dt}\left[\frac{4\pi}{3}\frac{p_l}{\gamma - 1}R_l^3\right] + 4\pi R_l^2 p_l V_l = F_E \tag{2.11}$$

where R_l is the radius of the lobe's shock, $V_l = dR_l/dt$ is the velocity of the shock, ρ_a is the ambient density of the undisturbed ISM, p_l is the pressure inside the lobe, and F_E is the mechanical power injected by the jet. For a self-similar expansion of the jet lobe, the above equations can be solved to yield:

$$R_l = 0.78 F_{43}^{1/5} n_a^{-1/5} t_{\rm Myr}^{3/5} \ \text{kpc} \tag{2.12}$$

$$p_l = 1.63 \times 10^{-9} F_{43}^{2/5} n_a^{3/5} t_{\rm Myr}^{-4/5} \ \text{dynes cm}^{-2} \tag{2.13}$$

$$V_l = 458 F_{43}^{1/5} n_a^{-1/5} t_{\rm Myr}^{-2/5} \ \text{km s}^{-1} \tag{2.14}$$

where F_{43} is in units of 10^{43} erg s^{-1}, $n_a (= \rho_a/(\mu_m m_p))$ is the ambient number density in cm^{-3}, and $t_{\rm Myr}$ is a dynamical age in Myr. Here μ_m is the mean molecular weight of the ISM and m_p is the proton mass. Equations 2.12−2.14 can be rearranged to isolate t_{Myr}, n_a, and V_l in terms of our observed parameters:

$$p_l = 7.76 \times 10^{-10} F_{43} t_{\mathrm{Myr}} R_l^{-3} \tag{2.15}$$

$$p_l = 1.17 \times 10^{-9}\, F_{43}^{2/3} n_a^{1/3} R_l^{-4/3} \tag{2.16}$$

$$p_l = 1.50 \times 10^{-12} F_{43} (V_l/c)^{-1} R_l^{-2} \tag{2.17}$$

While Sections 2.5.2 and 2.5.4 describe our estimates of radio source size, R_l, and pressure, p_l, estimating the jet power, F_{43}, is more uncertain. One approach is to assume that the jet power is related to the radio luminosity. While a number of studies have tried to establish such a link (e.g., Willott et al., 1999; Cavagnolo et al., 2010), others have argued that the relation is intrinsically quite scattered and has been amplified by selection bias (Godfrey & Shabala, 2016). Bearing these caveats in mind, we cautiously adopt the relation given by Ineson et al. (2017):

$$F_{43} = 5 \times 10^3 L_{151}^{0.89 \pm 0.09} \tag{2.18}$$

where L_{151} is the rest-frame 151 MHz radio luminosity in units of 10^{28} W Hz^{-1} Sr^{-1}. For our sample, we estimate L_{151} using the 1.4 GHz luminosity from NVSS and a spectral index $\alpha_{1.4}^{10}$ derived from the NVSS flux and our X-band flux. We exclude sources with flat/inverted indices ($\alpha_{1.4}^{10} > -0.3$) and low S/N sources with very steep indices ($\alpha_{1.4}^{10} < -2.0$) since the uncertainty in the extrapolation to rest-frame L_{151} is large.

The left panel in Figure 2.12 shows the relation given in Equation 2.15 between source pressure, source size and jet power, by plotting $3 \log R_l - \log F_{43}$ against $\log p_l$ so that the source dynamical age, t_{Myr}, appears as diagonal contours.

Using estimates for R_l and p_l from Sections 2.5.2 and 2.5.4, and L_{151} as described

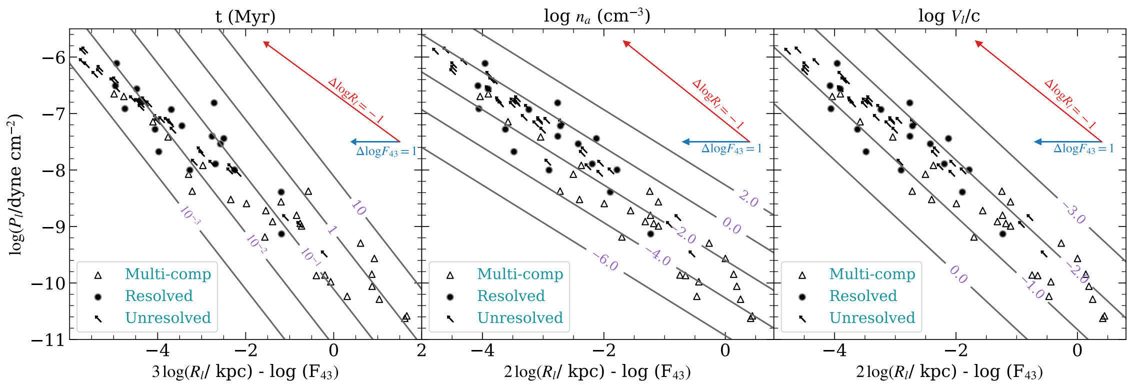

Figure 2.12: Application of adiabatic lobe expansion model to our sample sources with known redshifts (Equations 2.15−2.17). These panels isolate source age (t_{Myr}), ambient particle density (n_a), and lobe expansion speed (V_l/c). The observed parameters are R_l, p_l and F_{43} as described in the text. Open triangles are individual resolved lobe components for double or triple sources; filled circles are partially resolved sources; arrows are unresolved sources. Red and blue vectors illustrate the effect of a decrease in source size by one dex and increase in jet power by one dex.

above, we find a range of properties that depend mainly on the source size. The dynamical ages span from $\sim 10^6$ years for the larger sources to $< 10^3$ years for the unresolved sources. This is consistent with the overall picture that our sample contains young radio sources.

The central panel of Figure 2.12 includes contours of external density, n_a. Again, the most extended sources are located in relatively low density regions, with $n_a \sim 10^{-4}$ cm^{-3} while the most compact sources are expanding into a fairly dense medium with $n_a > 10$ cm^{-3}. This is consistent with our expectation that the most nuclear radio sources ar expanding into a relative high-density region. This is also consistent with high columns that are likely to be associated with the observed red-MIR colors. Closely related red-MIR Hot DOG populations are found to have Compton thick columns (e.g. Stern et al., 2014; Ricci et al., 2017b).

The right panel in Figure 2.12 includes contours of lobe expansion speed. It seems the sources expand with modest, sub-luminal, speeds $V_l \sim 0.003c - 0.1c$ with a median near $0.03c$. Proper motion studies of Compact Symmetric Objects (CSO) have identified lobe expansion speeds of a few percent of speed of light (e.g., An et al., 2012), consistent with these model results. We note that our velocities are also similar to those found in much more detailed simulations of a similarly powered jet interacting with a dense clumpy medium (Mukherjee et al., 2016, 2018).

The discussion of the growth of compact radio sources is often framed as two contrasting possibilities: the small sizes result from youth or from "frustrated" jets that cannot expand due to a dense surrounding medium (e.g., van Breugel et al., 1984; Bicknell et al., 2018). Our analysis suggests that both perspectives might be relevant for our sources — the sources are indeed young, but the ISM is also dense and this slows the source expansion.

2.7.3 Prevalence of Gas-rich Mergers

Perhaps the most straightforward indication of youth would be to find a direct association with a short-lived phase in the host galaxy, such as a merger. Unfortunately, by selecting optically faint hosts (to avoid low-redshift sources) a simple inspection of the optical morphology is difficult. In the absence of direct observations, what might we expect? Despite early numerical simulations suggesting that luminous AGN are associated with gas rich mergers (e.g., Hopkins et al., 2008), the observational evidence has been mixed. For example, Cisternas et al. (2011) and Villforth et al. (2017b) fail to find the AGN-merger connection. However, when the AGN are selected to be dusty and obscured, such as *WISE* AGN, the association with mergers is much clearer, particularly at high luminosity (e.g., Satyapal et al., 2014; Weston et al., 2017; Goulding et al., 2018).

Recent numerical simulations of galaxy mergers also support this association. Blecha et al. (2018) have tracked the evolution of *WISE* colors and luminosities for gas rich mergers, finding the closest match to our sample's very red *WISE* colors during the brief final stage of coalescence.

Thus, our own sample of *WISE* selected AGN is very likely to contain a significant fraction of recent gas-rich mergers. Such a merger would be consistent with a newly triggered AGN with a radio jet.

2.7.4 Are WISE-NVSS Sources Truly Newborn?

Another approach that places the *WISE*-NVSS sources in a wider context is to use the RLF and dynamical age estimates to help establish a link to the other classes of radio source. First, the RLF analysis in Section 2.6 suggests the *WISE*-NVSS sources have ~ 300 times lower space density than classical radio galaxies. Second, comparing the median dynamical age of $\sim 10^{4.3}$ years to a typical age for a classical radio galaxy of $\sim 10^{6-7}$ years, suggests a source age ratio of $\sim 0.2 - 2\%$. Combining this age ratio with the ratio in space density of $\sim 0.3\%$, indicates that $\sim 1 - 6\%$ of the classical radio galaxies might have been born directly from a *WISE*-NVSS source.

Finding alternate compact progenitors that might evolve into classical radio galaxies isn't hard. O'Dea (1998) performs a similar demographic analysis with GPS and CSS sources and shows that they actually over-produce the classical radio galaxies by a factor of ~ 10. O'Dea (1998) interprets this apparent over-production as evidence for recurrent activity in the GPS and CSS populations — meaning there might be multiple phases of compact emission before the source finally evolves into a large-scale, classical, radio galaxy.

The relation between the *WISE*-NVSS sources and the GPS and CSS sources is not yet clear. There seems to be a systematic difference in the MIR properties (Patil et al. in prep.), suggesting that although all these sources may be dynamically young, the *WISE*-NVSS sources might be truly "newborn" — meaning the radio source has emerged for the first time, into a dense near-nuclear ISM. In this case, the *WISE*-NVSS sources may either evolve directly into the classical radio galaxies, or perhaps join the more common GPS and CSS classes, and from there ultimately evolve into a classical radio phase.

2.8 Conclusion

We have presented a high-resolution 10 GHz VLA imaging study of a sample of ultra-luminous and heavily obscured quasars in the redshift range $0.4 < z < 3$ with a median $z \sim 1.53$. Our selection is similar to that of Hot DOGs in MIR colors, but adds a requirement for the presence of compact radio emission that allows us to select objects in which radio emitting jets are present. Of the 155 radio sources in our sample, 86 ($\sim 55\%$) remain unresolved even on sub-arcsecond scales. Our main conclusions are as follows:

1. The compactness of the majority of the sources on scales $< 0.2''$ implies typical physical sizes are ≤ 2 kpc at the median redshift ($z = 1.53$) of our sample.

2. We measured in-band spectral indices from 8–12 GHz and found a median spectral index of -1.0, consistent with (perhaps slightly steeper than) typical optically-thin synchrotron emission from radio jets or lobes.

3. We estimate equipartition pressures in the radio lobes and find them to be similar to other compact sources such as GPS or CSS, but significantly higher than the lobes of more extended classical radio galaxies. These high pressures support the possibility that the *WISE*-NVSS sources may be powered by recently triggered radio jets emerging into a dense, near-nuclear ISM.

4. Our radio sources have rest frame 1.4 GHz luminosities between those of the classical FRI and FRII radio galaxies, in the range $10^{25-27.5}$ W Hz^{-1}. On the

well-known Radio Power *vs.* Linear Size (PD) diagram, our sources fall in the same region as the other compact and medium scale radio sources such as GPS and CSS sources.

5. We perform a standard V/V_{max} analysis to generate a 1.4 GHz radio luminosity function for our sample, and compare it to other samples of radio sources. Overall, the *WISE*-NVSS sources are rare, with space densities roughly $\sim 2-3$ dex lower than the population of radio AGN studied by Best et al. (2014) and $\sim 0.5-1.0$ dex lower than samples of compact radio AGN (GPS, HFP; Snellen et al. 2000).

6. We use a simple adiabatic jet expansion model and an empirical relation between radio luminosity and jet power, to estimate dynamical ages, ambient densities and expansion velocities for our sample sources. We find source ages in the range $< 10^3 - 10^6$ years (median 20 kyr), ambient particle densities in the range $10^{-4} - 10$ cm^{-3} (median 0.1 cm^{-3}), and lobe expansion speeds in the range $0.003c - 0.1c$ (median $0.03c$). Within the framework of this model, these results broadly confirm our expectation that these sources are relatively young and are expanding at modest velocities.

7. In the absence of unknown selection effects, such as variability (Mooley et al., 2016), our RLF and dynamical age analyses suggest that ∼1-6% of the population of large-scale radio galaxies could have evolved directly from the *WISE*-NVSS sources. The over-abundance of the GPS and CSS sources relative to classical, large-scale radio sources raises the question of the relation between the *WISE*-NVSS sources and these other compact radio sources. We favor a scenario in which the *WISE*-NVSS sources harbor jets that have turned on for

the very first time, following the merger and dumping of ISM into the nucleus. Following this initial phase, it is possible that the *WISE*-NVSS sources evolve into GPS or CSS sources, of which some ultimately evolve into the larger classical radio galaxies.

Overall, we conclude that the radio properties of our sample are consistent with emission arising from recently-triggered, young jets. In a series of forthcoming studies, we will present an analysis of the broadband radio SEDs of our sources as well as new milliarcsecond-scale-resolution imaging with the VLBA and enhanced Multi Element Remotely Linked Interferometer Network (e-MERLIN). These studies will place tighter constraints on the source ages and provide deeper insights into their evolutionary stages. Ultimately, studies of the ISM content and conditions in the vicinity of young, ultra-luminous quasars will be needed to investigate the onset and energetic importance of jet-ISM feedback during the peak epoch of galaxy assembly. Observations with ALMA and the *James Webb Space Telescope*, and eventually the next-generation Very Large Array (e.g., Nyland et al. 2018; Patil et al. 2018), will be essential for improving our understanding of feedback driven by young radio AGN at $z \sim 2$ and its broader connection to galaxy evolution.

2.9 Figuresets and Data Tables

2.9.1 10 GHz Continuum Images

We provide individual 10 GHz continuum images of our sample ih Figure 2.13.

2.9.2 Tables

Observational details of our sample are provided in Table 2.3. Beam sizes and source measurements from the VLA observations are given in Table 2.4. Results from JMFIT for source spatial measurements for the VLA A- and B-array observations

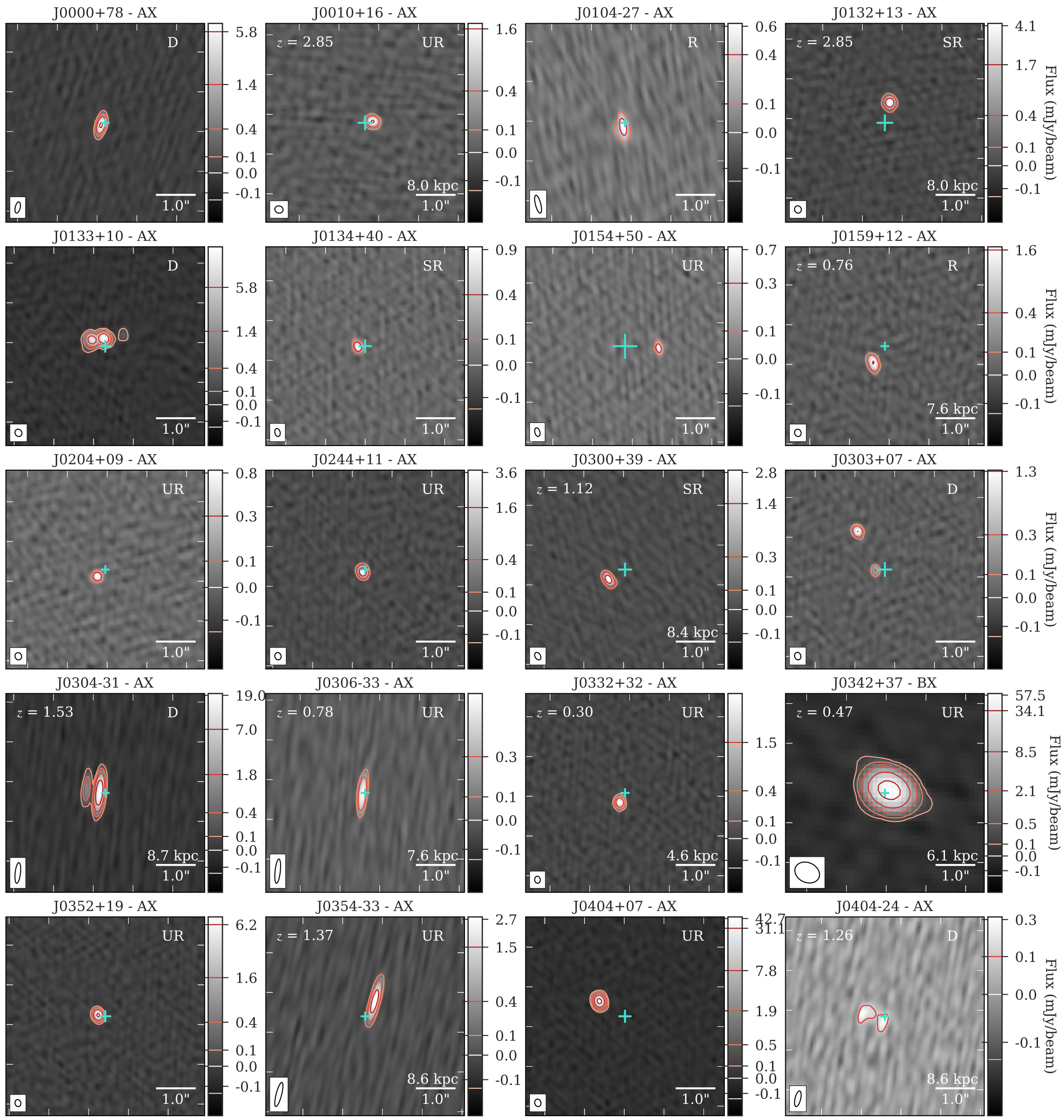

Figure 2.13: 10 GHz continuum images for our sample. The source name and VLA array used to produce the image are shown above each image. Contour levels are plotted in units of rms noise which can be found in Table 2.3. The positive contours (solid) increase by a factor of 4 starting from 5σ and the negative contours (dashed) are -5σ. The contour levels are also marked on the right hand colorbar, including a zero level (which is not plotted on the image as a contour). The cyan plus symbol gives the *WISE* source position with one sigma uncertainty. For clarity, a minimum of $0.2''$ is used. The synthesized beam is shown as a black ellipse in the lower-left corner. A white solid line on the lower-right gives a scale bar. When available, the redshift is given in the upper-left and the equivalent physical scale is given above the scale bar. The radio morphology code is given in the upper-right. The tick mark spacing is equal to the length of the scale bar. The complete figure set (162 elements) is available in the online Journal.

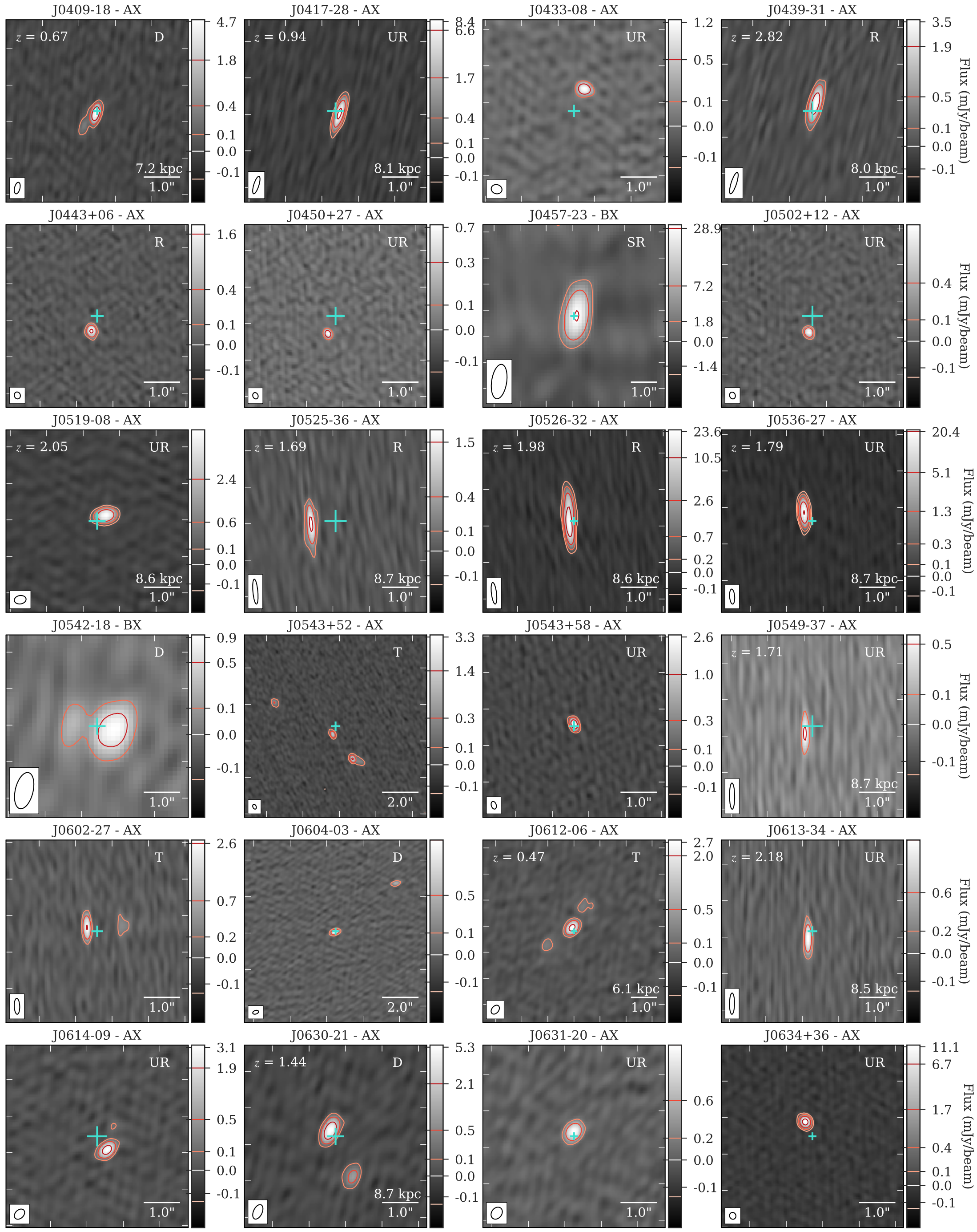

Figure 2.13: *Continued*

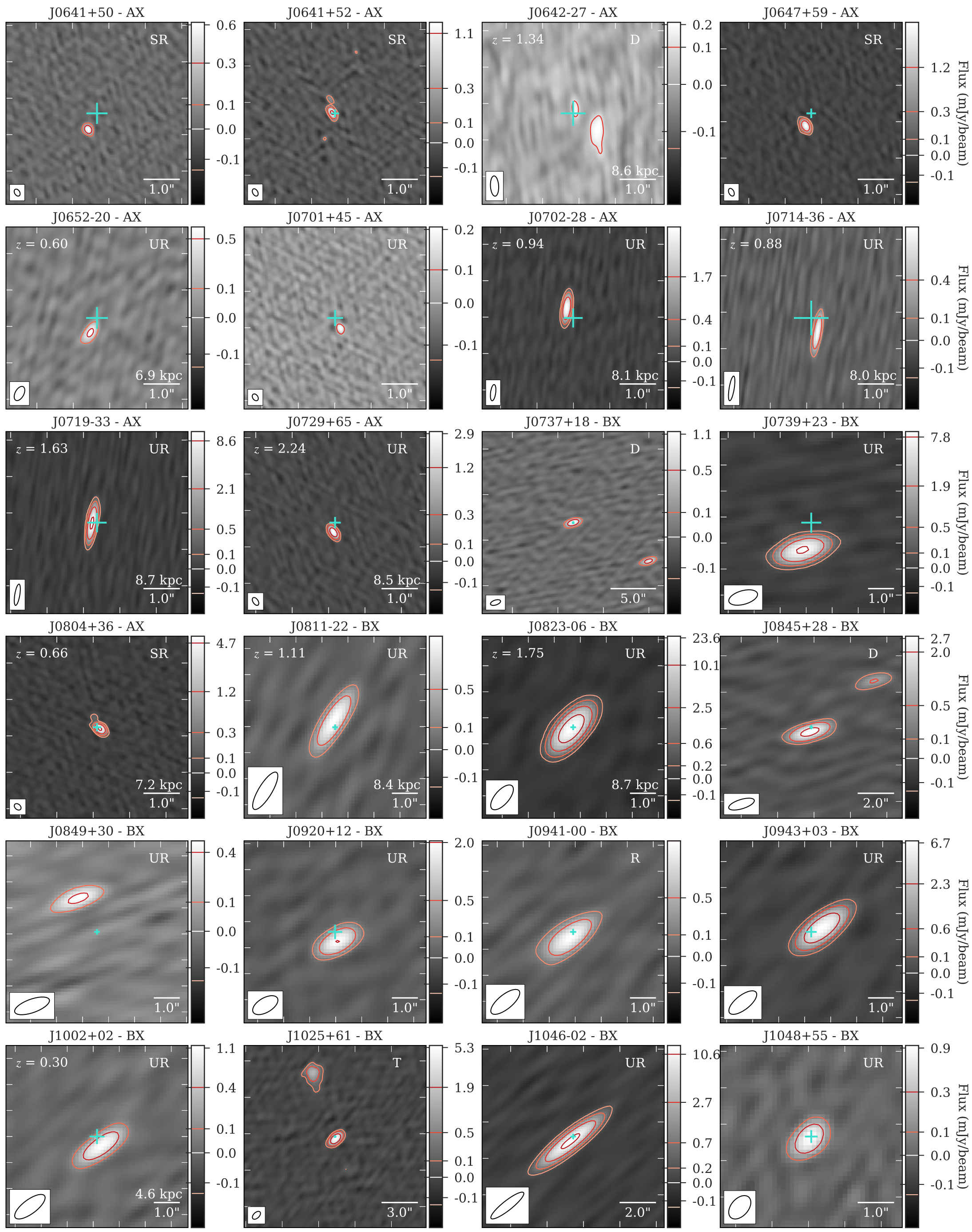

Figure 2.13: *Continued*

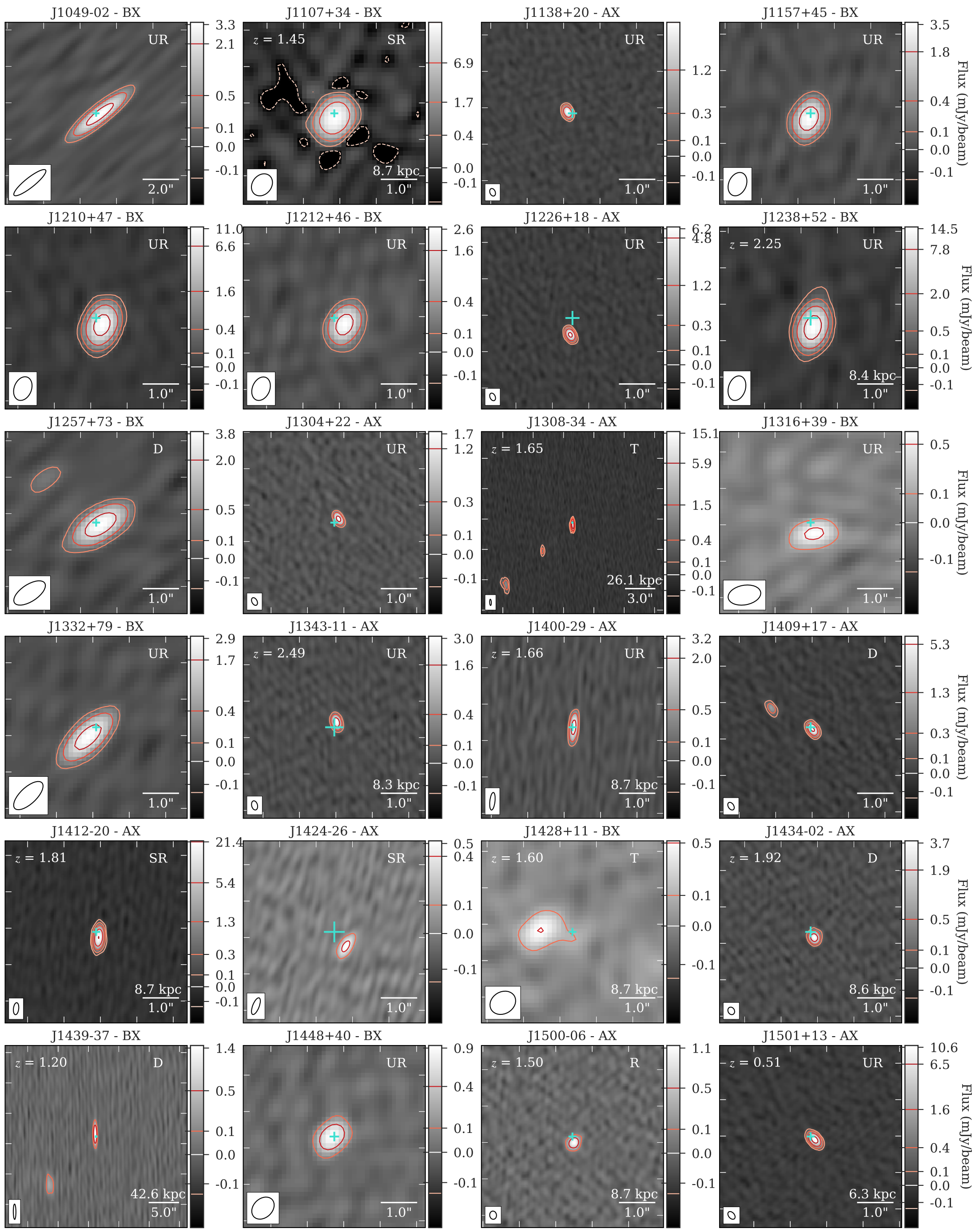

Figure 2.13: *Continued*

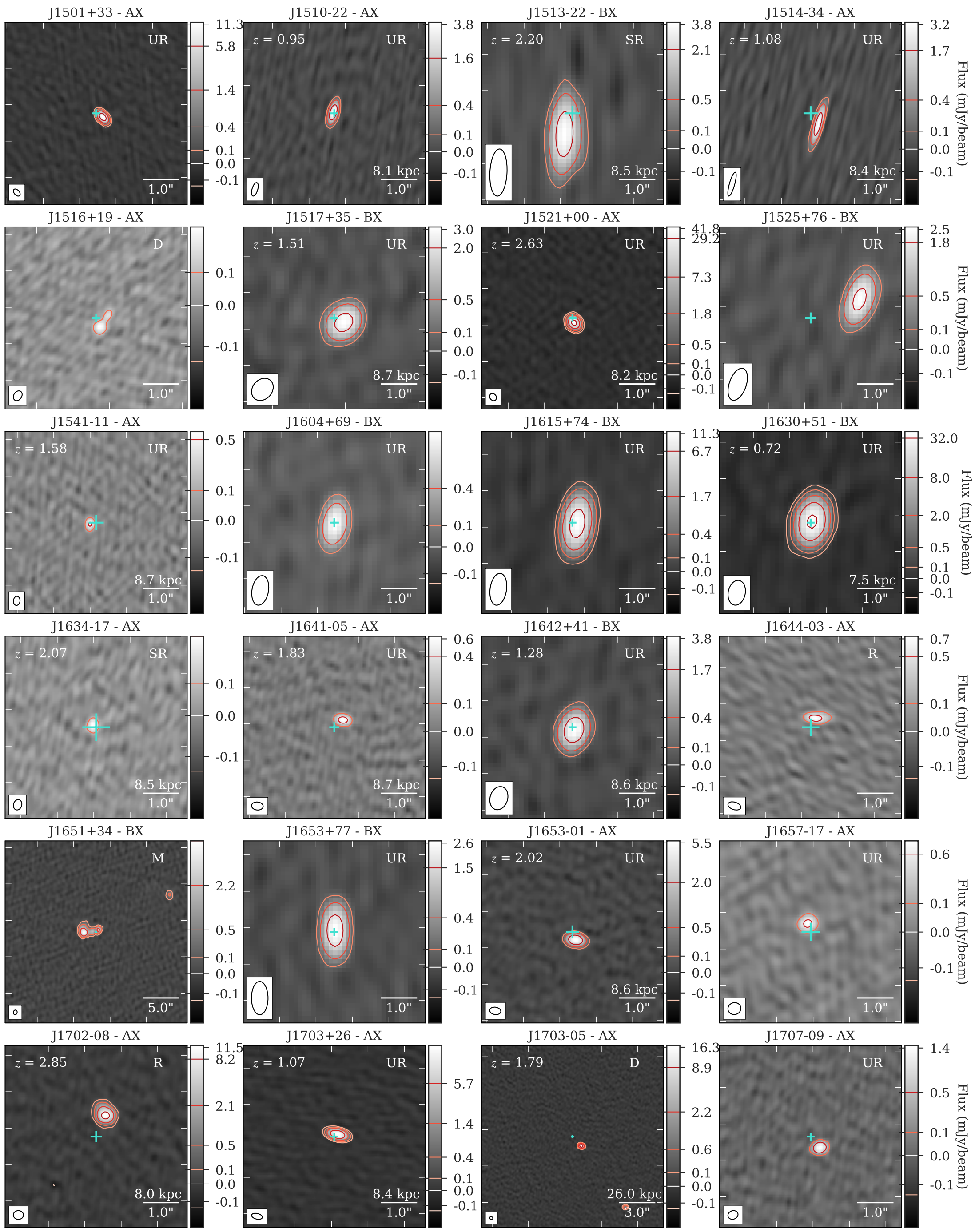

Figure 2.13: *Continued*

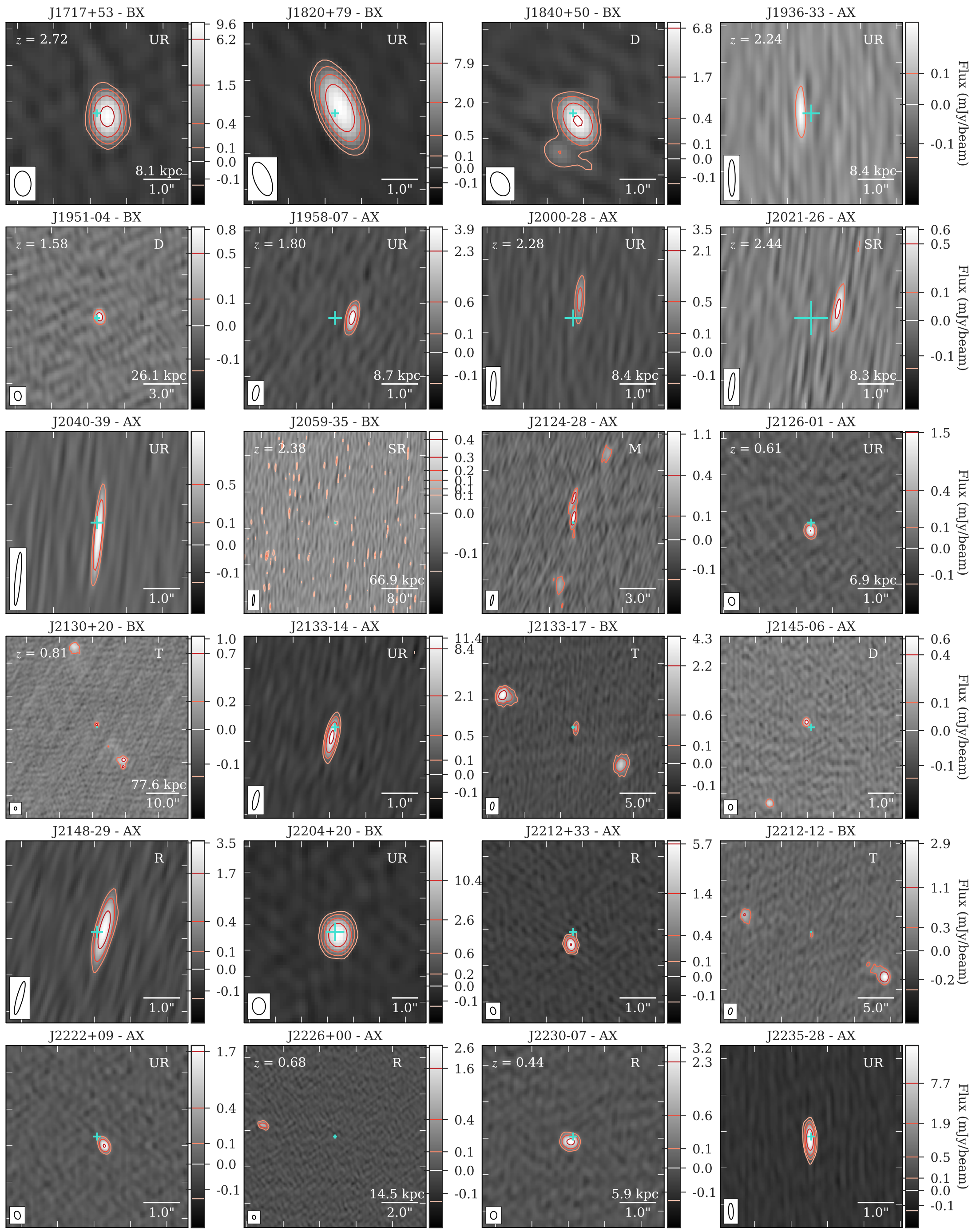

Figure 2.13: *Continued*

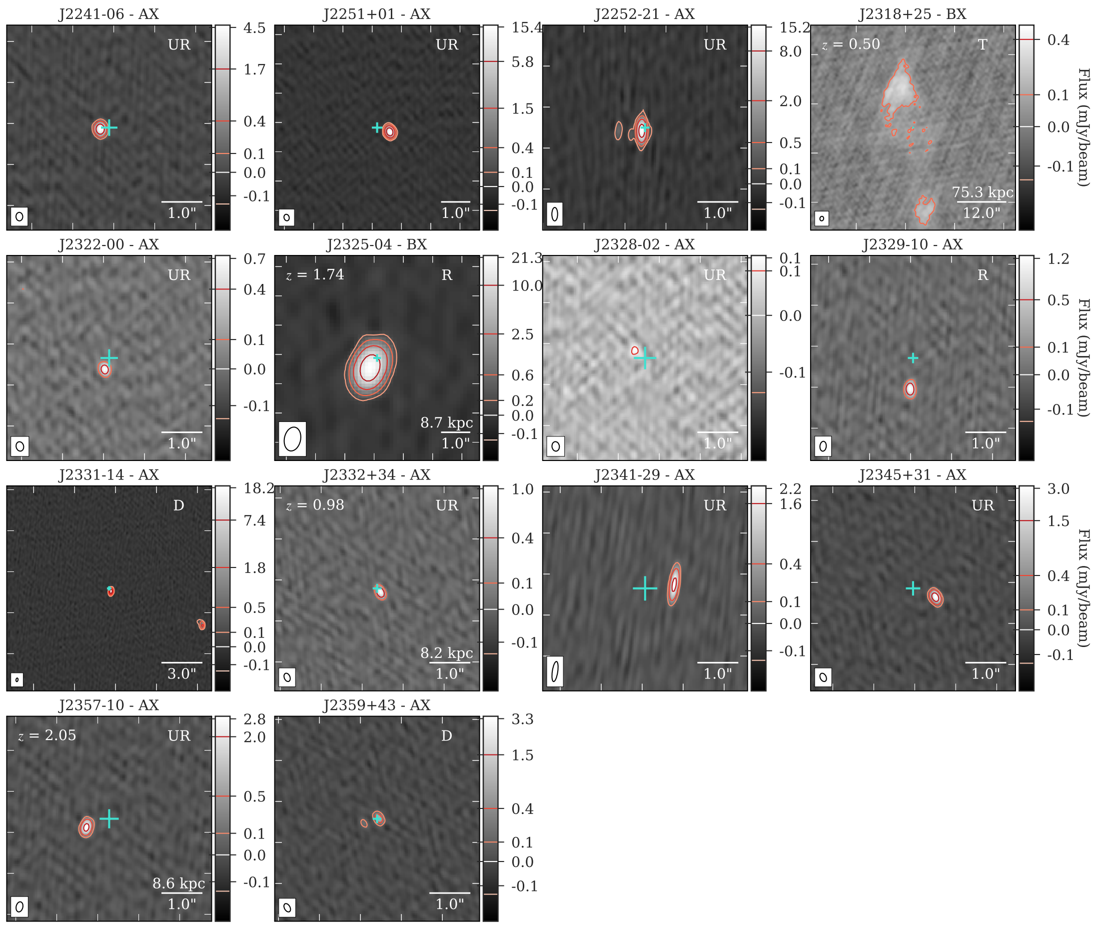

Figure 2.13: *Continued*

are available in Tables 2.5 and 2.6, respectively. Physical properties for our sample sources with redshift available are given in Table 2.7.

Table 2.3: Observational Details of Our Sample

Source	*WISE* ID	A-Array Obs Date yyyy-mm-dd	rms μJy beam^{-1}	S/N	Quality	B-Array Obs Date yyyy-mm-dd	rms μJy beam^{-1}	S/N	Quality
(1)	(2)	(3)	(4)	(5)	(6)	7	(8)	(9)	(10)
J0000+78	000035.88+780717.2	2012-10-31	19	383	G	...	...	...	...
J0010+16	001039.54+164328.7	2012-12-01	20	87	G	2012-06-13	21	94	G
J0104−27	010424.85−275029.0	2012-11-24	19	49	G	2012-06-13	31	46	G
J0132+13	013211.24+130326.8	2012-12-01	22	202	G	2012-08-27	27	175	G
J0133+10	013338.97+101943.9	2012-12-01	19	1064	G	2012-08-27	35	832	G
J0134+40	013419.27+403049.3	2012-10-31	19	51	G	2012-08-27	25	52	G
J0154+50	015442.57+504600.4	2012-10-31	18	39	G	2012-08-27	24	38	G
J0159+12	015919.56+120137.4	2012-12-01	21	87	G	2012-08-27	25	99	G
J0204+09	020411.96+092030.2	2012-12-01	17	49	G	2012-08-27	27	39	G
J0244+11	024423.99+112354.4	2012-12-01	21	182	G	2012-08-27	26	159	G
J0300+39	030037.53+390125.3	2012-10-31	18	163	G	2012-08-27	24	137	G
J0303+07	030333.57+073648.1	2012-12-01	17	79	G	2012-08-27	26	59	G
J0304−31	030427.53−310838.2	2012-11-24	23	890	G	2012-08-27	45	498	G
J0306−33	030629.21−335332.3	2012-11-24	18	77	G	2012-08-27	28	40	G
J0332+32	033228.23+320545.0	2012-12-01	20	255	G	2012-08-27	26	203	G
J0342+37	034222.94+375330.7	2012-10-31	13	2599	G	2012-08-27	28	2142	G
J0352+19	035205.35+194701.2	2012-12-01	20	379	G	2012-08-27	25	321	G
J0354−33	035448.24−330827.5	2012-11-24	19	152	G	2012-08-27	81	33	G
J0404+07	040440.93+071219.2	2012-12-01	25	1785	G	2012-08-27	26	1765	G
J0404−24	040403.61−243600.1	2012-11-24	21	20	G	2012-08-27	27	23	G
J0409−18	040937.67−183757.7	2012-11-24	23	219	G	2012-08-27	28	186	G
J0417−28	041754.10−281654.9	2012-11-24	21	417	G	2012-08-27	27	336	G
J0433−08	043345.58−083628.2	2012-12-20	27	47	G	2012-08-27	30	48	G
J0439−31	043921.92−315908.2	2012-11-24	25	153	G	2012-08-27	31	167	G
J0443+06	044332.56+064318.1	2012-12-01	20	95	G	2012-08-27	25	99	G
J0450+27	045032.88+272608.2	2012-12-01	17	44	G	2012-08-27	30	32	G
J0457−23	045731.90−232402.2	2012-11-24	97	187	G	2012-08-27	397	90	G

Table 2.3 continued

Table 2.3: Observational Details of Our Sample (continued)

Source	*WISE* ID	A-Array Obs Date yyyy-mm-dd	rms μJy beam^{-1}	S/N	Quality	B-Array Obs Date yyyy-mm-dd	rms μJy beam^{-1}	S/N	Quality
(1)	(2)	(3)	(4)	(5)	(6)	7	(8)	(9)	(10)
J0502+12	050204.71+121852.5	2012-12-01	21	77	G	2012-08-27	27	67	G
J0519−08	051905.84−081320.0	2012-12-20	31	298	G	2012-08-27	30	275	G
J0525−36	052533.47−361440.9	2012-11-11	20	99	G	2012-08-27	29	84	G
J0526−32	052624.72−322500.8	2012-11-11	34	713	G	2012-08-27	35	976	G
J0536−27	053622.59−270300.3	2012-11-11	17	1313	G	2012-08-27	31	726	G
J0542−18	054226.62−182515.0	2012-12-20	···	···	P	2012-08-27	28	37	G
J0543+52	054341.36+522854.8	2012-11-10	18	134	G	2012-08-27	29	78	G
J0543+58	054357.95+580950.5	2012-11-10	13	214	G	2012-08-27	32	99	G
J0549−37	054930.07−373939.7	2012-11-11	25	23	G	2012-08-27	46	16	G
J0602−27	060241.46−274110.4	2012-11-11	34	84	G	2012-08-27	45	57	G
J0604−03	060452.99−032847.8	2012-12-20	25	72	G	2012-08-30	23	81	G
J0612−06	061200.23−062209.1	2012-12-20	25	111	G	2012-08-30	29	97	G
J0613−34	061348.08−340728.8	2012-11-11	33	65	G	2012-08-27	30	71	G
J0614−09	061405.57−093658.5	2012-12-20	25	136	G	2012-08-27	···	···	P
J0630−21	063027.81−212058.7	2012-12-20	27	209	G	2012-08-27	26	212	G
J0631−20	063130.71−203411.7	2012-12-20	34	70	G	2012-08-27	29	94	G
J0634+36	063430.21+360938.4	2012-11-10	22	543	G	2012-08-27	21	615	G
J0641+50	064149.36+500907.5	2012-11-10	14	48	G	···	···	···	···
J0641+52	064132.66+520838.6	2012-11-10	14	100	G	2012-08-27	49	40	G
J0642−27	064228.92−272801.2	2012-11-11	22	18	G	2012-08-27	42	13	G
J0647+59	064714.15+593030.2	2012-11-10	16	256	G	2012-08-27	20	248	G
J0652−20	065215.85−200612.7	2012-12-20	27	25	G	2012-08-27	30	28	G
J0701+45	070149.35+451613.2	2012-11-10	13	16	G	2012-08-27	34	19	G
J0702−28	070257.20−280842.0	2012-11-11	23	305	G	2012-08-30	25	257	G
J0714−36	071433.54−363552.1	2012-11-11	23	66	G	2012-08-30	27	66	G
J0719−33	071912.58−334944.2	2012-11-11	28	405	G	2012-08-30	31	358	G
J0729+65	072902.70+654429.6	2012-11-10	16	193	G	2012-08-27	20	182	G

Table 2.3 continued

Table 2.3: Observational Details of Our Sample (continued)

Source	*WISE* ID	A-Array Obs Date yyyy-mm-dd	rms μJy beam^{-1}	S/N	Quality	B-Array Obs Date yyyy-mm-dd	rms μJy beam^{-1}	S/N	Quality
(1)	(2)	(3)	(4)	(5)	(6)	7	(8)	(9)	(10)
J0737+18	073721.89+182546.9	···	···	···	···	2012-08-27	25	45	G
J0739+23	073909.44+234740.7	···	···	···	···	2012-08-27	25	358	G
J0804+36	080431.01+360718.2	2012-11-10	15	379	G	2012-08-27	···	···	P
J0811−22	081131.61−222522.0	···	···	···	···	2012-08-30	25	66	G
J0823−06	082311.24−062408.3	···	···	···	···	2012-08-30	33	762	G
J0845+28	084501.62+283028.0	···	···	···	···	2012-08-27	25	112	G
J0849+30	084904.16+303337.0	···	···	···	···	2012-08-27	20	26	G
J0920+12	092014.69+125302.6	···	···	···	···	2012-08-30	26	80	G
J0929−20	092901.44−205345.7	···	···	···	···	2012-08-30	28	97	G
J0941−00	094157.66−002649.3	···	···	···	···	2012-08-30	26	73	G
J0943+03	094352.95+030323.2	···	···	···	···	2012-08-30	30	239	G
J1002+02	100258.15+025647.9	···	···	···	···	2012-08-30	23	49	G
J1025+61	102509.87+612832.7	···	···	···	···	2012-06-13	24	231	G
J1046−02	104632.81−025030.7	···	···	···	···	2012-08-30	35	394	G
J1048+55	104839.74+555356.6	2012-12-17	···	···	F	2012-06-13	17	55	G
J1049−02	104925.99−023212.5	···	···	···	···	2012-08-30	27	128	G
J1107+34	110734.34+342118.7	2012-12-17	···	···	F	2012-06-13	22	1205	G
J1138+20	113816.90+202834.8	2012-12-10	16	282	G	2012-06-13	22	203	G
J1157+45	115741.77+453802.8	2012-12-17	···	···	F	2012-06-13	23	158	G
J1210+47	121027.88+475003.2	···	···	···	···	2012-06-13	21	545	G
J1212+46	121204.91+465958.9	2012-12-17	···	···	F	2012-06-13	21	133	G
J1226+18	122646.64+181943.9	2012-12-10	15	427	G	2012-06-13	22	296	G
J1238+52	123832.54+524915.6	2012-12-17	···	···	F	2012-06-13	25	608	G
J1257+73	125755.27+730816.7	2012-12-17	···	···	F	2012-06-13	26	153	G
J1304+22	130445.36+222545.5	2012-12-10	15	115	G	2012-06-13	22	84	G
J1308−34	130817.00−344754.3	2012-12-07	19	723	G	2012-06-13	34	445	G
J1316+39	131615.74+394655.0	2012-12-17	···	···	F	2012-06-13	28	25	G

Table 2.3 continued

Table 2.3: Observational Details of Our Sample (continued)

Source	*WISE* ID	A-Array Obs Date yyyy-mm-dd	rms μJy beam^{-1}	S/N	Quality	B-Array Obs Date yyyy-mm-dd	rms μJy beam^{-1}	S/N	Quality
(1)	(2)	(3)	(4)	(5)	(6)	7	(8)	(9)	(10)
J1332+79	133230.91+790704.2	2012-12-17	...	...	F	2012-06-13	22	135	G
J1343−11	134331.37−113609.7	2012-12-28	20	156	G	2012-06-13	21	154	G
J1400−29	140050.13−291924.6	2012-12-07	26	130	G	2012-06-13	28	113	G
J1409+17	140928.83+173204.3	2012-12-10	17	389	G	2012-06-13	20	339	G
J1412−20	141243.15−202011.1	2012-12-07	17	1276	G	2012-06-13	27	822	G
J1424−26	142459.38−265128.8	2012-12-07	20	28	G	2012-06-13	21	33	G
J1428+11	142859.69+111318.7	2012-12-10	...	...	P	2012-06-13	24	20	G
J1434−02	143419.59−023543.6	2012-12-28	25	157	G	2012-06-13	24	182	G
J1439−37	143931.76−372523.8	2012-12-07	23	71	G	2012-06-13	28	54	G
J1448+40	144850.81+402244.3	2012-12-17	...	...	F	2012-06-13	21	48	G
J1500−06	150048.73−064939.8	2012-12-28	24	50	G	2012-06-13	25	74	G
J1501+13	150138.36+132449.9	2012-12-10	21	537	G	2012-06-13	25	453	G
J1501+33	150127.60+334121.7	2012-12-10	19	639	G	2012-06-13	24	506	G
J1510−22	151003.71−220311.7	2012-12-07	21	192	G	2012-06-13	24	163	G
J1513−22	151310.42−221004.6	2012-12-07	24	120	G	2012-06-13	27	148	G
J1514−34	151424.12−341100.6	2012-12-07	22	153	G	2012-06-13	27	126	G
J1516+19	151635.29+191809.7	2012-12-10	17	16	G	2012-06-13	22	20	G
J1517+35	151758.61+352354.3	...	...	...	...	2012-06-13	25	126	G
J1521+00	152116.59+001755.1	2012-12-28	24	1864	G	2012-06-13	29	1534	G
J1525+76	152502.31+764009.6	...	...	...	...	2012-06-13	24	110	G
J1541−11	154141.64−114409.2	2012-12-28	25	23	G	2012-06-13	25	26	G
J1604+69	160437.42+690012.5	...	...	...	...	2012-06-13	22	73	G
J1615+74	161511.78+743146.1	...	...	...	...	2012-06-13	22	550	G
J1630+51	163036.23+512612.7	...	...	...	...	2012-06-13	26	1533	G
J1634−17	163426.87−172139.4	2012-12-28	24	17	G	2012-06-13	35	17	G
J1641−05	164107.22−054827.0	2012-12-28	21	30	G	2012-06-13	33	22	G
J1642+41	164250.10+412318.2	...	...	...	...	2012-06-13	22	177	G

Table 2.3 continued

Table 2.3: Observational Details of Our Sample (continued)

Source	*WISE* ID	A-Array Obs Date yyyy-mm-dd	rms μJy beam^{-1}	S/N	Quality	B-Array Obs Date yyyy-mm-dd	rms μJy beam^{-1}	S/N	Quality
(1)	(2)	(3)	(4)	(5)	(6)	7	(8)	(9)	(10)
J1644−03	164425.54−035725.6	2012-12-28	26	30	G	2012-06-13	26	35	G
J1651+34	165110.37+343248.4	⋯	⋯	⋯	⋯	2012-06-13	28	477	G
J1653+77	165338.97+771324.8	⋯	⋯	⋯	⋯	2012-06-13	19	148	G
J1653−01	165305.40−010230.5	2012-12-28	25	228	G	2012-06-13	24	245	G
J1657−17	165742.88−174049.5	2012-12-28	31	26	G	2012-06-13	26	32	G
J1702−08	170204.65−081108.2	2012-12-28	27	457	G	2012-06-13	27	533	G
J1703+26	170334.21+261511.1	2012-12-10	19	1085	G	2012-06-13	26	793	G
J1703−05	170325.05−051742.5	2012-12-28	29	600	G	2012-06-13	25	718	G
J1707−09	170746.08−093916.3	2012-12-28	26	56	G	2012-06-13	25	59	G
J1717+53	171705.92+531342.6	⋯	⋯	⋯	⋯	2012-06-13	20	507	G
J1820+79	182048.95+791705.0	⋯	⋯	⋯	⋯	2012-06-13	26	1208	G
J1840+50	184023.37+501806.6	⋯	⋯	⋯	⋯	2012-06-13	22	363	G
J1936−33	193622.58−335420.4	2012-10-21	26	19	G	2012-06-13	30	21	G
J1951−04	195141.22−042024.5	2012-10-21	28	18	G	2012-06-13	24	33	G
J1958−07	195801.72−074609.3	2012-10-21	30	138	G	2012-06-13	26	172	G
J2000−28	200048.58−280251.6	2012-10-21	27	138	G	2012-06-13	24	37	G
J2021−26	202148.06−261159.2	2012-10-21	24	28	G	2012-06-13	27	37	G
J2040−39	204049.51−390400.5	2012-10-21	28	67	G	2012-06-13	27	72	G
J2059−35	205946.93−354134.7	2012-10-21	29	< 3.5	ND	2012-06-13	28	3	G
J2124−28	212455.07−281410.2	2012-10-21	22	51	G	⋯	⋯	⋯	⋯
J2126−01	212619.97−010354.3	2012-11-08	19	80	G	2012-06-13	23	69	G
J2130+20	213047.97+200900.6	2012-11-08	19	34	G	2012-06-13	38	199	G
J2133−14	213356.51−141904.6	2012-10-21	27	446	G	2012-06-13	26	464	G
J2133−17	213348.75−171148.7	2012-10-21	23	71	G	2012-06-13	29	399	G
J2145−06	214514.64−061811.4	2012-10-17	21	29	G	2012-06-13	12	48	G
J2148−29	214820.26−291356.8	2012-10-21	22	178	G	⋯	⋯	⋯	⋯
J2204+20	220427.98+203102.7	2012-11-08	20	1458	G	2012-06-13	34	1135	G

Table 2.3 continued

Table 2.3: Observational Details of Our Sample (continued)

Source	*WISE* ID	A-Array Obs Date yyyy-mm-dd	rms μJy beam^{-1}	S/N	Quality	B-Array Obs Date yyyy-mm-dd	rms μJy beam^{-1}	S/N	Quality
(1)	(2)	(3)	(4)	(5)	(6)	7	(8)	(9)	(10)
J2212+33	221258.88+332604.9	2012-11-08	19	338	G	2012-06-13	24	338	G
J2212−12	221205.05−125347.0	2012-10-17	27	49	G	2012-06-13	56	152	G
J2222+09	222248.76+095129.2	2012-11-08	21	88	G	2012-06-13	22	98	G
J2226+00	222625.12+002509.6	2012-11-08	21	81	G	2012-06-13	26	68	G
J2230−07	223007.75−072059.9	2012-10-17	30	118	G	2012-06-13	29	196	G
J2235−28	223512.79−283830.1	2012-10-17	25	1071	G	2012-06-13	31	928	G
J2241−06	224134.63−061003.1	2012-10-17	23	210	G	2012-06-13	27	181	G
J2251+01	225135.62+010627.8	2012-11-08	19	868	G	2012-06-13	24	700	G
J2252−21	225229.37−210233.5	2012-10-17	26	623	G	...	...	...	...
J2318+25	231807.33+255706.2	2012-11-08	20	< 5	ND	2012-06-13	20	903	G
J2322−00	232206.03−001550.3	2012-11-08	20	37	G	2012-06-13	23	32	G
J2325−04	232505.07−042948.1	2012-11-08	16	933	G	2012-06-13	32	693	G
J2328−02	232820.41−024555.3	2012-11-08	20	7	G	2012-06-13	24	5	G
J2329−10	232931.85−105417.2	2012-10-17	27	46	G	2012-06-13	25	63	G
J2331−14	233103.17−141152.2	2012-10-17	24	805	G	2012-06-13	27	833	G
J2332+34	233259.34+343029.7	2012-11-08	20	55	G	2012-06-13	20	53	G
J2341−29	234113.43−295517.3	2012-10-17	21	111	G	...	...	...	...
J2345+31	234541.23+312025.8	2012-11-08	19	166	G	2012-06-13	23	146	G
J2357−10	235744.85−104808.6	2012-10-17	25	119	G	2012-06-13	26	127	G
J2359+43	235940.26+430218.5	2012-11-08	19	43	G	2012-06-13	29	34	G

Note — Column 1; Source name. Column 2: *WISE* ID. Column 3: Date of observation for the A-array data. Column 4: 1σ rms noise level in the A-array continuum image. Column 5: Source peak flux S/N. Column 6: A quality flag for the final continuum image. G: A good quality image free of any artifacts or calibration issues; ND: No detection up-to specified S/N; P: Poor quality image due to bad calibration or phase closure errors; F: Pipeline failed to calibrate $uv-$data. We used images with G flags for our analysis. Columns 7-10: Date of observation, 1σ rms noise, S/N of the source detection, and an image quality flag for the B-array observations.

Table 2.4: Beam Sizes and Source Measurements

Source	Array	Morph	A-Array $\theta_M \times \theta_m$ $'' \times ''$	PA deg	S_{peak} mJy beam^{-1}	S_{tot} mJy	B-Array $\theta_M \times \theta_m$ $'' \times ''$	PA deg	S_{peak} mJy beam^{-1}	S_{tot} mJy
(1)	(2)	(3)	(4)	(5)	(6)	7	(8)	(9)	(10)	(11)
J0000+78	A	D	0.3×0.1	−13	7.1 ± 0.21	7.96 ± 0.22	···	···	···	···
J0010+16	A	UR	0.2×0.2	74	1.76 ± 0.06	1.87 ± 0.06	0.6×0.6	17	1.97 ± 0.06	1.95 ± 0.07
J0104−27	A	R	0.5×0.1	14	0.68 ± 0.02	0.94 ± 0.15	2.0×0.5	−24	1.44 ± 0.05	1.42 ± 0.07
J0132+13	A	SR	0.2×0.2	20	4.32 ± 0.13	4.64 ± 0.14	0.6×0.5	−26	4.69 ± 0.14	4.70 ± 0.15
J0133+10	A	D	0.2×0.2	35	19.9 ± 0.6	34.6 ± 0.71	0.6×0.5	−25	28.28 ± 0.85	34.59 ± 0.85
J0134+40	A	SR	0.2×0.1	13	0.95 ± 0.03	1.13 ± 0.05	0.6×0.5	21	1.29 ± 0.05	1.30 ± 0.06
J0154+50	A	UR	0.2×0.1	15	0.69 ± 0.03	0.73 ± 0.04	0.6×0.5	23	0.91 ± 0.04	0.97 ± 0.05
J0159+12	A	R	0.2×0.2	21	1.73 ± 0.06	2.73 ± 0.07	0.6×0.6	−21	2.47 ± 0.08	2.63 ± 0.09
J0204+09	A	SR	0.2×0.2	25	0.81 ± 0.03	0.90 ± 0.04	0.6×0.6	−44	1.04 ± 0.04	1.04 ± 0.06
J0244+11	A	UR	0.2×0.2	16	3.81 ± 0.12	3.91 ± 0.12	0.6×0.6	−62	4.05 ± 0.12	4.04 ± 0.13
J0300+39	A	SR	0.2×0.1	31	2.89 ± 0.09	3.16 ± 0.09	0.6×0.5	45	3.29 ± 0.1	3.35 ± 0.11
J0303+07	A	D	0.2×0.2	18	1.36 ± 0.04	1.78 ± 0.06	0.7×0.6	−58	1.53 ± 0.05	1.97 ± 0.08
J0304−31	A	D	0.5×0.1	−6	20.08 ± 0.6	21.41 ± 0.61	1.6×0.4	−172	18.24 ± 0.55	19.65 ± 0.55
J0306−33	A	UR	0.6×0.1	−6	1.37 ± 0.04	1.37 ± 0.05	1.9×0.4	−171	1.11 ± 0.04	1.27 ± 0.06
J0332+32	A	UR	0.2×0.1	8	5.02 ± 0.15	5.03 ± 0.15	0.6×0.5	66	5.26 ± 0.16	5.30 ± 0.16
J0342+37	B	UR	0.2×0.1	34	34.65 ± 1.04	35.05 ± 1.04	0.6×0.5	65	60.55 ± 1.82	60.66 ± 1.82
J0352+19	A	UR	0.2×0.1	16	7.61 ± 0.23	7.64 ± 0.23	0.6×0.5	87	7.97 ± 0.24	8.04 ± 0.24
J0354−33	A	UR	0.6×0.1	−14	2.91 ± 0.09	2.91 ± 0.09	1.9×0.4	0	2.61 ± 0.11	4.27 ± 0.21
J0404+07	A	UR	0.2×0.2	14	44.94 ± 1.35	45.10 ± 1.35	0.7×0.6	−59	45.8 ± 1.37	45.83 ± 1.37
J0404−24	A	D	0.4×0.1	−13	0.26 ± 0.01	0.73 ± 0.12	1.2×0.5	−2	0.61 ± 0.03	0.91 ± 0.06
J0409−18	A	D	0.3×0.1	−14	4.97 ± 0.15	5.66 ± 0.16	1.0×0.5	0	5.16 ± 0.16	5.67 ± 0.16
J0417−28	A	UR	0.5×0.1	−18	8.89 ± 0.27	8.89 ± 0.27	1.4×0.4	−3	8.9 ± 0.27	8.90 ± 0.27
J0433−08	A	UR	0.3×0.2	75	1.25 ± 0.05	1.21 ± 0.06	1.0×0.5	−38	1.44 ± 0.05	1.33 ± 0.07
J0439−31	A	R	0.6×0.1	−18	3.71 ± 0.11	5.16 ± 0.12	1.8×0.4	−3	5.24 ± 0.16	5.18 ± 0.17
J0443+06	A	R	0.2×0.2	17	1.93 ± 0.06	2.22 ± 0.07	0.8×0.6	−70	2.52 ± 0.08	2.56 ± 0.09
J0450+27	A	UR	0.2×0.1	24	0.72 ± 0.03	0.72 ± 0.04	0.8×0.5	−84	0.96 ± 0.04	0.94 ± 0.06
J0457−23	B	UR	0.4×0.1	−22	17.88 ± 0.54	18.96 ± 0.56	1.3×0.6	−9	31.2 ± 1.0	33.31 ± 1.13
J0502+12	A	UR	0.2×0.2	20	1.58 ± 0.05	1.62 ± 0.06	0.8×0.6	−70	1.77 ± 0.06	1.71 ± 0.07
J0519−08	A	UR	0.3×0.2	−81	9.08 ± 0.27	9.12 ± 0.28	1.3×0.5	−46	8.24 ± 0.25	8.68 ± 0.25
J0525−36	A	R	0.7×0.1	5	1.98 ± 0.06	2.20 ± 0.07	2.1×0.4	−4	2.41 ± 0.08	2.47 ± 0.09
J0526−32	A	R	0.6×0.1	7	23.48 ± 0.71	33.37 ± 0.71	1.7×0.4	−5	32.48 ± 0.98	33.81 ± 0.98
J0536−27	A	UR	0.4×0.1	4	21.72 ± 0.65	21.76 ± 0.65	1.4×0.4	−8	22.07 ± 0.66	22.08 ± 0.66
J0542−18	B	D	···	···	···	···	1.0×0.5	−14	1.0 ± 0.04	2.02 ± 0.09
J0543+52	A	T	0.3×0.2	24	1.53 ± 0.05	4.27 ± 0.24	0.7×0.5	64	2.27 ± 0.07	4.98 ± 0.13
J0543+58	A	UR	0.2×0.1	17	2.75 ± 0.08	2.79 ± 0.09	0.8×0.5	65	3.21 ± 0.1	3.17 ± 0.11

Table 2.4 continued

Table 2.4: Beam Sizes and Source Measurements (continued)

Source (1)	Array (2)	Morph (3)	A-Array $\theta_M \times \theta_m$ $'' \times ''$ (4)	PA deg (5)	S_{peak} mJy beam^{-1} (6)	S_{tot} mJy 7	B-Array $\theta_M \times \theta_m$ $'' \times ''$ (8)	PA deg (9)	S_{peak} mJy beam^{-1} (10)	S_{tot} mJy (11)
J0549−37	A	SR	0.7×0.1	1	0.58 ± 0.03	0.64 ± 0.05	2.2×0.4	−6	0.71 ± 0.05	0.70 ± 0.08
J0602−27	A	T	0.4×0.1	2	2.82 ± 0.09	4.57 ± 0.34	1.4×0.4	−7	2.52 ± 0.09	4.96 ± 0.19
J0604−03	A	D	0.3×0.2	−72	1.77 ± 0.06	2.31 ± 0.08	0.8×0.6	−43	1.87 ± 0.06	2.47 ± 0.08
J0612−06	A	T	0.4×0.3	−39	2.79 ± 0.09	3.63 ± 0.17	0.9×0.6	−34	2.76 ± 0.09	3.69 ± 0.1
J0613−34	A	UR	0.6×0.1	−1	2.1 ± 0.07	2.14 ± 0.08	2.0×0.4	−11	2.12 ± 0.07	2.18 ± 0.08
J0614−09	A	UR	0.3×0.2	−46	3.32 ± 0.1	3.32 ± 0.1	…	…	…	…
J0630−21	A	D	0.4×0.2	−25	5.63 ± 0.17	6.74 ± 0.19	1.2×0.5	−20	5.5 ± 0.17	6.76 ± 0.18
J0631−20	A	UR	0.4×0.3	−38	2.35 ± 0.08	2.50 ± 0.09	1.2×0.5	−22	2.69 ± 0.09	2.72 ± 0.10
J0634+36	A	UR	0.2×0.2	21	11.7 ± 0.35	11.65 ± 0.35	0.7×0.5	79	12.6 ± 0.38	12.70 ± 0.38
J0641+50	A	SR	0.2×0.1	32	0.64 ± 0.02	0.73 ± 0.03	…	…	…	…
J0641+52	A	SR	0.2×0.1	30	1.35 ± 0.04	1.35 ± 0.04	0.9×0.5	80	1.99 ± 0.08	2.22 ± 0.11
J0642−27	A	D	0.6×0.2	3	0.38 ± 0.02	1.03 ± 0.12	1.5×0.4	−13	0.51 ± 0.04	0.87 ± 0.10
J0647+59	A	SR	0.2×0.1	26	4.09 ± 0.12	4.38 ± 0.13	0.9×0.5	83	4.97 ± 0.15	5.01 ± 0.15
J0652−20	A	UR	0.4×0.2	−28	0.69 ± 0.03	0.66 ± 0.05	1.3×0.5	−25	0.84 ± 0.04	0.84 ± 0.06
J0701+45	A	UR	0.2×0.1	35	0.22 ± 0.01	0.22 ± 0.02	2.1×0.8	−67	0.61 ± 0.04	0.97 ± 0.08
J0702−28	A	UR	0.4×0.1	−8	6.85 ± 0.21	6.82 ± 0.21	1.8×0.5	−23	6.46 ± 0.2	6.40 ± 0.20
J0714−36	A	UR	0.7×0.1	−9	1.53 ± 0.05	1.56 ± 0.06	2.9×0.5	−22	1.78 ± 0.06	1.78 ± 0.06
J0719−33	A	UR	0.6×0.1	−9	11.09 ± 0.33	11.02 ± 0.34	2.6×0.5	−24	11.02 ± 0.33	11.09 ± 0.33
J0729+65	A	UR	0.2×0.1	34	3.09 ± 0.09	3.06 ± 0.10	1.0×0.4	83	3.62 ± 0.11	3.64 ± 0.11
J0737+18	B	D	…	…	…	…	1.2×0.5	−72	1.12 ± 0.04	1.9 ± 0.07
J0739+23	B	UR	…	…	…	…	1.1×0.5	−74	9.04 ± 0.27	9.05 ± 0.27
J0804+36	A	SR	0.2×0.1	50	5.78 ± 0.17	6.01 ± 0.18	…	…	…	…
J0811−22	B	UR	…	…	…	…	1.7×0.5	−31	1.66 ± 0.06	1.67 ± 0.07
J0823−06	B	UR	…	…	…	…	1.2×0.5	−41	24.88 ± 0.75	24.89 ± 0.75
J0845+28	B	D	…	…	…	…	1.5×0.5	−73	2.85 ± 0.09	3.47 ± 0.11
J0849+30	B	UR	…	…	…	…	1.4×0.5	−70	0.52 ± 0.03	0.48 ± 0.04
J0920+12	B	UR	…	…	…	…	1.1×0.6	−60	2.12 ± 0.07	2.11 ± 0.08
J0929−20	B	…	…	…	…	…	2.9×0.6	−42	2.71 ± 0.09	3.21 ± 0.10
J0941−00	B	R	…	…	…	…	1.4×0.5	−51	1.9 ± 0.06	2.29 ± 0.08
J0943+03	B	UR	…	…	…	…	1.3×0.5	−52	7.09 ± 0.21	7.11 ± 0.22
J1002+02	B	UR	…	…	…	…	1.4×0.5	−53	1.12 ± 0.04	1.14 ± 0.05
J1025+61	B	T	…	…	…	…	0.8×0.5	−47	5.61 ± 0.17	9.27 ± 0.47
J1046−02	B	UR	…	…	…	…	2.3×0.5	−52	13.56 ± 0.41	13.62 ± 0.41
J1048+55	B	UR	…	…	…	…	0.7×0.5	−41	0.92 ± 0.03	0.95 ± 0.04
J1049−02	B	UR	…	…	…	…	2.2×0.5	−52	3.43 ± 0.11	3.44 ± 0.11

Table 2.4 continued

Table 2.4: Beam Sizes and Source Measurements (continued)

Source (1)	Array (2)	Morph (3)	A-Array $\theta_M \times \theta_m$ $'' \times ''$ (4)	PA deg (5)	S$_{peak}$ mJy beam^{-1} (6)	S$_{tot}$ mJy 7	B-Array $\theta_M \times \theta_m$ $'' \times ''$ (8)	PA deg (9)	S$_{peak}$ mJy beam^{-1} (10)	S$_{tot}$ mJy (11)
J1107+34	B	SR	...	...	...	...	0.7 × 0.5	−39	26.92 ± 0.81	27.51 ± 0.81
J1138+20	A	UR	0.2 × 0.1	22	4.5 ± 0.14	4.51 ± 0.14	0.6 × 0.6	−50	4.46 ± 0.14	4.47 ± 0.14
J1157+45	B	UR	...	...	...	...	0.7 × 0.5	−24	3.65 ± 0.11	3.65 ± 0.12
J1210+47	B	UR	...	...	...	...	0.7 × 0.5	−22	11.6 ± 0.35	11.58 ± 0.35
J1212+46	B	SR	...	...	...	...	0.7 × 0.5	−23	2.76 ± 0.09	2.94 ± 0.09
J1226+18	A	UR	0.2 × 0.1	26	6.54 ± 0.2	6.55 ± 0.20	0.6 × 0.6	−10	6.44 ± 0.19	6.50 ± 0.20
J1238+52	B	UR	...	...	...	...	0.7 × 0.5	−18	15.31 ± 0.46	15.20 ± 0.46
J1257+73	B	D	...	...	...	...	1.0 × 0.5	−57	3.94 ± 0.12	4.3 ± 0.13
J1304+22	A	UR	0.2 × 0.1	28	1.74 ± 0.05	1.81 ± 0.06	0.6 × 0.5	−7	1.83 ± 0.06	1.86 ± 0.07
J1308−34	A	T	0.6 × 0.1	3	15.88 ± 0.48	21.29 ± 0.69	2.5 × 0.4	16	14.85 ± 0.45	19.36 ± 0.46
J1316+39	B	UR	...	...	...	...	0.9 × 0.5	−80	0.69 ± 0.03	0.70 ± 0.05
J1332+79	B	UR	...	...	...	...	1.0 × 0.4	−47	3.02 ± 0.09	3.03 ± 0.10
J1343−11	A	UR	0.3 × 0.2	14	3.15 ± 0.1	3.17 ± 0.10	0.9 × 0.5	−177	3.26 ± 0.1	3.23 ± 0.10
J1400−29	A	UR	0.5 × 0.1	−6	3.35 ± 0.1	3.35 ± 0.11	1.7 × 0.4	−174	3.22 ± 0.1	3.20 ± 0.11
J1409+17	A	D	0.2 × 0.1	33	6.68 ± 0.2	7.63 ± 0.21	0.6 × 0.6	−23	6.92 ± 0.21	8.02 ± 0.22
J1412−20	A	SR	0.3 × 0.1	−6	22.13 ± 0.66	22.52 ± 0.66	1.2 × 0.5	−179	21.42 ± 0.64	21.54 ± 0.64
J1424−26	A	SR	0.5 × 0.2	−21	0.54 ± 0.03	0.73 ± 0.04	1.5 × 0.4	0	0.69 ± 0.03	0.75 ± 0.04
J1428+11	B	T	...	...	...	...	0.7 × 0.6	−59	0.49 ± 0.03	1.67 ± 0.14
J1434−02	A	D	0.2 × 0.2	29	3.89 ± 0.12	4.32 ± 0.14	0.8 × 0.6	10	4.45 ± 0.14	5.11 ± 0.15
J1439−37	B	D	0.8 × 0.1	−11	1.64 ± 0.05	1.65 ± 0.06	2.5 × 0.4	0	1.52 ± 0.05	2.34 ± 0.11
J1448+40	B	UR	...	...	...	...	0.7 × 0.5	−47	0.99 ± 0.04	0.93 ± 0.05
J1500−06	A	R	0.2 × 0.2	8	1.16 ± 0.04	1.54 ± 0.06	0.8 × 0.5	−175	1.84 ± 0.06	1.97 ± 0.07
J1501+13	A	UR	0.2 × 0.2	41	11.15 ± 0.34	11.41 ± 0.34	0.7 × 0.5	−4	11.45 ± 0.34	11.46 ± 0.35
J1501+33	A	UR	0.2 × 0.1	42	11.9 ± 0.36	12.00 ± 0.36	0.7 × 0.6	−49	12.02 ± 0.36	11.96 ± 0.36
J1510−22	A	UR	0.4 × 0.2	−17	4.02 ± 0.12	4.07 ± 0.13	1.3 × 0.5	−3	3.97 ± 0.12	3.97 ± 0.13
J1513−22	B	SR	1.3 × 0.5	−16	4.02 ± 0.12	3.24 ± 0.18	1.3 × 0.5	−3	3.99 ± 0.12	4.18 ± 0.13
J1514−34	A	UR	0.7 × 0.1	−16	3.38 ± 0.1	3.38 ± 0.11	2.2 × 0.4	−5	3.33 ± 0.1	3.32 ± 0.11
J1516+19	A	D	0.3 × 0.2	−33	0.27 ± 0.02	0.47 ± 0.04	0.7 × 0.5	−12	0.44 ± 0.03	0.59 ± 0.05
J1517+35	B	UR	...	...	...	...	0.7 × 0.5	−42	3.2 ± 0.1	3.22 ± 0.11
J1521+00	A	UR	0.2 × 0.2	37	44.03 ± 1.32	44.03 ± 1.32	0.7 × 0.6	0	44.31 ± 1.33	44.27 ± 1.33
J1525+76	B	UR	...	...	...	...	0.9 × 0.5	−19	2.6 ± 0.08	2.58 ± 0.09
J1541−11	A	UR	0.3 × 0.2	−6	0.57 ± 0.03	0.56 ± 0.05	0.9 × 0.5	−8	0.64 ± 0.03	0.67 ± 0.05
J1604+69	B	UR	...	...	...	...	0.8 × 0.5	−10	1.58 ± 0.05	1.59 ± 0.06
J1615+74	B	UR	...	...	...	...	0.9 × 0.5	−8	11.91 ± 0.36	11.91 ± 0.36
J1630+51	B	UR	...	...	...	...	0.7 × 0.5	−11	40.13 ± 1.2	40.34 ± 1.20

Table 2.4 continued

Table 2.4: Beam Sizes and Source Measurements (continued)

Source	Array	Morph	A-Array $\theta_M \times \theta_m$ $'' \times ''$	PA deg	S_{peak} mJy beam^{-1}	S_{tot} mJy	B-Array $\theta_M \times \theta_m$ $'' \times ''$	PA deg	S_{peak} mJy beam^{-1}	S_{tot} mJy
(1)	(2)	(3)	(4)	(5)	(6)	7	(8)	(9)	(10)	(11)
J1634−17	A	SR	0.3×0.2	−17	0.41 ± 0.03	0.45 ± 0.05	1.1×0.5	−16	0.57 ± 0.04	0.77 ± 0.08
J1641−05	A	UR	0.3×0.2	84	0.63 ± 0.03	0.63 ± 0.04	0.8×0.6	−11	0.72 ± 0.04	0.74 ± 0.06
J1642+41	B	UR	...	...	...	...	0.6×0.5	−17	3.96 ± 0.12	3.95 ± 0.12
J1644−03	A	R	0.4×0.2	73	0.76 ± 0.03	1.00 ± 0.06	0.8×0.6	−13	0.91 ± 0.04	0.99 ± 0.06
J1651+34	B	M	...	...	...	...	0.6×0.5	−14	7.04 ± 0.21	21.79 ± 0.57
J1653+77	B	UR	...	...	...	...	0.9×0.5	−180	2.79 ± 0.09	2.78 ± 0.09
J1653−01	A	UR	0.3×0.2	81	5.79 ± 0.18	5.93 ± 0.18	0.8×0.6	−14	5.91 ± 0.18	5.83 ± 0.18
J1657−17	A	UR	0.4×0.3	−77	0.79 ± 0.04	0.82 ± 0.06	1.2×0.5	−18	0.83 ± 0.04	0.82 ± 0.05
J1702−08	A	R	0.3×0.2	89	12.05 ± 0.36	13.84 ± 0.36	0.9×0.5	−18	14.22 ± 0.43	14.58 ± 0.43
J1703+26	A	UR	0.3×0.2	77	20.08 ± 0.6	20.07 ± 0.60	0.6×0.5	−5	20.13 ± 0.6	20.15 ± 0.61
J1703−05	A	D	0.3×0.2	78	17.16 ± 0.52	18.8 ± 0.52	0.8×0.6	−18	17.69 ± 0.53	19.15 ± 0.54
J1707−09	A	UR	0.3×0.2	−71	1.44 ± 0.05	1.46 ± 0.06	0.9×0.5	−19	1.49 ± 0.05	1.58 ± 0.06
J1717+53	B	UR	...	...	...	...	0.7×0.5	−177	10.14 ± 0.3	10.09 ± 0.31
J1820+79	B	UR	...	...	...	...	1.0×0.4	22	31.29 ± 0.94	31.40 ± 0.94
J1840+50	B	D	...	...	...	...	0.7×0.5	28	7.96 ± 0.24	8.5 ± 0.25
J1936−33	A	UR	1.0×0.2	0	0.48 ± 0.03	0.49 ± 0.05	2.2×0.4	7	0.61 ± 0.03	0.56 ± 0.05
J1951−04	B	D	0.4×0.2	−15	0.5 ± 0.03	0.66 ± 0.06	0.8×0.6	9	0.81 ± 0.03	1.17 ± 0.08
J1958−07	A	UR	0.4×0.2	−12	4.12 ± 0.13	4.14 ± 0.13	0.9×0.5	8	4.53 ± 0.14	4.53 ± 0.14
J2000−28	A	UR	0.8×0.2	−3	3.72 ± 0.11	3.95 ± 0.12	1.6×0.4	−177	0.88 ± 0.04	0.89 ± 0.05
J2021−26	A	SR	0.8×0.2	−7	0.66 ± 0.03	0.80 ± 0.05	1.5×0.4	0	0.99 ± 0.04	1.06 ± 0.06
J2040−39	A	UR	1.5×0.1	−5	1.88 ± 0.06	1.84 ± 0.07	2.9×0.4	−2	1.94 ± 0.06	1.89 ± 0.07
J2059−35	B	SR	...	...	...	...	2.4×0.5	−6	0.08 ± 0.03	0.21 ± 0.09
J2124−28	A	M	0.9×0.2	−12	1.08 ± 0.04	4.38 ± 0.19	...	...	...	...
J2126−01	A	UR	0.2×0.2	11	1.51 ± 0.05	1.51 ± 0.06	0.7×0.6	−5	1.63 ± 0.05	1.61 ± 0.06
J2130+20	B	T	0.2×0.1	16	0.64 ± 0.03	0.62 ± 0.04	1.0×0.8	3	1.0 ± 0.05	9.98 ± 0.72
J2133−14	A	UR	0.5×0.2	−12	12.09 ± 0.36	12.09 ± 0.37	1.0×0.5	−8	12.2 ± 0.37	12.16 ± 0.37
J2133−17	B	T	0.4×0.2	−10	1.44 ± 0.05	16.52 ± 0.28	1.1×0.5	−9	4.52 ± 0.14	17.63 ± 0.96
J2145−06	A	D	0.2×0.2	0	0.61 ± 0.03	1.11 ± 0.06	0.9×0.6	−7	0.57 ± 0.02	1.35 ± 0.04
J2148−29	A	UR	0.8×0.1	−15	3.74 ± 0.11	5.38 ± 0.12	...	...	...	...
J2204+20	B	UR	0.2×0.1	16	29.72 ± 0.89	37.88 ± 0.89	0.7×0.5	−178	38.49 ± 1.16	39.64 ± 1.16
J2212+33	A	SR	0.2×0.1	17	6.13 ± 0.18	7.88 ± 0.19	0.6×0.5	−174	8.16 ± 0.25	8.50 ± 0.25
J2212−12	B	T	0.4×0.3	6	1.18 ± 0.04	11.12 ± 0.3	1.0×0.5	−14	3.09 ± 0.09	11.68 ± 1.19
J2222+09	A	UR	0.2×0.2	17	1.88 ± 0.06	2.02 ± 0.07	0.7×0.5	0	2.13 ± 0.07	2.14 ± 0.07
J2226+00	A	R	0.2×0.2	19	0.72 ± 0.02	1.71 ± 0.18	0.7×0.6	−7	1.69 ± 0.06	2.13 ± 0.07
J2230−07	A	R	0.2×0.2	−3	3.37 ± 0.11	5.68 ± 0.12	0.9×0.5	−2	5.65 ± 0.17	5.85 ± 0.18

Table 2.4 continued

Table 2.4: Beam Sizes and Source Measurements (continued)

Source	Array	Morph	A-Array $\theta_M \times \theta_m$ $'' \times ''$	PA deg	S$_{peak}$ mJy beam^{-1}	S$_{tot}$ mJy	B-Array $\theta_M \times \theta_m$ $'' \times ''$	PA deg	S$_{peak}$ mJy beam^{-1}	S$_{tot}$ mJy
(1)	(2)	(3)	(4)	(5)	(6)	7	(8)	(9)	(10)	(11)
J2235−28	A	UR	0.4 × 0.1	2	26.83 ± 0.81	26.84 ± 0.81	2.0 × 0.5	−21	27.74 ± 0.83	27.72 ± 0.83
J2241−06	A	UR	0.2 × 0.2	2	4.71 ± 0.14	4.77 ± 0.15	0.8 × 0.5	−4	4.91 ± 0.15	4.83 ± 0.15
J2251+01	A	UR	0.2 × 0.2	17	16.24 ± 0.49	16.42 ± 0.49	0.7 × 0.6	−7	16.38 ± 0.49	16.37 ± 0.49
J2252−21	A	UR	0.3 × 0.1	0	16.11 ± 0.48	16.10 ± 0.49	...	...	...	...
J2318+25	B	T	...	...	...	...	1.1 × 0.9	0	0.3 ± 0.01	18.69 ± 4.52
J2322−00	A	UR	0.2 × 0.2	14	0.72 ± 0.03	0.71 ± 0.04	0.8 × 0.6	−11	0.73 ± 0.03	0.68 ± 0.04
J2325−04	B	SR	0.3 × 0.2	−5	14.83 ± 0.45	28.2 ± 0.46	0.8 × 0.6	−12	22.26 ± 0.67	25.53 ± 0.67
J2328−02	A	SR	0.2 × 0.2	8	0.15 ± 0.02	0.18 ± 0.04	0.7 × 0.6	−15	0.13 ± 0.02	0.16 ± 0.05
J2329−10	A	SR	0.2 × 0.2	−6	1.22 ± 0.05	1.45 ± 0.06	0.9 × 0.5	−10	1.6 ± 0.05	1.59 ± 0.06
J2331−14	A	D	0.3 × 0.1	−8	19.12 ± 0.57	24.14 ± 0.58	1.0 × 0.5	−10	22.03 ± 0.66	25.93 ± 0.68
J2332+34	A	UR	0.2 × 0.1	23	1.08 ± 0.04	1.08 ± 0.05	0.6 × 0.5	29	1.07 ± 0.04	1.06 ± 0.05
J2341−29	A	UR	0.5 × 0.1	−8	2.33 ± 0.07	2.36 ± 0.08	...	...	...	...
J2345+31	A	UR	0.2 × 0.1	26	3.19 ± 0.1	3.26 ± 0.10	0.7 × 0.5	36	3.3 ± 0.1	3.30 ± 0.11
J2357−10	A	UR	0.2 × 0.2	−13	3.0 ± 0.09	2.99 ± 0.10	0.9 × 0.5	−14	3.35 ± 0.1	3.17 ± 0.11
J2359+43	A	D	0.2 × 0.1	30	0.83 ± 0.03	1.01 ± 0.05	0.7 × 0.5	38	0.97 ± 0.04	1.05 ± 0.06

NOTE — Column 1: Source name. Column 2: The VLA array of the best continuum image. Column 3: Source morphology based on the criteria defined in Section 2.4.3. UR=Unresolved, SR=Slightly resolved, R=Fully resolved, D=Double, T=Triple, M=Multi-component Sources. Column 4: Synthesized beam of the A-array data (major axis, θ_M × minor axis, θ_m) in arcseconds. Column 5: Position angle of the synthesized beam, measured anti-clockwise from North. Column 6: Peak flux density of the A-array image. Column 7: Integrated flux of source A-array image. In case of multi-component sources, we provide a sum total of fluxes from each component. Column 8: Synthesized beam of the B-array data (major axis, θ_M × minor axis, θ_m) in arcseconds. Column 9: B-array beam position angle, measured anti-clockwise from North. Column 10: Peak flux density of the radio emission in the B-array image. Column 11: Integrated flux in the B-array image.

Table 2.5: Source Spatial Measurements for the VLA A-array Observations: Results from JMFIT

Source (1)	Region (2)	RA-A (hh:mm:ss.s) (3)	Dec-A (dd:mm:ss.s) (4)	Source Size-A ($mas \times mas$) (5)	PA-A (deg) (6)	S_{peak}-A (mJy/beam) 7	S_{tot}-A (mJy) (8)
J0000+78	Reg 1	00:00:35.918	78:07:17.15	< 32	158 ± 0	7.10 ± 0.21	7.15 ± 0.22
	Reg 2	-15.72	5.82	$163 \pm 32 \times 100 \pm 10$	54 ± 3	0.47 ± 0.02	0.81 ± 0.05
J0010+16	Reg 1	00:10:39.529	16:43:28.81	< 73	12 ± 4	1.76 ± 0.06	1.87 ± 0.06
J0104−27	Reg 1	01:04:24.862	-27:50:29.16	976×472	$\cdots$	0.68 ± 0.02	0.94 ± 0.15
J0132+13	Reg 1	01:32:11.240	13:03:27.39	$65 \pm 4 \times 23 \pm 3$	153 ± 2	4.32 ± 0.13	4.64 ± 0.14
J0133+10	Reg 1	01:33:38.973	10:19:44.09	< 40	105 ± 0	19.90 ± 0.60	20.44 ± 0.60
	Reg 2	0.30	-0.03	$64 \pm 1 \times 56 \pm 1$	94 ± 1	12.34 ± 0.37	13.73 ± 0.37
J0134+40	Reg 1	01:34:19.290	40:30:49.34	$93 \pm 15 \times 7 \pm 6$	71 ± 2	0.95 ± 0.03	1.13 ± 0.05
J0154+50	Reg 1	01:54:42.481	50:46:00.36	< 89	157 ± 2	0.69 ± 0.03	0.73 ± 0.04
J0159+12	Reg 1	01:59:19.581	12:01:37.04	$223 \pm 4 \times 28 \pm 11$	18 ± 1	1.73 ± 0.06	2.73 ± 0.07
J0204+09	Reg 1	02:04:11.979	09:20:30.11	< 80	23 ± 78	0.81 ± 0.03	0.90 ± 0.04
J0244+11	Reg 1	02:44:24.000	11:23:54.36	< 50	39 ± 1	3.81 ± 0.12	3.91 ± 0.12
J0300+39	Reg 1	03:00:37.571	39:01:25.14	$88 \pm 3 \times 19 \pm 9$	41 ± 1	2.89 ± 0.09	3.16 ± 0.09
J0303+07	Reg 1	03:03:33.621	07:36:49.14	< 51	65 ± 3	1.36 ± 0.04	1.41 ± 0.05
	Reg 2	-0.45	-0.98	< 72	164 ± 7	0.37 ± 0.02	0.38 ± 0.03
J0304−31	Reg 1	03:04:27.549	-31:08:38.27	< 19	21 ± 0	20.08 ± 0.60	20.20 ± 0.60
	Reg 2	0.36	0.10	< 74	11 ± 0	1.15 ± 0.04	1.21 ± 0.05
J0306−33	Reg 1	03:06:29.223	-33:53:32.35	< 100	14 ± 0	1.37 ± 0.04	1.37 ± 0.05
J0332+32	Reg 1	03:32:28.245	32:05:44.84	< 25	151 ± 1	5.02 ± 0.15	5.03 ± 0.15
J0342+37	Reg 1	03:42:22.943	37:53:30.78	< 26	177 ± 0	34.65 ± 1.04	35.05 ± 1.04
J0352+19	Reg 1	03:52:05.364	19:47:01.23	< 22	76 ± 1	7.61 ± 0.23	7.64 ± 0.23
J0354−33	Reg 1	03:54:48.230	-33:08:27.22	< 90	130 ± 0	2.91 ± 0.09	2.91 ± 0.09
J0404+07	Reg 1	04:04:40.981	07:12:19.64	< 18	51 ± 0	44.94 ± 1.35	45.10 ± 1.35
J0404−24	Reg 1	04:04:03.651	-24:36:00.10	610×444	$\cdots$	0.26 ± 0.01	0.42 ± 0.10
	Reg 2	-0.57	-0.20	572×296	$\cdots$	0.24 ± 0.01	0.31 ± 0.06
J0409−18	Reg 1	04:09:37.678	-18:37:57.77	< 53	30 ± 0	4.97 ± 0.15	5.14 ± 0.15
	Reg 2	0.33	-0.34	$290 \pm 44 \times 101 \pm 21$	162 ± 3	0.32 ± 0.02	0.53 ± 0.05
J0417−28	Reg 1	04:17:54.094	-28:16:54.98	< 47	149 ± 0	8.89 ± 0.27	8.89 ± 0.27
J0433−08	Reg 1	04:33:45.564	-08:36:27.63	< 73	0 ± 5	1.25 ± 0.05	1.21 ± 0.06
J0439−31	Reg 1	04:39:21.923	-31:59:08.08	$214 \pm 16 \times < 0$	24 ± 0	3.71 ± 0.11	5.16 ± 0.12
J0443+06	Reg 1	04:43:32.573	06:43:17.70	$96 \pm 5 \times 35 \pm 7$	174 ± 2	1.93 ± 0.06	2.22 ± 0.07
J0450+27	Reg 1	04:50:32.901	27:26:07.71	< 54	12 ± 4	0.72 ± 0.03	0.72 ± 0.04
J0457−23	Reg 1	04:57:31.912	-23:24:02.24	$58 \pm 2 \times < 63$	168 ± 0	17.88 ± 0.54	18.96 ± 0.56
J0502+12	Reg 1	05:02:04.717	12:18:52.13	< 55	83 ± 3	1.58 ± 0.05	1.62 ± 0.06
J0519−08	Reg 1	05:19:05.827	-08:13:19.88	< 64	98 ± 0	9.08 ± 0.27	9.12 ± 0.28
J0525−36	Reg 1	05:25:33.530	-36:14:41.01	$155 \pm 33 \times 48 \pm 4$	173 ± 0	1.98 ± 0.06	2.20 ± 0.07
J0526−32	Reg 1	05:26:24.732	-32:25:00.88	$516 \pm 2 \times 27 \pm 1$	180 ± 0	23.48 ± 0.71	33.37 ± 0.71
J0536−27	Reg 1	05:36:22.617	-27:03:00.13	< 22	34 ± 0	21.72 ± 0.65	21.76 ± 0.65
J0543+52	Reg 1	05:43:41.259	+52:28:53.00	1050×583	$\cdots$	1.53 ± 0.05	2.41 ± 0.23
	Reg 2	1.80	1.35	< 86	36 ± 1	1.15 ± 0.04	1.21 ± 0.05
	Reg 3	7.01	3.08	$227 \pm 28 \times 180 \pm 18$	64 ± 7	0.35 ± 0.02	0.65 ± 0.05
J0543+58	Reg 1	05:43:57.955	58:09:50.58	< 43	165 ± 0	2.75 ± 0.08	2.79 ± 0.09
J0549−37	Reg 1	05:49:30.087	-37:39:39.92	< 261	175 ± 1	0.58 ± 0.03	0.64 ± 0.05
J0602−27	Reg 1	06:02:41.481	-27:41:10.32	< 99	3 ± 0	2.82 ± 0.09	2.81 ± 0.10
	Reg 2	-1.03	0.04	620×410	$\cdots$	0.30 ± 0.01	0.49 ± 0.13
	Reg 3	-5.15	-0.20	1210×460	$\cdots$	0.24 ± 0.01	1.26 ± 0.29
J0604−03	Reg 1	06:04:52.996	-03:28:47.93	< 41	115 ± 1	1.77 ± 0.06	1.79 ± 0.07
	Reg 2	-3.33	2.65	< 165	97 ± 3	0.47 ± 0.03	0.52 ± 0.05
J0612−06	Reg 1	06:12:00.237	-06:22:09.05	< 83	34 ± 1	2.79 ± 0.09	2.96 ± 0.10
	Reg 2	1.02	-0.69	598×510	$\cdots$	0.21 ± 0.01	0.30 ± 0.08
	Reg 3	-0.39	0.79	768×632	$\cdots$	0.20 ± 0.01	0.38 ± 0.12
J0613−34	Reg 1	06:13:48.099	-34:07:29.04	< 148	25 ± 0	2.10 ± 0.07	2.14 ± 0.08
J0614−09	Reg 1	06:14:05.554	-09:36:58.92	< 76	121 ± 1	3.32 ± 0.10	3.29 ± 0.11
	Reg 2	-0.18	0.60	$470 \pm 101 \times 202 \pm 70$	7 ± 14	0.13 ± 0.02	0.20 ± 0.05

Table 2.5 continued

Table 2.5: Source Spatial Measurements for the VLA A-array Observations: Results from JMFIT (continued)

Source (1)	Region (2)	RA-A (hh:mm:ss.s) (3)	Dec-A (dd:mm:ss.s) (4)	Source Size-A ($mas \times mas$) (5)	PA-A (deg) (6)	S_{peak}-A (mJy/beam) 7	S_{tot}-A (mJy) (8)
J0630−21	Reg 1	06:30:27.824	-21:20:58.62	< 37	117 ± 0	5.63 ± 0.17	5.67 ± 0.18
	Reg 2	-0.66	-1.25	$186 \pm 46 \times 116 \pm 16$	36 ± 3	0.83 ± 0.04	1.07 ± 0.06
J0631−20	Reg 1	06:31:30.716	-20:34:11.57	< 134	172 ± 2	2.35 ± 0.08	2.50 ± 0.09
J0634+36	Reg 1	06:34:30.233	36:09:38.88	< 28	43 ± 1	11.70 ± 0.35	11.65 ± 0.35
J0641+50	Reg 1	06:41:49.389	50:09:07.14	$82 \pm 36 \times 94 \pm 6$	37 ± 4	0.64 ± 0.02	0.73 ± 0.03
J0641+52	Reg 1	06:41:32.672	52:08:38.71	< 69	22 ± 1	1.35 ± 0.04	1.37 ± 0.05
	Reg 2	0.08	0.35	$181 \pm 33 \times < 0$	44 ± 4	0.15 ± 0.01	0.17 ± 0.03
J0642−27	Reg 1	06:42:28.927	-27:27:59.25	$1413 \pm 89 \times < 0$	11 ± 0	0.38 ± 0.02	0.65 ± 0.05
	Reg 2	-0.73	-2.43	1240×470	$\cdots$	0.21 ± 0.01	0.38 ± 0.10
J0647+59	Reg 1	06:47:14.171	59:30:29.88	< 53	105 ± 0	4.09 ± 0.12	4.38 ± 0.13
J0652−20	Reg 1	06:52:15.869	-20:06:13.18	< 191	123 ± 2	0.69 ± 0.03	0.66 ± 0.05
J0701+45	Reg 1	07:01:49.340	45:16:12.96	< 130	171 ± 6	0.22 ± 0.01	0.22 ± 0.02
J0702−28	Reg 1	07:02:57.218	-28:08:41.75	< 59	163 ± 0	6.85 ± 0.21	6.82 ± 0.21
J0714−36	Reg 1	07:14:33.530	-36:35:52.55	< 176	164 ± 0	1.53 ± 0.05	1.56 ± 0.06
J0719−33	Reg 1	07:19:12.596	-33:49:44.27	< 28	0 ± 0	11.09 ± 0.33	11.02 ± 0.34
J0729+65	Reg 1	07:29:02.712	65:44:29.40	< 34	23 ± 0	3.09 ± 0.09	3.06 ± 0.10
J0804+36	Reg 1	08:04:31.010	36:07:18.19	$59 \pm 2 \times 11 \pm 7$	63 ± 0	5.78 ± 0.17	6.01 ± 0.18
J1138+20	Reg 1	11:38:16.914	20:28:34.88	< 26	56 ± 0	4.50 ± 0.14	4.51 ± 0.14
J1226+18	Reg 1	12:26:46.648	18:19:43.45	< 21	24 ± 0	6.54 ± 0.20	6.55 ± 0.20
J1304+22	Reg 1	13:04:45.354	22:25:45.62	< 73	27 ± 1	1.74 ± 0.05	1.81 ± 0.06
J1308−34	Reg 1	13:08:17.003	-34:47:54.58	1730×500	$\cdots$	15.88 ± 0.48	17.39 ± 0.58
	Reg 2	8.00	-5.92	1370×900	$\cdots$	0.85 ± 0.03	2.90 ± 0.37
	Reg 3	3.65	-2.57	$237 \pm 58 \times 134 \pm 9$	144 ± 1	0.64 ± 0.03	1.00 ± 0.05
J1343−11	Reg 1	13:43:31.369	-11:36:09.58	< 46	17 ± 1	3.15 ± 0.10	3.17 ± 0.10
J1400−29	Reg 1	14:00:50.135	-29:19:24.63	< 54	145 ± 0	3.35 ± 0.10	3.35 ± 0.11
J1409+17	Reg 1	14:09:28.830	17:32:04.26	< 8	54 ± 0	6.68 ± 0.20	6.66 ± 0.20
	Reg 2	1.18	0.58	$116 \pm 12 \times 16 \pm 24$	27 ± 1	0.86 ± 0.03	0.97 ± 0.04
J1412−20	Reg 1	14:12:43.152	-20:20:11.25	$42 \pm 2 \times 11 \pm 1$	20 ± 0	22.13 ± 0.66	22.52 ± 0.66
J1424−26	Reg 1	14:24:59.358	-26:51:29.23	$229 \pm 72 \times 273 \pm 12$	8 ± 2	0.54 ± 0.03	0.73 ± 0.04
J1434−02	Reg 1	14:34:19.593	-02:35:43.84	< 69	58 ± 2	3.89 ± 0.12	4.11 ± 0.12
	Reg 2	-2.47	1.54	$268 \pm 80 \times 131 \pm 91$	95 ± 13	0.13 ± 0.02	0.21 ± 0.06
J1439−37	Reg 1	14:39:31.780	-37:25:23.72	< 102	163 ± 0	1.64 ± 0.05	1.65 ± 0.06
J1500−06	Reg 1	15:00:48.731	-06:49:40.01	$162 \pm 11 \times 38 \pm 9$	124 ± 5	1.16 ± 0.04	1.54 ± 0.06
J1501+13	Reg 1	15:01:38.359	13:24:49.89	< 56	44 ± 0	11.15 ± 0.34	11.41 ± 0.34
J1501+33	Reg 1	15:01:27.590	33:41:21.65	< 25	175 ± 0	11.90 ± 0.36	12.00 ± 0.36
J1510−22	Reg 1	15:10:03.721	-22:03:11.73	< 56	24 ± 0	4.02 ± 0.12	4.07 ± 0.13
J1513−22	Reg 1	15:13:10.437	-22:10:05.20	2870×1160	$\cdots$	4.02 ± 0.12	3.24 ± 0.18
J1514−34	Reg 1	15:14:24.107	-34:11:00.92	< 108	133 ± 0	3.38 ± 0.10	3.38 ± 0.11
J1516+19	Reg 1	15:16:35.287	19:18:09.44	< 138	149 ± 32	0.27 ± 0.02	0.31 ± 0.03
	Reg 2	-0.23	0.33	< 134	158 ± 8	0.16 ± 0.02	0.16 ± 0.03
J1521+00	Reg 1	15:21:16.589	00:17:55.05	< 11	40 ± 0	44.03 ± 1.32	44.03 ± 1.32
J1541−11	Reg 1	15:41:41.656	-11:44:09.32	< 102	32 ± 5	0.57 ± 0.03	0.56 ± 0.05
J1634−17	Reg 1	16:34:26.877	-17:21:39.43	< 97	38 ± 11	0.41 ± 0.03	0.45 ± 0.05
J1641−05	Reg 1	16:41:07.209	-05:48:26.89	< 121	46 ± 3	0.63 ± 0.03	0.63 ± 0.04
J1644−03	Reg 1	16:44:25.537	-03:57:25.38	$315 \pm 25 \times < 0$	101 ± 2	0.76 ± 0.03	1.00 ± 0.06
J1653−01	Reg 1	16:53:05.402	-01:02:30.78	< 66	89 ± 0	5.79 ± 0.18	5.93 ± 0.18
J1657−17	Reg 1	16:57:42.894	-17:40:49.30	< 176	127 ± 13	0.79 ± 0.04	0.82 ± 0.06
J1702−08	Reg 1	17:02:04.637	-08:11:07.64	$135 \pm 2 \times 32 \pm 1$	23 ± 1	12.05 ± 0.36	13.84 ± 0.36
J1703+26	Reg 1	17:03:34.206	26:15:11.18	< 19	60 ± 0	20.08 ± 0.60	20.07 ± 0.60
J1703−05	Reg 1	17:03:25.007	-05:17:43.34	$29 \pm 5 \times 19 \pm 4$	50 ± 0	17.16 ± 0.52	17.33 ± 0.52
	Reg 2	-3.65	-5.05	$146 \pm 18 \times 75 \pm 12$	130 ± 5	1.20 ± 0.05	1.47 ± 0.07
J1707−09	Reg 1	17:07:46.070	-09:39:16.65	< 100	84 ± 3	1.44 ± 0.05	1.46 ± 0.06
J1936−33	Reg 1	19:36:22.608	-33:54:20.38	< 395	46 ± 1	0.48 ± 0.03	0.49 ± 0.05
J1951−04	Reg 1	19:51:41.208	-04:20:24.58	$237 \pm 49 \times 90 \pm 23$	158 ± 2	0.50 ± 0.03	0.66 ± 0.06

Table 2.5 continued

Table 2.5: Source Spatial Measurements for the VLA A-array Observations: Results from JMFIT (continued)

Source	Region	RA-A (hh:mm:ss.s)	Dec-A (dd:mm:ss.s)	Source Size-A ($mas \times mas$)	PA-A (deg)	S_{peak}-A (mJy/beam)	S_{tot}-A (mJy)
(1)	(2)	(3)	(4)	(5)	(6)	7	(8)
J1958−07	Reg 1	19:58:01.693	-07:46:09.38	< 99	154 ± 0	4.12 ± 0.13	4.14 ± 0.13
J2000−28	Reg 1	20:00:35.567	-28:03:11.41	< 91	140 ± 0	3.72 ± 0.11	3.95 ± 0.12
J2021−26	Reg 1	20:21:48.009	-26:11:59.04	$341 \pm 78 \times 64 \pm 14$	154 ± 1	0.66 ± 0.03	0.80 ± 0.05
J2040−39	Reg 1	20:40:49.516	-39:04:00.84	< 316	159 ± 0	1.88 ± 0.06	1.84 ± 0.07
J2124−28	Reg 1	21:24:55.068	-28:14:09.93	$450 \pm 44 \times 161 \pm 8$	180 ± 0	1.08 ± 0.04	1.61 ± 0.06
	Reg 2	-0.05	1.64	$722 \pm 50 \times 84 \pm 12$	156 ± 1	0.76 ± 0.03	1.19 ± 0.05
	Reg 3	1.30	-5.43	1540×660	···	0.29 ± 0.01	0.80 ± 0.12
	Reg 4	-3.20	5.25	1540×720	···	0.25 ± 0.01	0.77 ± 0.13
J2126−01	Reg 1	21:26:19.980	-01:03:54.53	< 44	174 ± 2	1.51 ± 0.05	1.51 ± 0.06
J2130+20	Reg 1	21:30:47.978	20:09:01.39	< 69	174 ± 3	0.64 ± 0.03	0.62 ± 0.04
J2133−14	Reg 1	21:33:56.518	-14:19:04.88	< 60	158 ± 0	12.09 ± 0.36	12.09 ± 0.37
J2133−17	Reg 1	21:33:49.433	-17:11:44.52	913×530	···	1.44 ± 0.05	10.87 ± 0.18
	Reg 2	-10.47	-4.55	< 39	159 ± 2	0.92 ± 0.04	0.91 ± 0.05
	Reg 3	-16.95	-9.60	959×685	···	0.50 ± 0.03	4.74 ± 0.21
J2145−06	Reg 1	21:45:14.653	-06:18:11.27	< 55	162 ± 7	0.61 ± 0.03	0.62 ± 0.04
	Reg 2	1.42	-3.11	$144 \pm 38 \times 54 \pm 19$	76 ± 25	0.37 ± 0.02	0.50 ± 0.05
J2148−29	Reg 1	21:48:20.248	-29:13:56.75	$362 \pm 9 \times 124 \pm 2$	6 ± 0	3.74 ± 0.11	5.38 ± 0.12
J2204+20	Reg 1	22:04:27.977	20:31:02.53	$117 \pm 1 \times 17 \pm 0$	113 ± 0	29.72 ± 0.89	37.88 ± 0.89
J2212+33	Reg 1	22:12:58.893	33:26:04.57	$103 \pm 2 \times 72 \pm 1$	147 ± 0	6.13 ± 0.18	7.88 ± 0.19
J2212−12	Reg 1	22:12:04.369	-12:53:53.38	$845 \pm 20 \times 598 \pm 15$	62 ± 3	1.18 ± 0.04	7.39 ± 0.18
	Reg 2	19.60	8.39	1010×788	···	0.37 ± 0.03	3.41 ± 0.24
	Reg 3	10.21	5.85	< 150	167 ± 16	0.28 ± 0.03	0.32 ± 0.05
J2222+09	Reg 1	22:22:48.748	09:51:29.00	< 106	39 ± 1	1.88 ± 0.06	2.02 ± 0.07
J2226+00	Reg 1	22:26:25.395	+00:25:10.28	610×540	···	0.72 ± 0.02	1.71 ± 0.18
J2230−07	Reg 1	22:30:07.755	-07:21:00.09	$218 \pm 4 \times 83 \pm 3$	84 ± 2	3.37 ± 0.11	5.68 ± 0.12
J2235−28	Reg 1	22:35:12.798	-28:38:30.22	< 18	165 ± 0	26.83 ± 0.81	26.84 ± 0.81
J2241−06	Reg 1	22:41:34.654	-06:10:03.13	< 35	126 ± 1	4.71 ± 0.14	4.77 ± 0.15
J2251+01	Reg 1	22:51:35.593	01:06:27.67	< 28	92 ± 0	16.24 ± 0.49	16.42 ± 0.49
J2252−21	Reg 1	22:52:29.383	-21:02:33.58	< 30	139 ± 0	16.11 ± 0.48	16.10 ± 0.49
J2322−00	Reg 1	23:22:06.040	-00:15:50.62	< 60	175 ± 5	0.72 ± 0.03	0.71 ± 0.04
J2325−04	Reg 1	23:25:05.091	-04:29:48.54	$169 \pm 1 \times 96 \pm 0$	79 ± 0	14.83 ± 0.45	20.71 ± 0.45
	Reg 2	-0.24	0.15	$457 \pm 3 \times 45 \pm 2$	139 ± 0	3.43 ± 0.10	7.49 ± 0.11
J2328−02	Reg 1	23:28:20.427	-02:45:55.18	$127 \pm 82 \times 47 \pm 63$	50 ± 20	0.15 ± 0.02	0.18 ± 0.04
J2329−10	Reg 1	23:29:31.855	-10:54:18.04	$114 \pm 14 \times 52 \pm 9$	23 ± 2	1.22 ± 0.05	1.45 ± 0.06
J2331−14	Reg 1	23:31:03.167	-14:11:52.43	$51 \pm 4 \times 13 \pm 1$	68 ± 0	19.12 ± 0.57	20.21 ± 0.58
	Reg 2	-6.91	-2.48	830×500	···	2.25 ± 0.07	3.92 ± 0.09
J2332+34	Reg 1	23:32:59.339	34:30:29.69	< 66	50 ± 2	1.08 ± 0.04	1.08 ± 0.05
J2341−29	Reg 1	23:41:13.380	-29:55:17.26	< 114	166 ± 0	2.33 ± 0.07	2.36 ± 0.08
J2345+31	Reg 1	23:45:41.192	31:20:25.63	< 40	101 ± 1	3.19 ± 0.10	3.26 ± 0.10
J2357−10	Reg 1	23:57:44.890	-10:48:08.88	< 44	12 ± 1	3.00 ± 0.09	2.99 ± 0.10
J2359+43	Reg 1	23:59:40.257	43:02:18.58	< 41	30 ± 2	0.83 ± 0.03	0.84 ± 0.04
	Reg 2	0.49	-0.12	< 71	32 ± 8	0.16 ± 0.02	0.17 ± 0.03

NOTE — Column 1: Source name. Column 2: Region. For a single component source, the entire component is named Reg 1. For multi-component sources, brightest radio emission component is named Reg 1. Column 3 and 4: J2000 Right ascension and declination of the fitted source in the A-array image. In case of sources with more than one component, a source separation (in arcseconds) from the Reg 1 is provided. Column 5: Deconvolved source sizes for the A-array data. If source is resolved only along the major axis, the deconvolved minor axis is specified as 0. In case of unresolved source, we provide an upper limit on the major axis. A detailed description is provided in Section 2.4.2. For extended sources with non-gaussian like emission, we provide the size of 3σ contour as the angular size of the respective region. Column 6: Position angle of the fitted gaussian, measured anti-clockwise from North.

Table 2.6: Source Spatial Measurements for the VLA B-array Observations: Results from JMFIT

Source (1)	Region (2)	RA-B (hh:mm:ss.s) (3)	Dec-B (dd:mm:ss.s) (4)	Source Size-B ($mas \times mas$) (5)	PA-B (deg) (6)	S_{peak}-B (mJy/beam) 7	S_{tot}-B (mJy) (8)	α_{IB} (9)	S/N (10)
J0010+16	Reg 1	00:10:39.531	16:43:28.82	< 126	0 ± 5	1.97 ± 0.06	1.95 ± 0.07	-1.71 ± 0.09	87
J0104−27	Reg 1	01:04:24.867	-27:50:28.98	< 262	145 ± 0	1.44 ± 0.05	1.42 ± 0.07	-1.71 ± 0.33	49
J0132+13	Reg 1	01:32:11.239	13:03:27.39	< 127	168 ± 2	4.69 ± 0.14	4.70 ± 0.15	-1.26 ± 0.12	202
J0133+10	Reg 1	01:33:38.978	10:19:44.01	$388 \pm 2 \times 60 \pm 2$	98 ± 0	28.28 ± 0.85	34.59 ± 0.85	-1.01 ± 0.01	1065
J0134+40	Reg 1	01:34:19.281	40:30:49.41	< 182	45 ± 4	1.29 ± 0.05	1.30 ± 0.06	-1.66 ± 0.25	51
J0154+50	Reg 1	01:54:42.480	50:46:00.40	< 238	52 ± 4	0.91 ± 0.04	0.97 ± 0.05	-1.52 ± 0.18	39
J0159+12	Reg 1	01:59:19.576	12:01:37.04	$179 \pm 21 \times 105 \pm 31$	1 ± 9	2.47 ± 0.08	2.63 ± 0.09	-1.20 ± 0.15	87
J0204+09	Reg 1	02:04:11.975	09:20:30.18	< 212	179 ± 11	1.04 ± 0.04	1.04 ± 0.06	-1.24 ± 0.16	49
J0244+11	Reg 1	02:44:24.006	11:23:54.40	< 123	121 ± 2	4.05 ± 0.12	4.04 ± 0.13	-1.24 ± 0.04	182
J0300+39	Reg 1	03:00:37.571	39:01:25.06	$157 \pm 32 \times < 0$	23 ± 1	3.29 ± 0.10	3.35 ± 0.11	-0.16 ± 0.12	163
J0303+07	Reg 1	03:03:33.617	07:36:49.17	< 197	125 ± 5	1.53 ± 0.05	1.58 ± 0.06	-0.97 ± 0.10	79
	Reg 2	-0.46	-0.94	< 287	58 ± 13	0.40 ± 0.03	0.39 ± 0.05	-1.52 ± 0.37	22
J0304−31	Reg 1	03:04:27.557	-31:08:38.43	$357 \pm 16 \times 133 \pm 3$	179 ± 0	18.25 ± 0.55	19.65 ± 0.55	-0.89 ± 0.01	890
J0306−33	Reg 1	03:06:29.227	-33:53:31.88	$401 \pm 263 \times 71 \pm 26$	156 ± 1	1.11 ± 0.04	1.27 ± 0.06	-0.95 ± 0.09	77
J0332+32	Reg 1	03:32:28.239	32:05:44.87	< 104	60 ± 1	5.26 ± 0.16	5.30 ± 0.16	-1.28 ± 0.03	255
J0342+37	Reg 1	03:42:22.940	37:53:30.81	< 46	106 ± 0	60.55 ± 1.82	60.66 ± 1.82	-1.34 ± 0.01	2183
J0352+19	Reg 1	03:52:05.367	19:47:01.20	< 98	16 ± 1	7.97 ± 0.24	8.04 ± 0.24	-0.63 ± 0.02	379
J0354−33	Reg 1	03:54:48.242	-33:08:27.76	$1215 \pm 125 \times 186 \pm 24$	161 ± 1	2.61 ± 0.11	4.27 ± 0.21	-0.96 ± 0.05	152
J0404+07	Reg 1	04:04:40.978	07:12:19.68	< 52	78 ± 0	45.80 ± 1.37	45.83 ± 1.37	-0.63 ± 0.00	1787
J0404−24	Reg 1	04:04:03.620	-24:36:00.59	$591 \pm 201 \times 226 \pm 45$	65 ± 3	0.61 ± 0.03	0.91 ± 0.06	-0.74 ± 1.00	20
J0409−18	Reg 1	04:09:37.677	-18:37:57.81	$281 \pm 23 \times 97 \pm 8$	$143 \pm$	5.16 ± 0.16	5.67 ± 0.16	-1.02 ± 0.03	219
J0417−28	Reg 1	04:17:54.091	-28:16:55.50	< 122	39 ± 0	8.90 ± 0.27	8.90 ± 0.27	-1.00 ± 0.02	417
J0433−08	Reg 1	04:33:45.571	-08:36:27.61	< 124	0 ± 1	1.44 ± 0.05	1.33 ± 0.07	-0.75 ± 0.16	47
J0439−31	Reg 1	04:39:21.918	-31:59:08.08	< 96	0 ± 0	5.24 ± 0.16	5.18 ± 0.17	-0.87 ± 0.12	153
J0443+06	Reg 1	04:43:32.576	06:43:17.71	< 170	74 ± 1	2.52 ± 0.08	2.56 ± 0.09	-1.28 ± 0.16	95
J0450+27	Reg 1	04:50:32.896	27:26:07.72	< 307	79 ± 3	0.96 ± 0.04	0.94 ± 0.06	-0.58 ± 0.16	44
J0457−23	Reg 1	04:57:31.900	-23:24:02.20	$326 \pm 76 \times 289 \pm 19$	119 ± 1	31.20 ± 1.00	33.31 ± 1.13	-2.05 ± 0.25	90
J0502+12	Reg 1	05:02:04.709	12:18:52.37	< 167	0 ± 1	1.77 ± 0.06	1.71 ± 0.07	-0.89 ± 0.09	77
J0519−08	Reg 1	05:19:05.825	-08:13:20.02	$404 \pm 16 \times 86 \pm 13$	131 ± 0	8.24 ± 0.25	8.68 ± 0.25	-0.57 ± 0.03	298
J0525−36	Reg 1	05:25:33.520	-36:14:40.66	< 273	177 ± 0	2.41 ± 0.08	2.47 ± 0.09	-1.14 ± 0.16	99
J0526−32	Reg 1	05:26:24.720	-32:25:00.35	$469 \pm 7 \times 39 \pm 5$	177 ± 0	32.48 ± 0.98	33.81 ± 0.98	-0.41 ± 0.09	713
J0536−27	Reg 1	05:36:22.616	-27:03:00.29	< 57	9 ± 0	22.07 ± 0.66	22.08 ± 0.66	0.94 ± 0.01	1315
J0542−18	Reg 1	05:42:26.595	-18:25:15.13	$644 \pm 144 \times 710 \pm 27$	0 ± 4	1.00 ± 0.04	1.63 ± 0.07	0.64 ± 0.99	37
	Reg 2	1.14	0.13	$589 \pm 216 \times 258 \pm 104$	180 ± 5	0.30 ± 0.03	0.40 ± 0.06	-0.14 ± 0.32	11
J0543+52	Reg 1	05:43:41.262	52:28:52.80	$455 \pm 21 \times 136 \pm 24$	73 ± 1	2.27 ± 0.07	2.77 ± 0.09	-1.20 ± 0.13	134
	Reg 2	1.94	1.36	$338 \pm 42 \times 89 \pm 54$	39 ± 2	1.30 ± 0.05	1.41 ± 0.07	-0.95 ± 0.12	64
	Reg 3	7.09	3.05	$415 \pm 79 \times 203 \pm 63$	75 ± 4	0.64 ± 0.03	0.80 ± 0.06	-0.37 ± 0.51	21

Table 2.6 continued

Table 2.6: Source Spatial Measurements for the VLA B-array Observations: Results from JMFIT (continued)

Source (1)	Region (2)	RA-B (hh:mm:ss.s) (3)	Dec-B (dd:mm:ss.s) (4)	Source Size-B ($mas \times mas$) (5)	PA-B (deg) (6)	S_{peak}-B (mJy/beam) 7	S_{tot}-B (mJy) (8)	α_{IB} (9)	S/N (10)
J0543+58	Reg 1	05:43:57.949	58:09:50.38	< 106	90 ± 1	3.21 ± 0.10	3.17 ± 0.11	-1.08 ± 0.03	214
J0549−37	Reg 1	05:49:30.079	-37:39:39.53	< 1028	23 ± 1	0.71 ± 0.05	0.70 ± 0.08	-1.49 ± 0.32	23
J0602−27	Reg 1	06:02:41.486	-27:41:10.62	< 183	24 ± 0	2.52 ± 0.09	2.56 ± 0.11	-1.37 ± 0.10	84
	Reg 2	-4.83	0.06	$1158 \pm 142 \times 825 \pm 52$	8 ± 3	0.84 ± 0.05	2.39 ± 0.16	$\cdots$	15
J0604−03	Reg 1	06:04:52.997	-03:28:47.92	< 181	158 ± 1	1.87 ± 0.06	1.91 ± 0.07	-1.04 ± 0.12	72
	Reg 2	-3.34	2.67	< 231	110 ± 6	0.54 ± 0.03	0.56 ± 0.04	0.08 ± 0.40	19
J0612−06	Reg 1	06:12:00.237	-06:22:08.96	$652 \pm 18 \times 211 \pm 18$	143 ± 1	2.76 ± 0.09	3.69 ± 0.10	-0.86 ± 0.09	111
J0613−34	Reg 1	06:13:48.107	-34:07:28.98	< 472	143 ± 0	2.12 ± 0.07	2.18 ± 0.08	-1.75 ± 0.12	65
J0630−21	Reg 1	06:30:27.835	-21:20:58.80	< 103	146 ± 0	5.50 ± 0.17	5.60 ± 0.17	0.23 ± 0.03	209
	Reg 2	-0.64	-1.25	$418 \pm 118 \times 203 \pm 30$	9 ± 1	0.96 ± 0.04	1.15 ± 0.06	-0.78 ± 0.37	31
J0631−20	Reg 1	06:31:30.727	-20:34:11.81	< 279	126 ± 0	2.69 ± 0.09	2.72 ± 0.10	-0.46 ± 0.10	70
J0634+36	Reg 1	06:34:30.229	36:09:38.88	< 79	151 ± 0	12.60 ± 0.38	12.70 ± 0.38	-0.62 ± 0.01	543
J0641+52	Reg 1	06:41:32.686	52:08:38.48	$275 \pm 22\times < 333$	20 ± 2	1.99 ± 0.08	2.22 ± 0.11	-1.82 ± 0.07	100
J0642−27	Reg 1	06:42:28.862	-27:28:01.87	$575 \pm 809 \times 224 \pm 70$	83 ± 4	0.51 ± 0.04	0.87 ± 0.10	0.24 ± 1.94	18
J0647+59	Reg 1	06:47:14.163	59:30:29.84	< 98	54 ± 0	4.97 ± 0.15	5.01 ± 0.15	-1.13 ± 0.03	256
J0652−20	Reg 1	06:52:15.871	-20:06:13.07	< 550	138 ± 1	0.84 ± 0.04	0.84 ± 0.06	-0.99 ± 0.29	25
J0701+45	Reg 1	07:01:49.384	45:16:12.94	$2178 \pm 209 \times 577 \pm 84$	101 ± 2	0.61 ± 0.04	0.97 ± 0.08	-2.04 ± 0.46	16
J0702−28	Reg 1	07:02:57.217	-28:08:41.75	< 109	0 ± 0	6.46 ± 0.20	6.40 ± 0.20	-0.68 ± 0.02	305
J0714−36	Reg 1	07:14:33.541	-36:35:52.46	< 703	160 ± 0	1.78 ± 0.06	1.81 ± 0.07	-1.31 ± 0.12	66
	Reg 2	63.31	-23.53	< 1079	169 ± 0	0.79 ± 0.04	0.82 ± 0.05	-0.38 ± 0.24	29
J0719−33	Reg 1	07:19:12.598	-33:49:44.31	< 134	20 ± 0	11.02 ± 0.33	11.09 ± 0.33	-2.11 ± 0.02	405
J0729+65	Reg 1	07:29:02.756	65:44:29.36	< 114	121 ± 0	3.62 ± 0.11	3.64 ± 0.11	-1.76 ± 0.04	193
J0737+18	Reg 1	07:37:21.898	18:25:46.91	< 237	85 ± 1	1.12 ± 0.04	1.16 ± 0.06	-1.78 ± 0.18	45
	Reg 2	-8.70	-4.22	< 265	103 ± 1	0.76 ± 0.03	0.73 ± 0.05	-0.72 ± 0.24	30
J0739+23	Reg 1	07:39:09.466	23:47:39.73	< 99	69 ± 0	9.04 ± 0.27	9.05 ± 0.27	-2.26 ± 0.02	358
J0811−22	Reg 1	08:11:31.619	-22:25:21.76	< 374	122 ± 0	1.66 ± 0.06	1.67 ± 0.07	-1.36 ± 0.12	66
J0823−06	Reg 1	08:23:11.247	-06:24:08.42	< 65	153 ± 0	24.89 ± 0.75	24.89 ± 0.75	-0.30 ± 0.01	762
J0845+28	Reg 1	08:45:01.634	28:30:27.81	< 170	133 ± 0	2.85 ± 0.09	2.94 ± 0.10	-2.13 ± 0.08	112
	Reg 2	-3.97	2.80	< 217	125 ± 2	0.54 ± 0.03	0.53 ± 0.05	-4.66 ± 0.78	21
J0849+30	Reg 1	08:49:04.226	30:33:38.36	< 329	0 ± 1	0.52 ± 0.03	0.48 ± 0.04	-2.53 ± 0.28	26
J0920+12	Reg 1	09:20:14.689	12:53:02.24	< 179	159 ± 1	2.12 ± 0.07	2.11 ± 0.08	-1.18 ± 0.10	80
J0929−20	Reg 1	09:29:01.450	-20:53:45.70	$381 \pm 364 \times 229 \pm 13$	28 ± 0	2.71 ± 0.09	3.21 ± 0.10	-0.56 ± 0.16	97
J0941−00	Reg 1	09:41:57.676	-00:26:49.54	$507 \pm 59 \times 260 \pm 18$	110 ± 1	1.90 ± 0.06	2.29 ± 0.08	-0.88 ± 0.20	73
J0943+03	Reg 1	09:43:52.925	03:03:23.44	< 197	121 ± 0	7.09 ± 0.21	7.11 ± 0.22	-1.90 ± 0.04	239
J1002+02	Reg 1	10:02:58.143	02:56:47.63	< 423	101 ± 1	1.12 ± 0.04	1.14 ± 0.05	-1.09 ± 0.16	49
J1025+61	Reg 1	10:25:09.871	61:28:32.57	< 36	164 ± 0	5.61 ± 0.17	5.59 ± 0.17	-2.10 ± 0.13	231
	Reg 2	3.75	5.41	2780×2070	$\cdots$	1.36 ± 0.04	2.94 ± 0.38	-3.72 ± 0.23	121

Table 2.6 continued

Table 2.6: Source Spatial Measurements for the VLA B-array Observations: Results from JMFIT (continued)

Source	Region	RA-B (hh:mm:ss.s)	Dec-B (dd:mm:ss.s)	Source Size-B ($mas \times mas$)	PA-B (deg)	S_{peak}-B (mJy/beam)	S_{tot}-B (mJy)	α_{IB}	S/N
(1)	(2)	(3)	(4)	(5)	(6)	7	(8)	(9)	(10)
	Reg 3	-13.34	-41.03	1970×1700	$\cdots$	0.30 ± 0.01	0.74 ± 0.22	$\cdots$	31
J1046−02	Reg 1	10:46:32.825	-02:50:31.05	< 219	128 ± 0	13.56 ± 0.41	13.62 ± 0.41	-1.39 ± 0.02	394
J1048+55	Reg 1	10:48:39.754	55:53:56.59	< 218	178 ± 2	0.92 ± 0.03	0.95 ± 0.04	-0.99 ± 0.13	55
J1049−02	Reg 1	10:49:25.981	-02:32:12.62	< 364	129 ± 0	3.43 ± 0.11	3.44 ± 0.11	-0.89 ± 0.06	128
J1107+34	Reg 1	11:07:34.340	34:21:18.58	$122 \pm 4 \times 19 \pm 3$	3 ± 0	26.92 ± 0.81	27.51 ± 0.81	-1.29 ± 0.11	1234
J1138+20	Reg 1	11:38:16.909	20:28:34.91	< 111	132 ± 2	4.46 ± 0.14	4.47 ± 0.14	-1.06 ± 0.02	282
J1157+45	Reg 1	11:57:41.781	45:38:02.67	< 112	4 ± 1	3.65 ± 0.11	3.65 ± 0.12	-2.31 ± 0.06	158
J1210+47	Reg 1	12:10:27.868	47:50:03.08	< 61	5 ± 0	11.61 ± 0.35	11.58 ± 0.35	-0.47 ± 0.01	545
J1212+46	Reg 1	12:12:04.886	46:59:58.77	< 192	112 ± 1	2.76 ± 0.09	2.94 ± 0.09	-0.59 ± 0.05	133
J1226+18	Reg 1	12:26:46.648	18:19:43.41	< 126	5 ± 1	6.44 ± 0.19	6.50 ± 0.20	-0.39 ± 0.02	427
J1238+52	Reg 1	12:38:32.540	52:49:15.36	< 69	14 ± 0	15.31 ± 0.46	15.20 ± 0.46	-1.28 ± 0.01	608
J1257+73	Reg 1	12:57:55.242	73:08:16.69	< 143	150 ± 0	3.94 ± 0.12	4.05 ± 0.13	-1.02 ± 0.79	153
	Reg 2	5.23	1.23	< 352	155 ± 5	0.24 ± 0.03	0.25 ± 0.05	-0.63 ± 0.05	9
J1304+22	Reg 1	13:04:45.351	22:25:45.61	< 168	134 ± 2	1.83 ± 0.06	1.86 ± 0.07	-1.01 ± 0.06	115
J1308−34	Reg 1	13:08:17.009	-34:47:54.66	< 104	24 ± 0	14.85 ± 0.45	15.21 ± 0.45	-0.75 ± 0.04	723
	Reg 2	8.11	-5.88	$631 \pm 160 \times 388 \pm 13$	40 ± 0	2.18 ± 0.07	3.15 ± 0.10	-1.87 ± 0.29	120
	Reg 3	3.66	-2.51	$597 \pm 405 \times 158 \pm 46$	7 ± 1	0.90 ± 0.04	1.00 ± 0.07	-0.65 ± 0.42	35
J1316+39	Reg 1	13:16:15.738	39:46:54.74	< 373	137 ± 3	0.69 ± 0.03	0.70 ± 0.05	-1.76 ± 0.33	25
J1332+79	Reg 1	13:32:30.994	79:07:03.96	< 194	154 ± 0	3.02 ± 0.09	3.03 ± 0.10	-0.73 ± 0.05	135
J1343−11	Reg 1	13:43:31.369	-11:36:09.58	< 124	21 ± 0	3.26 ± 0.10	3.23 ± 0.10	-1.02 ± 0.05	156
J1400−29	Reg 1	14:00:50.139	-29:19:24.83	< 139	8 ± 0	3.22 ± 0.10	3.20 ± 0.11	-1.41 ± 0.06	130
J1409+17	Reg 1	14:09:28.830	17:32:04.30	< 105	159 ± 2	6.92 ± 0.21	6.99 ± 0.21	-0.52 ± 0.02	389
	Reg 2	1.17	0.58	$254 \pm 41 \times 165 \pm 46$	3 ± 8	0.92 ± 0.03	1.03 ± 0.05	-1.54 ± 0.26	50
J1412−20	Reg 1	14:12:43.158	-20:20:11.34	< 102	170 ± 0	21.42 ± 0.64	21.54 ± 0.64	1.50 ± 0.11	1300
J1424−26	Reg 1	14:24:59.362	-26:51:29.28	$248 \pm 204 \times < 0$	176 ± 1	0.69 ± 0.03	0.75 ± 0.04	-1.35 ± 0.43	28
J1428+11	Reg 1	14:28:59.755	11:13:18.83	$540 \pm 76 \times 266 \pm 79$	123 ± 6	0.49 ± 0.03	0.66 ± 0.05	-1.84 ± 1.55	20
	Reg 2	0.00	0.10	$1922 \pm 234 \times 493 \pm 129$	74 ± 4	0.21 ± 0.02	0.80 ± 0.11	-0.40 ± 0.46	9
	Reg 3	-3.06	-0.97	$812 \pm 372 \times 701 \pm 305$	120 ± 59	0.09 ± 0.02	0.21 ± 0.07	$\cdots$	4
J1434−02	Reg 1	14:34:19.590	-02:35:43.83	$146 \pm 24 \times 105 \pm 18$	170 ± 1	4.45 ± 0.14	4.61 ± 0.14	-1.38 ± 0.07	157
	Reg 2	-2.45	1.46	$567 \pm 142 \times 385 \pm 85$	105 ± 40	0.32 ± 0.03	0.50 ± 0.06	-0.41 ± 1.90	5
J1439−37	Reg 1	14:39:31.780	-37:25:23.44	< 199	36 ± 0	1.52 ± 0.05	1.47 ± 0.07	-0.98 ± 0.14	54
	Reg 2	9.44	-8.30	$1131 \pm 607 \times 637 \pm 87$	49 ± 3	0.35 ± 0.03	0.87 ± 0.09	-1.17 ± 0.70	13
J1448+40	Reg 1	14:48:50.820	40:22:44.29	< 186	172 ± 3	0.99 ± 0.04	0.93 ± 0.05	-1.33 ± 0.16	48
J1500−06	Reg 1	15:00:48.730	-06:49:40.04	$197 \pm 78 \times 121 \pm 23$	84 ± 1	1.84 ± 0.06	1.97 ± 0.07	-1.13 ± 0.27	50
J1501+13	Reg 1	15:01:38.359	13:24:49.89	< 62	37 ± 0	11.45 ± 0.34	11.46 ± 0.35	-1.45 ± 0.01	537
J1501+33	Reg 1	15:01:27.590	33:41:21.57	< 39	0 ± 0	12.02 ± 0.36	11.96 ± 0.36	-1.36 ± 0.01	639
J1510−22	Reg 1	15:10:03.719	-22:03:11.69	< 206	33 ± 0	3.97 ± 0.12	3.97 ± 0.13	-1.56 ± 0.04	192

Table 2.6 continued

Table 2.6: Source Spatial Measurements for the VLA B-array Observations: Results from JMFIT (continued)

Source (1)	Region (2)	RA-B (hh:mm:ss.s) (3)	Dec-B (dd:mm:ss.s) (4)	Source Size-B ($mas \times mas$) (5)	PA-B (deg) (6)	S_{peak}-B (mJy/beam) 7	S_{tot}-B (mJy) (8)	α_{IB} (9)	S/N (10)
J1513−22	Reg 1	15:13:10.436	-22:10:05.19	$152 \pm 92 \times 193 \pm 10$	5 ± 0	3.99 ± 0.12	4.18 ± 0.13	-1.08 ± 0.13	148
J1514−34	Reg 1	15:14:24.100	-34:11:00.59	< 304	19 ± 0	3.33 ± 0.10	3.32 ± 0.11	-1.00 ± 0.05	153
J1516+19	Reg 1	15:16:35.281	19:18:09.58	$515 \pm 72 \times 140 \pm 69$	139 ± 5	0.44 ± 0.03	0.59 ± 0.05	-0.52 ± 0.43	16
J1517+35	Reg 1	15:17:58.590	35:23:54.18	< 125	90 ± 1	3.20 ± 0.10	3.22 ± 0.11	-1.04 ± 0.06	126
J1521+00	Reg 1	15:21:16.589	00:17:54.97	< 43	136 ± 0	44.31 ± 1.33	44.27 ± 1.33	-2.06 ± 0.00	1866
J1525+76	Reg 1	15:25:01.928	76:40:10.19	< 107	159 ± 1	2.60 ± 0.08	2.58 ± 0.09	-0.42 ± 0.06	110
J1541−11	Reg 1	15:41:41.657	-11:44:09.27	< 445	6 ± 2	0.64 ± 0.03	0.67 ± 0.05	-1.57 ± 0.33	23
J1604+69	Reg 1	16:04:37.419	69:00:12.50	< 202	173 ± 1	1.58 ± 0.05	1.59 ± 0.06	-1.05 ± 0.10	73
J1615+74	Reg 1	16:15:11.750	74:31:46.09	< 57	2 ± 0	11.91 ± 0.36	11.91 ± 0.36	-1.01 ± 0.01	550
J1630+51	Reg 1	16:30:36.229	51:26:12.81	< 76	180 ± 0	40.13 ± 1.20	40.34 ± 1.20	-0.64 ± 0.00	1548
J1634−17	Reg 1	16:34:26.879	-17:21:39.58	$708 \pm 145 \times 154 \pm 66$	141 ± 3	0.57 ± 0.04	0.77 ± 0.08	-1.04 ± 0.43	17
J1641−05	Reg 1	16:41:07.212	-05:48:26.98	< 398	3 ± 4	0.72 ± 0.04	0.74 ± 0.06	-1.36 ± 0.33	30
J1642+41	Reg 1	16:42:50.100	41:23:18.19	< 106	166 ± 1	3.96 ± 0.12	3.95 ± 0.12	-1.26 ± 0.04	177
J1644−03	Reg 1	16:44:25.540	-03:57:25.46	$247 \pm 114 \times 336 \pm 38$	178 ± 4	0.91 ± 0.04	0.99 ± 0.06	-1.17 ± 0.39	30
J1651+34	Reg 1	16:51:10.516	+34:32:48.28	2771×1611	$\cdots$	7.04 ± 0.21	13.30 ± 0.55	-1.00 ± 0.05	477
	Reg 2	-2.40	0.41	$345 \pm 17 \times 117 \pm 13$	116 ± 2	2.85 ± 0.09	3.42 ± 0.10	-0.98 ± 0.15	103
	Reg 3	-1.37	0.18	$990 \pm 19 \times 172 \pm 15$	98 ± 1	1.86 ± 0.06	4.10 ± 0.10	0.43 ± 0.14	71
	Reg 4	-14.26	5.21	$604 \pm 56 \times 285 \pm 50$	13 ± 5	0.62 ± 0.03	0.98 ± 0.07	-0.37 ± 0.48	23
J1653+77	Reg 1	16:53:38.970	77:13:24.92	< 115	14 ± 0	2.79 ± 0.09	2.78 ± 0.09	-1.15 ± 0.05	148
J1653−01	Reg 1	16:53:05.400	-01:02:30.85	< 59	0 ± 1	5.91 ± 0.18	5.83 ± 0.18	-1.20 ± 0.04	228
J1657−17	Reg 1	16:57:42.896	-17:40:49.37	< 286	164 ± 1	0.83 ± 0.04	0.82 ± 0.05	-0.89 ± 0.27	26
J1702−08	Reg 1	17:02:04.642	-08:11:07.71	< 179	122 ± 0	14.22 ± 0.43	14.58 ± 0.43	-1.04 ± 0.10	457
J1703+26	Reg 1	17:03:34.210	26:15:11.09	< 57	29 ± 0	20.13 ± 0.60	20.15 ± 0.61	-1.36 ± 0.01	1086
J1703−05	Reg 1	17:03:25.009	-05:17:43.45	< 0	0 ± 0	17.69 ± 0.53	17.56 ± 0.53	-1.32 ± 0.11	600
	Reg 2	-3.63	-5.05	< 227	110 ± 2	1.47 ± 0.05	1.58 ± 0.06	-0.82 ± 0.33	42
J1707−09	Reg 1	17:07:46.071	-09:39:16.66	< 349	155 ± 1	1.49 ± 0.05	1.58 ± 0.06	-1.19 ± 0.15	56
J1717+53	Reg 1	17:17:05.892	53:13:42.59	< 38	0 ± 0	10.14 ± 0.30	10.09 ± 0.31	-0.87 ± 0.01	507
J1820+79	Reg 1	18:20:48.907	79:17:05.24	< 85	57 ± 0	31.29 ± 0.94	31.40 ± 0.94	-1.11 ± 0.01	1222
J1840+50	Reg 1	18:40:23.357	50:18:06.48	< 57	56 ± 0	7.96 ± 0.24	8.00 ± 0.24	-0.86 ± 0.34	363
	Reg 2	0.72	-0.85	< 415	110 ± 22	0.42 ± 0.03	0.50 ± 0.04	-1.01 ± 0.02	19
J1936−33	Reg 1	19:36:22.609	-33:54:20.33	< 369	0 ± 1	0.61 ± 0.03	0.56 ± 0.05	-1.35 ± 0.37	19
J1951−04	Reg 1	19:51:41.211	-04:20:24.49	< 43	174 ± 4	0.81 ± 0.03	0.79 ± 0.05	-2.73 ± 0.43	33
	Reg 2	-2.25	-11.42	$1071 \pm 180 \times 172 \pm 201$	178 ± 5	0.21 ± 0.02	0.38 ± 0.06	$\cdots$	9
J1958−07	Reg 1	19:58:01.696	-07:46:09.54	< 117	40 ± 1	4.53 ± 0.14	4.53 ± 0.14	-1.91 ± 0.07	138
J2000−28	Reg 1	20:00:48.571	-28:02:51.35	< 420	30 ± 1	0.88 ± 0.04	0.89 ± 0.05	-3.19 ± 0.06	138
J2021−26	Reg 1	20:21:48.006	-26:11:59.22	< 554	13 ± 1	0.99 ± 0.04	1.06 ± 0.06	-1.71 ± 0.54	28
J2040−39	Reg 1	20:40:49.510	-39:04:00.42	< 441	0 ± 0	1.94 ± 0.06	1.89 ± 0.07	-1.20 ± 0.12	67

Table 2.6 continued

Table 2.6: Source Spatial Measurements for the VLA B-array Observations: Results from JMFIT (continued)

Source (1)	Region (2)	RA-B (hh:mm:ss.s) (3)	Dec-B (dd:mm:ss.s) (4)	Source Size-B ($mas \times mas$) (5)	PA-B (deg) (6)	S_{peak}-B (mJy/beam) 7	S_{tot}-B (mJy) (8)	α_{IB} (9)	S/N (10)
J2059−35	Reg 1	20:59:46.925	-35:41:35.00	$2417 \pm 1592 \times 1208 \pm 353$	26 ± 8	0.08 ± 0.03	0.21 ± 0.09	···	3
J2126−01	Reg 1	21:26:19.977	-01:03:54.53	< 164	173 ± 2	1.63 ± 0.05	1.61 ± 0.06	-1.01 ± 0.10	80
J2130+20	Reg 1	21:30:47.976	20:09:01.43	< 355	20 ± 7	1.00 ± 0.05	1.11 ± 0.08	-0.30 ± 0.24	27
	Reg 2	-8.66	-10.55	4220×3770	···	0.99 ± 0.03	4.80 ± 0.51	-0.45 ± 0.35	199
	Reg 3	7.32	23.17	4080×3850	···	0.66 ± 0.02	4.07 ± 0.50	-0.79 ± 0.46	169
J2133−14	Reg 1	21:33:56.518	-14:19:04.72	< 70	11 ± 0	12.20 ± 0.37	12.16 ± 0.37	-0.75 ± 0.02	446
J2133−17	Reg 1	21:33:49.428	-17:11:44.38	3270×3238	···	4.52 ± 0.14	11.38 ± 0.65	-1.08 ± 0.07	399
	Reg 2	-10.47	-4.52	< 104	137 ± 1	1.02 ± 0.04	0.93 ± 0.06	-1.10 ± 0.04	36
	Reg 3	-16.83	-9.60	4361×2997	···	1.97 ± 0.06	5.33 ± 0.70	-1.79 ± 0.18	187
J2145−06	Reg 1	21:45:14.748	-06:18:14.26	$632 \pm 42 \times 257 \pm 36$	163 ± 2	0.57 ± 0.02	0.75 ± 0.03	-1.26 ± 0.31	29
	Reg 2	-1.38	3.00	$222 \pm 89 \times 173 \pm 52$	164 ± 2	0.56 ± 0.02	0.60 ± 0.03	-1.98 ± 0.77	18
J2204+20	Reg 1	22:04:27.980	20:31:02.58	< 136	26 ± 0	38.49 ± 1.16	39.64 ± 1.16	-2.73 ± 0.01	1142
J2212+33	Reg 1	22:12:58.889	33:26:04.66	< 150	140 ± 0	8.16 ± 0.25	8.50 ± 0.25	-1.04 ± 0.09	338
J2212−12	Reg 1	22:12:04.361	-12:53:53.24	$4105 \pm 90 \times 2051 \pm 53$	25 ± 5	3.09 ± 0.09	8.50 ± 1.04	-2.34 ± 0.22	152
	Reg 2	19.81	8.52	2616×1765	···	1.14 ± 0.03	2.82 ± 0.56	-1.99 ± 0.61	51
	Reg 3	10.29	5.76	< 265	31 ± 7	0.41 ± 0.06	0.36 ± 0.09	-1.24 ± 1.16	7
J2222+09	Reg 1	22:22:48.752	09:51:29.07	< 128	5 ± 2	2.13 ± 0.07	2.14 ± 0.07	-1.26 ± 0.09	88
J2226+00	Reg 1	22:26:25.383	00:25:10.27	$418 \pm 34 \times 263 \pm 17$	90 ± 6	1.69 ± 0.06	2.13 ± 0.07	-1.56 ± 0.30	81
J2230−07	Reg 1	22:30:07.758	-07:21:00.01	$167 \pm 105 \times 172 \pm 10$	158 ± 0	5.65 ± 0.17	5.85 ± 0.18	-1.41 ± 0.13	118
J2235−28	Reg 1	22:35:12.799	-28:38:30.34	< 86	130 ± 0	27.73 ± 0.83	27.72 ± 0.83	-0.87 ± 0.01	1073
J2241−06	Reg 1	22:41:34.654	-06:10:03.10	< 74	0 ± 1	4.91 ± 0.15	4.83 ± 0.15	-1.05 ± 0.04	210
J2251+01	Reg 1	22:51:35.596	01:06:27.68	< 56	17 ± 0	16.38 ± 0.49	16.37 ± 0.49	-0.98 ± 0.01	868
J2318+25	Reg 1	23:18:07.497	+25:57:15.95	23490×11210	···	0.30 ± 0.01	15.25 ± 4.46	-3.42 ± 0.32	903
	Reg 2	-6.67	-29.40	8950×4980	···	0.19 ± 0.01	3.44 ± 0.76	-3.09 ± 0.94	204
J2322−00	Reg 1	23:22:06.037	-00:15:50.64	< 188	0 ± 5	0.73 ± 0.03	0.68 ± 0.04	-1.56 ± 0.23	37
J2325−04	Reg 1	23:25:05.093	-04:29:48.45	$335 \pm 4 \times 134 \pm 2$	124 ± 0	22.26 ± 0.67	25.53 ± 0.67	-1.16 ± 0.10	693
J2328−02	Reg 1	23:28:20.431	-02:45:54.96	< 445	91 ± 71	0.13 ± 0.02	0.16 ± 0.05	4.79 ± 1.60	7
J2329−10	Reg 1	23:29:31.857	-10:54:17.91	< 335	24 ± 1	1.60 ± 0.05	1.59 ± 0.06	-1.40 ± 0.29	46
J2331−14	Reg 1	23:31:03.169	-14:11:52.31	< 40	147 ± 0	22.03 ± 0.66	21.07 ± 0.66	-1.42 ± 0.10	805
	Reg 2	-6.86	-2.45	$352 \pm 31 \times 377 \pm 8$	132 ± 0	4.19 ± 0.13	4.87 ± 0.14	-1.03 ± 0.12	99
J2332+34	Reg 1	23:32:59.340	34:30:29.70	< 153	0 ± 3	1.07 ± 0.04	1.06 ± 0.05	-1.38 ± 0.13	55
J2345+31	Reg 1	23:45:41.192	31:20:25.68	< 104	27 ± 1	3.30 ± 0.10	3.30 ± 0.11	-1.15 ± 0.04	166
J2357−10	Reg 1	23:57:44.891	-10:48:08.72	< 171	140 ± 1	3.35 ± 0.10	3.17 ± 0.11	-1.11 ± 0.07	119
J2359+43	Reg 1	23:59:40.265	43:02:18.62	< 331	23 ± 6	0.97 ± 0.04	1.05 ± 0.06	-0.94 ± 0.17	43

Table 2.6 continued

Table 2.6: Source Spatial Measurements for the VLA B-array Observations: Results from JMFIT (continued)

Source	Region	RA-B (hh:mm:ss.s)	Dec-B (dd:mm:ss.s)	Source Size-B ($mas \times mas$)	PA-B (deg)	S_{peak}-B (mJy/beam)	S_{tot}-B (mJy)	α_{IB}	S/N
(1)	(2)	(3)	(4)	(5)	(6)	7	(8)	(9)	(10)

NOTE — Column 1: Source name. Column 2: Region. For a single component source, the entire component is named Reg 1. For multi-component sources, brightest radio emission component is named Reg 1. Column 3 and 4: J2000 Right ascension and declination of the fitted source in the B-array image. In case of sources with more than one component, a source separation (in arcseconds) from the Reg 1 is provided. Column 5: Deconvolved source sizes for the A-array data. If source is resolved only along the major axis, the deconvolved minor axis is specified as 0. In case of unresolved source, we provide an upper limit on the major axis. A detailed description is provided in Section 2.4.2. For extended sources with non-gaussian like emission, we provide the size of 3σ contour as the angular size of the respective region. Column 6: Position angle of the fitted gaussian, measured anti-clockwise from North. Column 11: In-band spectral index for the best image available. We used A-array data when a good quality image is available. (see Section 2.4.4). Column 12: Source detection S/N averaged from the 8.6 and 11.4 GHz images used for calculating α_{IB}.

Table 2.7: Physical Properties for Our Sample

Source (1)	z (2)	Region (3)	Linear Size (kpc×kpc) (4)	$\log_{10} L_{1.4\,GHz}$ (W Hz^{-1}) (5)	$\alpha_{1.4}^{10}$ (6)	$\log P_l$ dyne cm^{-2} (7)
J0010+16	2.85	Reg 1	< 0.6	27.24	-1.20 ± 0.03	> -6.20
J0132+13	2.85	Reg 1	0.5×0.2	27.07	-0.79 ± 0.02	-6.51
J0159+12	0.76	Reg 1	1.7×0.2	25.78	-1.04 ± 0.02	-7.44
J0300+39	1.12	Reg 1	0.7×0.2	25.92	-0.75 ± 0.03	-7.22
J0304−31	1.53	Reg 1	< 0.2	26.73	-0.48 ± 0.02	> -6.65
		Reg 2	< 0.6	···	···	> -8.37
J0306−33	0.78	Reg 1	< 0.8	25.20	-0.77 ± 0.05	> -7.88
J0332+32	0.30	Reg 1	< 0.1	25.13	-1.08 ± 0.02	> -6.31
J0342+37	0.47	Reg 1	< 0.3	26.05	-0.48 ± 0.02	> -6.74
J0354−33	1.37	Reg 1	< 0.8	25.78	-0.50 ± 0.04	> -7.64
J0404−24	1.26	Reg 1	5.2×3.8	26.17	-1.38 ± 0.09	-8.95
		Reg 2	4.9×2.5	···	···	-8.80
J0409−18	0.67	Reg 1	< 0.4	26.00	-1.08 ± 0.02	> -7.41
		Reg 2	2.1×0.7	···	···	-8.72
J0417−28	0.94	Reg 1	< 0.4	25.69	-0.31 ± 0.03	> -7.15
J0439−31	2.82	Reg 1	$1.7\times < 0.0$	27.00	-0.71 ± 0.02	-8.00
J0519−08	2.05	Reg 1	< 0.5	26.72	-0.55 ± 0.02	> -6.84
J0525−36	1.69	Reg 1	1.3×0.4	25.77	-0.43 ± 0.06	-8.00
J0526−32	1.98	Reg 1	4.4×0.2	27.64	-0.84 ± 0.02	-6.81
J0536−27	1.79	Reg 1	< 0.2	25.61	0.50 ± 0.04	> -6.17
J0549−37	1.71	Reg 1	< 2.3	26.55	-1.48 ± 0.04	> -7.86
J0612−06	0.47	Reg 1	< 0.5	25.48	-1.12 ± 0.03	> -7.92
		Reg 2	3.6×3.1	···	···	-9.87
		Reg 3	4.7×3.8	···	···	-9.98
J0613−34	2.18	Reg 1	< 1.3	27.08	-1.24 ± 0.03	> -6.83
J0630−21	1.44	Reg 1	< 0.3	25.97	-0.32 ± 0.03	> -8.07
		Reg 2	1.6×1.0	···	···	-8.56
J0642−27	1.34	Reg 1	$12.2\times < 0.0$	25.83	-0.93 ± 0.07	-9.84
		Reg 2	10.7×4.1	···	···	-10.29
J0652−20	0.60	Reg 1	< 1.3	25.11	-1.20 ± 0.04	> -8.02
J0702−28	0.94	Reg 1	< 0.5	25.32	-0.08 ± 0.04	> -7.45
J0714−36	0.88	Reg 1	< 5.6	25.70	-1.05 ± 0.03	> -8.96
		Reg 2	< 8.6	···	···	> -9.49
J0719−33	1.63	Reg 1	< 0.2	26.40	-0.40 ± 0.02	> -6.42
J0729+65	2.24	Reg 1	< 0.3	26.82	-0.91 ± 0.02	> -6.14
J0804+36	0.66	Reg 1	0.4×0.1	26.24	-1.30 ± 0.02	-6.11
J0811−22	1.11	Reg 1	< 3.1	26.17	-1.21 ± 0.03	> -8.06
J0823−06	1.75	Reg 1	< 0.6	26.81	-0.39 ± 0.02	> -6.82
J1002+02	0.30	Reg 1	< 1.9	24.42	-1.04 ± 0.03	> -8.84
J1107+34	1.45	Reg 1	1.1×0.2	26.06	0.11 ± 0.02	-7.10
J1238+52	2.25	Reg 1	< 0.6	27.53	-0.92 ± 0.02	> -6.26
J1308−34	1.65	Reg 1	15.0×4.3	26.94	-0.59 ± 0.02	-9.29
		Reg 2	11.9×7.8	···	···	-8.59

Table 2.7 continued

Table 2.7: Physical Properties for Our Sample (continued)

Source	z	Region	Linear Size (kpc×kpc)	$\log_{10} L_{1.4\,GHz}$ (W Hz^{-1})	$\alpha_{1.4}^{10}$	$\log P_l$ dyne cm^{-2}
(1)	(2)	(3)	(4)	(5)	(6)	(7)
		Reg 3	2.1×1.2	...	...	-10.24
J1343−11	2.49	Reg 1	< 0.4	26.35	-0.49 ± 0.04	> -6.79
J1400−29	1.66	Reg 1	< 0.5	27.17	-1.39 ± 0.02	> -5.90
J1412−20	1.81	Reg 1	0.4×0.1	25.67	0.47 ± 0.03	-6.52
J1428+11	1.60	Reg 1	4.7×2.3	26.34	-1.01 ± 0.05	-9.57
		Reg 2	16.7×4.3	...	...	-8.99
		Reg 3	7.1×6.1	...	...	-9.86
J1434−02	1.92	Reg 1	< 0.6	27.04	-1.08 ± 0.02	> -7.14
		Reg 2	2.3×1.1	...	...	-8.52
J1439−37	1.20	Reg 1	< 1.7	25.85	-0.74 ± 0.04	> -8.91
		Reg 2	9.6×5.4	...	...	-10.06
J1500−06	1.50	Reg 1	1.4×0.3	26.60	-1.30 ± 0.03	-6.93
J1501+13	0.51	Reg 1	< 0.4	26.52	-1.58 ± 0.02	> -5.87
J1510−22	0.95	Reg 1	< 0.5	25.85	-0.74 ± 0.03	> -7.14
J1513−22	2.20	Reg 1	1.3×1.6	27.07	-1.01 ± 0.02	-7.68
J1514−34	1.08	Reg 1	< 0.9	25.81	-0.66 ± 0.03	> -7.71
J1517+35	1.51	Reg 1	< 1.1	26.92	-1.30 ± 0.02	> -6.76
J1521+00	2.63	Reg 1	< 0.1	26.75	0.08 ± 0.02	> -5.26
J1541−11	1.58	Reg 1	< 0.9	27.22	-2.09 ± 0.03	> -5.64
J1630+51	0.72	Reg 1	< 0.6	26.30	-0.49 ± 0.02	> -7.11
J1634−17	2.07	Reg 1	< 0.8	26.77	-1.55 ± 0.06	> -6.92
J1641−05	1.83	Reg 1	< 1.0	26.30	-1.20 ± 0.04	> -7.18
J1642+41	1.28	Reg 1	< 0.9	26.32	-0.89 ± 0.02	> -7.29
J1653−01	2.02	Reg 1	< 0.6	26.28	-0.38 ± 0.03	> -7.12
J1702−08	2.85	Reg 1	1.1×0.3	27.57	-0.81 ± 0.02	-6.56
J1703+26	1.07	Reg 1	< 0.2	26.42	-0.52 ± 0.02	> -6.08
J1703−05	1.79	Reg 1	0.3×0.2	26.47	-0.22 ± 0.02	-7.48
		Reg 2	1.3×0.6	...	...	-7.95
J1717+53	2.72	Reg 1	< 0.3	26.74	-0.35 ± 0.02	> -6.41
J1936−33	2.24	Reg 1	< 3.3	26.44	-1.22 ± 0.06	> -7.94
J1951−04	1.58	Reg 1	< 0.4	26.73	-1.46 ± 0.04	> -6.70
		Reg 2	9.3×1.5	...	...	-8.37
J1958−07	1.80	Reg 1	< 0.9	26.91	-1.06 ± 0.02	> -6.79
J2000−28	2.28	Reg 1	< 0.8	26.66	-0.72 ± 0.03	> -7.07
J2021−26	2.44	Reg 1	2.8×0.5	26.58	-1.09 ± 0.05	-7.54
J2059−35	2.38	Reg 1	20.2×10.1	27.11	-1.92 ± 0.23	-8.39
J2126−01	0.61	Reg 1	< 0.3	25.34	-1.09 ± 0.04	> -6.89
J2130+20	0.81	Reg 1	< 2.8	26.44	-1.06 ± 0.04	> -9.19
		Reg 2	32.7×29.3	...	...	-10.63
		Reg 3	31.7×29.9	...	...	-10.58
J2226+00	0.68	Reg 1	4.4×3.9	25.59	-1.17 ± 0.06	-9.13
J2230−07	0.44	Reg 1	1.3×0.5	25.56	-1.07 ± 0.02	-7.89
J2318+25	0.50	Reg 1	147.4×70.3	26.15	-1.02 ± 0.12	-11.47

Table 2.7 continued

Table 2.7: Physical Properties for Our Sample (continued)

Source	z	Region	Linear Size (kpc×kpc)	$\log_{10}\ L_{1.4\,GHz}$ (W Hz^{-1})	$\alpha_{1.4}^{10}$	$\log P_l$ dyne cm^{-2}
(1)	(2)	(3)	(4)	(5)	(6)	(7)
		Reg 2	56.2×31.2	⋯	⋯	-11.19
J2325−04	1.74	Reg 1	2.9×1.2	27.46	-0.90 ± 0.02	-7.28
		Reg 2	2.9×1.2	⋯	⋯	-7.40
J2332+34	0.98	Reg 1	< 0.5	25.96	-1.31 ± 0.03	> -6.78
J2357−10	2.05	Reg 1	< 0.4	26.57	-0.80 ± 0.03	> -6.56

Note — Column 1: Source name. Column 2: Redshift. Column 3: Region name. Column 4: Linear dimensions of the radio emission in each region. For an unresolved source, we use an upper limit on the angular major axis to estimate the limit on the source linear size. Column 5: Rest-frame 1.4 GHz luminosity. We use NVSS flux and the spectral index between NVSS and 10 GHz continuum observations to calculate the luminosity. Column 6: Spectral index between NVSS and 10 GHz observations. Fluxes from all of the regions are added up to estimate the spectral indices. Column 7: Equipartition lobe pressures as described in Section 2.5.4

Chapter 3

The Radio Spectra of WISE-NVSS Selected Obscured and Ultra-luminous Quasars

3.1 Introduction

Central supermassive black holes (SMBHs) are now known to influence galaxy evolution via energetic feedback (e.g., Kormendy & Ho, 2013; Heckman & Best, 2014). However, the prevalence and importance of this connection remain one of the poorly understood phenomena today. Cosmological simulations now routinely use the SMBH-galaxy interactions to explain the properties of massive end of galaxies (Di Matteo et al., 2005; Hopkins & Quataert, 2010; Sijacki et al., 2015; Kaviraj et al., 2017) and the existence of such interactions is strengthened by mounting observational evidence (e.g., McNamara & Nulsen, 2007; Fabian, 2012; Kormendy & Ho, 2013; Heckman & Best, 2014). This interlinked growth appears to be important in massive galaxies (e.g., Beckmann et al., 2017), where the feedback from actively accreting SMBH, known as Active Galactic Nucleus (AGN), regulates galactic star formation histories via injection of mechanical and radiative energies (Fabian, 2012).

Although evidence for the presence of AGN feedback is mounting at low redshift (Fabian, 2012; Harrison, 2017; Morganti, 2017a, and references therein), it is a challenging task to understand how the process works and whether it can have a long-lasting impact to alter the galaxy evolution (Harrison, 2017). In massive galaxies, AGN feedback is essential to drive multi-phase gas outflows and prevent them from cooling, thereby quenching the star formation. Two categories of feedback mechanisms are thought to operate depending on the accretion mechanism of the SMBH. The radiative winds from high Eddington ratio SMBHs (radiative-mode) AGN are considered to drive gas outflows on sub-galactic scales. Whereas, the powerful radio jets are well known to inhibit gas cooling flows on the intracluster scales (McNamara & Nulsen, 2007) in massive galaxies with low-accretion rate SMBH (jet-mode AGN). However, the relative importance of each mode as a function of redshift and host properties is still an open question (Villar Martín et al., 2014). Furthermore, on a smaller scale, the role of relativistic jets in feedback is observationally less clear (e.g., Nyland et al., 2013, 2018). Recent hydrodynamic simulations suggest that relativistic jets confined in a dense ISM are capable of dispersing and heating the ISM (e.g., Wagner et al., 2012; Mukherjee et al., 2016; Bicknell et al., 2018; Mukherjee et al., 2018).

One of the observational challenges in investigating jet-driven feedback is identifying young, powerful radio AGNs that are actively interacting with their hosts (Patil et al., 2020). Low$-z$ (< 0.5) compact radio sources are providing support for gas outflows associated with kpc-scale jets (O'Dea & Saikia, 2020, for review). Such systems are likely to be more widespread during the epoch of cosmic noon ($z \sim 1-3$), which marks the period of peak SMBH fueling and galaxy assembly. Also, the effects of feedback are known to scale with AGN luminosity (e.g., Woo et al., 2016). Thus, $z \sim 2$ quasars, with recently triggered, young radio jets embedded in large gas and dust reservoirs, will be ideal candidates to investigate the importance and nature of jet-driven feedback.

Cosmological simulations predict that the earliest growth of recently triggered SMBHs in luminous systems occurs in a heavily obscured state (Hopkins & Quataert, 2010). Such systems are expected to be faint in the optical and X-rays but identifiable in the Mid-Infrared (MIR) and radio via their intense reprocessed hot emission and compact radio source. Indeed, heavily obscured AGN selected in MIR and X-ray surveys are often associated with mergers (e.g., Kocevski et al., 2015; Fan et al., 2016; Donley et al., 2018) and have a higher merger incidence with increasing redshift and AGN luminosity (e.g., Koss et al., 2010; Treister et al., 2012).

The Widefield Infrared Sky Explorer (WISE; Wright et al. 2010) has opened the MIR sky and led to the discovery of some of the most luminous and heavily obscured quasars. These sources are expected to trace the early growth of SMBHs in massive galaxies (e.g., Assef et al., 2015). One such sample by (Lonsdale et al., 2015) combines WISE photometric selection with radio AGN selection to find $z \sim 2$, heavily obscured, luminous ($L_{Bol} \sim 10^{11.7} - 10^{14.2} L_{\odot}$) AGN shrouded in a dense column of the Interstellar Medium (ISM). In combination with WISE colors and luminosities characteristic of hyperluminous quasars (see Section 3.2), the requirement for a compact radio morphology at the resolution (45") of the NRAO VLA Sky Survey (NVSS; Condon et al. 1998) identifies AGN candidates with compact jets (Patil et al., 2020).

Intrinsically compact radio jets hosted by powerful, dusty quasars at $z \sim 2$ may represent young/re-started radio-loud activity, with similar properties to the population of young radio sources. Young radio sources with sub-galactic jets are seen in AGN classes such as Compact Steep Spectrum (CSS), Gigahertz-Peaked Spectrum

(GPS), and High-Frequency Peakers (HFP). These are radio powerful ($L_{1.4GHz} > 10^{26}$ W Hz^{-1}) sources with compact, sub-galactic jets and characteristic radio spectral curvature (O'Dea, 1998; Orienti, 2016; O'Dea & Saikia, 2020). We would expect to have some similarities between our sample and GPS/CSS sources, as we wish to identify recently triggered jets. To determine the radio morphologies and identify genuinely compact, and possibly young, sources, Patil et al. (2020, hereafter Paper I) conducted a high-angular-resolution VLA snapshot imaging of the entire WISE-NVSS selected sample of 166 sources. About 60% of the sample shows compact morphologies with sub-arcsecond angular size limits and no signs of any extended radio structures.

In compact radio sources, the synchrotron emission from the relativistic electrons is absorbed by the relativistic plasma itself or the external thermal gas resulting in a peaked spectrum with turnover frequencies of $\sim$ GHz or lower (de Kool & Begelman, 1989; Tingay & de Kool, 2003). The turnover location is usually anti-correlated with emitting region sizes (Kellermann, 1966; O'Dea, 1998), thus finding the peaked spectrum sources in our sample can provide clues to the compactness of those sources. Our high-resolution VLA imaging in Paper I already constrains the sizes to sub-arcsecond-scales in most of our sample. Thus, modeling radio spectra of our sample will provide further constraints on their physical properties and the surrounding medium. Many studies are emerging focusing on the impact of outflows driven by compact radio sources on their host's ISM, but they are limited to lower redshifts (e.g., O'Dea & Saikia, 2020). This sample provides a unique domain for investigating the nature and impact of cosmic noon, compact radio quasars possibly caught in a rare evolutionary phase just after (re)ignition of the radio AGN.

While Paper I constrained the morphologies, this work investigates the radio spectral properties for the entire sample. We combine various archival radio sky surveys with recently published (Patil et al., 2020) VLA observations at 10 GHz to construct broadband radio spectra. We aim to find the incidence of peaked spectrum radio sources in our sample and investigate whether our initial selection is consistent with finding compact, sub-galactic radio jets.

Our sample selection is summarized in Section 3.2. The radio observations including the VLA 10 GHz observations and archival radio data are described in Section 3.3. We present our radio spectral fitting technique and spectral classification in Section 3.5. A summary of the diversity of radio spectral shapes and their relation to the radio source morphologies is presented in Section 3.6. We discuss the key properties resulting from the radio spectral modelling of our entire sample in Sections 3.7, 3.8, and 3.9. We then analyze a subset of sources with peaked spectra in Sections 3.10 and 3.11. Section 3.12 summarizes the key results of this study. We adopt a ΛCDM cosmology with $H_0 = 67.7$ km s^{-1} Mpc^{-1}, $\Omega_\Lambda = 0.691$ and $\Omega_{\mathrm{M}} = 0.307$ (Planck Collaboration et al., 2016).

3.2 Sample Selection

Here we briefly review the sample selection, (see Lonsdale et al. 2015 for a detailed description). The primary sample was selected by cross-matching the WISE All Sky catalog (WISE; Wright et al. 2010) with the NRAO VLA Sky Survey (NVSS; Condon et al. 1998) and Faint Images of the Radio Sky at Twenty-one centimeters (FIRST; Becker et al. 1995). We required the sources to be unresolved with S/N > 7 in the *WISE* 22μm or 12μm bands. The sources were also selected to have compact radio emission at NVSS and FIRST and satisfy the criterion; $q = \log(f_{22\mu\mathrm{m}}/f_{21\,\mathrm{cm}}) < 0$. We further required the sources to have very red colors in the *WISE* 3.6($W1$)−4.5($W2$)−12($W3$)μm bands, with color cut: $(W1 - W2) + 1.25(W2 - W3) > 7$.

Sources that satisfied above criteria were then visually inspected in the Sloan Digital Sky Survey (SDSS; York et al. 2000) or Digitized Sky Survey (DSS) and required to be optically faint or undetected to reject low-z sources. As a result, our final sample comprised 155 sources.

A spectroscopic followup secured redshifts of 71/80 sources in the range $0.4 - 2.8$ with a median of 1.53 (Lonsdale et al. 2015, Ferris et al. submitted). Overall, their submillimeter and MIR properties indicate that these are MIR-bright heavily obscured quasars, with high IR luminosities ($L_{IR} > 10^{11.7} L_{\odot}$).

3.3 Radio Observations

3.3.1 VLA 10 GHz Imaging

We obtained 10 GHz (X-band) images of the entire sample using the Karl G. Jansky Very Large Array (VLA). Patil et al. (2020) presented these data and initial results. Briefly, the 10 GHz VLA images were obtained with A and B arrays, with a typical resolution of $0.2''$ and $0.6''$, respectively. Overall, 118 sources have good quality data in A-array, and 147 sources have data in B-array.

The A-array observations were taken in October and December, 2012, while the B-array data were taken in June, July and August 2012. An identical WIDAR correlator setup was used for both arrays that provided two $1-$GHz bands spanning $8-12$ GHz. The imaging was performed in snapshot mode with typical on-source integration time $\sim 4-5$ minutes.

The data was reduced in a standard manner using Common Astronomy Software Applications (CASA; McMullin et al. 2007) version 4.7.0. This involved manual data editing, pipeline calibration, followed by a few rounds of self-calibrations. The calibrated $uv-$data was then imaged using the CASA task CLEAN. Paper I gives further details of the data reduction and analysis.

3.3.2 Archival Radio Surveys

To construct the radio spectra of our sample, we searched for any possible detections in public archival radio surveys. We found 12 radio surveys that have at least one successful detection. Table 3.2 lists these catalogs, along with our own 10 GHz VLA survey. We also provide a short description of the archival radio surveys below.

NVSS

The NVSS observed the entire northern sky ($\delta > -40$ deg) at 1.4 GHz. This survey was conducted in the D configuration of the VLA, which resulted in an angular resolution of 45″. As NVSS was used for our primary selection, our entire sample is detected in the NVSS and all sources have compact emission brighter than 7 mJy.

FIRST

FIRST is a VLA survey that covered 10,575 deg^2 of the total sky at a resolution of about 5″ and sensitivity limit of ~ 0.15 mJy beam^{-1}. When available, the FIRST catalog [1] was also used to identify *WISE* sources with compact radio emission. In the original sample selection presented in Lonsdale et al. (2015), we did not apply any constraints based on FIRST source morphology. As a result, six out of 51 FIRST detections have extended structure. A detailed discussion on the effects of extended radio morphology on the measurement of radio spectra is given in Section 3.3.3.

TGSS-ADR1

The Tata Institute of Fundamental Research Giant Meterwave Radio Telescope Sky Survey Alternative Data Release (TGSS-ADR1; Intema et al. 2017) is a 150 MHz survey covering about 90% of the total sky (36,900 deg^2). TGSS has a resolution of

[1] The original sample selection by Lonsdale et al. (2015) used an earlier version of the FIRST catalog published in White et al. (1997). However, we have used the most-up-to date FIRST catalog (Helfand et al., 2015) for source cross-match and flux measurements.

about 25″ and rms noise of $3-5$ mJy beam^{-1}. Our entire sample falls within the TGSS footprint and yields 87 source detections and 68 non-detections with a median 3σ upper limit of 10.8 mJy.

VLASS

The VLA Sky Survey (VLASS; Lacy et al. 2020) is an ongoing 3 GHz (S-band: $2-4$ GHz) continuum survey covering 33,885 deg^2, which is similar to the footprint of NVSS. The planned survey takes place over 3 epochs, with the first recently completed. While the complete source catalog is still in preparation, quick-look images are currently available for public access. The typical 1σ sensitivity of a single epoch image is $\sim 120\,\mu$Jy beam^{-1} with an angular resolution of 2.5″. The VLASS fluxes used in our analysis are estimates based on this epoch 1 quick-look source catalog generated using the Python Blob Detector and Source Finder (PyBDSF; Mohan & Rafferty 2015) with standard input parameters. We use the peak flux from the source catalog for unresolved sources. When sources have multi-components or significantly extended single components, we measure the fluxes using CASA VIEWER and add to the flux uncertainties given by PyBDSF or CASA VIEWER an additional systematic flux uncertainty of 20% due to antenna pointing issues (Lacy et al., 2019). All of our sources except two are detected in the VLASS quick-look images. However, due to the preliminary nature of the quick-look imaging[2], we visually inspected all of the VLASS image cutouts for our sample. We found 6 sources with severe quick-look image artifacts for which reasonably accurate (within 20%; see Lacy et al. 2019) flux estimates cannot be obtained. We have excluded the VLASS fluxes in such cases.

[2]For details on the limitations of the VLASS quick-look images, see Lacy et al. (2020).

Other surveys

In addition to our 10 GHz VLA data and the radio surveys covering the majority of our sources with high detection rates, we also searched for counterparts in radio surveys with less complete sky coverage, shallower depths, and/or lower angular resolution. These include: The Galactic and Extra-galactic Murchinson Widefield Array (GLEAM; Hurley-Walker et al. 2017) survey, The Green-Bank 6-cm Radio Source Catalog (GB6; Gregory et al. 1996), the Sydney University Molonglo Sky Survey (SUMSS; Mauch et al. 2003), the Texas Survey of Radio Sources (TEXAS; Douglas et al. 1996), the Westerbork Northern Sky Survey (WENSS; Rengelink et al. 1997), and the VLA Low-Frequency Sky Survey (VLSSr; Lane et al. 2014). Due to the relatively low angular resolution ($\sim 1'$) of GLEAM, SUMSS, WENSS, and VLSSr, some sources with catalog detections suffer from source blending. We discuss this further in Section 3.3.3. The number of sources with available data from each survey, as well as the number of detected sources, is summarized for each radio survey in Table 2.1.

VLITE

Whenever possible, we also include in our analysis commensal 340 GHz (P-band) data from the VLA Low-band Ionosphere and Transient Experiment (VLITE; Clarke et al. 2016; Polisensky et al. 2016). VLITE operates over a subset of the VLA antennas during observing projects at other VLA bands. These data are processed by an automated imaging pipeline based on Obit (Cotton, 2008) and archived at the U.S. Naval Research Laboratory (NRL). The low-frequency VLITE data can provide potentially valuable constraints on the radio spectra, particularly those with peaks below 1 GHz.

Unfortunately, our VLA X-band data were taken prior to the start of VLITE

Table 3.1: VLITE Properties

Parameter	Specifications
Central frequency, ν	340 GHz
No. of sources	$4^{\dagger}$
Angular resolution, θ_{res}	$10 - 17.8''$
1σ rms noise	$1.9 - 10.2$ mJy beam^{-1}

NOTE — † These four sources were part of the multi-band VLA followup (Section 5.1.1).

operations, which began in November 2014. However, four of our targets were observed from 2015−2017 as part of a multi-band follow-up campaign (to be presented in a future study). All of these sources are detected in VLITE, and we include their 340 MHz flux measurements in our radio spectra analysis. These VLITE images have typical 1σ depths of $1.9 - 10.2$ mJy beam^{-1} and angular resolutions of $\theta_{\rm FWHM} \sim 10'' - 17.8''$. Table 3.1 summarizes these observations.

3.3.3 Multi-resolution Concerns

The radio observations come from a range of telescopes with different resolutions. This can affect the flux measurements and the form of the radio spectra. The low-frequency (<1 GHz) surveys typically have a larger synthesized beam and are thus more sensitive to diffuse emission, and are also more likely to suffer from source confusion. In contrast, higher-resolution observations, typically at higher frequencies, may resolve out extended low surface brightness emission. When combined, these effects can cause artificial steepening of the radio spectrum, since the high-frequency observations are missing flux.

To assess these possible resolution effects, we visually inspected our sample in all the available surveys We find that the majority of our sample (84/155) show no

Table 3.2: List of Radio Surveys used in the Construction of Multiband Radio Spectra

Survey	ν GHz	λ cm	θ_{res} $''$	σ_{rms} mJy/beam	Dec. Range deg	δ_{pos} $''$	θ_s $''$	N	n_{det}	n_{obs}	Ref
(1)	(2)	(3)	(4)	(5)	(6)	(7)	(8)	(9)	(10)	(11)	(12)
VLA-A	10	3	0.2	0.013	...	$0.04^{\dagger}$	...	...	118	118	1
VLA-B	10	3	0.6	0.013	...	$0.1^{\dagger}$	...	...	147	147	1
GB6	4.85	6	630		0:75		20	75,162	9	9	2
VLASS	3	10	2.5	0.15	> -40	0.5		$5{,}300{,}000^{\star}$	153	153	3
NVSS	1.4	21	45	0.45	> -40	$<\sim 1$	7	1,773,484	155	155	4
FIRST	1.4	21	5	0.15		$\lesssim 1$	5	946,432	52	52	5
SUMSS	0.843	35	45	6-10	< -30	2	12	211,063	15	18	6
TEXAS	365	82		20	35.5-71.5	~ 1	5	66,841	14	14	7
WENSS	325	92	54	3.6	28:76	1.5	10	211,234	31	49	8
GLEAM	74-231	405-130	100	6-10	< 30	$\sim$1.6	20	307,455	39	110	9
TGSS ADR1	150	200	25	3.5	> -53	2	20	623,604	86	155	10
VLSSr	74	405	75	100	> -30	...	20	92,965	9	143	11

NOTE — †: We adopt a positional accuracy of $\sim 20\%$ of the synthesized beam; $\star$: The number of sources in the VLASS is only an estimated count of individual source components. The references for the catalogs are – 1: Patil et al. (2020); 2: Gregory et al. (1996); 3: Lacy et al. (2020); 4: Condon et al. (1998); 5: Becker et al. (1995); 6: Mauch et al. (2003); 7: Douglas et al. (1996); 8: Rengelink et al. (1997); 9: Hurley-Walker et al. (2017); 10: Intema et al. (2017); 11: Lane et al. (2014).

complex structure in any of the primary surveys; which are TGSS, NVSS, FIRST, VLASS, and our VLA 10 GHz observations. The remaining surveys having lower angular resolution than NVSS were compared with NVSS image cutouts to look for possible source blending. We find 2/31 WENSS sources and 1/9 VLSSr sources show source confusion and are therefore excluded from our spectral analysis. As a further check, we inspected optical images of our sample in the Panoramic Survey Telescope and Rapid Response System (Pan-STARRS; Chambers et al. 2016) for potential false identifications or confusion with nearby sources, especially for surveys with $\sim$ arcminute resolution. We find 7/39 GLEAM sources may be affected in this way, and their GLEAM fluxes weren't included in our spectral analysis. In summary, the majority of our sources are compact at all frequencies.

3.3.4 Faint Detections and Upper Limits

Radio surveys typically publish source catalogs using a flux threshold of $\sim 5-7\sigma$ in order to reduce the inclusion of false detections and image artifacts. While this is appropriate for a blind survey, we have prior source positions and this allows us to measure fluxes that are below the formal catalog threshold. By inspecting the survey's images at our source locations, we find 6 VLSSr sources, 2 WENSS sources, 16 GLEAM sources, 3 SUMSS sources, and 24 TGSS sources below the corresponding catalog flux detection limit. We use CASA task IMFIT to obtain flux measurements of these faint sources. Typically, these sources have S/N ratio between $\sim 3.9-5$. Conversely, we found no measurable flux in 45 GLEAM sources, 12 WENSS sources, 124 VLSSr sources, and 48 TGSS sources. For these non-detections we use $3\,\sigma$ as an upper limit on the flux, where σ is the rms noise level in the image. Due to relatively poor sensitivity, the upper limits for fainter sources aren't usually useful in constraining the spectral shape. We exclude these unhelpful upper limits from our spectral fitting in 83/124 VLSSr non-detections, 2/12 WENSS non-detections, and 23/45 GLEAM non-detections.

3.4 Overview of Our Sample Selection

Figure 3.1 shows a flow chart describing our radio spectral modelling and analysis. Various radio surveys used for source search are given at the top (Section 3.3). Every box includes a total number of sources observed including upper limits. A diamond shaped box specifies the quality checks performed and number of sources accepted and rejected in the respective decision making. The final spectral shape classes and their distinguishing features are given at the bottom. In the next section, we explain our spectral fitting routine and spectral classification.

3.5 Radio Spectral Fitting

The radio spectrum of a source contains information about the source's physical condition. The observed radio spectrum is usually thought of as a combination of emission processes and energy loss and absorption processes. In the case of AGN the emission is thought to be synchrotron emission with a power-law energy distribution of relativistic electrons generating a power-law radio spectrum, increasing to lower frequency. Over time, the most energetic electrons can radiate their energy causing a break to steeper spectra at high frequencies. Conversely, at lower frequencies, the radiation can be absorbed by the relativistic electrons (synchrotron self-absorption) and/or by thermal electrons (thermal absorption), which cause a spectral turnover with characteristic inverted slope at low-frequencies. Thus, identifying and measuring these features in a radio spectrum can help ascertain a number of important physical properties of the radio source.

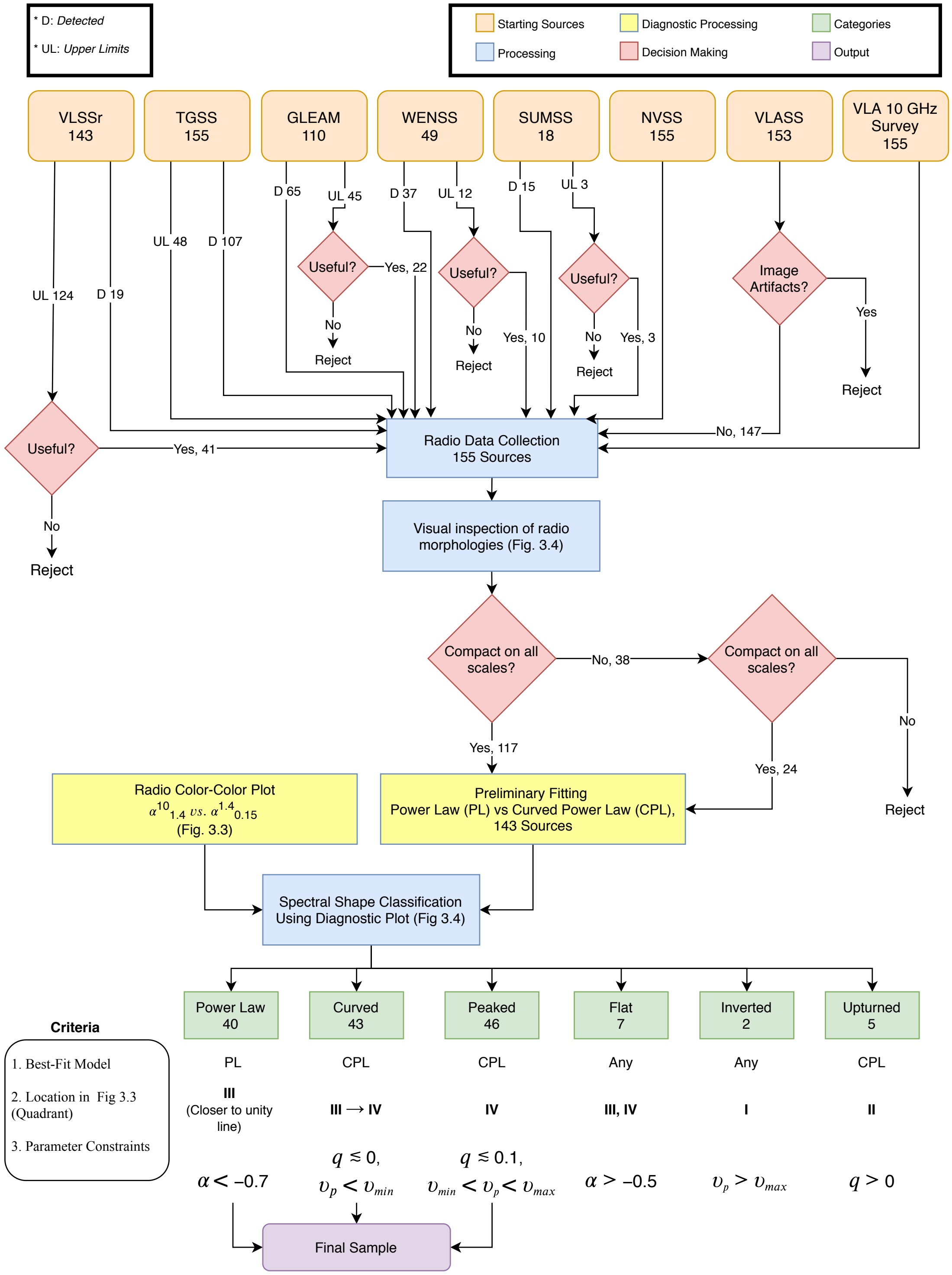

Figure 3.1: The flowchart summarizing the entire process of radio spectral analysis.

3.5.1 Visual Inspection

Constructing radio spectra from a wide range of telescopes requires care, because different instruments can have different sensitivities to different angular scales. For example, higher frequency observations typically have higher angular resolution which can lead to loss of flux on larger angular scales and this in turn causes an artificially steep spectrum. To guard against this, we carefully inspected the images of all our sources at all available frequencies, to identify which sources might be subject to these resolution-dependent errors.

In particular, we find 38 sources which are extended in higher-resolution observations (e.g. our 10-GHz observations, VLASS, or FIRST). Of these 24 appear to have missing flux at higher frequencies and we exclude them from the sample. The remaining 14 have power law spectra at all frequencies and we include these in our final sample.

Table 3.5 Column 3 gives our 10 GHz morphology classification while Column 7 gives a quality code denoting whether a source is excluded from the final sample.

3.5.2 Fitting Procedure

Given the sparse spectral sampling we initially choose not to fit idealized physical models to the spectra, such as synchrotron self absorption (SSA) or free-free absorption (FFA) (e.g., Tingay & de Kool, 2003; Tingay et al., 2015; Callingham et al., 2015). Instead, we use simple functions to characterize the overall form of the spectrum in $\log\nu - \log S_\nu$, and then use these to help guide our physical interpretation. Our overall approach is to first fit a power law, and if significant deviations are found then fit a parabola (similar to Callingham et al., 2017). Hence, the underlying synchrotron emission mechanism can be captured by the power law, while any curvature on the high or low frequency side, including a turnover, can be captured by the parabola.

The power law is given by:

$$S_\nu = S_o\, \nu^\alpha \tag{3.1}$$

where S_ν is the flux density in mJy at frequency ν GHz, S_o is the normalizing flux in mJy, and α is the spectral index.

The parabola is given by:

$$S_\nu = S_o\, \nu^\alpha\, e^{q(ln\nu)^2} \tag{3.2}$$

which has peak frequency and flux, ν_{peak} and S_{peak} given by

$$\nu_{peak} = e^{-\alpha/2q} \tag{3.3}$$

and

$$S_{peak} = ae^{-\alpha^2/4q} \tag{3.4}$$

This function describes a parabola in $\log S_\nu$ *vs* $\log\nu$ (a Gaussian in S_ν *vs* $\log\nu$), where q characterizes the width of the peak, or the degree of curvature, with full width at half the peak flux (for negative q), $S_{peak}/2$ of $\log FWHM = 0.72/\sqrt{-q}$. The function becomes a power-law as $q \to 0$. Significant spectral curvature is usually defined as $|q| \geq 0.2$ (Duffy & Blundell, 2012).

We perform the data fitting using a nonlinear least-square minimization routine[3] that uses the Lavenberg-Marquardt algorithm. This method is useful for solving non-linear equations, but tends to find a local minimum to the best-fit solutions. To

[3]We used the curve_fit function available in a Python module, called SciPy (Virtanen et al., 2020) .

guard against this tendency, we visually inspected the best-fit solutions and those with poor-fits were fitted again after adjusting the range of initial parameters. In addition to the flux measurements, we include our 10 GHz in-band spectral indices, α_{IB} (see Paper I). Following Section 4.4 from Paper I and the analysis given in Condon (2015), we find that a S/N ratio greater than 70 is required to yield an in-band spectral index with uncertainty $\sigma_\alpha \lesssim 0.1$. We only use α_{IB} for point sources since extended emission can suffer from sensitivity loss in the higher frequency channels of the 10 GHz bandwidth. To incorporate α_{IB} in the fitting procedure, we incorporate the derivatives of Equations 3.1 and 3.2 to parameterize their slopes, and incorporate these in the minimization routine. This method proves useful when distinguishing between power law and curved spectra in the marginal cases.

3.5.3 Spectral Shape Classification

We inspect all radio spectra to assess the best-fit model, also checking the reduced χ^2 and q to decide which model fits best. We divide our sample into six broad categories:

- **Power Law (PL):** This is a standard power law given by Equation 3.1 spanning the full spectral range with relatively steep spectral index $\alpha < -0.7$ consistent with optically thin synchrotron emission. Either the reduced χ^2 is lower for the power-law model or the q value in the parabolic fit is consistent with zero within it's uncertainty.

- **Peaked (PK):** A turnover is detected within the observed spectral range. Thus, if ν_u and ν_l are the 1σ upper and lower limits on the best-fit ν_{peak}, then $\nu_u < \nu_{max}$ and $\nu_l > \nu_{min}$. Where, ν_{max} and ν_{min} are the lowest and highest frequency of the observations in an individual spectrum.

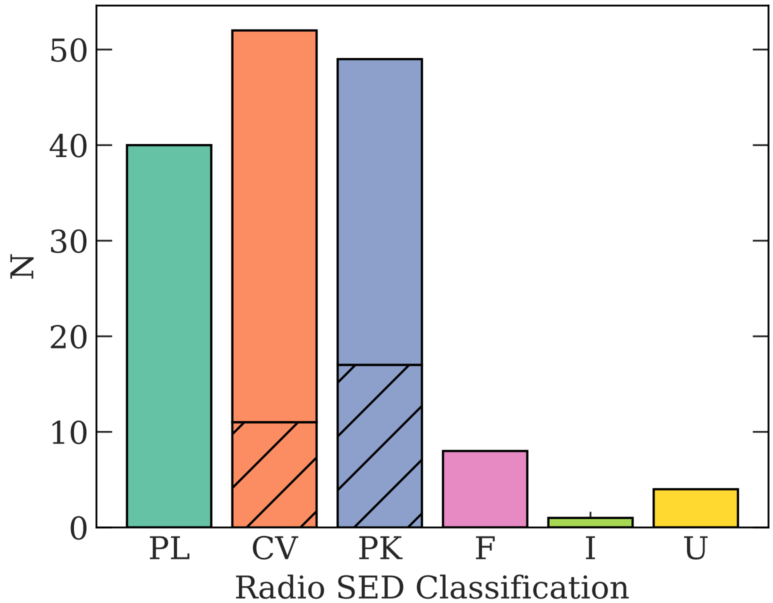

Figure 3.2: The distribution of radio spectral shape classes in our sample. The hatched portion gives the number of sources with relatively poor quality data. The $x-$axis labels are the radio spectral shape classes defined in Section 3.5.3. The codes are PL: Power-law, CV: Curved, PK: Peaked, F: Flat, I: Inverted, and U: Upturned.

- **Curved (CV):** A radio spectrum is classified as curved when there is a significant deviation from the power-law model, but no peak is seen within our spectral range. Either the reduced χ^2 value is lower for the curved power law model or the $|q| \gtrsim 0.1$. Usually the lowest frequency observation is greater than the calculated peak frequency, $\nu_{peak} + \sigma_{\nu_{peak}}$.

- **Flat (F):** When the α estimated from either power-law or curved-power model is less than -0.5.

- **Inverted (I):** Sources from this class have a rising spectrum, i.e., flux increases with frequency.

- **Upturned (U):** Sources that show a concave spectrum are categorized as having upturned spectrum.

Figure 3.2 shows the distribution of spectral classes for our entire sample with less reliable spectra shown hatched. We find 40 sources with power-law spectrum, 54 sources with curved, 47 sources with peaked, 7 sources with flat, 2 sources with inverted spectra, and 5 sources with upturned spectra. Table 3.5 lists the spectral shape classification of our entire sample.

Radio Color-Color Plot

To complement spectral fitting, Figure 3.3 shows a simpler approach to characterizing spectral shapes, using fluxes measured at three widely separated frequencies to define two radio colors. In our case, we choose fluxes at 10 GHz (our survey), 1.4 GHz (NVSS) and 150 MHz (TGSS), which together define two spectral indices: $\alpha_{1.5}^{1.4}$ and $\alpha_{1.4}^{10}$.

Different spectral shapes tend to occupy different regions in the radio color-color plane. The radio spectral classes defined using model fitting are plotted using different colored symbols. All the steep power-law sources lie close to the equality line, and the curved sources lie within the lower left quadrant but further from the equality line. Peaked sources with ν_{peak} between 10 GHz and 0.15 GHz (TGSS) frequencies fall within or close to the lower right quadrant. Most of the upturned spectra lie in the upper left quadrant, and the single source with an inverted spectrum lies in the upper right quadrant. Overall, then, this radio color-color plot is a useful complement to, and broadly consistent with, our more detailed model fitting approach to spectral shape classification.

The Final Sample

Figure 3.4 illustrates the various issues described above that result in our final sample of sources with reliable power law, peaked, or curved spectra. Visual inspection of the various survey images allows us to keep only sources that are unresolved

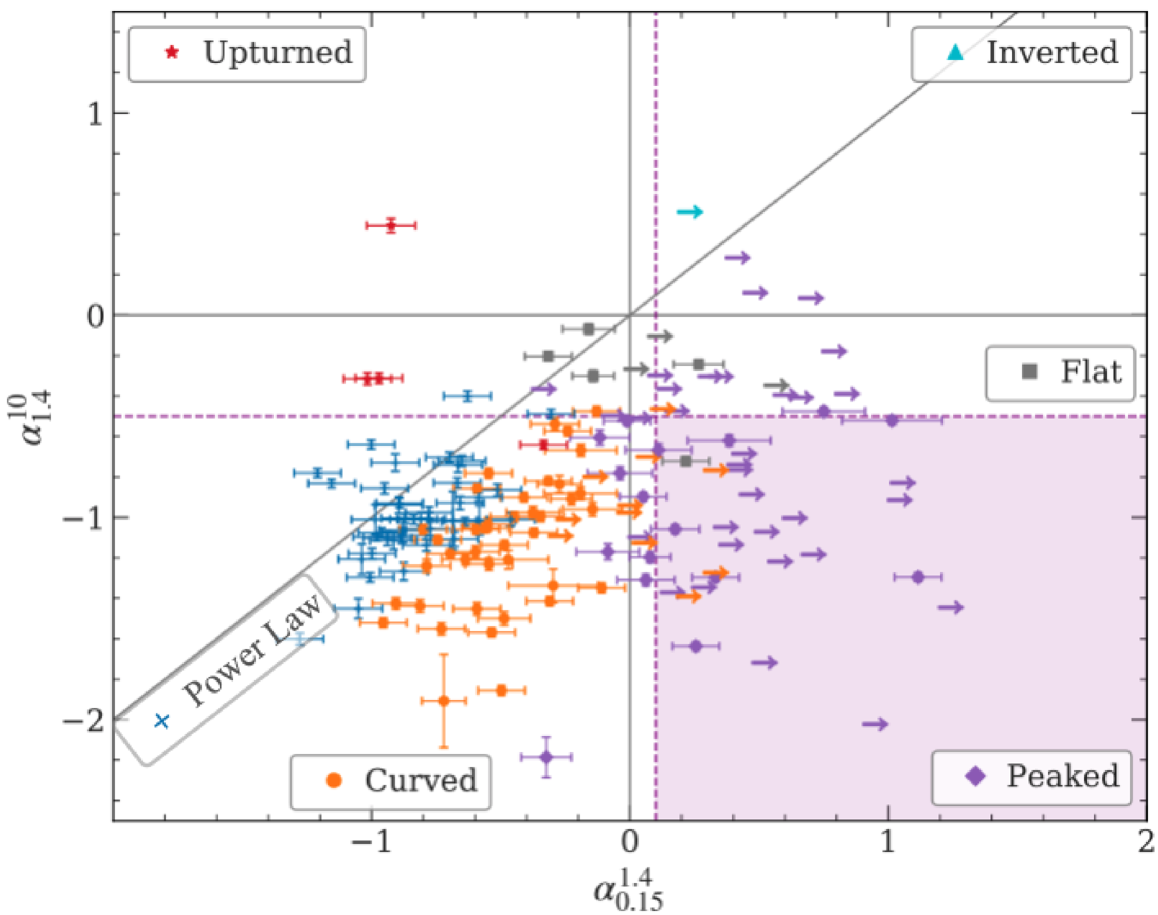

Figure 3.3: The radio color-color plot showing spectral indices, $\alpha_{1.4}^{10}$ and $\alpha_{0.15}^{1.4}$ calculated using fluxes from TGSS (0.15 GHz), NVSS (1.4 GHz), and our VLA 10 GHz survey. Different symbols represent different radio spectral shape classes described in Section 3.5.3. These include: Red cross: Power law, Light Blue circle: Curved, Green diamond: Peaked, Orange square: Flat, light green triangle: inverted, and dark blue star: Upturned. The horizontal arrows are lower limits to the value of $\alpha_{0.15}^{1.4}$. The two dashed lines are taken from Callingham et al. (2017) and they define the peaked spectral shapes which lie in the purple shaded region.

in all surveys. The spectral shape class is assigned based on a comparison of the two fitted spectra (power law or parabola) and the location of the source in the radio color-color plot. Our final sample includes 29, 43 and 46 unresolved power law, curved, and peaked spectrum sources respectively, with 11, 9 and 3 sources rejected due to the presence of some extended emission.

All of the results are tabulated in Table 3.5 which provides the spectral shape classification (where ":" indicates an uncertain classification), the two band spectral indices used in Figure 3.3, and an indication of whether the source is included in the final sample.

3.5.4 Spectral Shape Parameters

Although we use a straight line and parabolic fits to help classify the spectral shape, we measure additional parameters that are more commonly used to discuss the physical properties of the radio source. These parameters include: the location of the peak frequency, ν_{peak}, spectral indices, α_{high} and α_{low}, at frequencies greater and less than ν_{peak}, and the q parameter from Equation 3.2 to indicate the width of the peak or degree of curvature. These are now defined in slightly more detail.

- α_{high}: This spectral index is though to characterize the optically thin part of the underlying synchrotron emission. It is most useful for steep power-law, curved, and peaked sources. For peaked sources we estimate α_{high} using all the flux measurements available at $\nu > \nu_{peak}$. For curved sources we use fluxes at $\nu \gtrsim 1$ GHz. For power-law spectra α_{high} is simply the best-fit value of α.

- α_{low}: We only estimate α_{low} for sources with peaked and inverted spectra. Since spectral turnover is likely to result from absorption, the value of α_{low} can help distinguish between different kinds of absorption, such as free-free absorption (FFA) or synchrotron self-absorption (SSA). We estimate its value using all flux

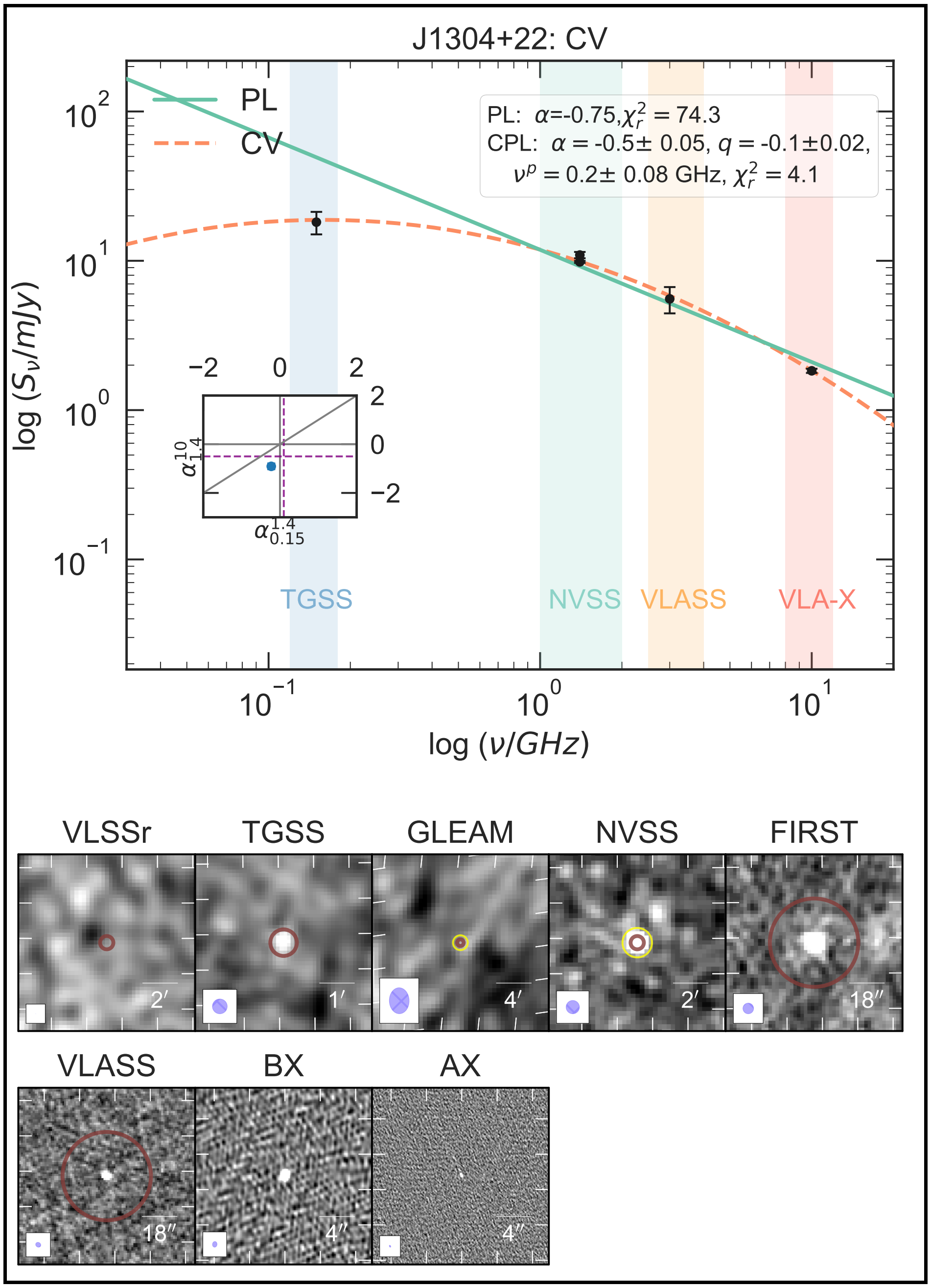

Figure 3.4: Example illustrating our approach to classifying spectral shape class and assessing its reliability. The main top panel shows the radio spectrum of J1304+22. The green solid line and orange dashed line are the best fit power-law (PL) and curved parabola (CV, Equation 3.2), respectively. The text box lists their best-fit parameters, certainties, and reduced χ^2. The colored vertical stripes show the spectral range for each radio survey. The radio color-color plot is inset (see Figure 3.3 for reference) with the location of the J1304+22 shown by the blue dot. The bottom panel shows image cutouts from each survey, with its synthesized beam in the lower-left and angular scale on the lower-right of each cutout. The red and yellow circles show typical NVSS and GLEAM beams respectively.

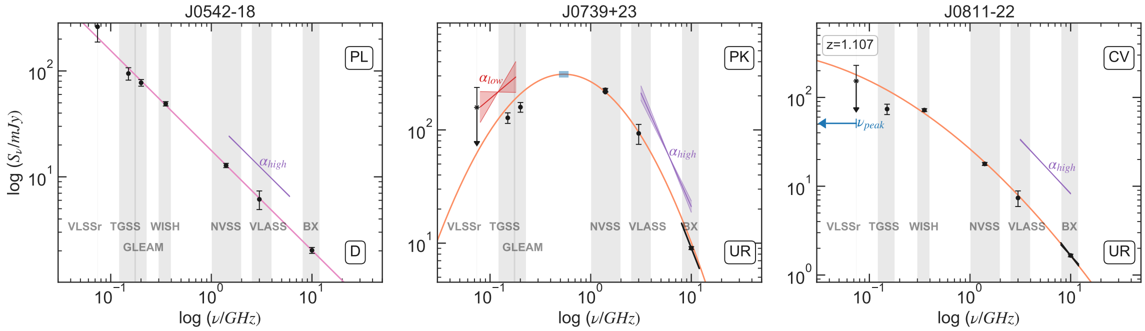

Figure 3.5: Three different spectral shapes illustrate our parameters. The overall format of each panel is described in the caption to Figure 3.4. The best-fit power-law (pink) or parabola (orange) is shown. Spectral shape class and 10 GHz radio morphology class are given in the upper and lower right boxes. In the top left the spectroscopic redshift is given, when available. Left: Power-law spectrum. The purple line with its bow-tie is the best-fit power-law and uncertainty. Middle: Peaked spectrum. The purple and red lines with bow-ties show α_{high} and α_{low}, with their uncertainties. The blue shaded box in the center gives the location of ν_{peak} and S_{peak} with their 1 σ uncertainties. Right: A curved-spectrum. The purple line and bow-tie show α_{high} and its uncertainty estimated from the VLASS, NVSS and our 10 GHz data. The blue arrow denotes the limit to ν_{peak}.

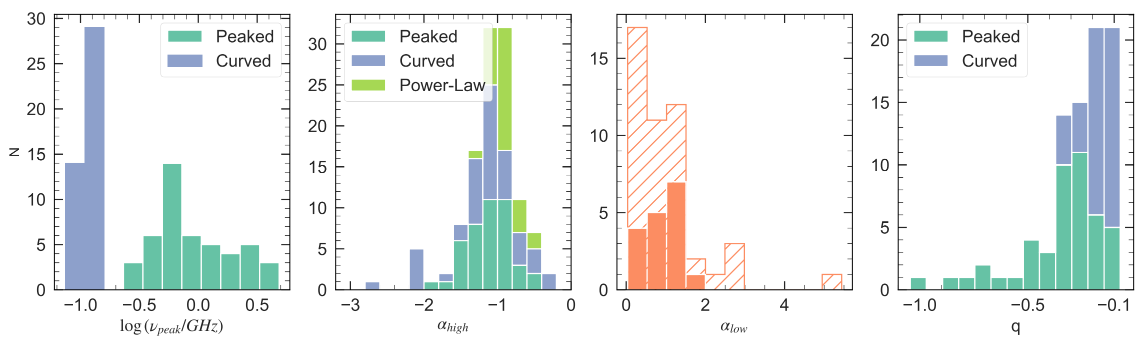

Figure 3.6: Distribution of radio spectral shape parameters. The hatched portions indicates limits only.

measurements at $\nu < \nu_{peak}$.

- ν_{peak}: For peaked spectra, we calculate the ν_{peak} using Equation 3.3, with an uncertainty estimated by propagation of errors. For curved spectra, we use ν_{min} as the upper limit of ν_{peak}, where ν_{min} is the lowest frequency observations available. Similarly, for inverted spectra we take 10 GHz as the lower limit to ν_{peak}. If the radio spectrum is peaked due to absorption, the value of ν_{peak} and S_{peak} can give valuable information on the source properties (see Section 3.11).

- q: This parameter is only given for peaked or curved spectra, and is taken directly from the fit of Equation 3.2. It indicates the width of the peak or the degree of spectral curvature. Its value is likely determined by the nature of the absorption (on low frequency side) and spectral aging (on the high-frequency side) and also on the complexity of the source (e.g. simple *vs* multiple screen; single *vs* multiple electron populations).

Figure 3.5 illustrates these parameters using three sources with different radio spectral class. We list all these parameters and their uncertainties for the final sample in Table 3.5, and Figure 3.6 shows their distributions.

We find turnover frequencies in the range 300 MHz to 3 GHz with median ~ 720 MHz, though this range reflects, in part, the frequency range used in our study. For sources classified as having curved spectra, the upper limit of peak frequency is either 150 MHz or 74 MHz depending on whether data from TGSS or VLSSr is available. The distribution of α_{high} (all spectral types) ranges from -0.5 to -2.2 with a median near -1.05. Many sources therefore have somewhat steeper spectra than the canonical index of -0.7 for optically thin synchrotron, and we discuss this result further in Section 3.7. The distribution of spectral index below the peak, α_{low}, (peaked sources only) is dominated by lower limits (formal median ~ 0.7), with measured values spanning the range $0 - 2$ with a median of 1.0. Finally, we find the q values span the range -0.1 to -1.0 with equivalent range in full-width half maximum (FWHM) of 4.0 to 0.5 dex.

3.6 Radio Spectral Shape *vs.* Radio Morphology

In Patil et al. (2020), we used our VLA images to classify the 10 GHz radio morphology of the sample, at resolutions of $\sim 0.1''$and $\sim 0.6''$for the A- and B-array observations, respectively. We now compare the trends of morphologies with their spectral shapes.

Figure 3.7 shows histograms of source morphology, with increasing compactness to the left, for the three radio spectral shape classes, PK, CV, and PL. The radio morphological classes as defined in Patil et al. (2020) are unresolved (UR), slightly/marginally resolved (SR), resolved (R), double (D), and multi-component/triple (M/T). There is a clear tendency for the sources with peaked spectra to be unresolved. Indeed, while 84% of the peaked sources are unresolved, only 25% of the power law sources are unresolved. We ran the Fisher exact test for a 4×4 contingency table and found this difference to be significant at 5.14σ (p-value $= 2.65\times10^{-7}$) level. There is some evidence that the sources classified as "curved" (CV) are also preferentially compact, as one would expect if they were also self-absorbed but with peaks at lower frequencies (below our lowest spectral window), suggesting a lower degree of compactness compared to peaked sources.

A turnover in the radio spectrum is associated with the presence of absorption mechanism caused by either thermal gas (free-free absorption; FFA) or the synchrotron emitting plasma (synchrotron self-absorption; SSA; Kellermann 1966). If the source is synchrotron self-absorbed, the turnover frequency is inversely proportional to the emitting region sizes; thus, the peaked spectrum implies very compact spatial scales of the emitting regions. Thus, our result in Figure 3.7 is consistent with the expectations of compact morphologies having a higher-frequency turnover. In Section 3.11 we make use of synchrotron theory to obtain additional constraints

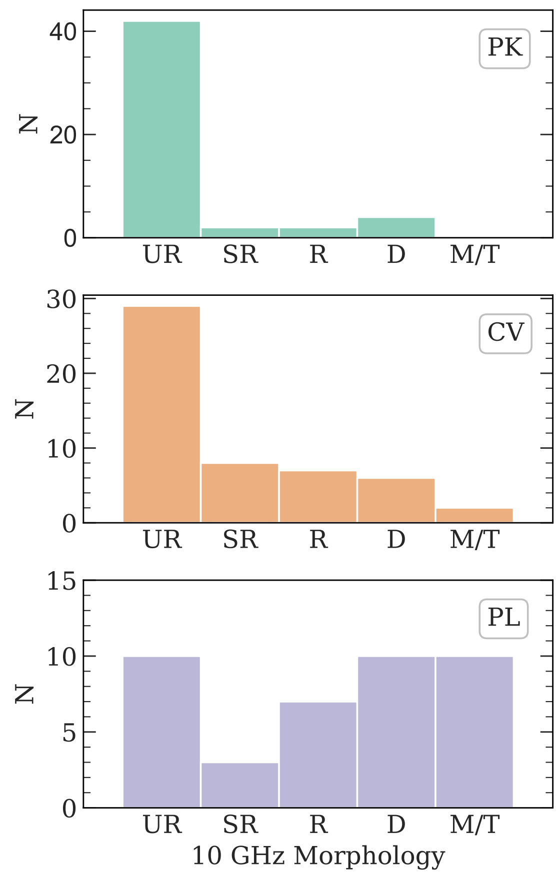

Figure 3.7: Histograms of source morphologies at 10 GHz for three spectral shape classes, PK, CV, and PL. The morphological categories goes from most compact (unresolved; UR) on the left to most extended (multi- or triple-component; M/T) on the right. We find a tendency for the peaked sources to have most compact and unresolved morphologies

on the source sizes for the peaked sources, finding angular extents that are indeed somewhat below the $\sim 0.2''$ resolution of the VLA A-array observations.

3.7 High-frequency Spectral Indices

3.7.1 Distributions

In Paper I, we presented in-band spectral indices, α_{IB}, measured from our X-band observations using the two WIDAR side-bands at $8-9$ and $11-12$ GHz. We found a rather broad distribution centered near $\alpha_{IB} \sim -1$. Here, we confirm the reliability of these in-band indices, and explore why they are somewhat steeper than the canonical value of $\alpha \sim -0.7$ for radio sources dominated by optically thin synchrotron.

Figure 3.8 compares α_{IB} with α_{3}^{10}, showing good agreement for most sources. Similar comparisons between α_{IB} and α_{high} and $\alpha_{1.4}^{10}$ confirm that our 10 GHz in-band spectral indices reproduce the indices derived from true multi-frequency data, which are perhaps more reliable. α_{high}, $\alpha_{1.4}^{3}$ and $\alpha_{1.4}^{10}$ have very similar distributions with median values of -1.06, -1.03 and -1.01, respectively. Thus, we find all measures of high frequency indices are consistent with each other and suggest more negative (steeper) values than the standard -0.7 value for most radio-loud AGN. Since many of the sources in our sample are also GPS or CSS sources, we now compare the spectral indices of our sample with those of well-known GPS and CSS sources. O'Dea (1998) found that for such sources, the median spectral index above the peak frequency was about -0.77, which is flatter than the median value for our sample. A non-parametric Kolmogorov$-$Sminrov test confirms that the distributions of α_{high} for our sample and the sample in Figure-2 of O'Dea (1998) are different with 5.8 σ significance.

In a wide range of astrophysical systems, optically thin synchrotron emission has a spectral index near $\alpha \sim -0.7$. A number of processes, however, can lead to deviations from this value, such as radiative and adiabatic losses from aging electron populations; inverse Compton scattering off a lower energy photon background; and various absorption processes which in turn may depend on the radio source environment. We now explore possible reasons for this spectral steepening.

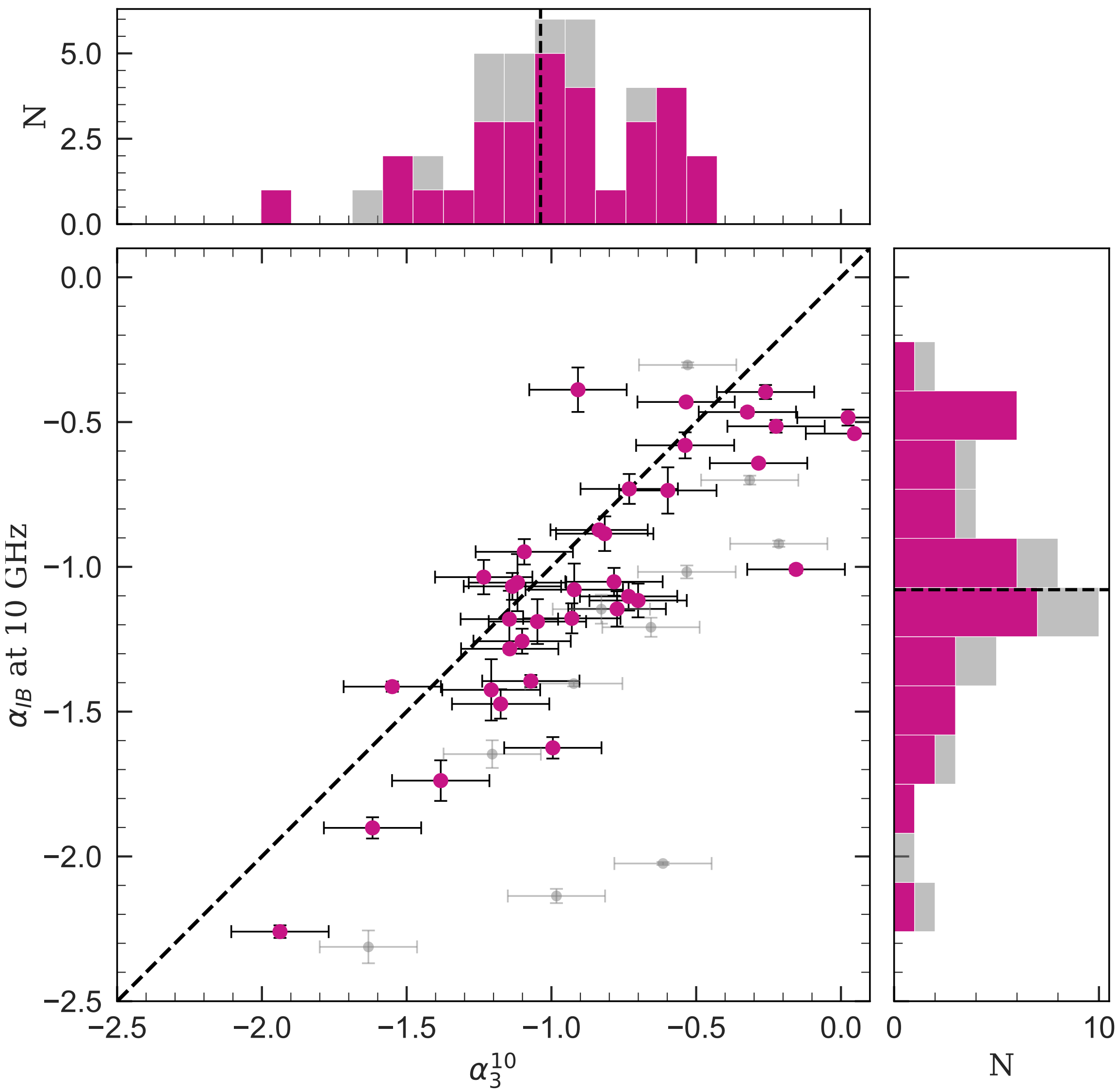

Figure 3.8: Comparison of 10 GHz in-band spectral index, α_{IB}, with α_{10}^{3}. We only include sources that are unresolved on all scales and have 10 GHz flux S/N > 70 to ensure a robust estimation of α_{IB} (Patil et al., 2020; Condon, 2015). The gray points are peaked spectra with $\nu_{peak} > 1$ GHz, so we expect lower values of α_{10}^{3} since the spectra will begin to flatten by 3 GHz. For the other sources, there is a good agreement between the two spectral indices, vindicating our in-band indices and confirming the steepness of high-frequency spectral slopes. The top and right panels show distributions of each index and its median value is shown by a dashed line.

3.7.2 Causes of Spectral Steepening

Resolution Effects

Before we consider a physical origin of spectral steepening, it's important to rule out the possibility that it has arisen due to systematic loss of extended flux in the high-frequency, higher-resolution observations. As discussed in Section 3.3.3, our final sample used in the spectral analysis excludes sources with any indication of extended emission, particularly in the lower-frequency survey images. Specifically, amongst the high-frequency observations, all the sources in our spectral analysis are essentially unresolved. While a definitive statement must await multi-frequency observations at matched resolution, we feel that our approach to defining our final sub-sample is not significantly compromised by resolution effects.

K-Correction and Spectral Aging

Although our spectral indices are measured near 10 GHz, at redshifts of $z \sim 1-3$ this corresponds to rest frame $20-40$ GHz. At such high frequencies the electron lifetimes are quite short, especially in compact sources of relatively high magnetic pressure ($\sim 10^2 - 10^5$ yr in our sources). As a result, one expects spectral aging with an associated spectral steepening (e.g., Pacholczyk, 1970; Krolik & Chen, 1991). Using alternate terminology, the observed spectral steepening due to redshift is an example of K-correction.

To test this possibility, we looked for a correlation between spectral index, α_{high} and redshift, z. A Kendall$-\tau$ test (Section 3.8.3) finds no correlation ($\tau = 0.08$ with $P_{null} = 0.42$).

For extended classical radio sources, such a correlation between α and z does indeed exist (e.g., Krolik & Chen, 1991; Ker et al., 2012; Morabito & Harwood, 2018) and has even been used to find high-redshift radio galaxies (e.g., Miley & De Breuck, 2008). However, the existence of such a correlation in compact radio sources is less strong (Ker et al., 2012), and in any case the $\alpha - z$ correlations are quite weak, so it is unclear whether the absence of a correlation in our sample can be taken as evidence against spectral aging. We therefore consider high-frequency radiative losses causing steepening at higher frequencies to be a possible contributing cause to the observed steep spectra near 10 GHz.

Inverse Compton Losses off the CMB

Another explanation for a correlation between α and z in extended radio sources is inverse Compton Scattering of the relativistic electrons by Cosmic Microwave Background (CMB) photons. As the CMB photon energy density is proportional to $(1+z)^4$, the losses can become significant at $z > 1$. Indeed, it is thought that this gives rise, at least in part, to the class of Ultra Steep Spectrum (USS) sources at high redshift (e.g., Miley & De Breuck, 2008).

As before, the absence of a correlation between α_{High} and z in our sample argues against the importance of this process, though perhaps by itself does not rule it out for the reasons given in the previous section. A stronger argument against its importance is that the magnetic field energy density, u_{mag}, in our radio sources is significantly greater than the energy density in the CMB, u_{CMB}. In this situation the cross-section for synchrotron self-absorption dominates and IC losses off the CMB are of secondary importance.

The ratio of these two energy densities, which sets the threshold above which inverse Compton scattering off the CMB is important, is:

$$R_{CMB} = \frac{u_{CMB}}{u_{mag}} \tag{3.5}$$

The energy density in the CMB radiation field is

$$u_{CMB} = aT_0^4(1+z)^4 = 4.22 \times 10^{-13}(1+z)^4 \text{erg cm}^{-3} \tag{3.6}$$

where $T_0 = 2.725$ K is the CMB temperature at the current epoch.

The energy density in the magnetic field is $u_{mag} = B_{min}^2/8\pi$ where B_{min} is magnetic field in Gauss calculated from synchrotron theory assuming minimum energy (approximately equipartiton) conditions, and is given by (Miley, 1980):

$$B_{min} \approx 0.0152 \left[\frac{a}{f_{rl}} \frac{(1+z)^{4-\alpha}}{\theta_{mas}^3} \frac{S_{mJy}}{\nu_{GHz}^{\alpha}} \frac{X_{0.5}(\alpha)}{r_{Mpc}} \right]^{2/7}, \tag{3.7}$$

where the radio source has flux S_{mJy} in mJy at frequency ν_{GHz} GHz with spectral form $S_\nu \propto \nu^\alpha$ and angular size θ_{mas} milliarcsec, z is the redshift of the source, and r_{Mpc} is the comoving distance in Mpc (assuming a flat geometry). For our sources, we choose $\alpha \simeq -1$, the filling factor for the relativistic plasma $f_{rl} = 1$, and the relative contribution of the ions to the energy $a = 2$. The function $X_{0.5}(\alpha)$ handles integration over the frequency range from $\nu_1 = 0.01$ GHz to $\nu_2 = 100$ GHz, and is defined as:

$$X_q(\alpha) = \frac{(\nu_2^{q+\alpha} - \nu_1^{q+\alpha})}{(q+\alpha)}, \tag{3.8}$$

where q is 0.5 in this case, and for $\alpha = -1$ we have $X_{0.5}(-1) \simeq 20$. Using these values, we find:

$$u_{mag} \approx 7.54 \times 10^{-5} \left(\frac{S_{mJy}\nu_{GHz}(1+z)^5}{\theta_{mas}^3 r_{Mpc}} \right)^{4/7} \quad \text{erg cm}^{-3} \tag{3.9}$$

Finally, given the limits of this kind of analysis, we make use of a good approximation for the comoving distance in Mpc:

$$r_{Mpc} \approx 4430 \frac{z}{(1+z/2)(1+0.5q_0 z/(1+z))} \tag{3.10}$$

where $q_0 = -0.55$ is the deceleration parameter, and 4430 Mpc is the Hubble radius associated with $H_0 = 67.7$ km s^{-1} Mpc^{-1}. Substituting these into Equation 3.5 we find:

$$R_{CMB} \approx 1.36 \times 10^{-6}\ z \left[\frac{\theta_{mas}^3}{S_{mJy}\nu_{GHz}}\right]^{4/7} \tag{3.11}$$

where the combined z dependence is well approximated by $2z$, and this yields the leading z in Equation 3.11.

For our sources, with typical $\theta_{mas} \sim 100$, $S_{mJy} \sim 10$, $\nu_{GHz} = 10$, and $z \sim 1$ we find $R_{CMB} \sim 10^{-4}$ and so inverse Compton scattering off the CMB is unlikely. This is perhaps not surprising, since our sources are compact with significantly higher magnetic fields than the high$-z$, well-extended USS sources, for which $R_{CMB} > 1$.

Inverse Compton Losses off the AGN Radiation

While the CMB radiation field is relatively weak in the vicinity of our radio sources, the radiation from the AGN itself may be sufficiently intense that inverse Compton scattering off this might cause spectral steepening. This seems promising, since a luminous MIR source is a key component of our selection criteria, yielding IR luminosities in the range $\log(L_{IR}/L_\odot) \sim 12.4{-}14$ (Lonsdale et al., 2015). Such effects have been proposed before in similar contexts (e.g., Blundell & Lacy, 1995; Blundell et al., 1999).

Following a similar approach to the previous section, we consider the ratio of the AGN bolometric photon energy density to the magnetic energy density, averaged over the volume of the radio source:

$$R_{bol} = \frac{u_{bol}}{u_{mag}} \tag{3.12}$$

For a spherical region of angular diameter θ_c radians with bolometric flux f_{bol} erg s^{-1} cm^{-2} the energy density averaged over the sphere is:

$$u_{bol} = 12\,\frac{f_{bol}(1+z)^4}{\theta_c^2\ c}\ \ \text{erg cm}^{-3} \tag{3.13}$$

where the factor $(1+z)^4$ is the standard relativistic dimming of surface brightness. We choose to specify the bolometric flux using the MIR flux and a bolometric correction factor, B_c:

$$f_{bol} = \nu_{34} f_{\nu 34} \times B_c\ \ \text{erg s}^{-1}\text{cm}^{-2} \tag{3.14}$$

where "34" here refers to the mean frequency and flux of the WISE W3 and W4 bands. Converting θ to milliarcsec, we find:

$$u_{bol} = 1.5 \times 10^{-6}\frac{(W3+W4)_{mJy}(1+z)^4 B_c}{\theta_{mas}^2}\ \ \text{erg cm}^{-3} \tag{3.15}$$

Combining Equations 3.9 and 3.15 we find a relatively simple expression for R_{bol}:

$$R_{bol} \approx 4.74\frac{z\ (W3+W4)_{mJy}\ B_c}{(\theta_{mas}^{1/2}\ S_{\nu,mJy}\ \nu_{GHz})^{4/7}} \tag{3.16}$$

where once again the combined z dependence is well approximated by $2z$, and this yields the leading z in the Equation for R_{bol}. An important quality of this relation is the muted dependence on the angular size of the source. Smaller sources have higher photon flux, but for a given radio flux a smaller source has higher magnetic field.

The last parameter of interest is the bolometric correction factor, B_c. We esti-

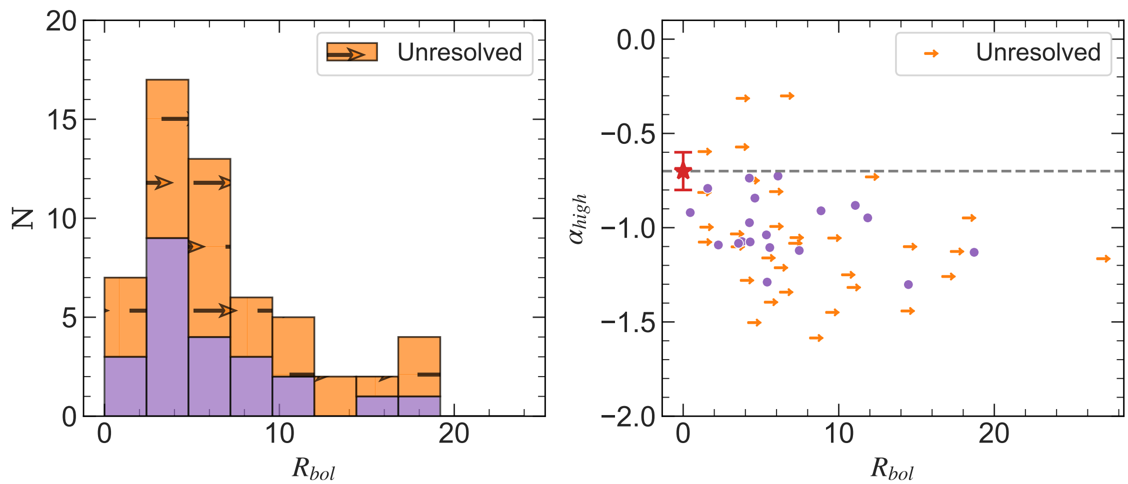

Figure 3.9: **Left(a)** Distribution of R_{bol} for our sub-sample of 110 sources. The unresolved sources yield lower limits and are shown in orange. Sources with resolved 10 GHz morphologies are shown in purple. **Right (b)** α_{high} *vs.* R_{bol}. The large symbol shows the location of classical sources with spectral index, $\alpha_{high} \sim -0.7$.

mate this by inspecting the Optical−IR SEDs for our sample presented in Lonsdale et al. (2015). These SEDs were fit using the following three components: starlight (constrained by the optical flux); AGN/torus emission peaking in the MIR; and a colder black body from larger scale starburst or AGN heated dust, (constrained by 345 GHz ALMA fluxes). For our purposes, we only include radiation that is cospatial with the radio source, so we only consider the compact AGN/torus emission. In a plot of $\log \nu$ *vs* $\log \nu f_\nu$ this component peaks in the MIR and falls either side. An upper limit to B_c assumes a flat Spectral Energy Distribution (SED) spanning 2 dex in $\log \nu$, giving $B_c = \ln 100 = 4.6$. A lower limit comes from a typical AGN/torus fit given by Equation 2 in Lonsdale et al. (2015), for which $B_c \simeq 1.7$. We adopt $B_c \simeq 2$ recognizing (a) there is likely some emission from a compact nuclear starburst and (b) the approximations don't warrant further refinement.

Figure 3.9a shows the distribution of R_{bol} for our sample, with lower limits shown for unresolved sources. Almost all the values are greater than 1.0, with most falling in the range $2-10$, with some as high as 20. Figure 3.9b plots α_{high} against R_{bol}, with the canonical value of $\alpha_{high} \simeq -0.7$ for more extended classical radio sources shown as a red star symbol. The data suggest a weak tendency (a significance of 2.4σ for a Kendall$-\tau$ test) for sources with larger R_{bol} to have steeper α_{high} though a robust analysis is undermined by the large number of lower limits.

In summary, it does seem that inverse Compton scattering off a near-nuclear AGN radiation field provides a plausible explanation of the steep high-frequency spectra. In retrospect, this is perhaps not too surprising: for this process to be relevant, one needs high luminosity AGN with compact radio sources. Our sample provides both these – the WISE-NVSS sample are luminous AGN, and the radio sources are physically small (but not as small as the classical flat spectrum cores).

Dense Ambient Medium

The environment in which a radio source develops may also affect its spectral index. For example, the tendency for radio sources at higher redshift (e.g. USS) to have steeper spectral indices has been explained as arising from their development in a much denser ambient medium (Athreya & Kapahi, 1998; Klamer et al., 2006; Bornancini et al., 2010). Since one of the selection criteria for our sample is a high MIR/optical ratio, the near-nuclear regions are likely to be highly obscured (Lonsdale et al., 2015). Thus, the radio jets in are likely to be interacting with a denser near-nuclear medium, and for this reason exhibit steeper spectra.

3.8 The MIR$-$Radio Connection

Since our sample is defined by a joint selection by MIR emission (WISE) and radio emission (NVSS), it is natural to ask whether there is any physical connection between the MIR and radio emitting regions. Such a physical connection might generate a correlation between measured MIR and radio properties. First we analyze the MIR properties of our sample and compare them with closely related samples of compact radio AGN, and then we look for direct correlations between the MIR and radio properties.

3.8.1 WISE Colors of Compact Radio AGN

Figure 3.10, shows WISE colors (W1-W2 *vs* W2-W3) for our sample (green) and a sample of FR I and FR II radio sources compiled by An & Baan (2012) (blue) and GPS, CSS and HFP sources from Jeyakumar (2016) (orange). Very few FRI/II and GPS/CSS sources have WISE colors as red as our sample. The FRI/II sources have colors that are similar to optically selected QSOs (Wright et al., 2010) with some lying within the much "bluer" region occupied by elliptical galaxies (e.g., Mingo et al., 2019). Although most GPS/CSS have similar colors to FRI/IIs, they extend to much "bluer" colors than AGNs. A similar result is seen by Chhetri et al. (2020), who found that compact radio AGN have bluer WISE colors than AGN selected by optical/IR techniques. Thus, although our sample was pre-selected to have very red WISE colors, we have confirmed that objects with similarly compact radio sources do not share these MIR colors. This is consistent with our findings in Paper I that our sources are rare and likely caught in a short-lived evolutionary phase when dense gas has arrived near the nucleus during a merger event the AGN has only recently turned on.

We also compare WISE colors with so-called Infrared Faint Radio Sources (IFRS; e.g., Norris et al. 2013; Middelberg et al. 2008; Huynh et al. 2010; Herzog et al. 2014; Collier et al. 2014; Maini et al. 2016; Singh et al. 2014). IFRS are selected to have WISE 3.6 μm flux $< 30\,\mu$Jy and an excess of radio emission with a flux ratio of $S_{20\mathrm{cm}}/S_{3.6\mu\mathrm{m}} > 500$ (Zinn et al., 2011) and many are at $z > 2$ (Orenstein et al., 2019). Radio observations have revealed many IFRS are compact and have steep radio spectra (Middelberg et al., 2011; Collier et al., 2014; Herzog et al., 2016). A study by (Herzog et al., 2016) found that at least 18% of IFRS are GPS and CSS sources consistent with being young radio AGN. In Figure 3.10, we plot IFRS detected in all three WISE bands from the Collier et al. (2014) sample (pink). The WISE colors of IFRS are similar to that of obscured AGN and quasars with some overlap with our sample. Since there is no constraint on the WISE colors, IFRS show a broader range of colors. Given the similarities in MIR and radio properties (compact and peaked-spectrum), we believe that the nature of IFRS and some of our sample sources could be similar. Detailed studies focusing on the host and AGN properties of our sample as well as IFRS could help understand the link between them.

3.8.2 MIR and Radio Parameters

Table 3.3 lists parameters that are relatively easily measured and that characterize the MIR and radio emission. They include, for the radio emission and radio source, measures of linear extent, luminosity, pressure, shape of radio spectra and, from Paper I, model dependent estimates for the dynamical age, expansion velocity and ambient density. For the MIR parameters, we consider the 6μm luminosity, the MIR colors, and an MIR energy density estimated using the radio source size and the 6μm luminosity. For completeness, we also include the 870μm luminosity from Lonsdale et al. (2015), when available.

3.8.3 Correlation Analysis

To test for the presence of a significant correlation between MIR and radio parameters, we use the censored Kendall$-\tau$ correlation test (Isobe et al., 1986). We performed a Monte Carlo simulation to sample each parameters assuming a Gaussian distribution with a given 1σ uncertainty. We model upper limits as a truncated

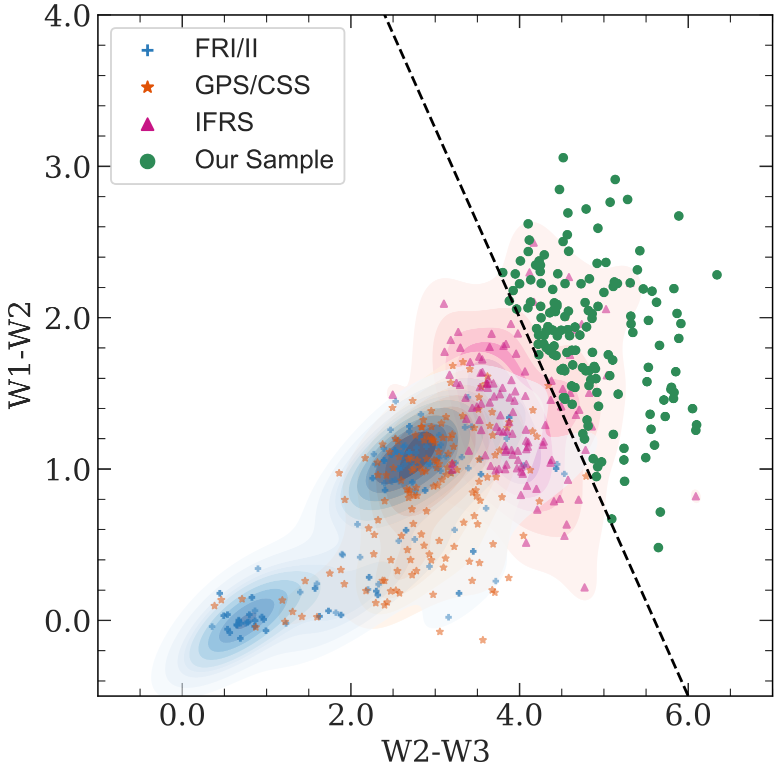

Figure 3.10: WISE $3.6 - 4.5\,\mu$m and $12 - 22\,\mu$m color diagram. The green dots are our sources, blue dots are classical FRI and FRII sources taken from the references given in An & Baan (2012, Figure 2), orange dots are well-known GPS, CSS, and HFP sources from Jeyakumar (2016). We also show a density plot in the background for the FRI/II as well as compact GPS/CSS sources. The magenta triangles are IFRS taken from Collier et al. (2014). Most of FRI/II and compact radio sources are bluer than our sample, although the IFRS sources show some overlap with our sources.

Gaussian with a central value and 1σ standard deviation taken to be the upper limit itself.

We perform 10,000 iterations of the sample draw and adopt the median values for statistical outputs. The correlation coefficient, τ, has value 1, 0 and -1 for perfect direct-, none-, and perfect anti-correlation, respectively. We also evaluate a $p-$value to quantify the significance of the correlation. Table 3.6 provides a list of all the correlations for which $p < 0.02$, for the full sample, and for just those with peaked

Table 3.3: List of Parameters used in Correlation Analysis; LLS: Largest Linear Size in kpc from 10 GHz radio morphology; $L_{1.4\,GHz}$: 1.4 GHz luminosity; P_{lobe}: Radio source pressures from Patil et al. (2020); t_{dyn}, n_a: Dynamical age and ambient density calculated using a self-similar lobe expansion model (Patil et al., 2020). See Section 3.5.4 for the explanation of the radio spectral paramaters. $L_{6\,\mu m}$: 6 μm luminosity; W1−W2, W2−W3: WISE colors using WISE 3.4 μm (W1), 4.6 μm (W2), and 12 μm (W3) bands; u_{IR}: IR energy density calculated using Equation 3.13, but without applying the bolometric correction factor; $S_{870\mu m}$: ALMA Band 7 flux presented in Lonsdale et al. (2015).

Selection Criteria	Parameters
10 GHz Continuum	LLS, $L_{1.4\,GHz}$, P_{lobe}, t_{dyn}, n_a
Radio Spectra	α_{high}, α_{low}, q, ν_{peak}, $\nu_{peak,rf}$
MIR	$L_{6\mu m}$, W1-W2, W2-W3, u_{IR}
FIR	$S_{870\mu m}$

spectra.

Perhaps not surprisingly, most MIR-radio parameter pairs are not significantly correlated, while some are correlated for uninteresting reasons. For example, MIR and radio luminosity correlate because of a common dependence on redshift, and MIR energy density correlates with radio source size because the size is used to define the MIR energy density. Similarly, the dynamical model from Paper I leads to a number of physically plausible correlations, such as radio source pressure and ambient gas density; source size and dynamical age; source luminosity and dynamical age. However, we choose not to consider these apparent correlations to be meaningful because the model parameters such as dynamical age, t_{age} and ambient gas density, n_a, are themselves defined by functions of radio luminosity, source size, and lobe pressure, and so the two variables are co-dependent on another measured parameter and their apparent correlation cannot be taken at face value.

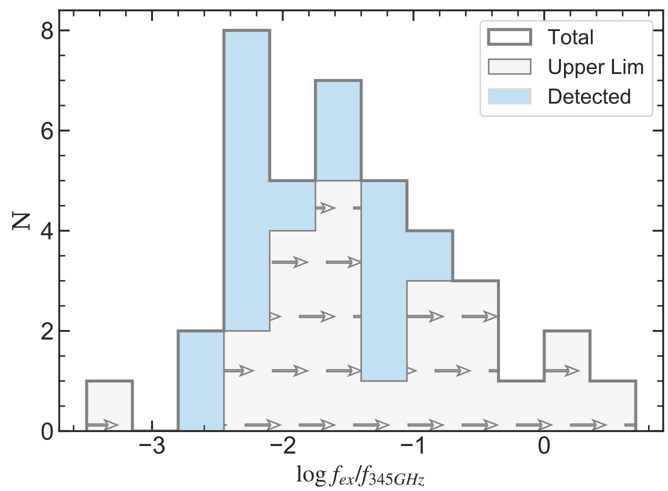

Figure 3.11: Ratio of extrapolated synchrotron flux to the observed ALMA flux at 870 μm. The blue histogram represent sources detected in our preliminary ALMA imaging. The snow histogram with arrows indicates lower limits on the ratio of sources with non-detections at 870 μm. We use 3σ as the upper limit on the ALMA flux to estimate the ratio.

3.9 Origin of the ALMA 870 μm Emission

After defining the primary WISE-NVSS sample, Lonsdale et al. (2015) used ALMA to perform a 345 GHz (0.87 mm) snapshot survey of a southern sub-sample of 49 sources, and detected 26 above 3σ. Fitting SEDs to the WISE MIR fluxes and the ALMA 345 GHz fluxes suggested both were of thermal origin, with a hotter AGN-heated component and a cooler component heated either by the AGN or star formation. Now that we have radio spectra extending to 10 GHz we are in a position to check whether the ALMA submillimeter emission is indeed thermal, or whether it might arise from a non-thermal extension of the radio synchrotron emission, which has been raised as a possibility (e.g., Falkendal et al., 2019).

To assess the synchrotron contribution to the ALMA emission, we use our radio spectral fits to extrapolate to 345 GHz and ask how that extrapolation compares to the measured 345 GHz flux, using the ratio f_{ex}/f_{345GHz}. A conservative approach is to adopt a power law rather than a parabolic fit which might capture a spectral steepening to high frequencies. For the power law index, we use α_{high} if available, but if not we take α_{3}^{10} and failing that $\alpha_{1.4}^{10}$.

Figure 3.11 shows the distribution of $\log(f_{ex}/f_{345GHz})$ with arrows showing lower limits for the 22 ALMA non-detections. The objects are color-coded by radio spectral shape, since a power law extrapolation of a "Peaked" or "Curved" spectrum may overestimate f_{ex}. Thus, our flux ratios are conservative in the sense that the true synchrotron flux at 345 GHz is either close to f_{ex} or lower.

Clearly, all the detected sources have $f_{ex}/f_{345HGz} < 1$ confirming that non-thermal synchrotron from the radio source does *not* contribute significantly to the 345 GHz ALMA fluxes, which are likely the long wavelength extension of the thermal component. Unfortunately, a stronger conclusion isn't possible because of the large number of lower limits, with at least four sources with $f_{ex}/f_{345HGz} \gtrsim 1$ (J0354−33, J0519−08, J0823−06, and J1308−34).

3.10 The Linear Size *vs.* Turnover Frequency

Figure 3.12 shows the well-known linear size (LS) *vs.* rest-frame turnover frequency ($\nu_{peak,rf}$) relation for various samples of CSS, GPS, and HFP sources compiled by Jeyakumar (2016), together with a fit to GPS sources taken from O'Dea & Baum (1997) (Falcke et al. (2004) and Orienti & Dallacasa (2014) derived similar relationships for their sample of CSS/GPS sources). Also shown on the upper diagrams are 44 peaked and curved sources with redshifts, with size limits indicated for unresolved sources, and peak frequency limits for the curved sources taken to be the lowest measured frequency. The remaining 46 sources with no redshift are shown on the lower diagram as tracks that span $0.5 < z < 3$ which is the full range seen in our sample

(Section 2.1 in Patil et al. 2020).

Most of our peaked spectrum sources (purple circles) are within the scatter seen for the HFP, GPS, and CSS sources (gray points). Although many peaked sources lie above the relation, many have upper limits on linear size (they are unresolved) and so are in fact consistent with the underlying relation. Four extreme outliers fall at least 3.6σ off the relation given by O'Dea (1998), where $1\sigma = 0.22$. The curved spectrum sources (blue stars) have a smaller scatter than the peaked spectrum sources, and most lie below the relation, of which a few upper limits on size at least these could be lying significantly off the relation. It is possible that the overall uncertainties on the peaked frequency and the linear size can account for at least some of these outliers. It is also the case that the extreme outliers also have lower 1.4 GHz luminosity than those closer to the relation. Similar discrepancies have been seen in recent studies (e.g., Coppejans et al., 2016; Collier et al., 2018; Keim et al., 2019). In a high-resolution study of low-luminosity ($L_{1.4\mathrm{GHz}} < 10^{27}$ WHz^{-1}) GPS/CSS sources by Collier et al. (2018), two of the five sources they studied fell significantly away from the relation. As the previous relations are derived using brighter samples of peaked sources, low-luminosity peaked sources may now follow this interesting relation.

The empirical LS $vs.$ $\nu_{peak,rf}$ relation is useful to constrain the turnover mechanism and the radio source evolution (O'Dea & Baum, 1997). SSA provides a natural explanation for the dependence of the turnover frequency on the emitting component sizes, which ultimately scales with the linear extent of the radio source (e.g., O'Dea & Baum, 1997; Jeyakumar, 2016). We further discuss the implications of the SSA on constraining the emitting region sizes in Section 3.11.2. Alternatively, the analytical model of Bicknell et al. (1997) and hydrodynamical simulations of Bicknell et al. (2018) are also able to reproduce the observed $\nu_{peak} - LS$ correlation assuming the FFA model. However, these models require a dense, inhomogeneous medium of ionized

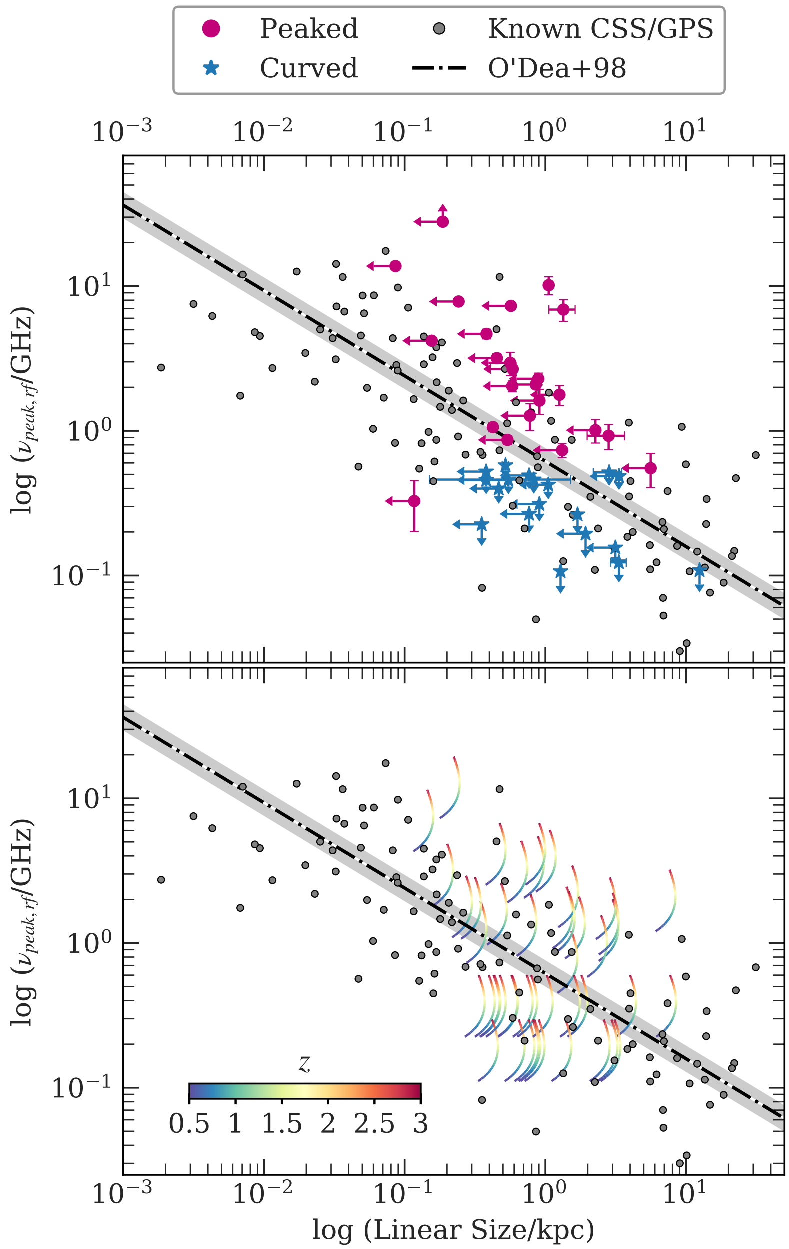

Figure 3.12: The liner size *vs.* rest-frame turnover frequency relation. Purple circles and blue stars in the top panel are peaked (pink) and curved (blue) sources from our sample with known z. Small gray circles in both panels are known GPS, CSS, and HFP sources compiled by Jeyakumar (2016). The dashed-dotted line is the best-fit relation from O'Dea (1998), with the grey band indicating the $1\,\sigma$ errors on the best-fit. The lower panel includes sources with no redshift, which are shown as tracks for $0.5 < z < 3$.

gas external to the source, which may not be applicable for the general population of young radio sources. Furthermore, GPS/CSS sources with independent evidence for FFA also seem to lie far from the $\nu_{peak,rf} - LS$ relation (e.g., Keim et al., 2019). On the other hand, since our sources are likely to have significant dense gas in the nuclear regions, some may indeed be subject to FFA and so fall away from the relation for that reason. Given the limits of our angular resolution and spectral analysis, further improvement in Figure 3.12 requires more detailed spectral shape analysis, particularly at frequencies below ν_{peak} and higher resolution VLBA imaging, which will be addressed in future studies.

Although the specialized FFA models of Bicknell et al. (1997) and Bicknell et al. (2018) can explain the $\nu_{peak} - LS$ relation, SSA is generally accepted as the primary cause of this correlation (Orienti, 2016). Whatever may be the underlying cause, we find a good overall agreement with the O'Dea & Baum (1997) relationship for most of our sources.

3.11 The Peaked Sources

One of the important results of this study is that a significant fraction of our sources show peaked radio spectra (35% PK) or curved spectra (30% CV), suggesting absorption of low-frequency emission. Furthermore, as discussed in Section 3.6, a high fraction of these are spatially unresolved in our VLA imaging (83% PK; 58% CV), suggesting compact sources. In this section, we discuss the nature of the absorption and try to use it to constrain the properties of the emitting region.

3.11.1 SSA or FFA?

As we discussed in the previous section, the origin of the turnover mechanism is still debated in the literature (e.g., Tingay & de Kool, 2003; Callingham et al., 2015).

The SSA occurs when the relativistic electrons absorb their own synchrotron emission (Slish, 1963; Kellermann, 1966). The simplest model considers a homogeneous population of relativistic electrons and yields an inverted power law with spectral index, $\alpha_{thick} = +2.5$. Typically, shallower α_{thick} values are observed, likely due to contribution from multiple electron populations (e.g., O'Dea, 1998; Orienti & Dallacasa, 2014; Callingham et al., 2017). SSA has been the favored interpretation of peaked sources in many studies (e.g., Snellen et al., 2000; de Vries et al., 2009; Jeyakumar, 2016; Orienti, 2016). Furthermore, it can explain the global properties of the GPS/CSS population, e.g., the observed linear size *vs.* turnover relation (O'Dea & Baum, 1997) and provides magnetic field estimates consistent with the equipartition fields estimated from the optically thin part of the spectrum (Orienti & Dallacasa, 2008a). The consensus, then, is that SSA will always be present to some degree in radio-emitting plasma (Fanti, 2009; Orienti, 2016; O'Dea & Saikia, 2020).

A competing hypothesis is FFA by thermal electrons, in which the absorption is caused by a screen of either homogeneous or inhomogeneous thermal gas, either interior or exterior, to the radio-emitting plasma. Certainly, the fact that our sources are obscured in the optical and exhibit strong red MIR colors suggests there is abundant dense gas in the nuclear regions that might contribute to FFA. Analytic models of several possible gas geometries can be found in Bicknell et al. (1997); Tingay & de Kool (2003), and Callingham et al. (2015). FFA can generate a variety of optically thick spectra, including an exponential cut-off at lower frequencies yielding significantly steeper indices than the theoretical SSA limit of +2.5 (e.g., Callingham et al., 2017; Mhaskey et al., 2019). FFA is the favored mechanism in some individual sources (e.g., Marr et al., 2014; Tingay et al., 2015) and is expected to occur in compact radio sources residing in a dense ambient medium. One way to distinguish between the two models is to accurately model high-quality data in the optically thick part of the spectra (Callingham et al., 2015). Until recently, such observations have been limited, but improved low-frequency telescopes show promise for more detailed modelling of peaked radio sources.

As shown in the third panel of Figure 3.6, almost all of our peaked sources are less steep than the SSA limit of +2.5 ($\alpha_{low} < 2$) and are therefore at least consistent with SSA. Four sources have $\alpha_{low} > 2.5$ and might therefore be candidates for FFA. Unfortunately, our data only includes one or two observations below the turnover frequency, significantly reducing our ability to determine the cause of the turnover. In the absence of further data, we refrain from favoring FFA or SSA, but instead proceed on the assumption that our sources belong in the larger cohort of peaked sources for which SSA is thought to be dominant.

3.11.2 Deriving Emitting Region Properties

Under the assumption that the peaked sources are synchrotron self-absorbed, we can use standard synchrotron theory to derive important properties of the emitting region. For a source at redshift z with angular size θ_{mas} mas, whose self-absorbed spectrum peaks at observed frequency ν_{peak} GHz with flux of S_{peak} mJy, the magnetic field is given by (Kellermann & Pauliny-Toth, 1981):

$$B_{SSA} = 23\,\frac{\theta_{mas}^4}{S_{peak}^2}\frac{\nu_{peak}^5}{1+z}\ \text{Gauss} \tag{3.17}$$

To illustrate, Figure 3.13 shows the steeply rising dot-dashed line of θ_{mas} and B_{SSA} values that satisfy Equation 3.17 for J2204+20, using values of S_{peak} and ν_{peak} taken from Table 3.5. Uncertainties in the measurements, and a range of redshift $0.8 < z < 3$ (since this source has unknown redshift) yield the band that surrounds the line.

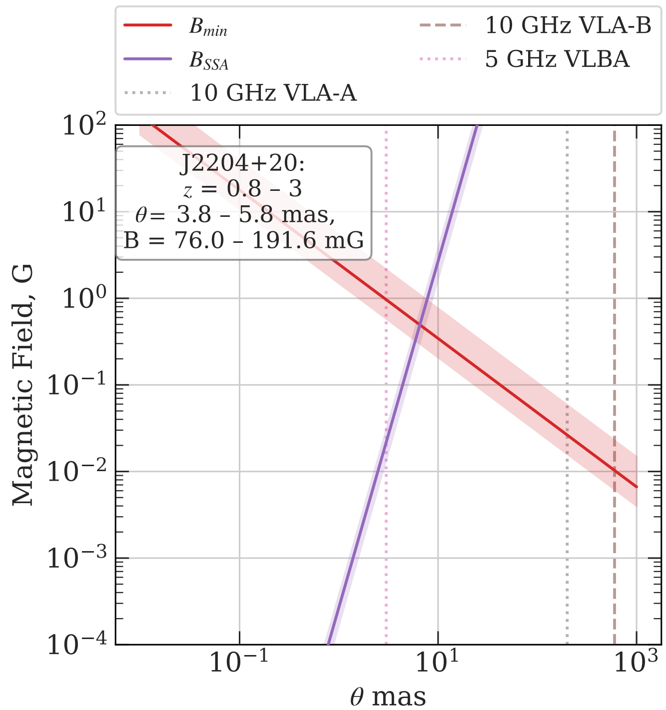

Figure 3.13: An example of applying the SSA (purple) and B_{min} (red) relations to the source J2204+20, yielding independent solutions for emitting region sizes and magnetic fields. The band widths reflect uncertainties in the spectral measurements and the redshift range of $0.8 < z < 3$ (J2204+20 has no measured redshift). The intersection suggests a region sizes of $\theta_{mas} \sim 3.8 - 5.8$ mas and $B \sim 76 - 191.6$ mG. The gray dotted and brown dashed lines at $\theta_{mas} \sim 200$ & 600 shows the limiting resolution of our VLA 10 GHz A- and B-array observations. The pink dotted line at 3 mas shows the limiting resolution of 5 GHz VLBA observationss.

However, this same emitting region is also generating the power-law emission on the optically thin high-frequency side of the peak, which yields independent constraints on θ_{mas} and B_{min} from the minimum energy (approximately equipartition) condition, as given by Equation 3.7. These constraints are also shown on Figure 3.13 as the more gently decreasing dashed line, with its band for uncertainties. Also shown are two vertical dashed lines at $\theta_{mas} = 200$ & 600 which indicate the resolution of our 10 GHz VLA A- and B-array observations. Recall from Section 3.6 that most peaked sources, including this one, are unresolved (UR), suggesting their sources lie to the left of these vertical lines.

Since the SSA and B_{min} analyses apply to the *same* emitting region, then they should yield the same magnetic field and source size. Graphically, this is where the two lines cross on Figure 3.13. Algebraically, we simply set:

$$B_{SSA} = B_{min} \tag{3.18}$$

and use Equations 3.7 and 3.17 to find the source size:

$$\theta_{mas} = 0.38\ (1.2 + z/4)\ S_{peak}^{0.41}\ \nu_{peak}^{-1.03} (S_{mJy} \nu_{GHz})^{1/17}\ \text{mas} \tag{3.19}$$

where the total redshift dependence is well approximated by (1.2 + z/4). Once θ_{mas} is found, it is easy to find the magnetic field using Equation 3.17.

There is some evidence to support the assumption that $B_{SSA} \approx B_{min}$. Orienti & Dallacasa (2008a) measure angular source sizes and spectral peaks in a sample of HFP and GPS sources and are able to separately evaluate B_{SSA} and B_{min}, finding broad agreement. Recognizing that the agreement may be only approximate in individual cases, we nevertheless proceed to use the condition to estimate source sizes and magnetic field strengths.

Table 3.7 gives the angular source sizes and region magnetic fields for the 46 sources with peaked spectra. For the 24 sources with redshifts, Table 3.7 also gives the source size in pc, the region pressure and total energy, as well as radiative cooling timescale given by the total energy divided by the radio luminosity. The table also includes synchrotron electron lifetimes at 10 GHz.

Figure 3.14 shows the distribution of component sizes and magnetic fields esti-

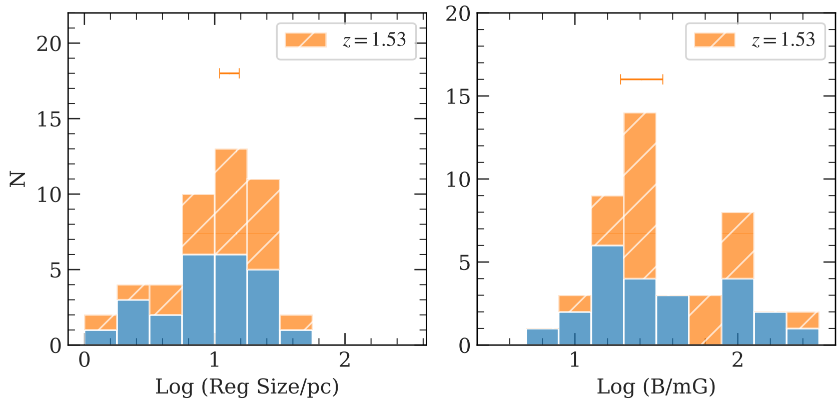

Figure 3.14: Distributions of physical sizes of emitting regions (left) and magnetic fields (right), derived assuming $B_{SSA} = B_{min}$. Sources with redshifts are in blue, while sources without are in hatched orange, and assume the median redshift $z = 1.53$ (the redshift dependence is weak, with the error bar showing values for $0.8 < z < 3$).

mated using the method described above. We also plot sources without redshifts (hatched) using the median redshift of our sample, $z_{med} = 1.53$ (the redshift dependence is weak, with values shifting less than one bin width across the redshift range $0.8 < z < 3$). Overall, the distributions of sources with and without redshift are quite similar. Typical region sizes are $2 - 52$ pc, magnetic fields $6 - 400$ mG, and pressures $10^{-6} - 10^{-3}$ dyne cm^{-2}. These are comparable to the region sizes and pressures found for the luminous HFP sources, estimated using long-baseline observations (e.g., Orienti & Dallacasa, 2008a, 2014). Thus, although only indicative, our sample's physical properties derived here are similar to those seen in young radio sources. The magnetic field estimates using equipartition and peak parameters show a good agreement for most compact radio sources (e.g., Readhead, 1994; Orienti & Dallacasa, 2008b). Nevertheless, a few exceptions have also been detected, in which sources depart from the equipartition, and their spectra favor FFA. (Orienti & Dallacasa, 2008a). Thus, consistency seen with observations under the SSA assumption supports our analysis.

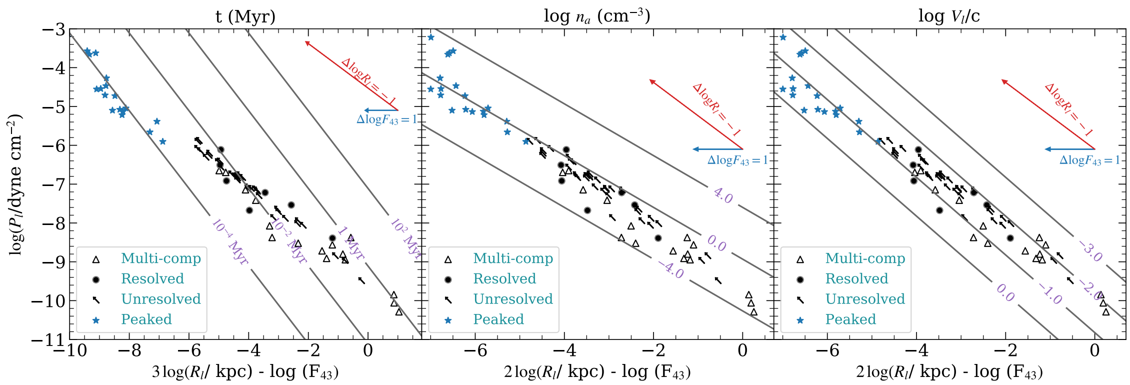

Figure 3.15: Updating adiabatic lobe expansion model from Section 2.7.2 for peaked sources (Equations 2.15–2.17). These panels isolate source age (t_{Myr}), ambient particle density (n_a), and lobe expansion speed (V_l/c). The observed parameters are R_l, p_l and F_{43} as described in the text. The blue stars are peaked and unresolved sources with known redshifts. Their location in the plot is estimated using new estimates of regions sizes and lobe pressures (Section 3.11.2). The arrows, triangles, and filled circles are same as from Figure 2.12. Open triangles are individual resolved lobe components for double or triple sources; filled circles are partially resolved sources; arrows are unresolved sources. Red and blue vectors illustrate the effect of a decrease in source size by one dex and increase in jet power by one dex.

3.11.3 Revisiting Lobe Expansion Model

In Section 2.7.2, we presented a simple "bubble model", which provides an analytical solution for a radio lobe expanding into an ambient medium. We now use improved constraints on the lobe pressures and sizes for the peaked and unresolved sources to update the lobe expansion model. Figure 3.15 shows the updated values along with older constraints from Paper I. The arrows show unresolved sources with the linear extent taken as the limit to lobe sizes. The blue stars represent peaked sources among the arrows with new limits on linear sizes and pressures are shown as blue stars. The updated model yields younger ages ($28 - 1000$ years with a median of 76 years), relatively high ISM densities ($0.02 - 10^{3.1}$ cm^{-3} with a median of 0.9 cm^{-3}, and modest to high expansion velocities ($0.005c - 0.5c$ with a median of $0.13c$). This is consistent with the expectations that the peaked sources are likely to represent the most compact and young sources expanding into a dense ISM.

3.11.4 Timescales

Since one of the primary themes of this work is to identify young radio sources, it is appropriate to consider some direct estimates of relevant timescales. We will discuss three somewhat different timescales. First, in Paper I we presented a simple dynamical model that took a jet power and estimated the dynamical time, t_{dyn}, for it to inflate a lobe to a given size and pressure. The model assumed basic energy and momentum conservation and assumed only adiabatic losses as the lobe did work expanding into an ambient medium. The jet power was estimated from the radio source power, and the value of t_{dyn} gave the time to arrive at the observed lobe size and pressure. For our resolved and slightly resolved sources we found $5 < \log t_{dyn} < 7$ years. Our unresolved sources gave only upper limits, but we can now include them if we use the source sizes and pressures derived above. Perhaps not surprisingly, we find shorter timescales, $1 < \log t_{dyn} < 3$ years. When one recalls that some of the source sizes we derive are only a few parsecs, these short timescales are not unreasonable. Even the shortest derived timescales are credible: although our sources were clearly active 25 years ago when the NVSS and FIRST surveys were undertaken, the recent VLASS survey has identified a similar class of compact peaked spectrum sources that have "turned on" since the FIRST survey, suggesting ages of only 10-20 years (Nyland et al., 2020). If we trust our rather simple model of source evolution, then our sources span a range of a few decades for the most compact up to a few Myr for the more extended sources that are resolved in our VLA images.

Our second timescale is a radiative cooling timescale:

$$t_{rad} = E_{lobe}/L_{rad} \tag{3.20}$$

where E_{lobe} is the total energy stored in the lobes and L_{rad} is the total radio luminosity. This timescale is simply the time to drain the lobe of its energy via radio emission, assuming no other energy gains or losses. Evaluating E_{lobe} and L_{rad} for the unresolved peaked sources gives cooling times of $3.1 < \log t_{rad} < 4.8$ years. Overall, then, this radiative cooling timescales, t_{rad}, is significantly longer than the time to create the lobes, t_{dyn}. This is important because it justifies excluding radiative losses in the simple dynamical model of lobe inflation that only considered adiabatic losses. In practice, of course, as long as the jet remains active the lobes will continue to inflate, and the radiative losses won't compete with the energy input from the jet.

Our third timescale, t_{syn}, gives the cooling time of the relativistic electrons that generate synchrotron emission near ν_{GHz}:

$$t_{syn} = 5.0 \times 10^4 \, P_{-8}^{-3/4} \, \nu_{GHz}^{-1/2} \, \mathrm{yr} \tag{3.21}$$

where P_{-8} is the equipartition pressure in units of 10^{-8} dyne cm^{-2}. For our unresolved peaked sources, the synchrotron lifetimes at 10 GHz are $1.5 < \log t_{syn} < 3.9$ years. While this range overlaps the range in t_{dyn}, object by object we find $t_{syn} > t_{dyn}$ typically by factors $\sim 20 - 50$. We conclude that the electron lifetimes at 10 GHz are significantly longer than the lobe inflation dynamical times, t_{dyn}, suggesting that spectral steepening at high-frequencies is not occurring for these compact sources. As discussed in Section 3.7, the fact that the high-frequency spectra are steeper than normal, $\alpha_{high} \approx -1$, can be explained by inverse Compton scattering off the intense AGN radiation field.

3.11.5 VLBA Detection of Peaked Sources

Since the peaked sources are mostly unresolved in our VLA data, and since the above analysis indicates compact sources, it is important to follow up with high-

Table 3.4: The VLBA Detection Rate of Peaked *vs*. Non-Peaked Sources

Sample	Detections	Non-detections
Non-Peaked	26 (58%)	19 (42%)
Peaked	25 (89%)	3 (11%)

resolution long baseline imaging. An observing program that partly achieves this was the VLBA snapshot survey of 90 sources (program BL-188). While the full analysis of this dataset remains to be completed (Lonsdale et al. in prep), here we make preliminary use of the source detection rates.

The source selection for the VLBA snapshot survey was primarily based on positional and brightness constraints. We have successfully imaged 73 out of 88 sources, while the remaining sources were rejected due to poor quality data or imaging issues. The angular resolution is in the range $1-3$ milliarcsec, and the median 1σ rms noise level is 83 μJy beam^{-1}. Of the 73 sources imaged, 51 are detected with peak fluxes ranging from $0.28-71.4$ mJy with a median value of 2.4 mJy. Based on the low-resolution radio spectra (this work), 28/73 sources have a peaked spectrum. Within this class, we find a significantly higher VLBA detection rate with 25 detections. Their peak fluxes range between $0.38-71.4$ mJy with a median value of 4.3 mJy. Table 3.4 provides the breakdown of the number of detections and non-detections for peaked and non-peaked sources.

We performed a chi-square test and found a χ^2 value of 8.1 with $p-$value 0.004. Thus, as expected, the VLBA detections confirm that the peaked sources are preferentially compact, which in turn endorses our analysis using the $B_{SSA} \approx B_{min}$ condition to infer angular sizes of a few to tens of milliarcsec. These small sizes are also expected from our overall understanding of source evolution, whereby a source expands to become optically thin, causing the tendency for peaked sources to be more compact than non-peaked sources (Section 3.10).

3.12 Summary and Conclusion

By combining radio archival observations with our own 10 GHz snapshot survey, we have constructed radio spectra spanning 150 MHz to 10 GHz of 155 heavily obscured, luminous quasars in the redshift range $0.4 < z < 2.8$. Our sample selection has identified optically faint, MIR-bright quasars with a luminous ($L_{1.4GHz} \gtrsim 10^{25}$ W Hz^{-1}) and compact ($< 45''$) radio source. Our follow-up 10 GHz VLA imaging revealed that 55% of the sources are compact even on sub-arcsecond scales ($\lesssim 1.7$ kpc at $z \sim 2$) (Patil et al., 2020). In this study, we aim to measure the spectral shapes of the sample and identify young radio AGN. Our main results are as follows:

1. In this sample, 46 (30%±6.8%) of the 155 sources have peaked spectra, making them GPS/CSS and possibly young radio AGN candidates. The spectra of an additional 43 sources show curvature with a possible turnover below our lowest frequency data (150 MHz). Combined, about 57% of our sample shows a clear turnover or signs of a turnover supporting the presence of very compact radio emission.

2. Our sources have significantly steeper high-frequency (optically thin) spectral indices compared to the general population of jetted AGN. Of the 118 sources with secured power-law, curved, or peaked spectrum, about $80\% \pm 9.7\%$ of the sources have steep high-frequency indices: $\alpha_{high} < -0.8$ with a median value near -1. About $16.7\% \pm 5\%$ show extremely steep indices, $\alpha_{high} < -1.3$ similar to high-redshift sources such as USS, HzRGs, and IFRS. Comparing the near-nuclear AGN radiation field to the magnetic energy density confirms that inverse Compton scattering off the radiation field could explain the steeper spectra. Jet

interactions with the dense ambient medium may also explain the steep spectra.

3. We tested for correlations between radio spectral properties and several MIR and radio continuum parameters. Other than mutually dependant variables, no new statistically significant two-parameter correlations were found. When compared in the WISE color phase space, we find no overlap between our sample and either classical FRI/II sources, and compact GPS/CSS sources. There is greater overlap with the high-redshift IFRS population indicating similarities in the MIR properties of our sample and the IFRS.

4. Extrapolating our 10 GHz fluxes to 345 GHz, confirms that the synchrotron contribution to the 345 GHz ALMA detections is typically $< 10\%$ confirming that thermal dust emission dominates at sub-mm wavelengths. This result further supports our estimates of physical properties such as AGN luminosity, and SFRs presented in Lonsdale et al. (2015).

5. Most of our peaked and curved sources lie close to the linear size *vs*. turnover frequency relation seen for other GPS/CSS samples. SSA is likely to be dominant in those sources or FFA under particular circumstances such as the presence of a dense ambient medium (e.g., Bicknell et al., 2018). A few sources lying significantly far from the relation raise two possibilities. Either low-luminosity peaked sources occupy different phase spaces in the LS$-\nu_{peak,rf}$ plane, or those outliers have different underlying absorption mechanisms such as FFA.

6. Assuming the same magnetic field underlies SSA at low frequencies and equipartition at higher frequencies we invoke the condition $B_{SSA} \approx B_{eq}$ we derive emitting region sizes and magnetic fields for the peaked sources. We find the emitting components to have sizes in the range $2 - 52$ pc and magnetic fields in

the range $6 - 400$ mG, similar to values found in luminous GPS/HFP sources. The high detection rate for the peaked sources in our VLBA snapshot survey supports our approach that derives compact sizes for the peaked sources. We reapply the dynamical model from Chapter 2 using the new values of source size and magnetic field and find even younger ages. The ages of the youngest sources are now consistent with the recent discovery of a new class of compact peaked sources that turned on in the last $10 - 20$ years (Nyland et al., 2020).

Overall, we find many sources that have peaked or curved radio spectra indicating compact emission regions likely arising from recently triggered radio jets. In a companion paper we will present high-resolution VLBA observations that further constrain our sample's radio properties and evolutionary stage. To further understand the nature of the absorption requires more detailed radio spectra and spectral modeling. Such studies will also further our understanding of the impact of young radio jets on the host galaxy during a critical stage in it's evolution.

3.13 Tables and Figuresets

3.13.1 Radio Spectra of the Entire Sample

Figure 3.16 shows radio spectra of our entire sample. The figure caption is same as that of Figures 3.4 and 3.5.

3.13.2 Data Tables

Table 3.5 provides our spectral shape classification, two-band spectral indices, and best-fit spectral fitting parameters. Table 3.6 lists the results of the statistical tests performed to find correlations between pairs of parameters. Table 3.7 summarizes the results from our analysis in Section 3.11.2.

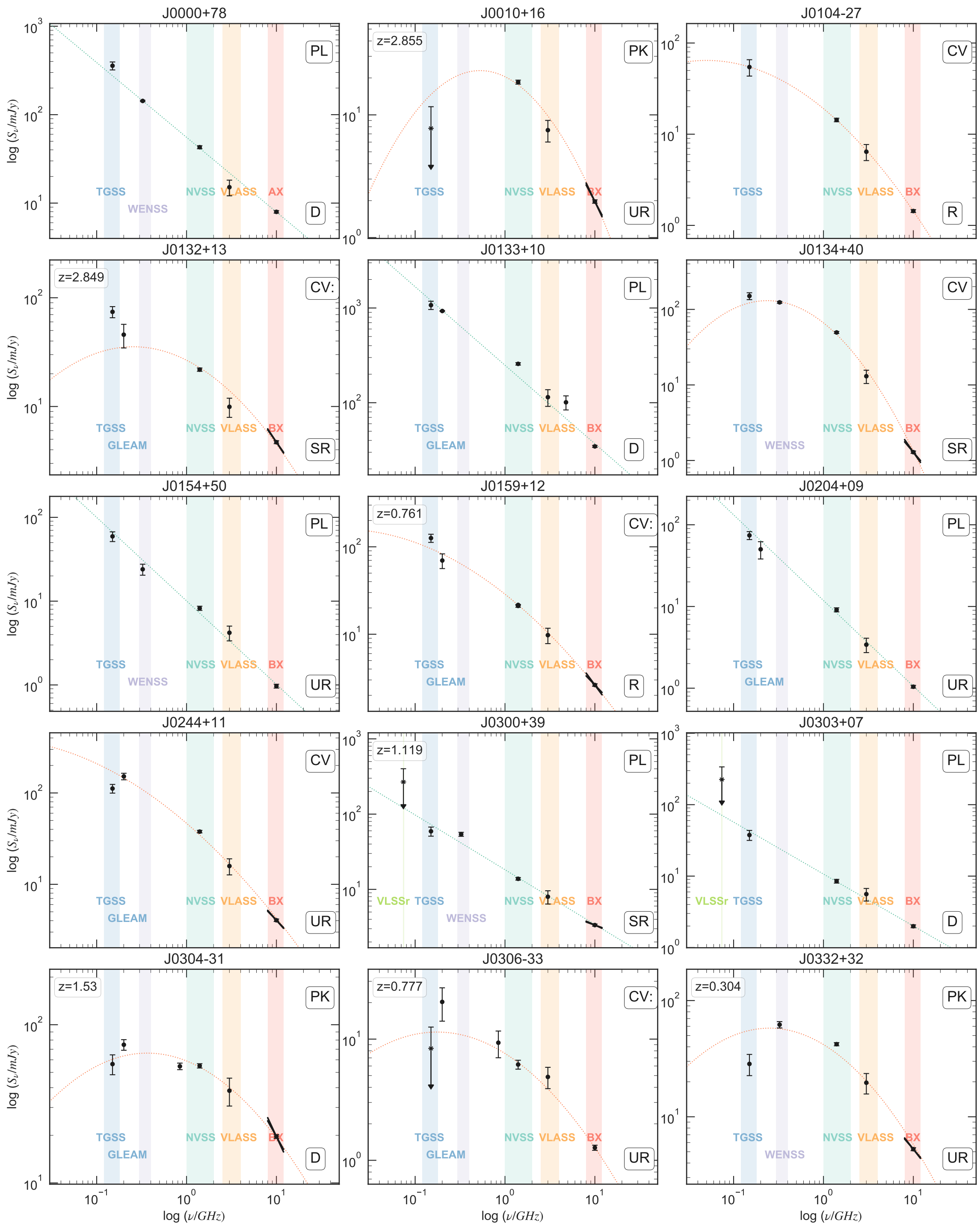

Figure 3.16: Radio spectra of our entire sample. See Figures 3.4 and 3.5 for the caption.

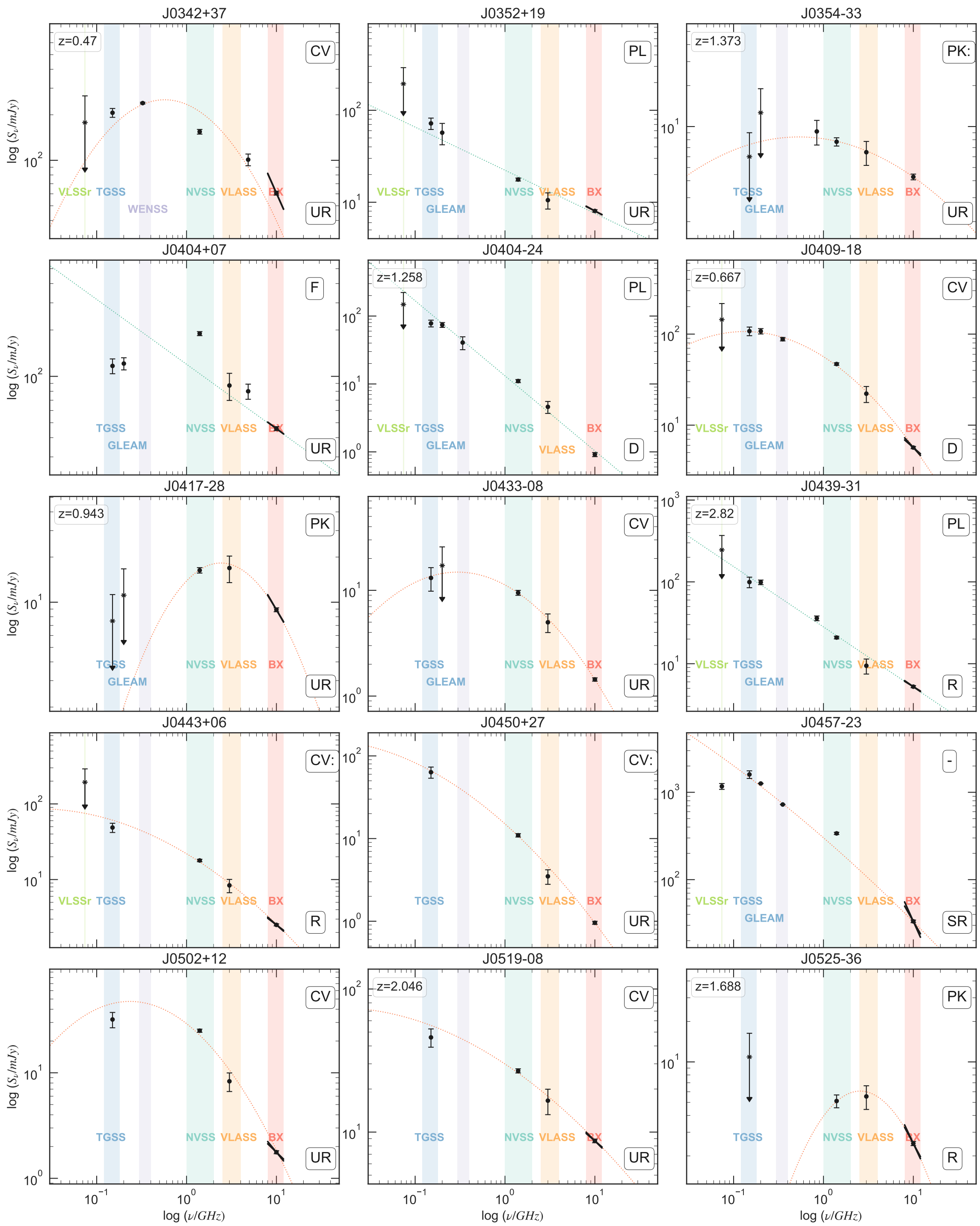

Figure 3.16: *Continued*

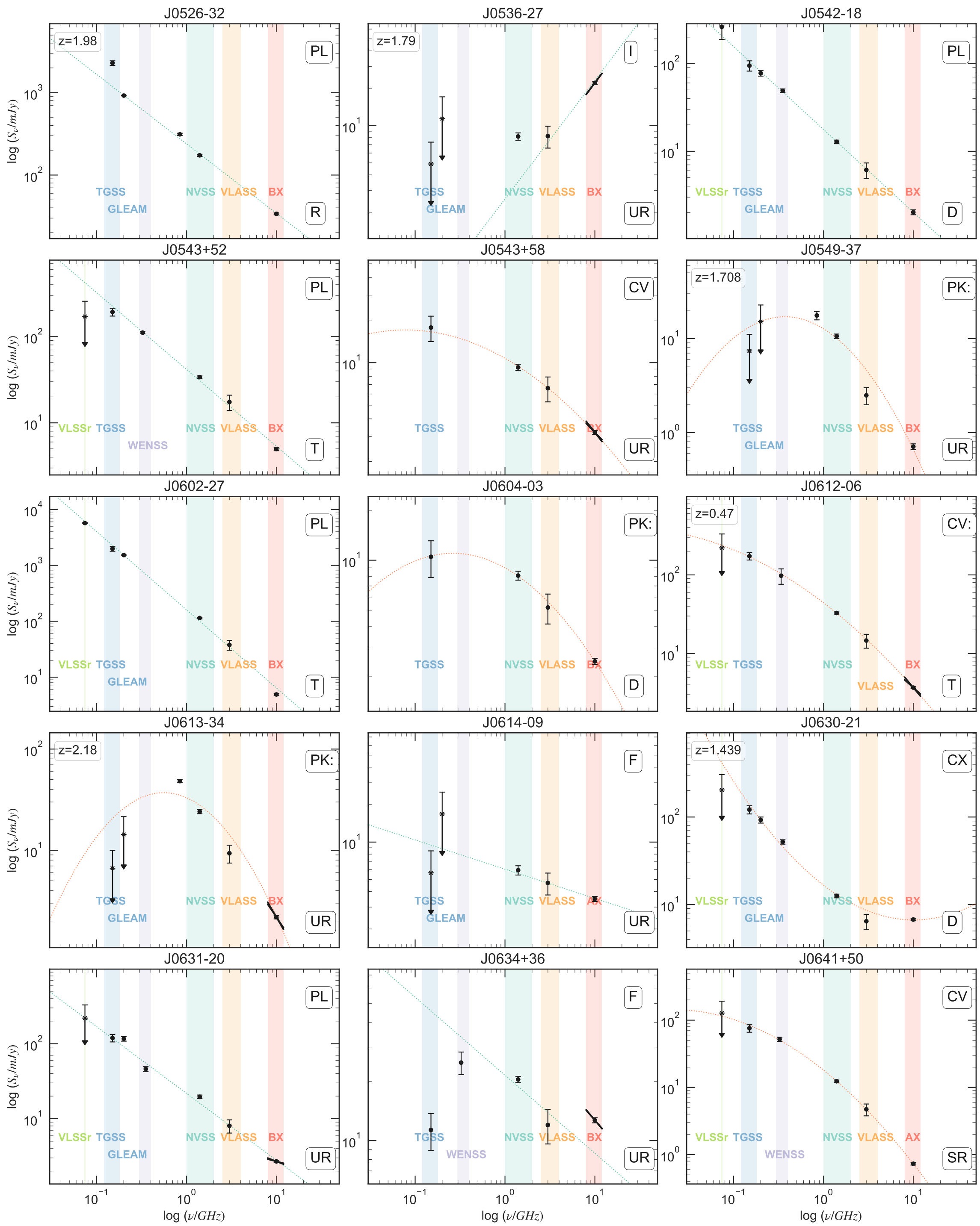

Figure 3.16: *Continued*

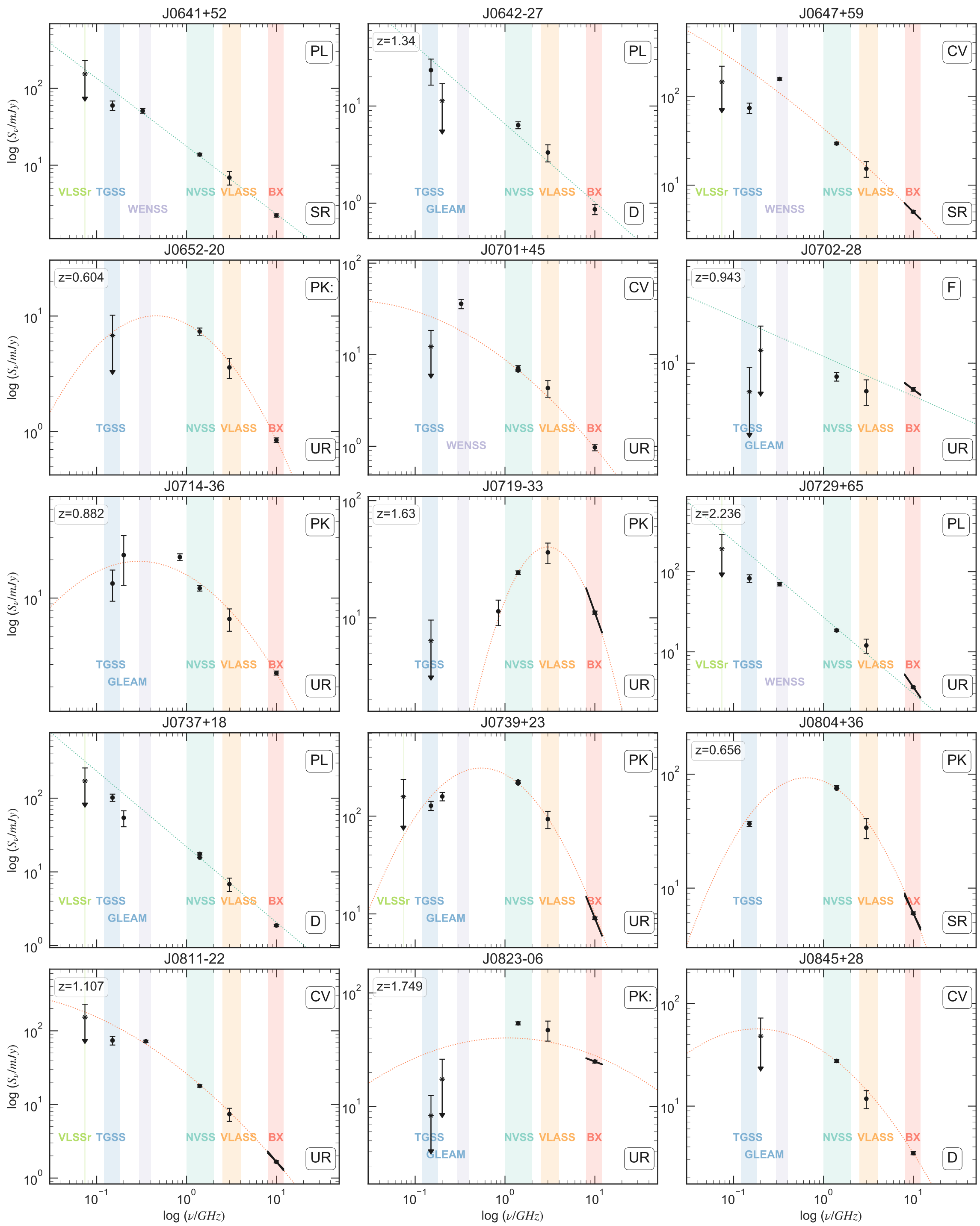

Figure 3.16: *Continued*

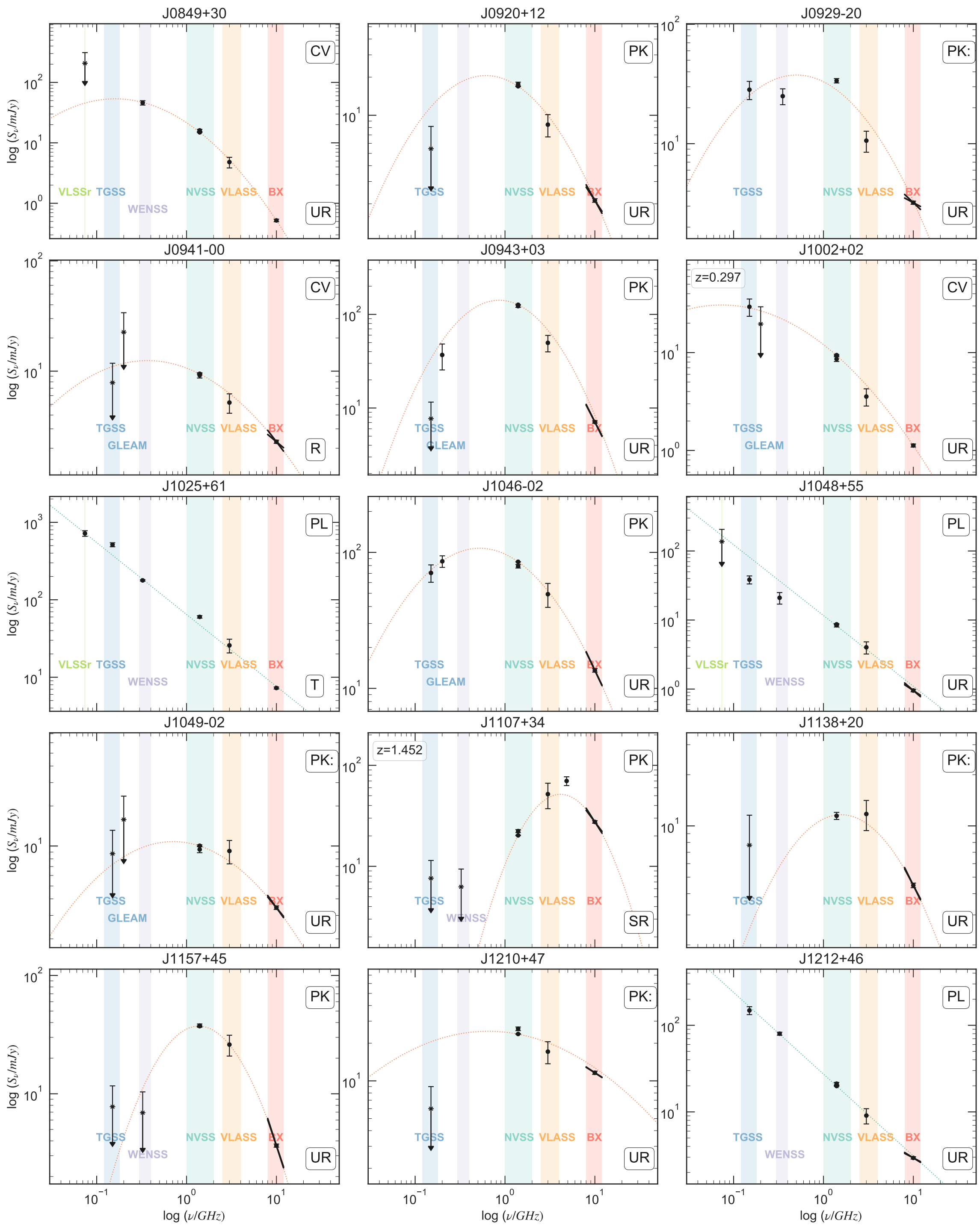

Figure 3.16: *Continued*

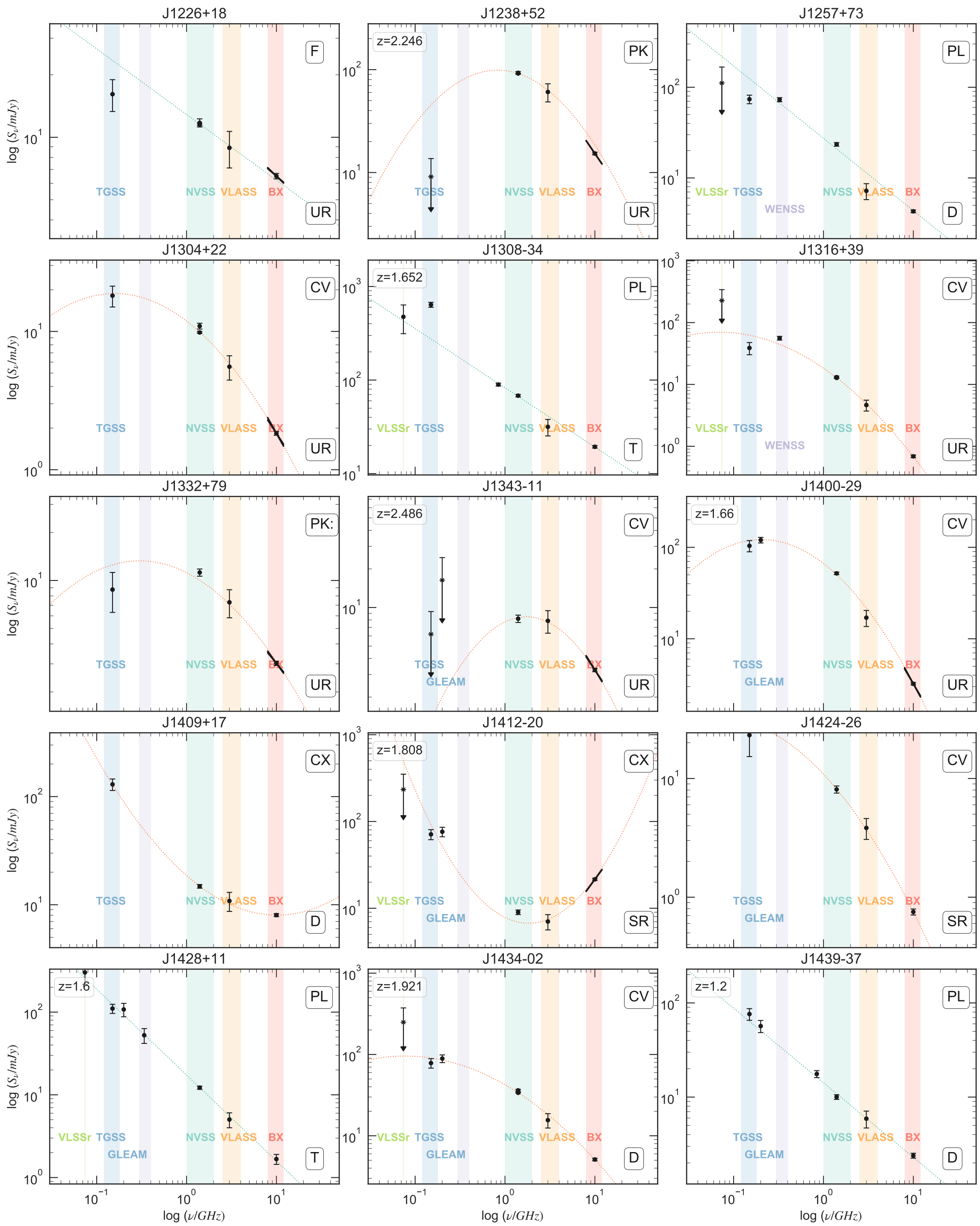

Figure 3.16: *Continued*

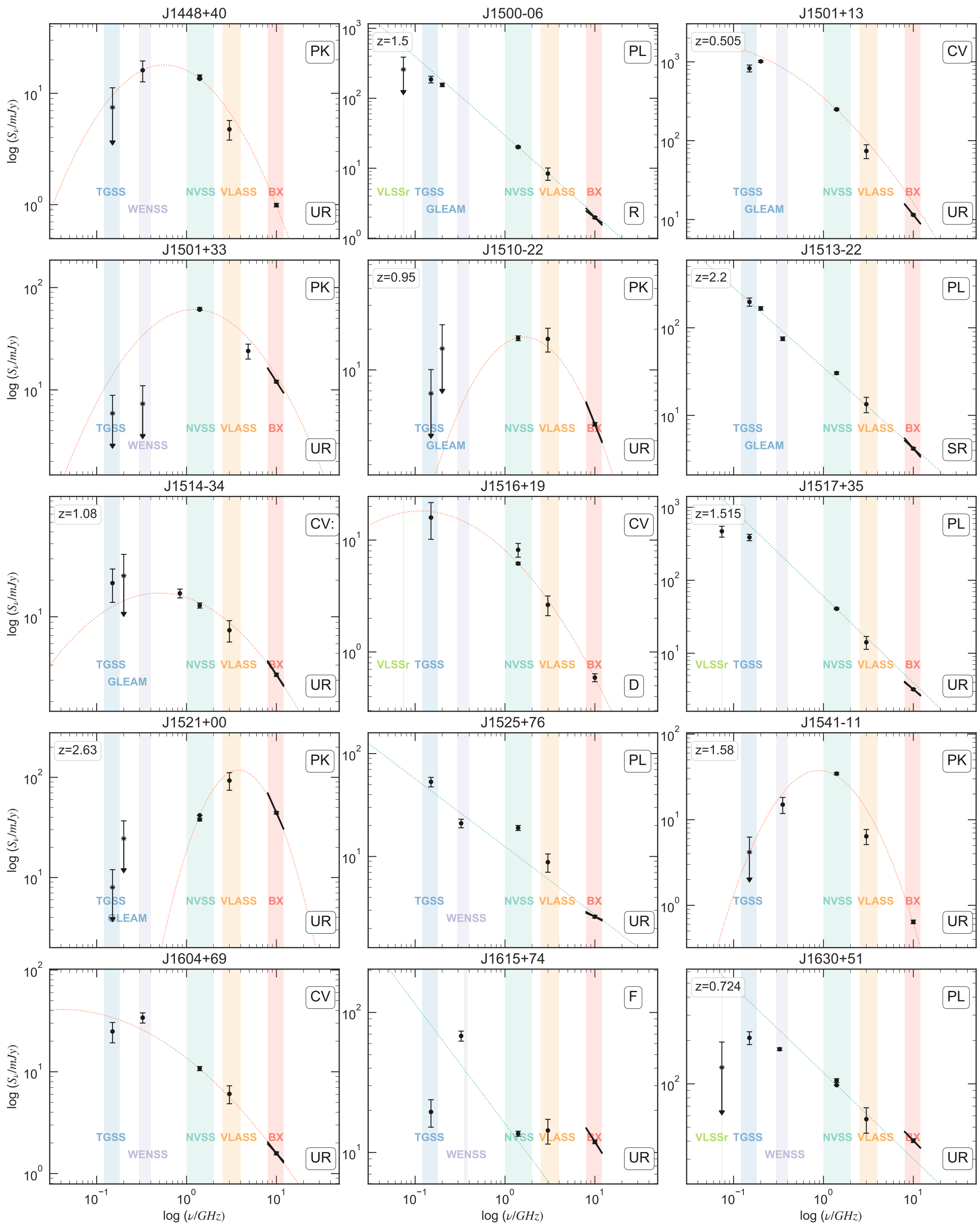

Figure 3.16: *Continued*

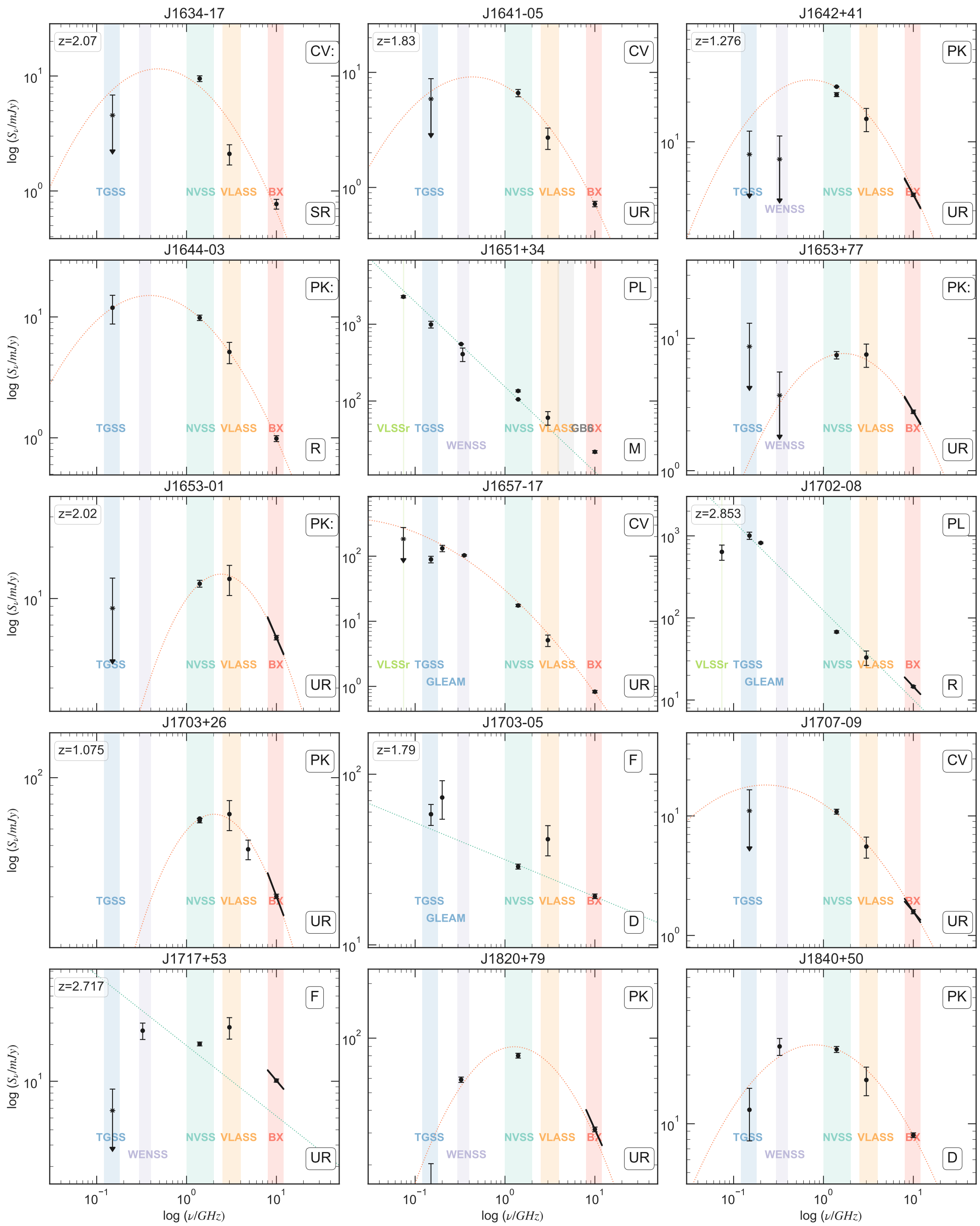

Figure 3.16: *Continued*

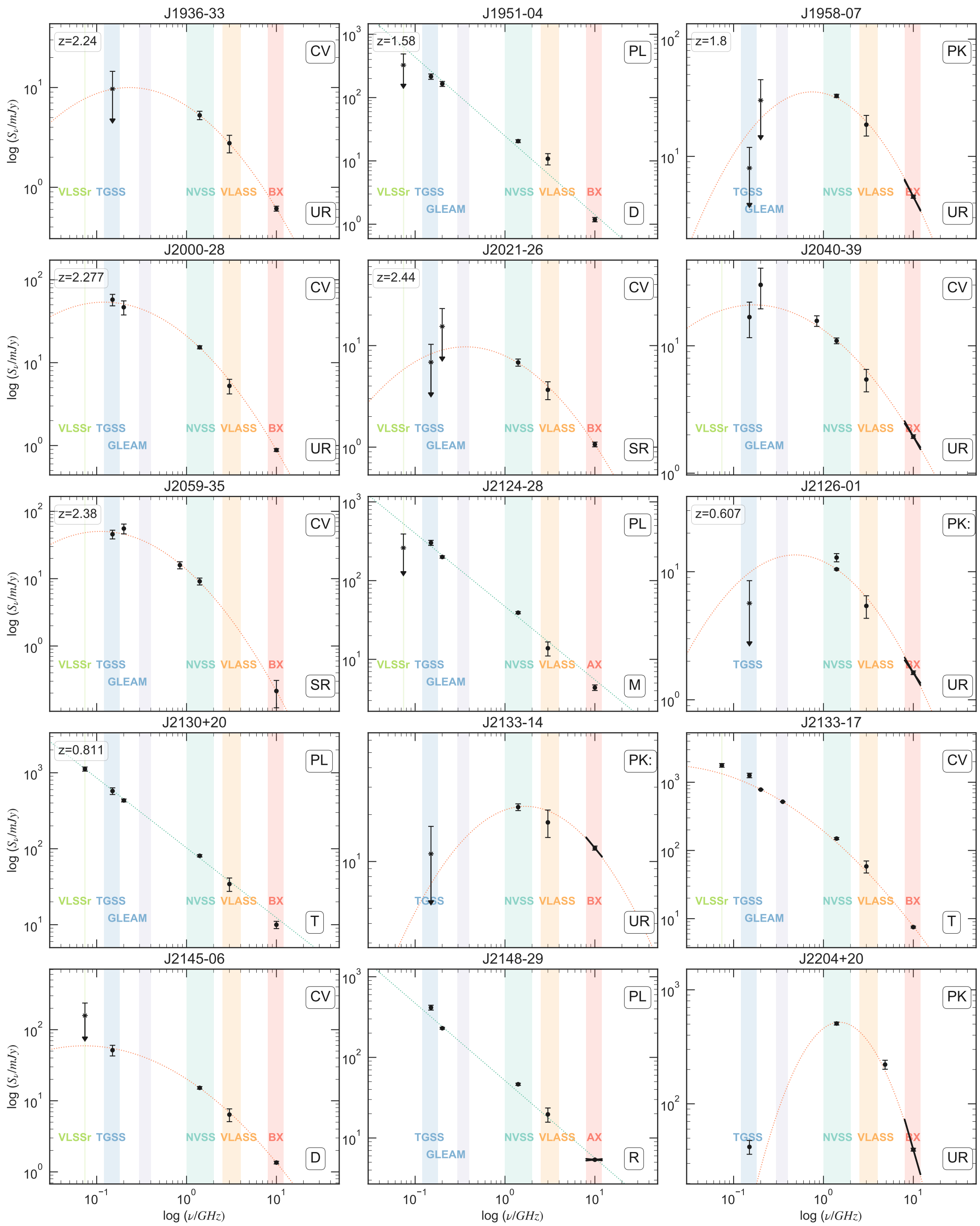

Figure 3.16: *Continued*

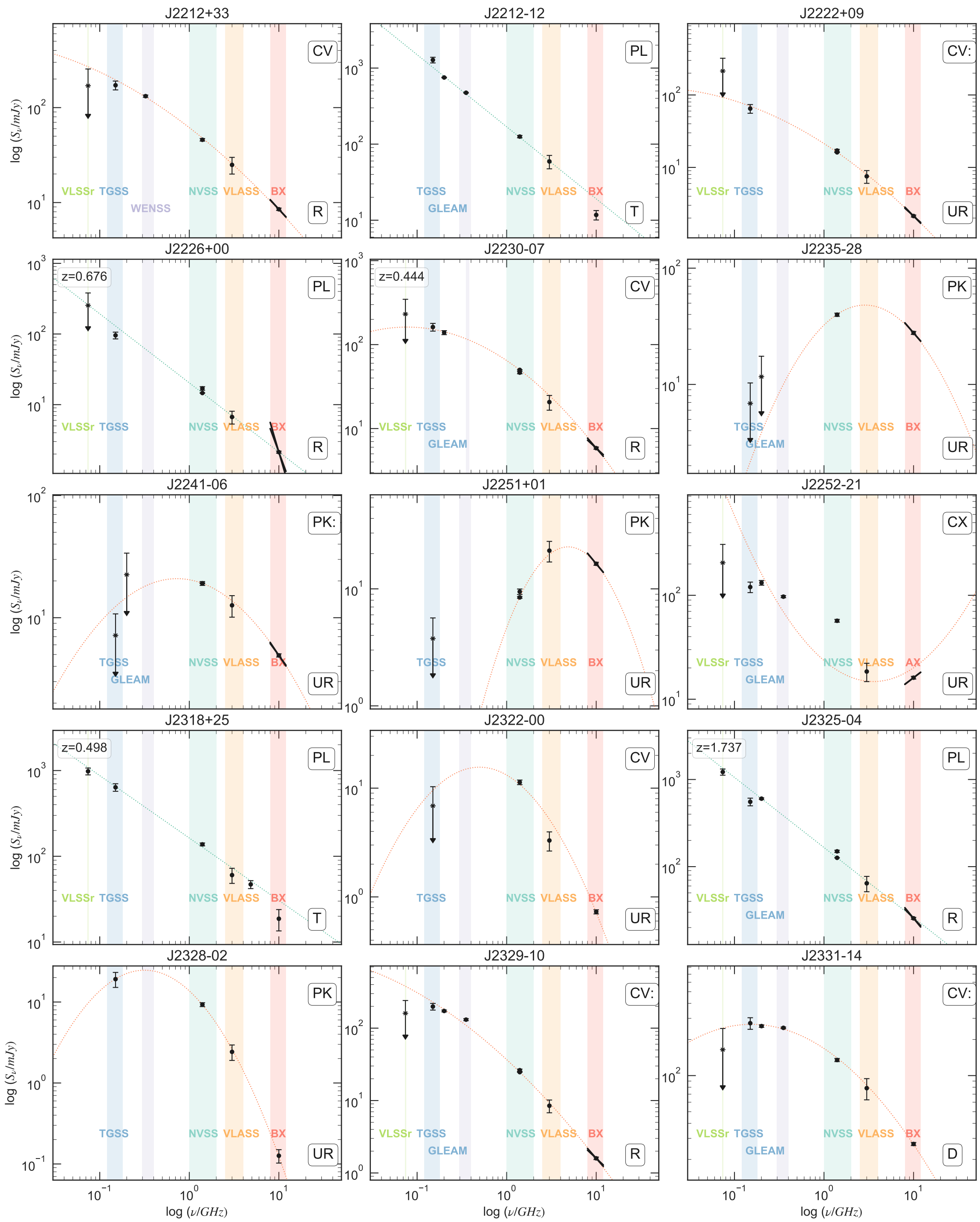

Figure 3.16: *Continued*

Table 3.5: Radio Spectral Shape Parameters and Two-band Spectral Indices of our Sample

Source	z	Morph	Sp Class	$\alpha_{1.4}^{10}$	$\alpha_{0.15}^{1.4}$	QC	ν_{peak} GHz	q	S_{peak} mJy	α_{high}	α_{low}
(1)	(2)	(3)	(4)	(5)	(6)	(7)	(8)	(9)	(10)	(11)	(12)
J0000+78	⋯	D	PL	-0.86 ± 0.03	-0.95 ± 0.09	N	⋯	0.00 ± 0.03	⋯	-0.85 ± 0.02	⋯
J0010+16	2.855	UR	PK	-1.14 ± 0.02	> 0.39	Y	0.53 ± 0.18	-0.28 ± 0.06	22.95 ± 4.19	-1.17 ± 0.07	0.39 ± 0.22
J0104−27	⋯	R	CV	-1.17 ± 0.03	-0.60 ± 0.09	Y	< 0.15	-0.14 ± 0.00	⋯	-1.17 ± 0.01	⋯
J0132+13	2.849	SR	CV:	-0.78 ± 0.02	-0.55 ± 0.09	Y	< 0.15	-0.15 ± 0.05	⋯	-0.88 ± 0.13	⋯
J0133+10	⋯	D	PL	-1.02 ± 0.02	-0.64 ± 0.09	Y	⋯	-0.09 ± 0.01	⋯	-0.83 ± 0.03	⋯
J0134+40	⋯	SR	CV	-1.86 ± 0.02	-0.50 ± 0.09	Y	< 0.15	-0.33 ± 0.05	⋯	-1.85 ± 0.03	⋯
J0154+50	⋯	UR	PL	-1.09 ± 0.04	-0.88 ± 0.09	Y	⋯	-0.07 ± 0.03	⋯	-1.00 ± 0.05	⋯
J0159+12	0.761	R	CV:	-1.06 ± 0.02	-0.80 ± 0.09	Y	< 0.15	-0.10 ± 0.02	⋯	-1.07 ± 0.01	⋯
J0204+09	⋯	UR	PL	-1.10 ± 0.04	-0.94 ± 0.09	Y	⋯	-0.04 ± 0.02	⋯	-1.05 ± 0.03	⋯
J0244+11	⋯	UR	CV	-1.14 ± 0.02	-0.49 ± 0.09	Y	< 0.15	-0.08 ± 0.03	⋯	-1.12 ± 0.02	⋯
J0300+39	1.119	SR	PL	-0.72 ± 0.03	-0.65 ± 0.09	Y	⋯	0.05 ± 0.03	⋯	-0.73 ± 0.06	⋯
J0303+07	⋯	D	PL	-0.74 ± 0.04	-0.67 ± 0.09	N	⋯	-0.01 ± 0.03	⋯	-0.72 ± 0.02	⋯
J0304−31	1.53	D	PK	-0.52 ± 0.02	-0.01 ± 0.09	Y	0.37 ± 0.15	-0.11 ± 0.03	66.16 ± 8.71	-0.55 ± 0.09	0.97 ± 0.74
J0306−33	0.777	UR	CV:	-0.80 ± 0.05	> -0.14	Y	< 0.15	-0.13 ± 0.05	⋯	-0.81 ± 0.05	⋯
J0332+32	0.304	UR	PK	-1.06 ± 0.02	0.18 ± 0.09	Y	0.25 ± 0.16	-0.17 ± 0.06	57.88 ± 20.74	-1.04 ± 0.03	1.01 ± 0.28
J0342+37	0.47	UR	CV	-0.48 ± 0.02	-0.13 ± 0.09	N	< 0.07	-0.23 ± 0.03	⋯	-1.27 ± 0.23	0.19 ± 0.26
J0352+19	⋯	UR	PL	-0.40 ± 0.02	-0.63 ± 0.09	Y	⋯	-0.02 ± 0.03	⋯	-0.47 ± 0.03	⋯
J0354−33	1.373	UR	PK:	-0.30 ± 0.04	> 0.11	Y	0.54 ± 0.25	-0.08 ± 0.03	8.39 ± 0.81	-0.30 ± 0.01	2.59 ± 2.46
J0404+07	⋯	UR	F	-0.72 ± 0.02	0.22 ± 0.09	Y	⋯	-0.04 ± 0.03	⋯	⋯	⋯
J0404−24	1.258	D	PL	-1.27 ± 0.04	-0.88 ± 0.09	Y	⋯	-0.08 ± 0.01	⋯	-1.11 ± 0.05	⋯
J0409−18	0.667	D	CV	-1.07 ± 0.02	-0.37 ± 0.09	Y	< 0.07	-0.16 ± 0.02	⋯	-1.07 ± 0.01	⋯
J0417−28	0.943	UR	PK	-0.31 ± 0.03	> 0.35	Y	2.41 ± 0.36	-0.36 ± 0.02	18.26 ± 2.12	-1.00 ± 0.08	0.35 ± 0.22
J0433−08	⋯	UR	CV	-0.96 ± 0.03	-0.14 ± 0.11	Y	< 0.15	-0.19 ± 0.01	⋯	-0.96 ± 0.01	⋯
J0439−31	2.82	R	PL	-0.70 ± 0.02	-0.70 ± 0.09	Y	⋯	0.01 ± 0.01	⋯	-0.74 ± 0.02	⋯
J0443+06	⋯	R	CV:	-1.00 ± 0.02	-0.45 ± 0.09	Y	< 0.07	-0.09 ± 0.03	⋯	-1.00 ± 0.00	⋯
J0450+27	⋯	UR	CV:	-1.24 ± 0.03	-0.79 ± 0.09	Y	< 0.15	-0.10 ± 0.04	⋯	-1.24 ± 0.04	⋯
J0457−23	⋯	SR	-	-1.18 ± 0.02	-0.70 ± 0.09	Y	⋯	-0.03 ± 0.04	⋯	⋯	⋯
J0502+12	⋯	UR	CV	-1.35 ± 0.02	-0.11 ± 0.09	Y	< 0.15	-0.23 ± 0.09	⋯	-1.33 ± 0.06	⋯
J0519−08	2.046	UR	CV	-0.57 ± 0.02	-0.24 ± 0.09	Y	< 0.15	-0.05 ± 0.02	⋯	-0.57 ± 0.00	⋯
J0525−36	1.688	R	PK	-0.37 ± 0.06	> -0.34	Y	2.56 ± 1.18	-0.49 ± 0.08	6.07 ± 2.52	-1.08 ± 0.29	⋯
J0526−32	1.98	R	PL	-0.83 ± 0.02	-1.16 ± 0.09	Y	⋯	-0.01 ± 0.02	⋯	-0.84 ± 0.02	⋯
J0536−27	1.79	UR	I	0.51 ± 0.04	> 0.23	Y	0.69 ± 0.22	⋯	6.19 ± 12.60	⋯	0.53 ± 0.08
J0542−18	⋯	D	PL	-0.94 ± 0.04	-0.90 ± 0.09	Y	⋯	-0.00 ± 0.01	⋯	-0.94 ± 0.01	⋯
J0543+52	⋯	T	PL	-0.98 ± 0.03	-0.78 ± 0.09	N	⋯	-0.05 ± 0.01	⋯	-0.89 ± 0.03	⋯
J0543+58	⋯	UR	CV	-0.54 ± 0.03	-0.29 ± 0.09	Y	< 0.15	-0.07 ± 0.01	⋯	-0.56 ± 0.05	⋯
J0549−37	1.708	UR	PK:	-1.38 ± 0.05	> 0.16	Y	0.37 ± 0.17	-0.30 ± 0.09	17.06 ± 5.60	-1.34 ± 0.08	2.50 ± 2.46
J0602−27	⋯	T	PL	-1.60 ± 0.03	-1.28 ± 0.09	N	⋯	-0.03 ± 0.01	⋯	-1.40 ± 0.03	⋯

Table 3.5 continued

Table 3.5: Radio Spectral Shape Parameters and Two-band Spectral Indices of our Sample (continued)

Source (1)	z (2)	Morph (3)	Sp Class (4)	$\alpha_{1.4}^{10}$ (5)	$\alpha_{0.15}^{1.4}$ (6)	QC (7)	ν_{peak} GHz (8)	q (9)	S_{peak} mJy (10)	α_{high} (11)	α_{low} (12)
J0604−03	⋯	D	PK:	-0.61 ± 0.04	-0.12 ± 0.11	N	0.26 ± 0.05	-0.11 ± 0.01	11.01 ± 0.62	-0.61 ± 0.00	-0.12 ± 0.11
J0612−06	0.47	T	CV:	-1.11 ± 0.02	-0.74 ± 0.09	Y	< 0.07	-0.09 ± 0.01	⋯	-1.11 ± 0.01	⋯
J0613−34	2.18	UR	PK:	-1.22 ± 0.03	> 0.58	Y	0.56 ± 0.20	-0.34 ± 0.09	37.06 ± 9.24	-1.25 ± 0.02	2.67 ± 2.46
J0614−09	⋯	UR	F	-0.27 ± 0.05	> 0.02	N	⋯	-0.05 ± 0.04	⋯	⋯	⋯
J0630−21	1.439	D	CX	-0.31 ± 0.03	-1.02 ± 0.09	Y	⋯	0.17 ± 0.02	⋯	⋯	⋯
J0631−20	⋯	UR	PL	-1.01 ± 0.03	-0.81 ± 0.09	Y	⋯	0.05 ± 0.05	⋯	-0.89 ± 0.05	⋯
J0634+36	⋯	UR	F	-0.24 ± 0.02	0.27 ± 0.10	Y	⋯	-0.13 ± 0.02	⋯	⋯	⋯
J0641+50	⋯	SR	CV	-1.44 ± 0.03	-0.81 ± 0.09	Y	< 0.07	-0.14 ± 0.01	⋯	-1.44 ± 0.02	⋯
J0641+52	⋯	SR	PL	-0.93 ± 0.03	-0.66 ± 0.09	Y	⋯	-0.04 ± 0.02	⋯	-0.88 ± 0.04	⋯
J0642−27	1.34	D	PL	-1.01 ± 0.07	-0.58 ± 0.14	N	⋯	-0.13 ± 0.03	⋯	-0.86 ± 0.10	⋯
J0647+59	⋯	SR	CV	-0.90 ± 0.02	-0.41 ± 0.09	Y	< 0.07	-0.04 ± 0.04	⋯	-0.94 ± 0.04	⋯
J0652−20	0.604	UR	PK:	-1.10 ± 0.04	> 0.04	Y	0.46 ± 0.08	-0.26 ± 0.03	10.05 ± 0.83	-1.10 ± 0.02	0.04 ± 0.23
J0701+45	⋯	UR	CV	-1.01 ± 0.05	> -0.24	Y	< 0.15	-0.09 ± 0.07	⋯	-0.98 ± 0.05	⋯
J0702−28	0.943	UR	F	-0.11 ± 0.04	> 0.11	Y	⋯	-0.18 ± 0.04	⋯	⋯	⋯
J0714−36	0.882	UR	PK	-0.78 ± 0.03	-0.04 ± 0.13	Y	0.29	-0.16 ± 0.06	19.47	-0.82 ± 0.03	0.24 ± 0.11
J0719−33	1.63	UR	PK	-0.40 ± 0.02	> 0.60	Y	2.98 ± 0.16	-0.88 ± 0.02	40.27 ± 4.41	-2.03 ± 0.27	1.50 ± 0.49
J0729+65	2.236	UR	PL	-0.83 ± 0.02	-0.67 ± 0.09	Y	⋯	-0.15 ± 0.07	⋯	-0.95 ± 0.13	⋯
J0737+18	⋯	D	PL	-1.14 ± 0.03	-0.79 ± 0.09	N	⋯	-0.08 ± 0.03	⋯	-1.03 ± 0.05	⋯
J0739+23	⋯	UR	PK	-1.64 ± 0.02	0.26 ± 0.09	Y	0.54 ± 0.05	-0.40 ± 0.02	310.23 ± 14.70	-2.00 ± 0.23	0.75 ± 0.77
J0804+36	0.656	SR	PK	-1.30 ± 0.02	0.33 ± 0.09	Y	0.64 ± 0.08	-0.36 ± 0.03	92.99 ± 4.25	-1.29 ± 0.04	0.33 ± 0.09
J0811−22	1.107	UR	CV	-1.21 ± 0.03	-0.64 ± 0.09	Y	< 0.07	-0.09 ± 0.03	⋯	-1.21 ± 0.02	⋯
J0823−06	1.749	UR	PK:	-0.39 ± 0.02	> 0.84	Y	1.07	-0.07 ± 0.05	40.16	-0.32 ± 0.02	0.77 ± 0.12
J0845+28	⋯	D	CV	-1.05 ± 0.03	⋯	N	< 0.20	-0.17 ± 0.06	⋯	-1.05 ± 0.01	⋯
J0849+30	⋯	UR	CV	-1.74 ± 0.03	⋯	Y	< 0.07	-0.27 ± 0.02	⋯	-1.71 ± 0.03	⋯
J0920+12	⋯	UR	PK	-1.08 ± 0.03	> 0.53	Y	0.61 ± 0.22	-0.29 ± 0.07	20.59 ± 3.27	-1.06 ± 0.02	0.53 ± 0.22
J0929−20	⋯	UR	PK:	-1.20 ± 0.03	0.08 ± 0.08	Y	0.50 ± 0.23	-0.27 ± 0.10	37.59 ± 12.64	-1.19 ± 0.04	0.08 ± 0.08
J0941−00	⋯	R	CV	-0.71 ± 0.03	> 0.07	Y	< 0.15	-0.15 ± 0.03	⋯	-0.72 ± 0.01	⋯
J0943+03	⋯	UR	PK	-1.45 ± 0.02	> 1.24	Y	0.86 ± 0.19	-0.47 ± 0.07	141.59 ± 12.98	-1.55 ± 0.10	5.44 ± 2.04
J1002+02	0.297	UR	CV	-1.03 ± 0.03	-0.55 ± 0.09	Y	< 0.15	-0.14 ± 0.03	⋯	-1.08 ± 0.03	⋯
J1025+61	⋯	T	PL	-1.08 ± 0.02	-0.96 ± 0.09	Y	⋯	-0.05 ± 0.03	⋯	-0.93 ± 0.03	⋯
J1046−02	⋯	UR	PK	-0.90 ± 0.02	0.05 ± 0.09	Y	0.52 ± 0.04	-0.24 ± 0.01	107.24 ± 2.63	-1.17 ± 0.15	0.68 ± 0.77
J1048+55	⋯	UR	PL	-1.11 ± 0.04	-0.68 ± 0.09	Y	⋯	-0.10 ± 0.02	⋯	-1.03 ± 0.06	⋯
J1049−02	⋯	UR	PK:	-0.51 ± 0.03	> 0.03	Y	0.71 ± 0.16	-0.16 ± 0.02	10.79 ± 0.47	-0.57 ± 0.06	2.06 ± 2.46
J1107+34	1.452	SR	PK	0.11 ± 0.02	> 0.48	Y	4.14 ± 1.45	-0.79 ± 0.11	51.62 ± 31.46	-1.08 ± 0.21	1.11 ± 0.37
J1138+20	⋯	UR	PK:	-0.48 ± 0.03	> 0.18	N	1.57 ± 0.27	-0.28 ± 0.03	11.63 ± 0.98	-0.67 ± 0.19	0.18 ± 0.22
J1157+45	⋯	UR	PK	-1.19 ± 0.02	> 0.71	Y	1.37 ± 0.09	-0.59 ± 0.03	37.30 ± 1.18	-2.17 ± 0.24	1.16 ± 0.34
J1210+47	⋯	UR	PK:	-0.41 ± 0.02	> 0.66	Y	0.65 ± 0.46	-0.09 ± 0.03	24.92 ± 3.54	-0.43 ± 0.03	0.66 ± 0.22

Table 3.5 continued

Table 3.5: Radio Spectral Shape Parameters and Two-band Spectral Indices of our Sample (continued)

Source (1)	z (2)	Morph (3)	Sp Class (4)	$\alpha_{1.4}^{10}$ (5)	$\alpha_{0.15}^{1.4}$ (6)	QC (7)	ν_{peak} GHz (8)	q (9)	S_{peak} mJy (10)	α_{high} (11)	α_{low} (12)
J1212+46	···	UR	PL	−1.00 ± 0.02	−0.87 ± 0.09	Y	···	0.02 ± 0.03	···	−0.94 ± 0.04	···
J1226+18	···	UR	F	−0.30 ± 0.03	−0.14 ± 0.08	Y	···	−0.05 ± 0.01	···	···	···
J1238+52	2.246	UR	PK	−0.92 ± 0.02	> 1.04	Y	0.82 ± 0.27	−0.27 ± 0.04	98.91 ± 10.65	−1.28 ± 0.01	1.04 ± 0.22
J1257+73	···	D	PL	−0.86 ± 0.03	−0.51 ± 0.09	Y	···	−0.04 ± 0.04	···	−0.80 ± 0.05	···
J1304+22	···	UR	CV	−0.91 ± 0.03	−0.23 ± 0.08	Y	< 0.15	−0.14 ± 0.02	···	−0.87 ± 0.03	···
J1308−34	1.652	T	PL	−0.64 ± 0.02	−1.00 ± 0.09	N	···	0.02 ± 0.03	···	−0.63 ± 0.03	···
J1316+39	···	UR	CV	−1.50 ± 0.03	−0.49 ± 0.10	Y	< 0.07	−0.19 ± 0.03	···	−1.49 ± 0.02	···
J1332+79	···	UR	PK:	−0.67 ± 0.03	0.11 ± 0.13	Y	0.30	−0.12 ± 0.04	13.28	−0.68 ± 0.02	0.11 ± 0.13
J1343−11	2.486	UR	CV	−0.47 ± 0.04	> 0.12	Y	< 0.15	−0.31 ± 0.04	···	−1.06 ± 0.11	···
J1400−29	1.66	UR	CV	−1.41 ± 0.02	−0.31 ± 0.09	Y	< 0.15	−0.24 ± 0.02	···	−1.44 ± 0.07	···
J1409+17	···	D	CX	−0.31 ± 0.03	−0.97 ± 0.09	Y	···	0.16 ± 0.01	···	···	···
J1412−20	1.808	SR	CX	0.44 ± 0.03	−0.92 ± 0.09	Y	···	0.42 ± 0.02	···	···	···
J1424−26	···	SR	CV	−1.21 ± 0.05	−0.47 ± 0.16	Y	< 0.15	−0.15 ± 0.03	···	−1.21 ± 0.04	···
J1428+11	1.6	T	PL	−1.01 ± 0.07	−0.99 ± 0.09	Y	···	0.01 ± 0.01	···	−1.04 ± 0.02	···
J1434−02	1.921	D	CV	−1.00 ± 0.03	−0.35 ± 0.09	N	< 0.07	−0.12 ± 0.02	···	−0.96 ± 0.03	···
J1439−37	1.2	D	PL	−0.73 ± 0.04	−0.91 ± 0.09	Y	···	0.04 ± 0.02	···	−0.79 ± 0.03	···
J1448+40	···	UR	PK	−1.35 ± 0.03	> 0.28	Y	0.57 ± 0.09	−0.35 ± 0.04	18.00 ± 1.37	−1.33 ± 0.01	0.99 ± 0.70
J1500−06	1.5	R	PL	−1.18 ± 0.03	−1.00 ± 0.09	Y	···	−0.04 ± 0.00	···	−1.13 ± 0.03	···
J1501+13	0.505	UR	CV	−1.57 ± 0.02	−0.54 ± 0.09	Y	< 0.15	−0.15 ± 0.04	···	−1.51 ± 0.04	···
J1501+33	···	UR	PK	−0.83 ± 0.02	> 1.05	Y	1.21 ± 0.28	−0.34 ± 0.04	61.09 ± 4.32	−1.23 ± 0.17	1.46 ± 0.34
J1510−22	0.95	UR	PK	−0.74 ± 0.03	> 0.42	Y	1.63 ± 0.24	−0.45 ± 0.04	17.50 ± 1.81	−1.59 ± 0.14	0.42 ± 0.22
J1513−22	2.2	SR	PL	−1.01 ± 0.02	−0.84 ± 0.09	Y	···	−0.04 ± 0.03	···	−0.91 ± 0.04	···
J1514−34	1.08	UR	CV:	−0.67 ± 0.03	−0.19 ± 0.14	Y	< 0.15	−0.17 ± 0.03	···	−0.75 ± 0.12	···
J1516+19	···	D	CV	−1.34 ± 0.08	−0.30 ± 0.17	Y	< 0.07	−0.17 ± 0.07	···	−1.32 ± 0.04	···
J1517+35	1.515	UR	PL	−1.30 ± 0.02	−1.01 ± 0.09	Y	···	−0.07 ± 0.03	···	−1.26 ± 0.04	···
J1521+00	2.63	UR	PK	0.08 ± 0.02	> 0.70	Y	3.79 ± 0.17	−1.04 ± 0.02	117.80 ± 13.61	−2.02 ± 0.01	1.18 ± 0.27
J1525+76	···	UR	PL	−1.01 ± 0.03	−0.46 ± 0.09	N	···	−0.01 ± 0.10	···	−0.66 ± 0.10	···
J1541−11	1.58	UR	PK	−2.03 ± 0.03	> 0.95	Y	0.89 ± 0.21	−0.70 ± 0.13	37.49 ± 7.22	−2.03 ± 0.02	1.50 ± 0.64
J1604+69	···	UR	CV	−0.98 ± 0.03	−0.38 ± 0.10	Y	< 0.15	−0.11 ± 0.03	···	−0.98 ± 0.02	···
J1615+74	···	UR	F	−0.07 ± 0.03	−0.16 ± 0.10	Y	···	−0.47 ± 0.11	···	···	···
J1630+51	0.724	UR	PL	−0.49 ± 0.02	−0.31 ± 0.09	Y	···	−0.05 ± 0.01	···	−0.60 ± 0.04	···
J1634−17	2.07	SR	CV:	−1.28 ± 0.06	> 0.33	Y	< 0.15	−0.31 ± 0.21	···	−1.30 ± 0.20	0.33 ± 0.23
J1641−05	1.83	UR	CV	−1.13 ± 0.05	> 0.05	Y	< 0.15	−0.26 ± 0.07	···	−1.13 ± 0.01	···
J1642+41	1.276	UR	PK	−0.89 ± 0.02	> 0.47	Y	0.71 ± 0.32	−0.28 ± 0.06	29.45 ± 5.07	−1.00 ± 0.07	0.77 ± 0.34
J1644−03	···	R	PK:	−1.17 ± 0.04	−0.09 ± 0.12	Y	0.39 ± 0.00	−0.26 ± 0.00	15.05 ± 0.03	−1.17 ± 0.04	···
J1651+34	···	M	PL	−0.93 ± 0.02	−0.89 ± 0.09	Y	···	0.01 ± 0.04	···	−1.11 ± 0.03	···
J1653+77	···	UR	PK:	−0.50 ± 0.04	> −0.07	Y	1.68 ± 0.30	−0.32 ± 0.03	7.68 ± 0.81	−1.11 ± 0.10	0.48 ± 0.35

Table 3.5 continued

Table 3.5: Radio Spectral Shape Parameters and Two-band Spectral Indices of our Sample (continued)

Source (1)	z (2)	Morph (3)	Sp Class (4)	$\alpha_{1.4}^{10}$ (5)	$\alpha_{0.15}^{1.4}$ (6)	QC (7)	ν_{peak} GHz (8)	q (9)	S_{peak} mJy (10)	α_{high} (11)	α_{low} (12)
J1653−01	2.02	UR	PK:	-0.37 ± 0.03	> 0.15	Y	2.42 ± 0.35	-0.43 ± 0.03	13.89 ± 1.82	-1.16 ± 0.13	0.15 ± 0.22
J1657−17	···	UR	CV	-1.55 ± 0.03	-0.73 ± 0.09	Y	< 0.07	-0.15 ± 0.05	···	-1.55 ± 0.01	···
J1702−08	2.853	R	PL	-0.78 ± 0.02	-1.21 ± 0.09	Y	···	-0.01 ± 0.03	···	-1.12 ± 0.07	···
J1703+26	1.075	UR	PK	-0.52 ± 0.02	1.01 ± 0.19	Y	2.02 ± 0.08	-0.44 ± 0.01	61.03 ± 1.65	-1.40 ± 0.03	1.03 ± 0.17
J1703−05	1.79	D	F	-0.20 ± 0.02	-0.32 ± 0.09	N	···	0.03 ± 0.03	···	···	···
J1707−09	···	UR	CV	-0.98 ± 0.03	> -0.01	Y	< 0.15	-0.17 ± 0.06	···	-0.98 ± 0.01	···
J1717+53	2.717	UR	F	-0.35 ± 0.02	> 0.56	Y	···	-0.25 ± 0.03	···	···	···
J1820+79	···	UR	PK	-0.48 ± 0.02	0.75 ± 0.16	Y	1.27 ± 0.19	-0.27 ± 0.02	89.65 ± 7.05	-1.09 ± 0.13	1.77 ± 0.46
J1840+50	···	D	PK	-0.62 ± 0.03	0.38 ± 0.16	Y	0.80 ± 0.14	-0.20 ± 0.03	30.67 ± 1.80	-0.62 ± 0.01	1.16 ± 0.49
J1936−33	2.24	UR	CV	-1.10 ± 0.06	> -0.27	Y	< 0.15	-0.20 ± 0.00	···	-1.10 ± 0.05	···
J1951−04	1.58	D	PL	-1.45 ± 0.05	-1.05 ± 0.09	N	···	-0.10 ± 0.02	···	-1.26 ± 0.07	···
J1958−07	1.8	UR	PK	-1.01 ± 0.02	> 0.63	Y	0.75 ± 0.13	-0.30 ± 0.03	35.48 ± 2.90	-1.09 ± 0.12	0.63 ± 0.22
J2000−28	2.277	UR	CV	-1.45 ± 0.03	-0.59 ± 0.09	Y	< 0.15	-0.21 ± 0.01	···	-1.45 ± 0.00	···
J2021−26	2.44	SR	CV	-0.95 ± 0.05	> -0.00	Y	< 0.15	-0.20 ± 0.03	···	-0.95 ± 0.02	···
J2040−39	···	UR	CV	-0.88 ± 0.03	-0.19 ± 0.14	N	< 0.15	-0.14 ± 0.02	···	-0.90 ± 0.05	···
J2059−35	2.38	SR	CV	-1.91 ± 0.23	-0.72 ± 0.08	N	< 0.15	-0.27 ± 0.05	···	-1.91	···
J2124−28	···	M	PL	-1.11 ± 0.04	-0.92 ± 0.09	Y	···	-0.07 ± 0.02	···	-0.93 ± 0.05	···
J2126−01	0.607	UR	PK:	-1.05 ± 0.04	> 0.37	Y	0.49 ± 113.83	-0.23 ± 0.06	13.52 ± 1.66	-1.06 ± 0.02	0.37 ± 0.23
J2130+20	0.811	T	PL	-1.06 ± 0.06	-0.88 ± 0.09	Y	···	-0.03 ± 0.02	···	-0.92 ± 0.03	···
J2133−14	···	UR	PK:	-0.31 ± 0.03	> 0.31	Y	1.68 ± 0.26	-0.20 ± 0.01	22.60 ± 1.46	-0.69 ± 0.04	0.31 ± 0.22
J2133−17	···	T	CV	-1.52 ± 0.02	-0.95 ± 0.09	N	< 0.07	-0.13 ± 0.02	···	-1.52 ± 0.02	···
J2145−06	···	D	CV	-1.23 ± 0.03	-0.55 ± 0.09	N	< 0.07	-0.16 ± 0.02	···	-1.23 ± 0.01	···
J2148−29	···	R	PL	-1.10 ± 0.02	-0.98 ± 0.09	Y	···	-0.04 ± 0.06	···	-0.96 ± 0.05	···
J2204+20	···	UR	PK	-1.30 ± 0.02	1.12 ± 0.09	Y	1.51 ± 0.15	-0.72 ± 0.03	518.91 ± 67.18	-2.73 ± 0.02	1.12 ± 0.09
J2212+33	···	R	CV	-0.86 ± 0.02	-0.59 ± 0.09	Y	< 0.07	-0.06 ± 0.01	···	-0.94 ± 0.06	···
J2212−12	···	T	PL	-1.21 ± 0.07	-1.04 ± 0.09	N	···	-0.07 ± 0.01	···	-0.95 ± 0.05	···
J2222+09	···	UR	CV:	-1.06 ± 0.03	-0.60 ± 0.09	Y	< 0.07	-0.09 ± 0.02	···	-1.04 ± 0.02	···
J2226+00	0.676	R	PL	-1.06 ± 0.03	-0.77 ± 0.09	Y	···	-0.04 ± 0.07	···	-0.97 ± 0.03	···
J2230−07	0.444	R	CV	-1.05 ± 0.02	-0.56 ± 0.09	Y	< 0.07	-0.14 ± 0.01	···	-1.09 ± 0.02	···
J2235−28	···	UR	PK	-0.18 ± 0.02	> 0.79	Y	2.87 ± 0.33	-0.36 ± 0.02	48.13 ± 4.79	-0.89 ± 0.01	0.74 ± 0.07
J2241−06	···	UR	PK:	-0.69 ± 0.02	> 0.44	Y	0.73 ± 0.10	-0.21 ± 0.02	20.88 ± 0.55	-0.73 ± 0.07	0.44 ± 0.22
J2251+01	···	UR	PK	0.28 ± 0.03	> 0.41	Y	4.86 ± 0.33	-0.64 ± 0.02	22.86 ± 2.87	-0.92 ± 0.01	1.06 ± 0.27
J2252−21	···	UR	CX	-0.64 ± 0.02	-0.33 ± 0.09	Y	···	0.29 ± 0.05	···	···	···
J2318+25	0.498	T	PL	-1.02 ± 0.14	-0.69 ± 0.09	N	···	-0.06 ± 0.01	···	-0.73 ± 0.04	···
J2322−00	···	UR	CV	-1.39 ± 0.03	> 0.22	Y	< 0.15	-0.34 ± 0.12	···	-1.39 ± 0.03	0.22 ± 0.22
J2325−04	1.737	R	PL	-0.90 ± 0.02	-0.59 ± 0.09	Y	···	-0.01 ± 0.01	···	···	···
J2328−02	···	UR	PK	-2.19 ± 0.10	-0.32 ± 0.10	N	0.32 ± 0.01	-0.44 ± 0.01	24.71 ± 1.01	-2.16 ± 0.11	···

Table 3.5 continued

Table 3.5: Radio Spectral Shape Parameters and Two-band Spectral Indices of our Sample (continued)

Source	z	Morph	Sp Class	$\alpha_{1.4}^{10}$	$\alpha_{0.15}^{1.4}$	QC	ν_{peak} GHz	q	S_{peak} mJy	α_{high}	α_{low}
(1)	(2)	(3)	(4)	(5)	(6)	(7)	(8)	(9)	(10)	(11)	(12)
J2329−10	⋯	R	CV:	-1.43 ± 0.03	-0.91 ± 0.09	Y	< 0.07	-0.10 ± 0.02	⋯	-1.39 ± 0.02	⋯
J2331−14	⋯	D	CV:	-0.82 ± 0.02	-0.32 ± 0.09	N	< 0.07	-0.13 ± 0.01	⋯	-0.82 ± 0.01	⋯
J2332+34	0.981	UR	PK	-1.31 ± 0.03	0.06 ± 0.11	Y	0.44 ± 0.06	-0.30 ± 0.03	20.39 ± 1.80	-1.32 ± 0.04	0.64 ± 0.39
J2341−29	⋯	UR	CV	-0.84 ± 0.04	-0.27 ± 0.09	N	< 0.15	-0.11 ± 0.02	⋯	-0.87 ± 0.05	1.11 ± 0.98
J2345+31	⋯	UR	PK	-0.77 ± 0.03	> 0.42	Y	0.71 ± 0.08	-0.23 ± 0.02	16.38 ± 0.73	-0.85 ± 0.11	1.35 ± 0.70
J2357−10	2.048	UR	CV	-0.77 ± 0.03	> 0.33	Y	< 0.15	-0.21 ± 0.05	⋯	-0.73 ± 0.09	0.33 ± 0.22
J2359+43	⋯	D	PK	-1.72 ± 0.03	> 0.52	Y	0.56 ± 0.09	-0.45 ± 0.06	44.76 ± 6.15	-1.72 ± 0.03	1.91 ± 0.66

Note — Column 1: Source name. Column 2: Spectroscopic redshift. Column 3: 10 GHz Radio morphology as seen in VLA imaging (Patil et al., 2020). The morphological codes are UR: Unresolved; SR: Slightly/Marginally resolved; R: Resolved and single component; D: Double; T: Triple; M: Multi-component. Column 4: Spectral shape classes as described in Section 3.5.3. The notation ":" in front of the spectral shape indicates uncertainty in determination of the spectral shape. Column 5: $\alpha_{1.4}^{10}$, spectral index calculated between NVSS and VLA 10 GHz data. Column 6: $\alpha_{0.15}^{1.4}$, TGSS-NVSS spectral index. Column 7: Quality Code (QC) for individual sources. Y indicates that the source is included in the final sample, where N indicates source is rejected for a variety of reasons as explained in Section 3.5. Column 8−12: Spectral shape parameters for the curved and peaked spectrum sources. The definition of each parameter is described in Section 3.5.4. ν_{peak}: The turnover frequency; q: best-fit value for the curvature parameter in Equation 3.2; α_{high}: High-frequency spectral index calculated using frequencies above ν_{peak}; $\alpha)_{low}$: Low-frequency spectral index calculated using frequencies below ν_{peak}.

Table 3.6: Results from the Censored Kendall$-\tau$ Correlation Test

X (1)	Y (2)	N (3)	τ (4)	σ_τ (5)	P_{null} (6)
All Sources					
$L_{1.4GHz}$	$L_{6\mu m}$	70	0.63	0.00	0.000
u_{IR}	$L_{6\mu m}$	58	0.39	0.00	0.000
$L_{1.4GHz}$	t_{age}	70	−0.33	0.00	0.000
$L_{1.4GHz}$	u_{IR}	70	0.32	0.00	0.000
Lin. Size	u_{IR}	58	−0.52	0.04	0.000
Lin. Size	t_{age}	70	0.33	0.03	0.000
P_{lobe}	n_a	70	0.52	0.03	0.000
u_{IR}	t_{age}	70	−0.44	0.00	0.000
P_{lobe}	u_{IR}	70	0.56	0.03	0.000
ν_{peak}	$\nu_{peak,rf}$	43	0.69	0.04	0.000
Lin. Size	P_{lobe}	70	−0.41	0.04	0.000
u_{IR}	n_a	70	0.27	0.00	0.001
P_{lobe}	$L_{6\mu m}$	70	0.28	0.03	0.001
Lin. Size	n_a	70	−0.24	0.03	0.003
$L_{1.4GHz}$	P_{lobe}	70	0.22	0.03	0.008
$\nu_{peak,rf}$	u_{IR}	43	0.28	0.04	0.009
$\nu_{peak,rf}$	P_{lobe}	48	0.26	0.05	0.010
z	W1−W2	58	0.23	0.00	0.012
ν_{peak}	P_{lobe}	48	0.23	0.06	0.019
P_{lobe}	t_{age}	70	−0.19	0.03	0.021
$\nu_{peak,rf}$	$L_{1.4GHz}$	48	0.22	0.04	0.026
ν_{peak}	n_a	48	0.22	0.04	0.026
Peaked Sources Only					
$L_{1.4GHz}$	$L_{6\mu m}$	26	0.66	0.00	0.000
ν_{peak}	$\nu_{peak,rf}$	24	0.73	0.06	0.000
P_{lobe}	u_{IR}	26	0.5	0.06	0.000
P_{lobe}	n_a	26	0.57	0.05	0.000
$L_{1.4GHz}$	t_{age}	26	−0.45	0.00	0.001
$\nu_{peak,rf}$	$L_{6\mu m}$	24	0.44	0.05	0.002
ν_{peak}	n_a	26	0.43	0.06	0.002
$L_{1.4GHz}$	u_{IR}	26	0.41	0.00	0.004
u_{IR}	$L_{6\mu m}$	24	0.42	0.00	0.004
$\nu_{peak,rf}$	n_a	26	0.38	0.05	0.006
ν_{peak}	α_{high}	46	0.26	0.06	0.014

Table 3.6 continued

Table 3.6: Results from the Censored Kendall$-\tau$ Correlation Test (continued)

X (1)	Y (2)	N (3)	τ (4)	σ_τ (5)	P_{null} (6)
Lin. Size	u_{IR}	24	-0.36	0.10	0.015
$\nu_{peak,rf}$	P_{lobe}	26	0.32	0.07	0.023
ν_{peak}	P_{lobe}	26	0.31	0.07	0.026
ν_{peak}	$L_{6\mu m}$	24	0.33	0.05	0.026
u_{IR}	t_{age}	26	-0.31	0.00	0.029

NOTE — Column 1: First parameter; Column 2: Second parameter; Column 4: Number of sources used in the test; Column 5: Correlation coefficient, τ; Column 6: 1σ Uncertainty on τ; Column 7: p-value for the Null hypothesis; Column 8: Condition used to select a subsample based on the spectral shapes (see Section 3.5.3).

Table 3.7: Summary of Emitting Region Components in Peaked Spectrum Sources

Source	z	θ_{reg}	B	Reg Size	P_{reg}	t_{syn}	t_{rad}
		mas	mG	pc	$\times 10^{-5} dyne\, cm^{-2}$	yr	yr
(1)	(2)	(3)	(4)	(5)	(6)	(7)	(8)
J0010+16	2.855	2.0	30.0	16.0	2.8	7.8e+02	2.3e+03
J0304−31	1.53	3.8	11.5	33.2	0.4	3.3e+03	9.8e+03
J0332+32	0.304	4.2	6.3	19.3	0.1	8.0e+03	2.3e+04
J0354−33	1.373	0.9	17.1	7.9	0.9	1.8e+03	2.6e+03
J0417−28	0.943	0.3	93.1	2.4	26.9	1.4e+02	2.7e+03
J0525−36	1.688	0.2	139.5	1.7	60.3	7.7e+01	1.7e+03
J0549−37	1.708	2.1	16.0	18.1	0.8	2.0e+03	4.7e+03
J0613−34	2.18	2.2	25.1	18.4	2.0	1.0e+03	3.5e+03
J0652−20	0.604	1.1	14.0	7.3	0.6	2.4e+03	6.2e+03
J0714−36	0.882	2.3	8.4	18.6	0.2	5.2e+03	1.0e+04
J0719−33	1.63	0.5	244.7	4.1	185.6	3.3e+01	1.8e+04
J0739+23	–	6.5 – 9.2	10.9 – 19.9	50.0 – 72.4	1.7	...	...
J0804+36	0.656	2.2	16.4	15.8	0.8	1.9e+03	6.5e+03
J0823−06	1.749	1.0	33.1	8.9	3.4	6.7e+02	1.3e+03
J0920+12	–	1.6 – 2.3	17.3 – 31.6	12.4 – 18.0	1.7	...	...
J0929−20	–	2.6 – 3.7	13.7 – 25.0	20.3 – 29.4	1.1	...	...
J0943+03	–	2.8 – 4.0	18.7 – 34.0	21.8 – 31.5	3.0	...	...
J1046−02	–	4.1 – 5.8	12.0 – 21.9	31.5 – 45.7	1.2	...	...
J1049−02	–	1.0 – 1.4	21.4 – 39.0	7.9 – 11.4	2.1	...	...
J1107+34	1.452	0.3	169.9	2.7	89.5	5.7e+01	5.6e+03
J1157+45	–	0.9 – 1.3	34.2 – 62.3	7.3 – 10.5	32.7	...	...
J1210+47	–	1.7 – 2.4	18.7 – 34.1	13.0 – 18.8	1.4	...	...

Table 3.7 continued

Table 3.7: Summary of Emitting Region Components in Peaked Spectrum Sources (continued)

Source	z	θ_{reg} mas	B mG	Reg Size pc	P_{reg} $\times 10^{-5} dyne\, cm^{-2}$	t_{syn} yr	t_{rad} yr
(1)	(2)	(3)	(4)	(5)	(6)	(7)	(8)
J1238+52	2.246	2.5	41.7	20.9	5.4	4.7e+02	5.0e+03
J1332+79	–	2.7 – 3.8	9.8 – 17.8	20.9 – 30.3	0.5	...	...
J1448+40	–	1.6 – 2.3	16.2 – 29.4	12.5 – 18.2	1.8	...	...
J1501+33	–	1.3 – 1.9	29.0 – 52.9	10.4 – 15.0	7.9	...	...
J1510−22	0.95	0.5	84.1	3.8	21.9	1.7e+02	5.9e+03
J1521+00	2.63	0.7	399.8	5.9	495.5	1.6e+01	6.5e+04
J1541−11	1.58	1.3	42.0	11.4	5.5	4.7e+02	1.7e+03
J1642+41	1.276	1.3	24.6	11.2	1.9	1.0e+03	4.4e+03
J1644−03	–	2.2 – 3.1	11.3 – 20.6	16.8 – 24.4	0.8	...	...
J1653−01	2.02	0.4 – 0.5	55.0 – 100.3	2.9 – 4.1	35.9	...	...
J1653+77	–	0.3	123.2	2.7	47.1	9.3e+01	3.3e+03
J1703+26	1.075	0.7	87.5	5.7	23.8	1.6e+02	5.9e+03
J1820+79	–	1.5 – 2.2	28.1 – 51.2	11.7 – 17.0	8.3	...	...
J1840+50	–	1.5 – 2.1	21.5 – 39.2	11.4 – 16.5	2.1	...	...
J1958−07	1.8	1.5	30.4	13.0	2.9	7.6e+02	2.7e+03
J2126−01	0.607	1.2	15.5	8.0	0.7	2.1e+03	6.2e+03
J2133−14	–	0.6 – 0.8	43.3 – 78.9	4.6 – 6.7	12.7	...	...
J2204+20	–	2.9 – 4.1	27.1 – 49.5	22.6 – 32.7	42.9	...	...
J2235−28	–	0.5 – 0.7	60.8 – 110.8	3.8 – 5.5	37.3	...	...
J2241−06	–	1.4 – 1.9	20.5 – 37.4	10.5 – 15.2	2.1	...	...
J2251+01	–	0.2 – 0.3	89.8 – 163.7	1.5 – 2.1	132.1	...	...
J2332+34	0.981	1.7	15.3	14.0	0.7	2.1e+03	7.7e+03

Table 3.7 continued

Table 3.7: Summary of Emitting Region Components in Peaked Spectrum Sources (continued)

Source	z	θ_{reg} mas	B mG	Reg Size pc	P_{reg} $\times10^{-5} dyne\, cm^{-2}$	t_{syn} yr	t_{rad} yr
(1)	(2)	(3)	(4)	(5)	(6)	(7)	(8)
J2345+31	–	$1.2 - 1.8$	$20.7 - 37.8$	$9.6 - 13.9$	2.4	...	...
J2359+43	–	$2.5 - 3.6$	$13.8 - 25.2$	$19.5 - 28.3$	1.6	...	...

Note — Column 1: Source name. Column 2: Redshift. Column 3: Angular size of the emitting region in mas (see Section 3.11.2). Column 4: Magnetic field estimate in Gauss. Column 5: Physical sizes of the region. Column 6: Source pressures estimated using magnetic field estimates given in Column 4. Column 7: Synchrotron electron lifetimes at 10 GHz (Equation 3.21. Column 8: Radiative cooling times, $t_{rad} = E_{tot}/L_{10GHz}$.

Chapter 4

Multi-band Optical and Near-infrared Properties of Faint Submillimeter Galaxies with Serendipitous ALMA Detections

4.1 Introduction

Dusty Star-Forming Galaxies (DSFGs) are a class of galaxies enshrouded in dust that have star formation rates of at least a few tens of solar masses per year (Casey et al., 2014). A characteristic feature of this class is the bright dust emission at Far-infrared (FIR) wavelengths, which is the re-radiated optical/ultra-violet light from star-forming regions. Their discovery became possible by the advances in IR instruments during the 1980s-1990s, and the *Infra-Red Astronomical Satellite (IRAS)* allowed a large number of detections of Luminous and Ultraluminous Infrared Galaxies (LIRGs and ULIRGs). Furthermore, the Cosmic Background Explorer (COBE) satellite was the first to measure the Cosmic Infrared Background (CIB) light and establish the overall importance of the DFSG population. The results from COBE showed that the energy density of the CIB emission is comparable to the optical and UV background light (Dole et al., 2006; Hauser et al., 1998). Studies in the late 1990s (Smail et al. 1997; Barger et al. 1998; Hughes et al. 1998; Blain et al. 2002, and references therein) identified the galaxies responsible for the CIB submm/mm emission. These galaxies, popularly known as Submillimeter Galaxies (SMG; Blain et al. 2002), belong to the more general class of DFSGs.

SMGs are extremely luminous galaxies ($L_{IR} > 10^{12} L_{\odot}$) with star formation rates up to $1000\, M_{\odot}$ yr^{-1} (Ivison et al., 1998; Smail et al., 2002; Chapman et al., 2004; Barger et al., 2012; Swinbank et al., 2014; Simpson et al., 2017; Michałowski et al., 2017). They are most likely undergoing a merger (Engel et al., 2010; Ivison et al., 2012; Alaghband-Zadeh et al., 2012; Fu et al., 2013; Chen et al., 2015a; Oteo et al., 2016), and have a median redshift, $\langle z \rangle \sim$ 2-3 (Chapman et al., 2002, 2005; Wardlow et al., 2011; Simpson et al., 2014; Miettinen et al., 2015; Chen et al., 2016a). Although early studies of SMGs only utilized observation windows at $850\, \mu$m and 1.1 mm due to atmospheric transmission, the negative k-correction helped to probe SMGs up to high redshift ($z \sim 5$). For a given luminosity, the dimming of the flux with increasing redshift is balanced by the shifting of the peak of the Spectral Energy Distribution (SED) into the observing window (Franceschini et al. 1991; Blain et al. 2002; See Fig. 4 in Blain et al. (2002)). Therefore, the flux remains approximately constant for redshifts up to $z \sim 8$.

Single-dish instruments such as the Submillimetre Common User Bolometer Array (SCUBA; e.g. Smail et al. 1997; Hughes et al. 1998; Barger et al. 1998) on the James Clark Maxwell Telescope (JCMT), AzTEC (Ezawa et al., 2004; Perera et al., 2008; Austermann et al., 2010; Aretxaga et al., 2011; Scott et al., 2010, 2012) on the

Atacama Submillimeter Telescope Experiment (ASTE), the Large Apex Bolometer Camera (LABOCA) on the Atacama Pathfinder Experiment (APEX) (Siringo et al., 2009; Weiß et al., 2009), Bolocam on the Caltech Submillimeter Observatory (CSO) (Laurent et al., 2005), the Max Planck Millimeter Bolometer (MAMBO; Greve et al. 2004; Bertoldi et al. 2007) on the IRAM 30-meter telescope, and SCUBA-2 on JCMT (Chen et al., 2013b; Casey et al., 2013; Geach et al., 2013, 2017) identified a significant number of SMGs. However, large beam sizes ($15''$ for SCUBA at 850 μm and $11''$ for MAMBO-1 at 1.2 mm) prevented accurate multi-wavelength counterpart identification. A few indirect techniques were used to identify multi-wavelength counterparts, such as using the radio-FIR correlation to find targets in radio interferometric observations (Ivison et al., 2007), 24 μm MIPS observations from *Spitzer* (e.g. Pope et al. 2006), and assigning probabilities to the possible optical/NIR counterparts (e.g. Ivison et al. 2002; Dunlop et al. 2004; Chapin et al. 2011; Smith et al. 2011; Kim et al. 2012; Alberts et al. 2013, Biggs et al. 2011). These techniques have limitations as not all counterparts can be accurately identified due to large beam sizes of single dish telescopes. Therefore, interferometric observation is required to obtain a bias-free sample of submm sources with sub-arcsecond positional accuracy.

Number count studies revealed that a significant population was missed by the single dish as well as space-based observations at submm and mm wavelengths (Lagache et al. 2005). On the other hand, most of the population contributing to the CIB at wavelengths less that 200 μm was already identified, and found to reside at $z \sim 1$ (Viero et al., 2013). Number counts as well as models, showed that the redshift of the dominant contributor to the CIB increases with increasing wavelength (Lagache et al., 2005). This indicates the need for high sensitivity and finer spatial resolution surveys. During the pre-Atacama Large Millimeter Array (ALMA) era, 1.1 mm surveys were mainly conducted with AzTEC (Perera et al., 2008; Scott et al., 2012;

Hatsukade et al., 2011; Austermann et al., 2010; Scott et al., 2010; Aretxaga et al., 2011) and about $10-20\%$ of the CIB was resolved (Hatsukade et al., 2011; Scott et al., 2010). In contrast, $850/870\,\mu$m surveys using SCUBA, the LABOCA has resolved up to 50% of the CIB (Blain et al., 1999; Coppin et al., 2006; Weiß et al., 2009)[1]. The high confusion limit limited the detection threshold to $\sim$ 1-2 mJy at $850\,\mu$m. Studies of gravitationally-lensed SMGs allowed to probe the faint population (Hsu et al., 2016; Chen et al., 2013a,b; Smail et al., 1997; Cowie et al., 2002; Knudsen et al., 2008; Johansson et al., 2011; Chen et al., 2014). However, these studies were limited by small number statistics and uncertainties in the lensing models for the clusters. In summary, all of the previous results have shown that the major contributors of the CIB at $850\,\mu$m and 1.1 mm have flux densities fainter than 1 mJy. Such galaxies would correspond to normal galaxies, or LIRGs (with luminosities $L < 10^{12}\,L_{\odot}$).

It is now possible to study this fainter population, the so-called faint SMGs, as ALMA provides sub-arcsecond resolution and high sensitivity at submm and mm wavelengths. However, the small field of view of ALMA makes large surveys challenging. Several groups have tried different approaches to optimize ALMA's resources and search for the faint population. One approach is to look for serendipitous detections using archival observations obtained for other scientific goals (Hatsukade et al., 2013; Ono et al., 2014; Carniani et al., 2015; Fujimoto et al., 2016; Oteo et al., 2016). Another approach is to observe a contiguous field using ALMA (Dunlop et al., 2017; Kohno et al., 2016; González-López et al., 2017; Franco et al., 2018).

A third approach made use of the available deep optical-NIR surveys to develop a triple color selection technique for identification faint galaxies (Chen et al., 2016a). These pilot studies are attempting to address the contribution of faint SMGs to the

[1]We have provided only a selected number of references here. Refer to Section 3 in Casey et al. (2014) for a complete list.

CIB, their multi-wavelength counterparts, and their role in shaping galaxy formation. The number count studies revealed that faint SMGs contribute significantly to the extragalactic background light (EBL) at 1.1 mm. Fujimoto et al. (2016) found that the contribution of faint SMGs ($0.02\,\mathrm{mJy} < S_{1.2\,mm} < 1\,\mathrm{mJy}$) can account for all of the CIB at 1.2 mm If we assume a median redshift, $z \sim 2$, the IR luminosities of faint SMGs are expected to be in the range $10^{11-12}\,\mathrm{L}_{\odot}$ (Chen et al. 2016a). Therefore, this population bridges the gap between extreme star-forming galaxies (bright SMGs) and optical-color selected galaxies with moderate star-formation rates, e.g., Lyman Break Galaxies (LBGs)[2] and star forming BzK galaxies (sBzKs)[3] (Chen et al., 2016a).

Based on optical-NIR color-color plots, the faint SMGs from Fujimoto et al. (2016) were found to represent LBG/sBzK galaxies. However, these studies suffer from small number statistics, and very little is known about this newly discovered population. Robust estimates of demographics, such as number counts, the redshift distribution, the contribution to the cosmic star formation rate density (SFRD), the nature of their multi-wavelength counterparts, and the star formation rate distribution are some of the key issues that need to be addressed.

In this paper, we study faint SMGs in the XMM Large Scale Structure (XMM-LSS) field with multi-band optical and infrared survey data that have serendipitous submm counterparts identified in archival ALMA observations. Many of the sources identified in our sample are faint SMGs, with $\sim$ 1 mm fluxes below 1 mJy. We investigate the properties of this cosmologically important galaxy population by performing multi-band forced photometry to obtain photometric redshifts and place constraints on star formation. Our study also highlights the growing opportunities for probing high-redshift galaxy properties and gaining new insights on cosmic assembly by

[2]See Steidel et al. (1996) for more on the properties of LBGs.
[3]See Daddi et al. (2004) for the formal definition of SBzKs.

mining the ALMA archive.

In Section 4.2, we describe our sample selection procedure. Details on our reduction of the archival ALMA data, source finding strategy, multi-band photometric catalog construction, and photometric redshift determination are given in Section 4.3. We discuss the multi-wavelength source properties of our sample in Section 4.4 and provide a summary of our results in Section 4.5. Throughout this study we adopt a ΛCDM cosmology with $\Omega_{\rm M} = 0.3$, $\Omega_\Lambda = 0.7$, and $\rm H_0 = 70$ km s^{-1} Mpc^{-1}.

4.2 Sample

4.2.1 Optical and Infrared Data

Our sample is drawn from the XMM-LSS field. The XMM-LSS field includes abundant multi-band data at optical and infrared wavelengths from a variety of wide-field surveys. Of particular importance is the availability of deep *Spitzer* IRAC observations at 3.6 and 4.5 μm from the *Spitzer* Extragalactic Representative Volume Survey (SERVS; Mauduit et al. 2012) and DeepDrill (P.I. Mark Lacy). SERVS is a post-cryogenic IRAC survey of five well-studied astronomical deep fields with a depth of 2 μJy and a total sky footprint of 18 deg^2. The DeepDrill survey expands upon the sky coverage of SERVS and provides deep IRAC imaging in three of the four predefined Deep Drilling Fields for the Large Synoptic Survey Telescope over an area of 38.4 deg^2 ($\sim$1 Gpc^3 at $z > 2$).

Observations at 3.6 and 4.5 μm are crucial for detecting rest-frame optical emission from galaxies at $z > 4$, and, when combined with additional photometry at optical and NIR wavelengths, provide constraints on important galaxy properties such as photometric redshift. The SERVS and DeepDrill observations in the XMM-LSS field are complemented by additional NIR data from the ground-based VISTA Deep Extragalactic Survey (VIDEO; Jarvis et al. 2013) in the Z, Y, J, H, and Ks bands. In the optical, wide-field data are available from the Canada-France-Hawaii Telescope Legacy Survey Wide field 1 (CFHTLS-W1; Gwyn 2012) and multiple tiers from the first data release of the Hyper Suprime-Cam Subaru Strategic Program (HSC; Aihara et al. 2017). We include the NIR data from SERVS/DeepDrill and VIDEO, as well as broad-band optical data from HSC in the $grizy$ filter set and data from CFHTLS-W1 in the u band in our analysis. Thus, we have a total of 13 bands available for determining photometric redshifts. We illustrate the sky coverage of these surveys in Figure 4.1.

4.2.2 Archival ALMA Data

We mined the ALMA archive to search for continuum observations within the XMM-LSS field that were publicly available as of July 2017. We required the following criteria for selecting the archival ALMA data: 1) observations performed in Band 6 ($211 - 275$ GHz) or Band 7 ($275 - 370$ GHz), 2) a source integration time longer than 150 seconds to ensure sufficient sensitivity to the inherently faint SMG population , and 3) an angular resolution of $\theta_{\mathrm{FWHM}} > 0.4''$ to ensure adequate surface brightness sensitivity. After evaluating the central depths for all the available programs making the resolution cut, we found that our integration time criterion leads to a maximum 1σ rms noise of 150 μJy beam^{-1} in Band 6 and 300 μJy beam^{-1} in Band 7, respectively. Given the nature of our source search, the source depth is variable [4] and therefore, finding a complete census of faint SMG is not a primary goal of our search in this paper. We aim to find as many faint galaxies as we can to build up a large sample of

[4]The source search depth depends on the integration time as well as the distance of the source from the ALMA pointing center. As the noise increases towards the edge of the field of view due to the primary beam response, the sensitivity is variable within each pointing. Therefore, specifying the completeness limit would not be meaningful for our study, which aims to explore the properties of the faint SMG population rather perform a statistically complete analysis.

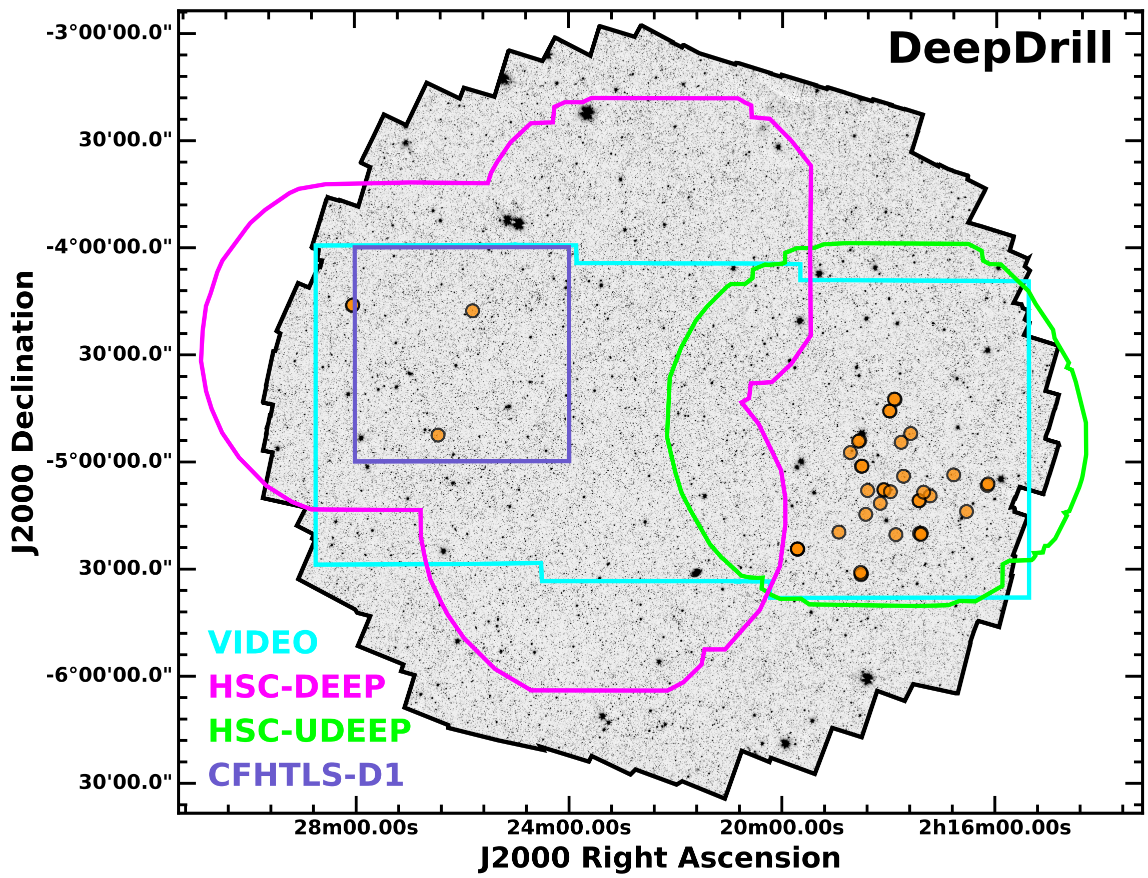

Figure 4.1: The multi-band coverage by the surveys used in our study in XMM-LSS field. The grayscale image is the DeepDrill 3.6 μm mosaic, the cyan region traces the VIDEO coverage, the green region shows the HSC ultradeep tier, the magenta region denotes the HSC deep tier, and the purple region shows the CFHT-LS coverage. The orange circles indicate the ALMA sources with optical/NIR counterparts identified in this study.

the faint population having comprehensive multiwavelength coverage. Such a sample will allow us to conduct detailed studies which will help guide future statistical studies.

Our search identified 75 continuum maps from nine different projects [5], all but one observed in Band 6. The typical RMS noise levels for Band 6 ($\sim$1.2 mm) and Band 7 (870 μm) are 15-140 μJy beam^{-1} and 200-300 μJy beam^{-1}, respectively.

[5]The nine public archival ALMA projects were undertaken for entirely different science goals. Brief descriptions of those goals are given in Appendix 4.2.2.

Therefore, we note that the image depth is not uniform throughout our sample. Table 4.2 summarizes the list of ALMA pointings considered for our study. The angular resolutions of the archival data ranged from 0.53″ to 1.46″.

The ALMA Archival Projects

Nine ALMA projects satisfied our selection criteria given above and were publicly available. These projects were undertaken for entirely different science goals. The data is taken from Ouchi et al. (2013), who observed a giant starburst galaxy at redshift z ~7, called Himiko, at Band 6. The total integration time was about 3 hours reaching noise levels ~ 19 μJy beam^{-1}. Other deep maps were taken from ALMA 2013.1.00815.S (Willott et al., 2015). They have investigated continuum dust emission and [CII] line detections for three more UV-luminous galaxies similar to Himiko found at $z \sim 6$. The total time on the source is about an hour and a half with rms noise levels of 18 μJy beam^{-1}. The ALMA 2012.1.00934.S [PI: Phillip Best] covers four maps in the XMM-field to study the star formation activity in moderately star-forming galaxies at $z \sim 2.53$ using CO molecular line emission. Ikarashi et al. (2015) have observed 30 potential high-z SMG candidates selected from the AzTEC survey. These galaxies are highly likely to be at z >3. This project, ALMA 2012.1.00326.S, has 4 minutes on source time with rms levels between 135-65 μJy beam^{-1}. A 100-minute observation was undertaken by Inoue et al. (2016) [ALMA 2012.1.00374.S, PI: Kazuaki Ota] to study the state of the epoch of reionization and star formation activity at z ~7 using spectroscopically confirmed galaxies at that redshift. The same target was observed for another 75 minutes in the project ALMA 2013.A.00021.S to improve the sensitivity of [CII] line detection. The data from ALMA 2011.0.00648.S is taken to study interstellar medium of 20 star-forming galaxies at z ~1.4 (Seko et al., 2016a,b). The typical rms noise levels range from 60~100 μJy beam^{-1} with 10 minutes of the on-source time. Pentericci et al. (2016) studied a very high redshift galaxy (z ∼7) to understand the role of high-z galaxies in the epoch of reionization. The target was observed for 35 minutes which resulted in 20 μJy noise level. The project 2011.0.00539.S was used to study the ALMA properties of the lensed, bright submillimeter galaxies selected from *Herschel*. The time on each map is about a minute, with typical rms noise levels of 250 μJy beam^{-1}. This ALMA project is the only Band 7 observations we have used in our search.

4.3 Data Analysis

4.3.1 ALMA

Calibration and Imaging

We reduced the archival ALMA data using the Common Astronomy Software Applications (CASA; McMullin et al. 2007) package. We ran the calibration scripts that are provided along with the raw data from the ALMA archive. The calibration scripts include a-priori flagging, bandpass calibration, flux calibration and gain calibration. The calibrated products were examined for further flagging in the uv-plane as well as image plane. We found that the provided script had flagged most of the bad data and very little additional flagging was required.

We used the CLEAN task to form and deconvolve images with the recommended parameters provided by the ALMA observatory. Specifically, CLEAN was run in multi-frequency synthesis (MFS) mode with nterms = 1. The weighting was either Natural or Briggs weighting with a robust parameter of 0.5, and was determined on a case by case basis. Maps with bright targets were self calibrated (using one round of phase-only self calibration) and re-imaged.

Source Extraction

The Python Blob Detector and Source Finder (PyBDSF) tool was used to extract sources from the ALMA maps (Mohan & Rafferty, 2015). Continuum maps without primary beam corrections were used to search for sources. The algorithm looks for image pixels above a specified threshold (here we used threshpix = 3.0). Contiguous pixels above the threshold with a minimum size of 1/3 of the synthesized beam are formed into a single island. An island is considered a valid source if a single or multiple component Gaussian fit is successful.

We have found that PyBDSF works well with the default parameters. However, we set the pixel threshold parameter to 3.5σ instead of 5σ, as the default threshold was too conservative to probe the fainter population. By lowering the threshold, we are increasing the contamination, but prior source position information from the multi-wavelength optical/infrared data will eliminate most of the spurious sources. The preliminary catalog contains all extracted sources, including the science targets of the proposed observations. We have also removed the sources lying at a distance larger than the radius where the primary beam sensitivity drops to 10% of its maximum, and four strongly lensed galaxies that were the targets of some of the original observations. Although PyBDSF provides estimates of several parameters; total and peak flux densities, convolved and deconvolved source sizes, and uncertainties on each parameter, we chose only to use it to identify ALMA source position. Those source positions were then cross-matched with the multi-band optical/infrared data (see Section 4.3.2).

In order to avoid known issues with flux overestimation of faint sources with PyBDSF (Hopkins et al., 2015), we used the JMFIT task from the Astronomical Image Processing Software (AIPS) to measure source fluxes and their uncertainties. For each

ALMA source, we used JMFIT to fit a two-dimensional, single-component Gaussian at the position from our source extraction with PyBDSF. All JMFIT measurements were based on the primary-beam-corrected ALMA images. We have tabulated the ALMA fluxes of our sample sources in Table 4.3.

Detection Threshold

Some spurious detections are likely to contaminate the source catalog, assuming pure Gaussian-like noise. Therefore, it is necessary to determine the signal-to-noise ratio (SNR) cutoff at which an optimal compromise is made between minimizing the number of spurious sources and maintaining a reasonable level of completeness for faint objects. One way to quantify the level of spurious source contamination is to perform a negative peak analysis (Fujimoto et al. 2016; Hatsukade et al. 2013; Ono et al. 2014; Carniani et al. 2015). To accomplish this, we multiplied each ALMA image by -1 and ran PyBDSF using the same input parameters as the ones used in the original source extraction. We then plot separate SNR distributions for all sources extracted from the negative and positive peak analyses.

If a given map only contains noise and no real emission, then the total number of sources in the positive and negative maps would be approximately the same. This will result in a similar source distribution as a function of SNR. However, when real sources are present, we will start to see an excess of positive sources over negative sources above a certain SNR value. The detection threshold for the source catalog can, then, be chosen at a certain value after which the number of positive detections are greater than negative ones. Figure 4.2 shows the number of sources extracted from both the positive and negative maps from our work. Based on this figure, we selected a detection threshold of 3.9σ for the archival ALMA data. Once this threshold was applied, our ALMA catalog was reduced to 176 objects. We then cross-matched this

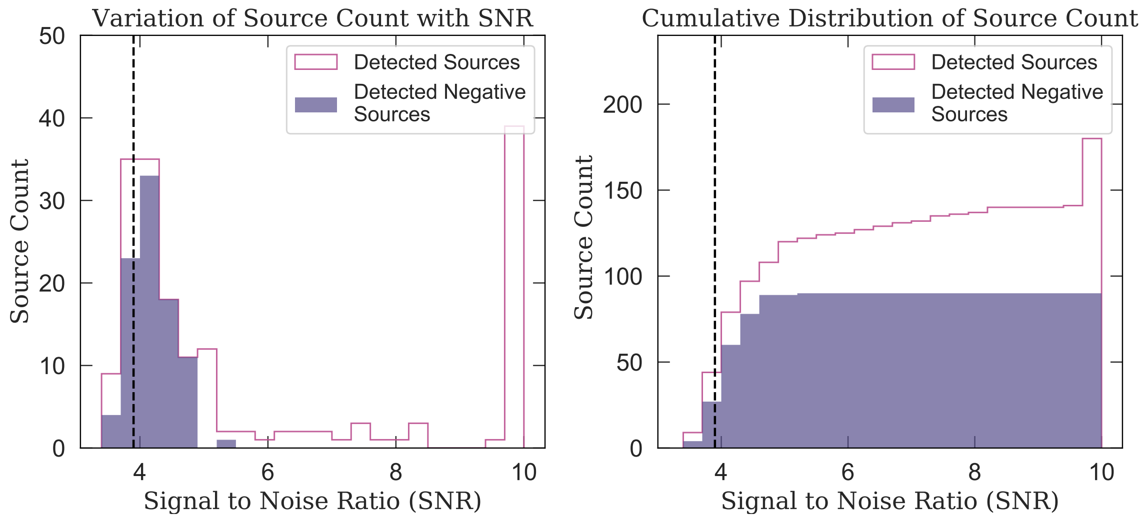

Figure 4.2: Detection threshold for the archival ALMA images. The left panel shows the differential source count and the right panel shows cumulative source count. This analysis was used to select a detection threshold of 3.9σ for the archival ALMA images.

catalog with the optical-NIR photometry (see Section 4.3.2) and found 26 faint SMGs with counterparts within a search radius of $1''$.

In order to check the fidelity of our source selection, we performed the same counterpart matching steps for our negative ALMA source catalog and found 7 out of 88 sources with optical-NIR counterparts. Whereas, we found optical-NIR cross-matches for 26 out of 176 sources in the positive source search. Thus, the combination of our detection threshold in the ALMA data and an optical-NIR counterpart leads to a significantly greater level of fidelity compared to the level (50%) that the 3.9σ ALMA detection threshold alone would provide.

In extracting sources from the negative maps, we did find a few targets with multi-Gaussian structures. As we do not expect to see any complex sources, this could be due to image artifacts. Therefore, we excluded sources with such structures from our catalog. We note that we have not estimated the formal completeness of our ALMA catalog, nor are we conducting a number count analysis. Since we are limited by the availability of data in the archive, our sample will naturally be incomplete. In this paper, we focus on investigating the multi-wavelength properties of our sample of faint SMGs.

Comparison with Previous Studies

A few of the ALMA pointings in our sample and that of Fujimoto et al. (2016) overlap, which provides us with an opportunity to compare methodologies, source counts, and source fluxes in the respective samples. In total, 20 ALMA pointings from three different archival programs (ALMA #2011.0.00115.S, #2011.0.00648.S, #2012.1.00934.S) are common with Fujimoto et al. (2016). The source extraction parameters for our study are different from Fujimoto et al. (2016). The authors have selected sources above SNR of 3.4σ within a search radius having primary beam sensitivity of 50% or larger. Whereas, we used 3.9σ as an SNR threshold and a search radius having primary beam sensitivity greater than 10% of its maximum. In our source extraction, we found 26 sources above 3.9σ within those 20 pointings. And Fujimoto et al. (2016) found 14 sources above 3.4σ, out of which 6 sources are above 3.9σ. Those six sources are also detected in our sample. Therefore, source counts of both the studies are consistent when same source extraction parameters are selected. Furthermore, the estimated flux densities also agree within the quoted uncertainties for those six sources.

4.3.2 Multi-band Forced Photometry

In order to proceed with our photometric redshift and SED analysis, construction of a robust multi-band photometric source catalog is necessary. However, the difference in angular resolution between the *Spitzer* IRAC ($\sim 2''$) and ground-based optical/NIR survey data ($\lesssim 1''$), coupled with the crowded nature of these observations, make the IRAC data prone to issues with source blending. This is problematic for accurate source cross-identification between bands and reliable multi-band photometry.

Recently, Nyland et al. (2017) demonstrated a means of mitigating many of the issues inherent to mixed-resolution optical/NIR datasets using a "forced photometry" approach based on the *Tractor* imaging modeling code (Lang et al., 2016). This code uses prior information on source position and surface brightness profile from a high-resolution, "fiducial" band, along with image calibration parameters including the point spread function (PSF), to model the source flux in lower-resolution bands. After applying the *Tractor* to a one square degree test region of the XMM-LSS field, Nyland et al. (2017) found a number of improvements in the resulting multi-band forced photometry compared to traditional position-matched source catalogs. In particular, they found that the *Tractor* forced photometry decreased susceptibility to blending issues, led to more reliable source cross-matching between bands, identified a larger number of candidate high-redshift ($z > 5$) objects, and produced more accurate photometric redshifts when compared to available spectroscopic redshift data.

We have adopted a strategy similar to that described in Nyland et al. (2017) in constructing the optical/NIR source catalog used for determining photometric redshifts of the ALMA sources in our study. This strategy requires an initial, position-matched input catalog that is constructed by cross-matching the positions of the ALMA sources with positions from VIDEO[6] using a search radius of $1''$. Thus, each source in this "VIDEO-selected" input catalog has a detection in the VIDEO catalog in at least one band.

In addition, a "fiducial" VIDEO band is selected for each source that is used for determining the source surface brightness profile model to be applied during the

[6]VIDEO source catalogs and images were obtained from the fifth data release available at http://horus.roe.ac.uk/vsa/.

Tractor forced photometry. We preferentially select the VIDEO Ks-band to be the fiducial band, but if the source is not detected at Ks-band, we set the fiducial VIDEO band to the next closest filter in wavelength to the IRAC 3.6 μm band that has a detection reported in the VIDEO source catalog. We note that of 26 ALMA sources with optical-NIR counterparts in our catalog, 23 reside in the UltraDeep tier of HSC (5σ i-band depth $\sim$ 27.2 mag) and 3 sources reside in the Deep HSC tier (5σ i-band depth $\sim$26.5 mag).

For each source in our VIDEO-selected input catalog, we extracted a cutout of the image in each of the 13 bands in our analysis with a half-width of $10''$. To account for spatial variations in the image properties, we measured the sky (RMS) noise and the median background sky level in each image cutout using iterative sigma clipping with Photutils[7]. We then fit the source fluxes using the *Tractor*, which convolves the source surface brightness profile model with the image PSF and uses a maximum likelihood method to optimize the flux of each source in each band, holding the source position, shape, and image calibration properties fixed. We provide the resulting *Tractor* catalog of the forced photometry in Table 4.4. We also compare the photometry using the *Tractor* with other surveys covering the same field to check consistency of our results. Here we utilize publicly available data release 8 of the UKIDSS-UDS survey. We refer our readers to Appendix 4.3.3 for the detailed discussion.

4.3.3 Photometry Consistency Check

As we compare colors of the faint SMGs with the selection criteria specified by Chen et al. (2016b), it is essential to perform a consistency check within both the data catalogs. Our *Tractor* method utilizes VIDEO catalog whose photometry is in the AB magnitude system. The sample of Chen et al. (2016b) is taken from UKIDSS-

[7] http://photutils.readthedocs.io/en/stable/

Ultra Deep Survey (UDS) data release 8 (DR8). We compare J, H, and K bands from the publicly available DR8[8] with the VIDEO catalog in Figure 4.3. The data points plotted here are the field galaxies lying within the ALMA pointings used in our search. The positions of those objects were cross-matched with the publicly available UDS DR8 catalog. We show Petrosian magnitudes for both the catalogs in the AB system. Overall, there is a good level of agreement between our photometry and the UDS photometry. We can see a small offset between the K filter used in the UKIDSS-UDS surveys and the K_s filter used in the VIDEO survey. The offset is mainly due to the differences in the filter response functions of K and K_s.

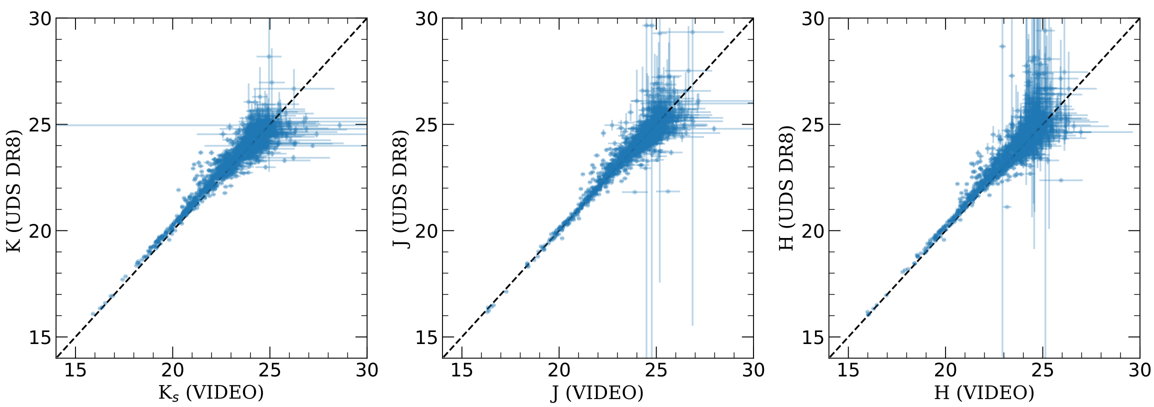

Figure 4.3: The plot shows a comparison of the photometry from our work and the publicly available UKIDSS-UDS DR8 catalog. Our photometry is derived from the VIDEO catalog (See Section 4.3.2). We show Petrosian magnitudes in the AB system for both catalogs. The black dashed line is the equality line. We see overall good agreement between both the observations. A slight offset in the K band is mainly due to the differences in the filter response function.

4.3.4 Photometric Redshifts

Photometric redshifts were estimated using the Easy and Accurate z_{phot} from Yale (EAZY; Brammer et al. 2008, 2011) software. EAZY performs least square fitting

[8]We used the following link to access the UDS photometry. http://wsa.roe.ac.uk:8080/wsa/crossID_form.jsp

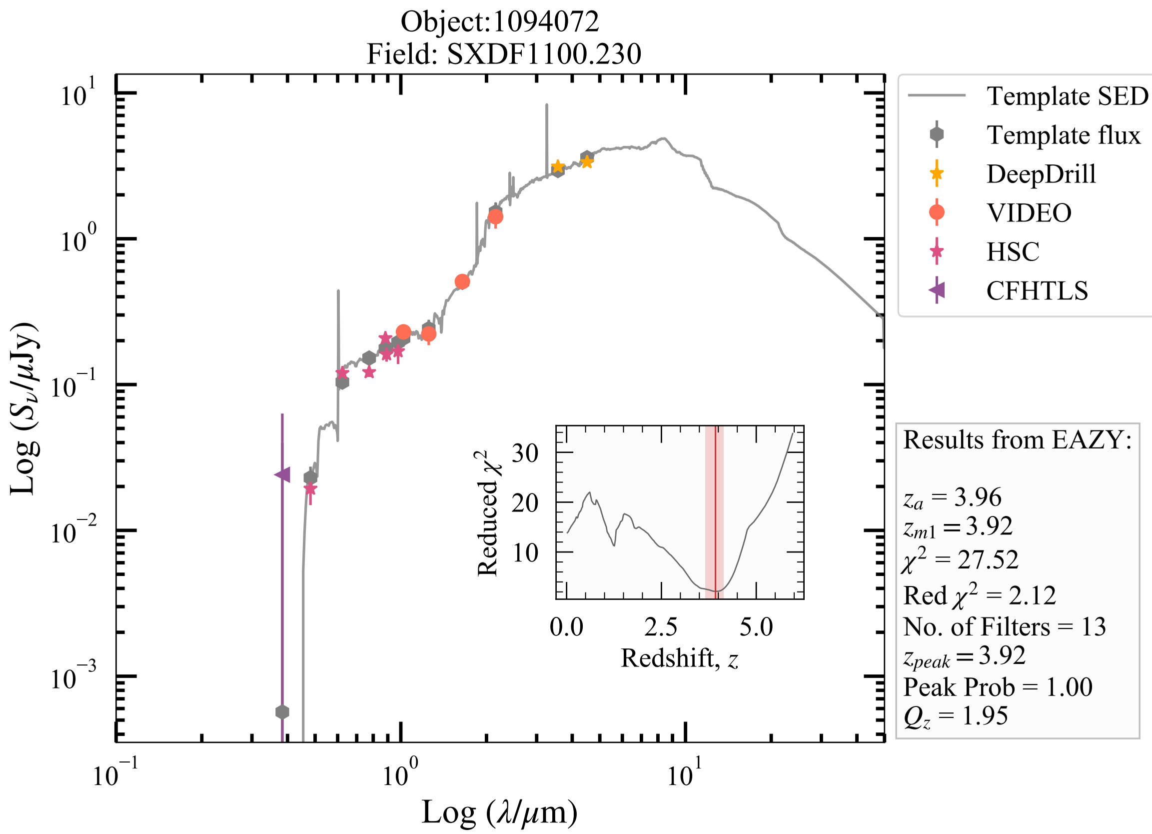

Figure 4.4: An example of our photometric redshift fitting using EAZY for one of the sources in our sample. The main plot is the observed galaxy SED. Different colored symbols correspond to the observed 13-band photometry obtained using the *Tractor* image modeling code (Section 4.3.2). Yellow stars highlight *Spitzer* DeepDrill measurements at 3.6 and 4.5 μm, orange circles denote measurements from the VIDEO survey, the purple triangle represents the optical u-band data from CFHTLS, and pink stars mark the optical data points from HSC. The fitted SED template is plotted in gray and the estimated template flux for each filter is shown by the gray filled circles. The box on the right lists key output parameters from EAZY. The inset figure shows the χ^2 distribution of the fit at each redshift bin. The peak of the redshift distribution after applying the prior is shown by the red vertical line and the shaded region is the 95% confidence interval of the fit.

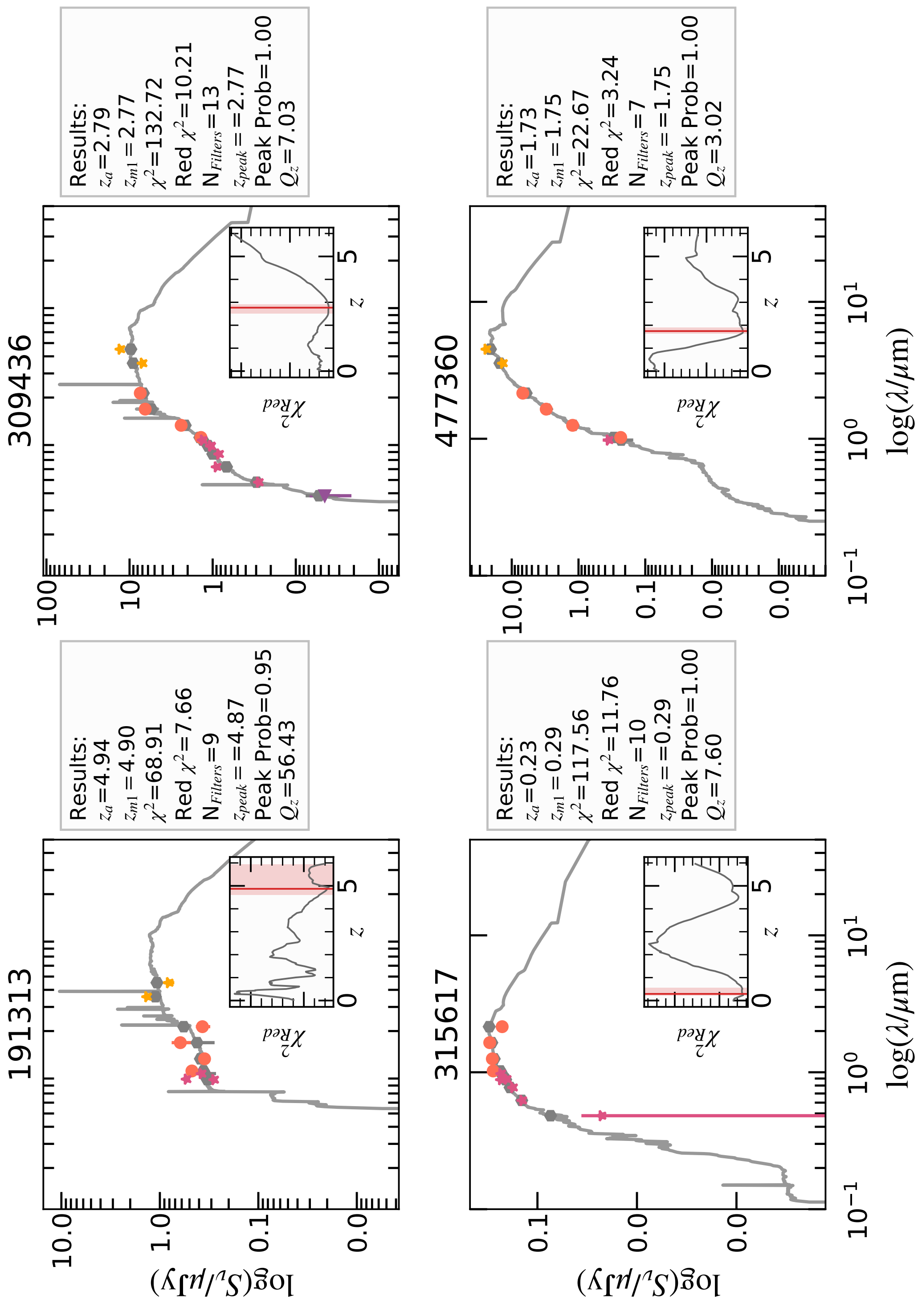

Figure 4.4: Continued

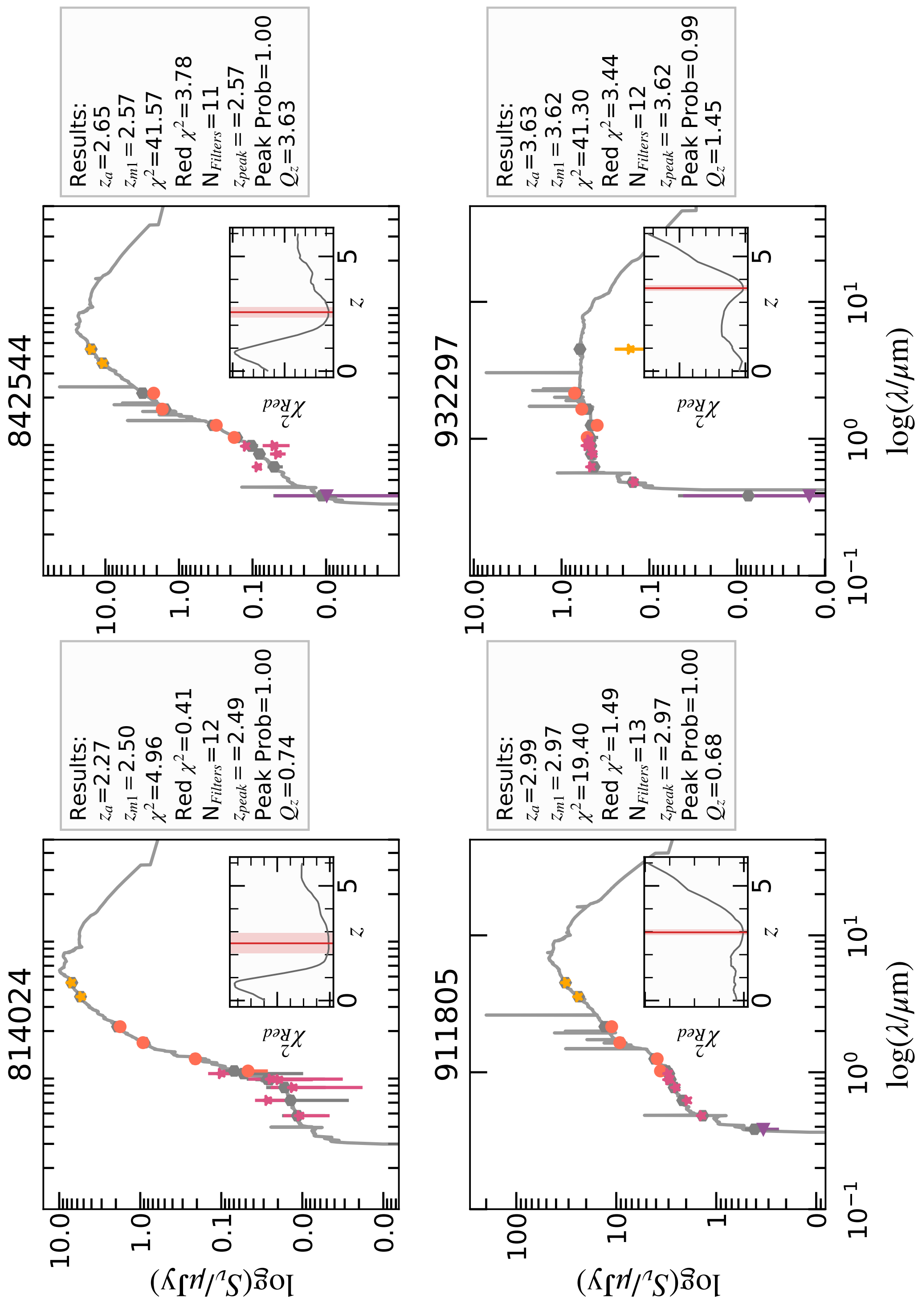

Figure 4.4: Continued

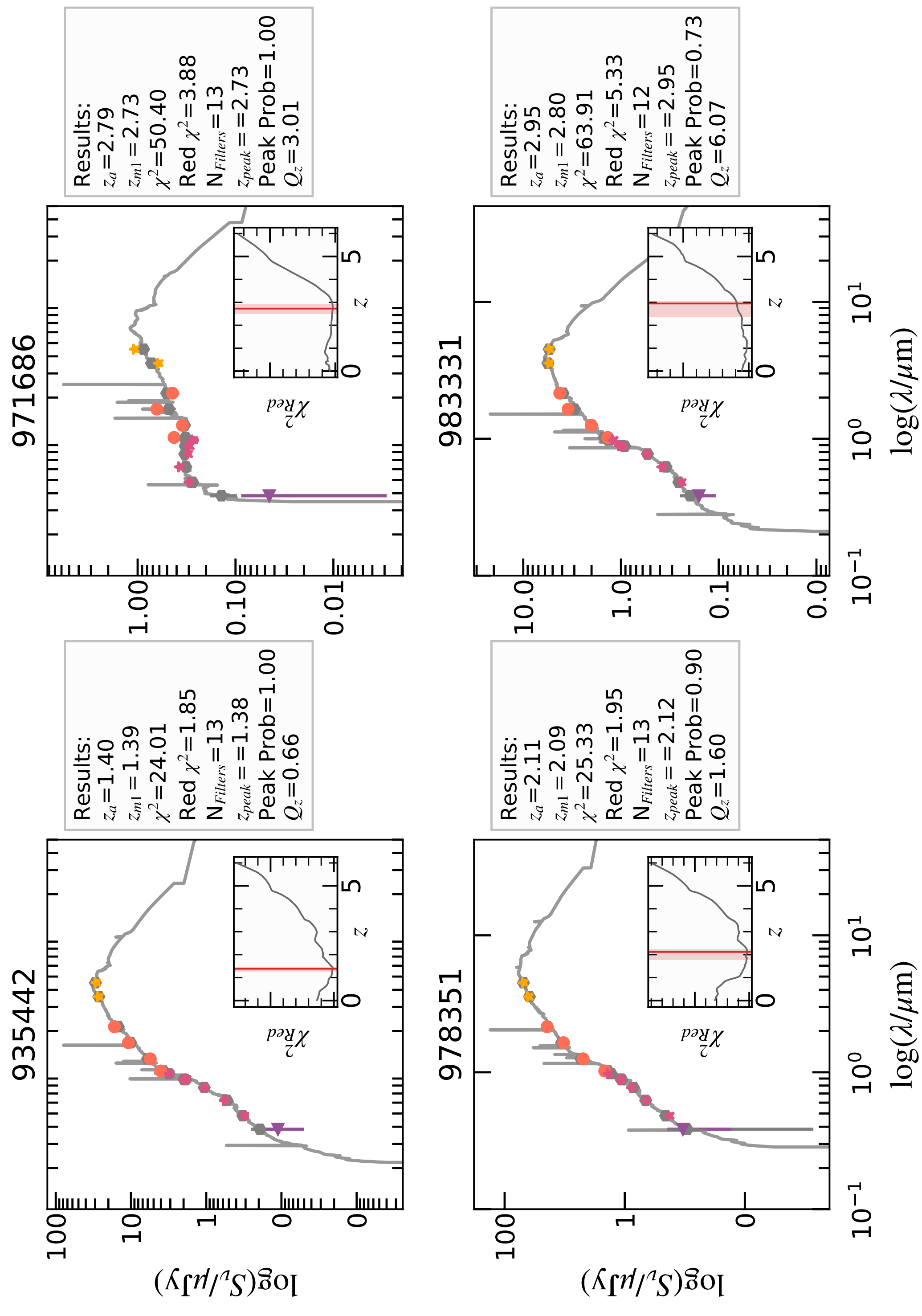

Figure 4.4: Continued

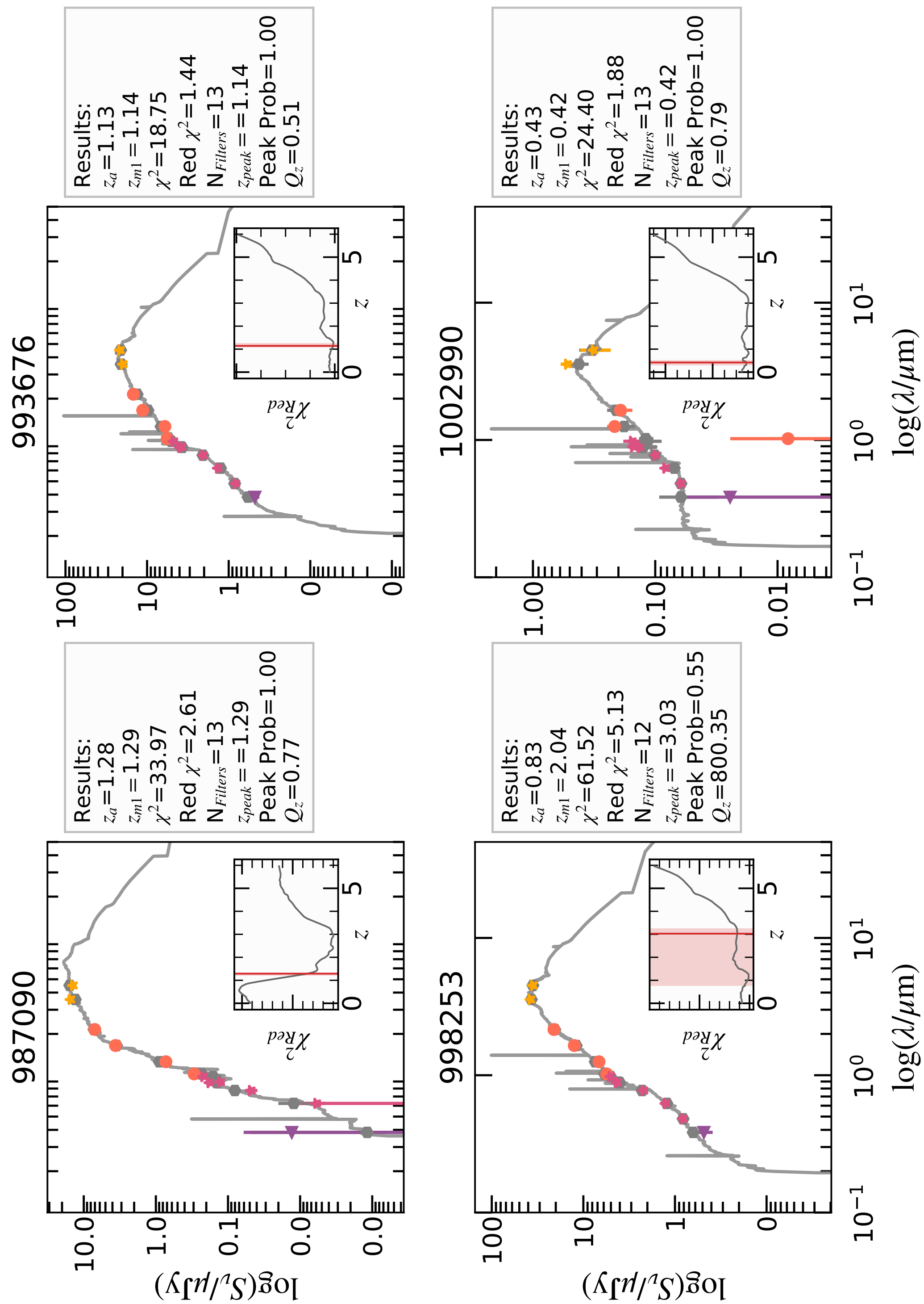

Figure 4.4: Continued

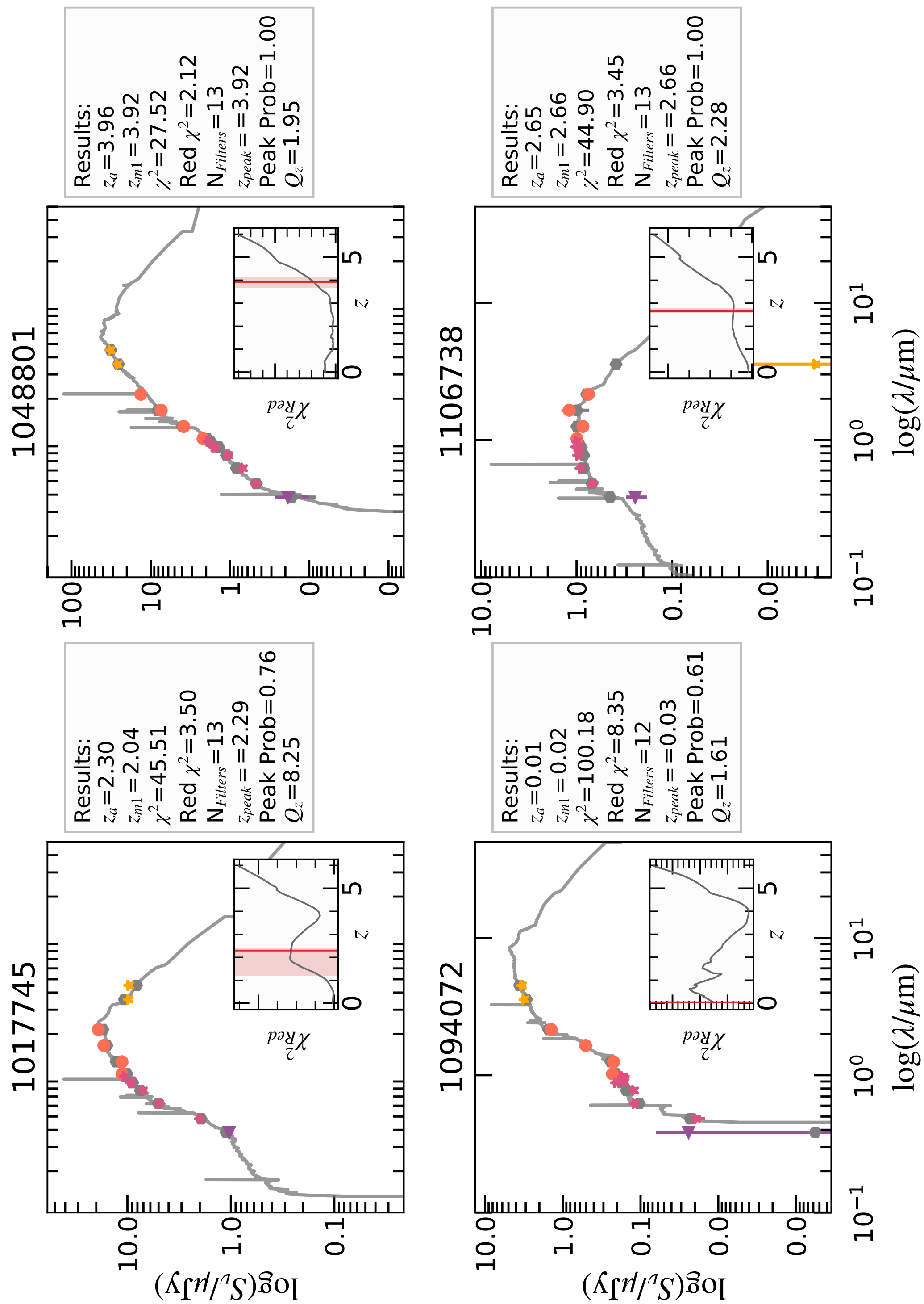

Figure 4.4: Continued

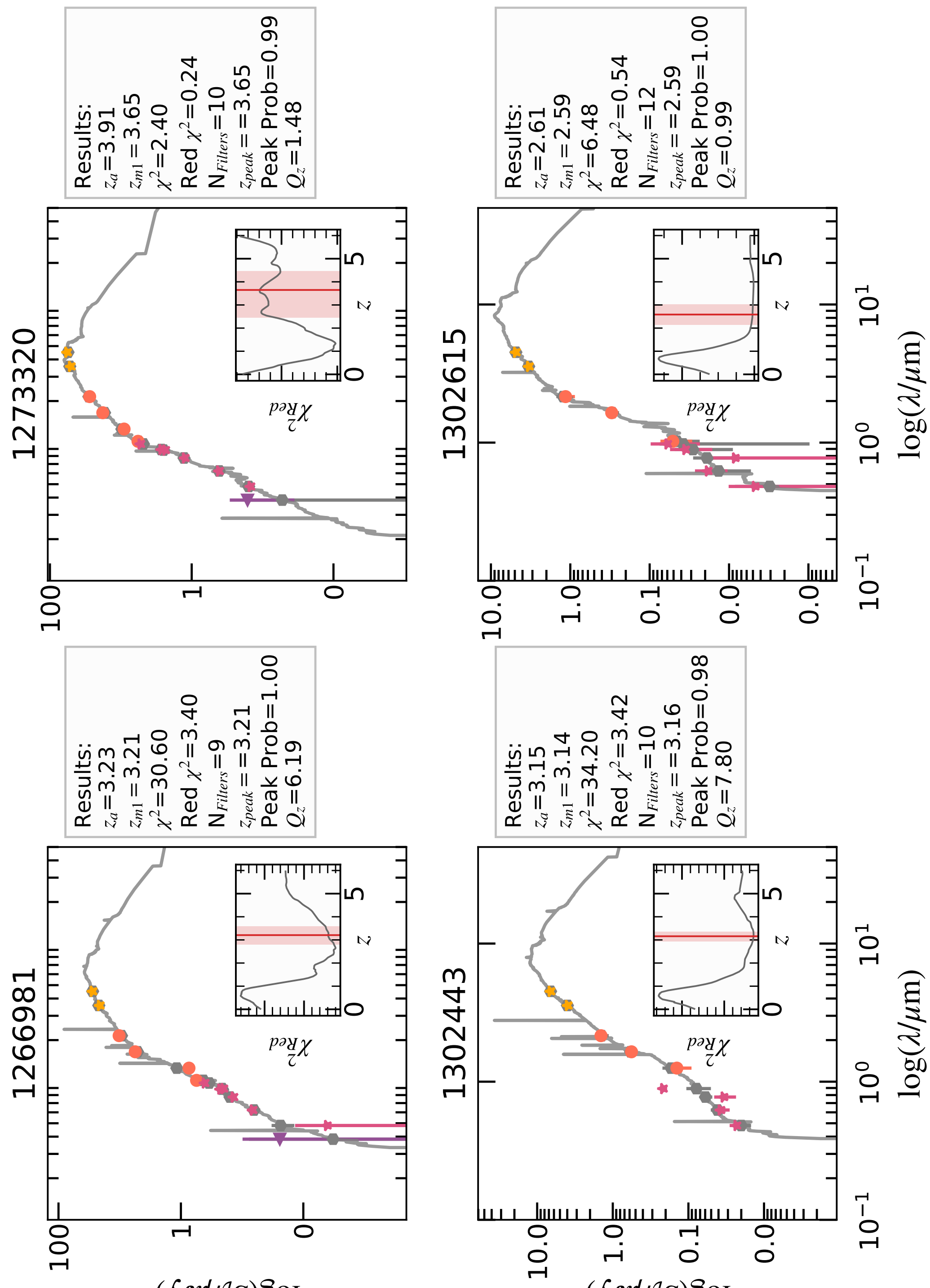

Figure 4.4: Continued

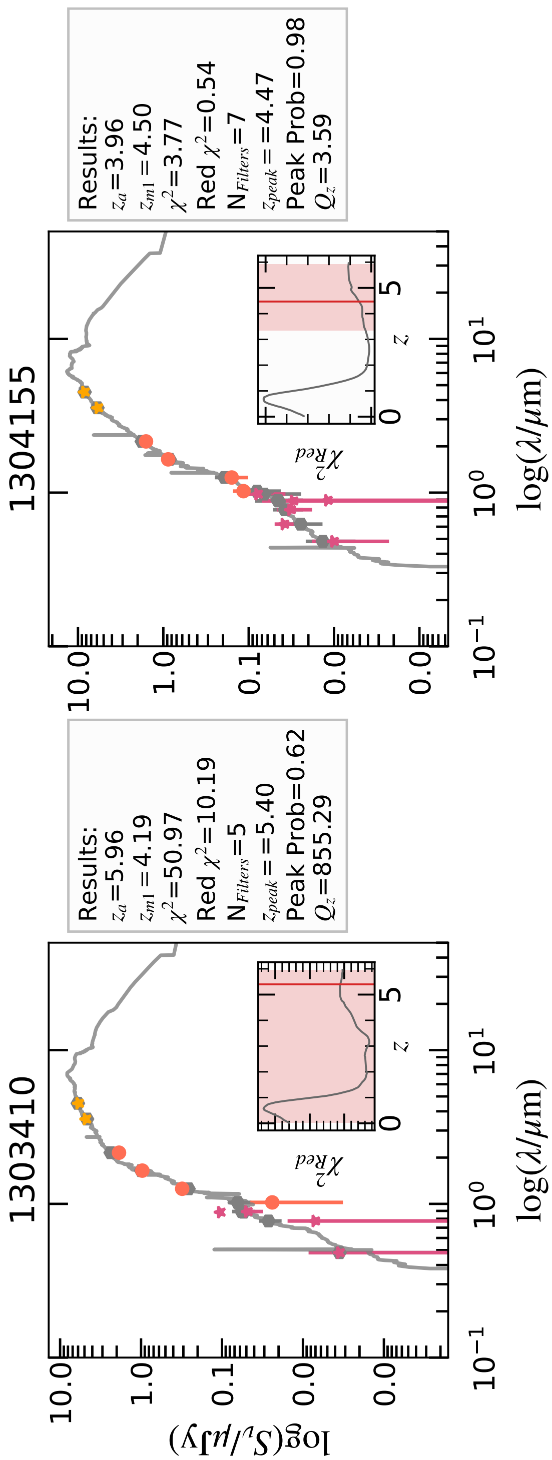

Figure 4.4: Continued

with a linear combination of minimal template sets that can accommodate most of the variations in galaxy properties up to high redshift.

We use a default set SED templates available in EAZY. These templates adequately span the wavelength range to cover the 13-bands used in our analysis (4.5 μm to u band). EAZY provides a full probability distribution for the redshift values in the range $0 < z_{\rm phot} < 6$. We select the photometric redshift of a given source at the value with the highest probability ($z_{\rm peak}$). The confidence intervals are selected such that the integrated probability distribution is equal to 95%, corresponding to the EAZY output parameters $l95$ and $u95$). Table 4.3 provides the photometric redshifts along with the 95% confidence limits of our sample.

We illustrate the EAZY photometric redshift fitting results for our sample galaxies in Figure 4.4. As shown in the green-shaded box in this figure, EAZY provides several diagnostic parameters to quantify the quality of the fit. We emphasize that our photometric redshifts are based on multi-band forced photometry using the *Tractor*, a technique that has demonstrated improved photometric redshift accuracy compared to the use of position-matched multi-band photometric catalogs (Nyland et al., 2017). However, given the inherently dusty nature of our sources that may cause deviations in their SEDs that are not well represented by the templates considered in this study, further verification of their redshifts will require a more in-depth SED analysis (to be presented in a forthcoming study) as well as future spectroscopic observations.

The rest frame colors are also evaluated using best fit SED template in EAZY. To estimate colors, we have used filters U, V, and J[9]. EAZY provides interpolated color indices for each filter of the rest-frame color, such that the colors can be calculated using the following formula; $U - V = -2.5 \times \log(L_U/L_V)$, where L_U and L_V are the

[9] U and V are standard Bessel filters and the J filter follows the definition of Mauna Kea Consortium defined in Tokunaga et al. (2002).

calculated U and V-band luminosities, respectively.

4.3.5 The Final Catalog

We present a catalog of 26 galaxies obtained by cross-matching the ALMA source catalog with optical-NIR observations (Section 4.2.1). The catalog contains 15 new, serendipitously discovered ALMA detections. From the remaining 11 known sources, nine were detected in the previous studies, and three correspond to a single bright *Herschel* source (Bussmann et al., 2015). We explain the properties of all previous detections later in this section. Figure 4.5 shows the four-band (ALMA Band 6 or 7, *Spitzer* 3.6 and 4.5 μm, and VIDEO K_s) snapshots of the entire catalog. Table 4.3 summarizes the ALMA properties of our sample sources, our photometric redshifts, and any previously published redshift information. Throughout this paper, we will be identifying sources by their IAU names given in column 1 of Table 4.3.

Nearly half of our targets (11/26) were previously detected in the SIRTF Wide-area Infra Red Extragalactic Survey (SWIRE; Lonsdale et al. 2004) and have published photometric redshifts using the five-band SWIRE observations (Rowan-Robinson et al., 2008, 2013). Another study that included a large number of our sample galaxies (13 out of 26) is that of Williams et al. (2009). These authors presented a K-band-selected galaxy catalog combining optical-mid IR photometry from SWIRE, the Ultra Deep Survey (UDS) tier of the UKIRT Infrared Deep Sky Survey (UKIDSS; Lawrence et al. 2007), and the Subaru-XMM Deep Survey (SXDS; Sekiguchi & SXDS Team 2004; Furusawa et al. 2008). They have used EAZY to estimate photometric redshifts based on $BRi'z'JK$[3.6 μm][4.5 μm] photometry. Our photometric redshifts are in good agreement with previously published values (when available) within the margin of the uncertainties. We emphasize that the 13-band forced photometry presented here provides redshift estimates that are robust against the effects of source blending

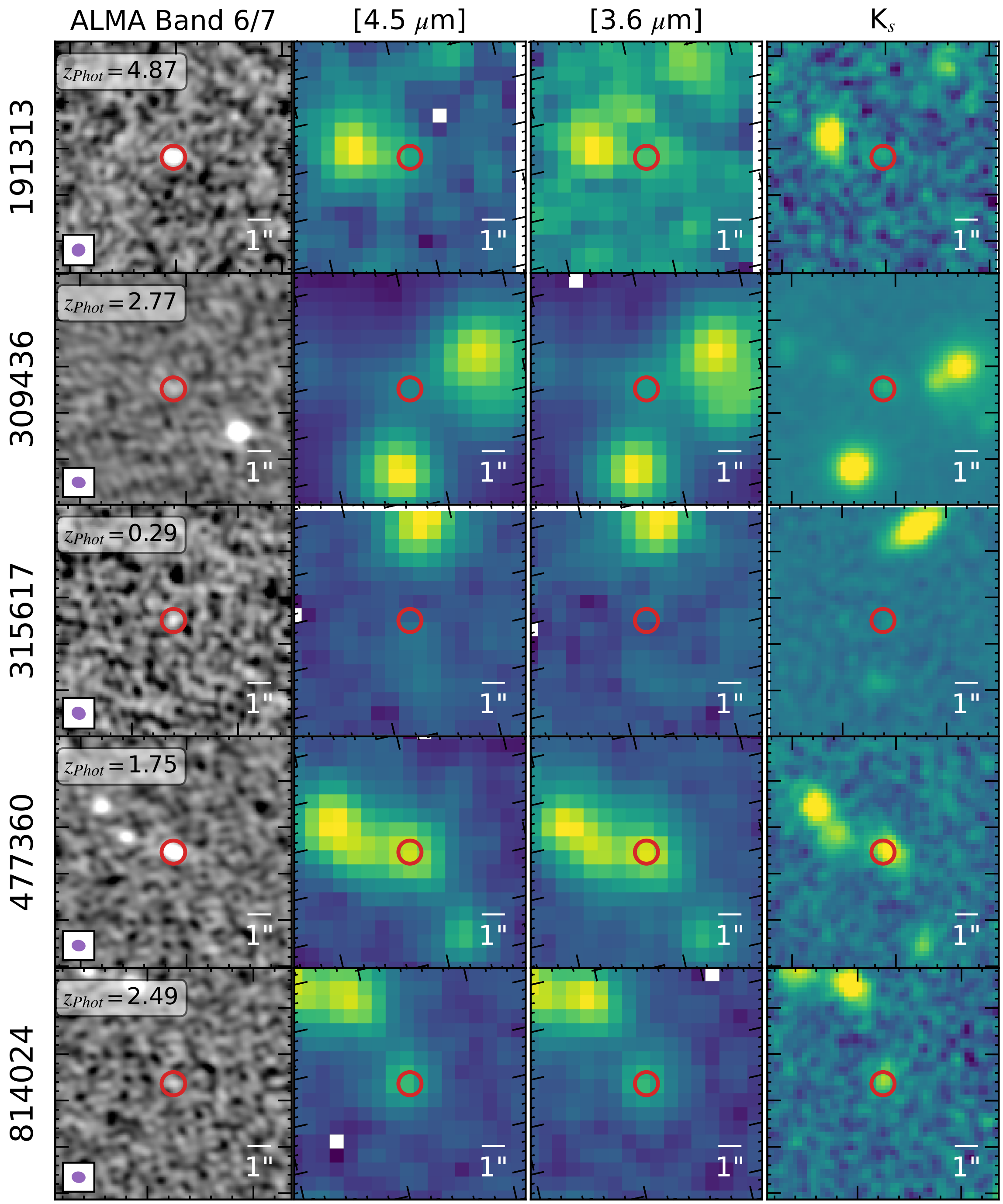

Figure 4.5: Image snapshots of our entire sample in four bands. The grayscale image on the left is the ALMA Band 6/7 image obtained from the archive. The rest are the *Spitzer* 4.5 μm, *Spitzer* 3.6 μm, and VIDEO K_s image left to right. The red circle in each image indicates the position of the ALMA source. Our photometric redshift estimates are also given in the top left corner. Each cutout has a size of $10'' \times 10''$.The purple filled circle in the bottom left corner is the synthesized beam of the ALMA observation.

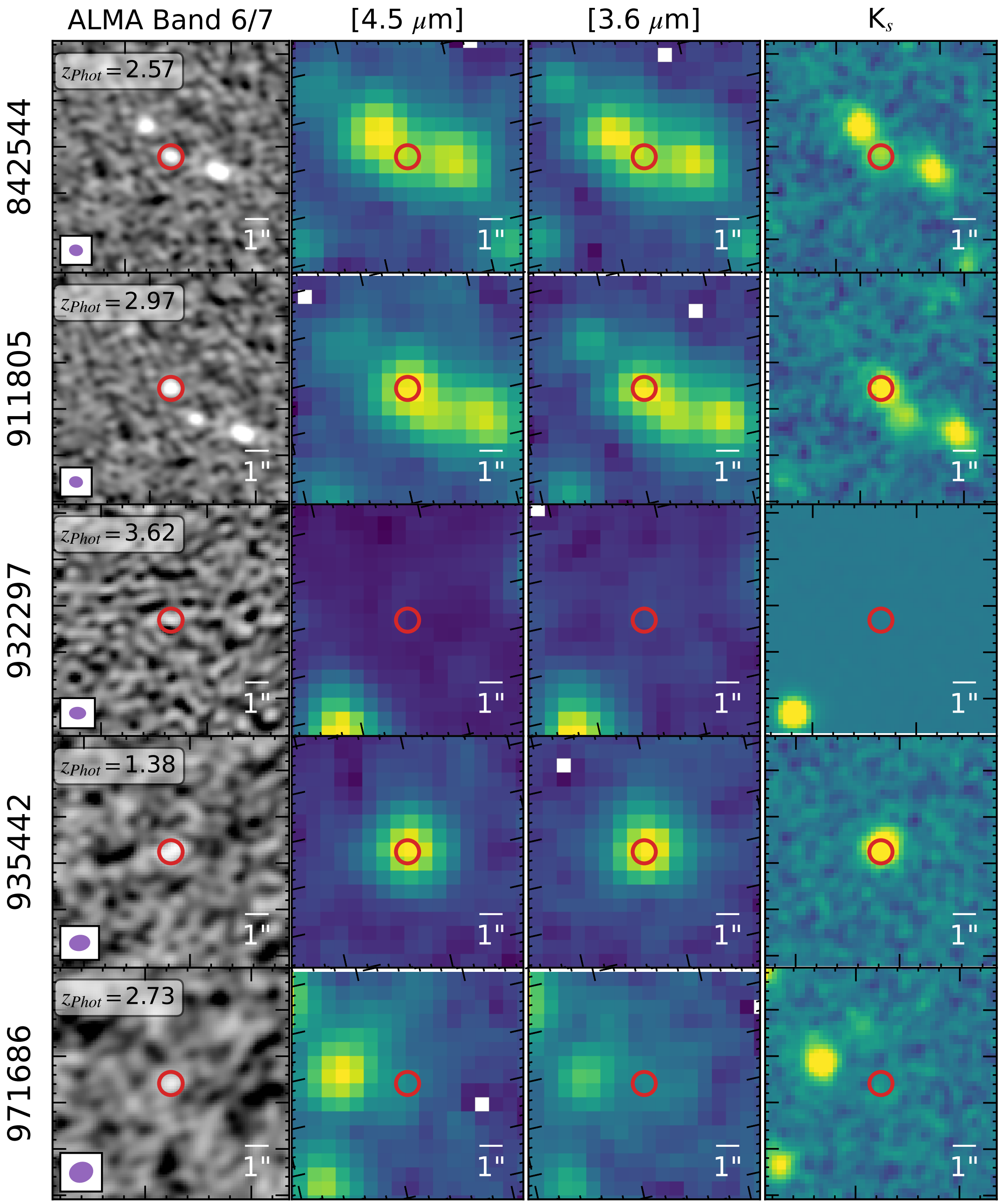

Figure 4.5: *Continued*

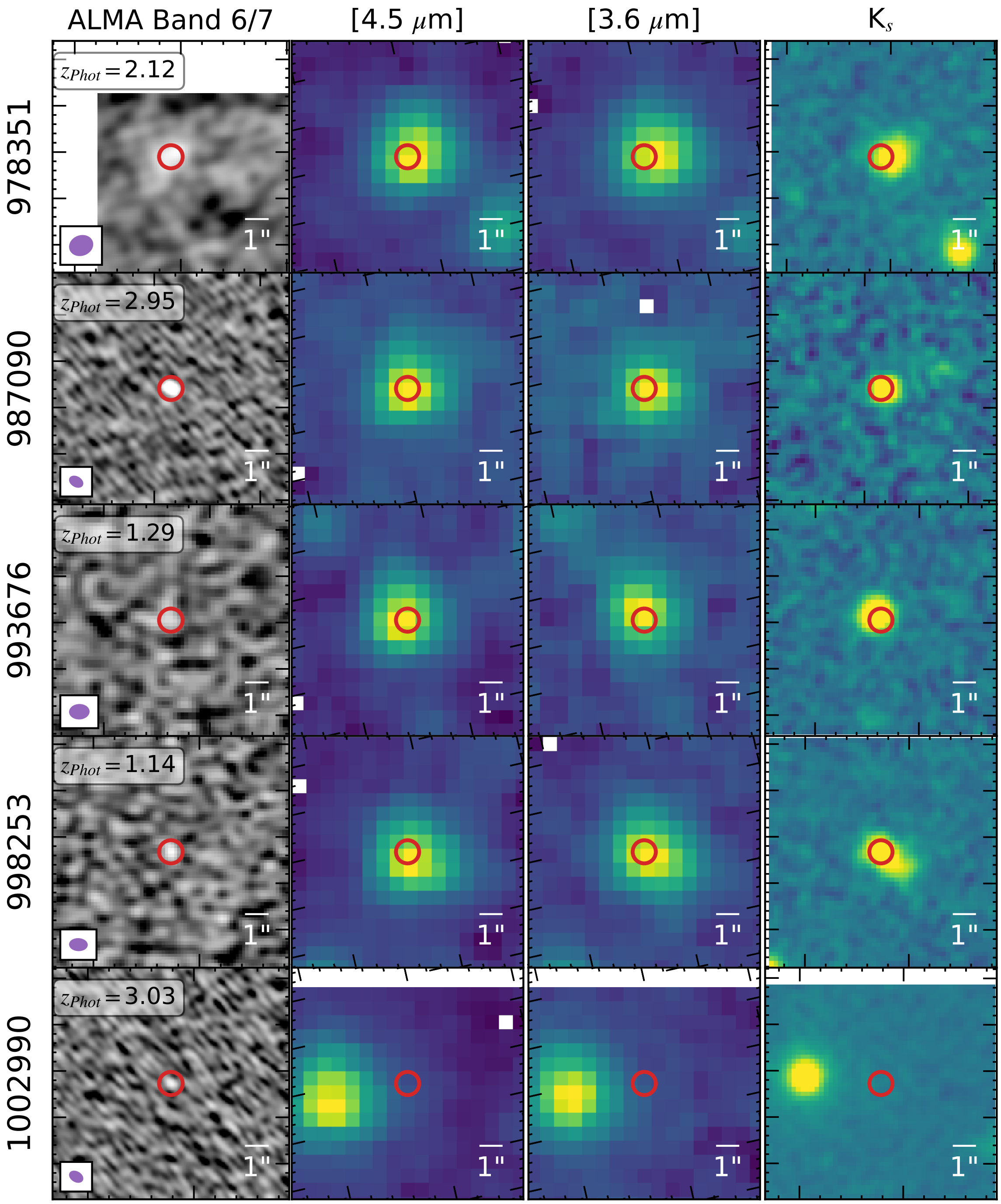

Figure 4.5: *Continued*

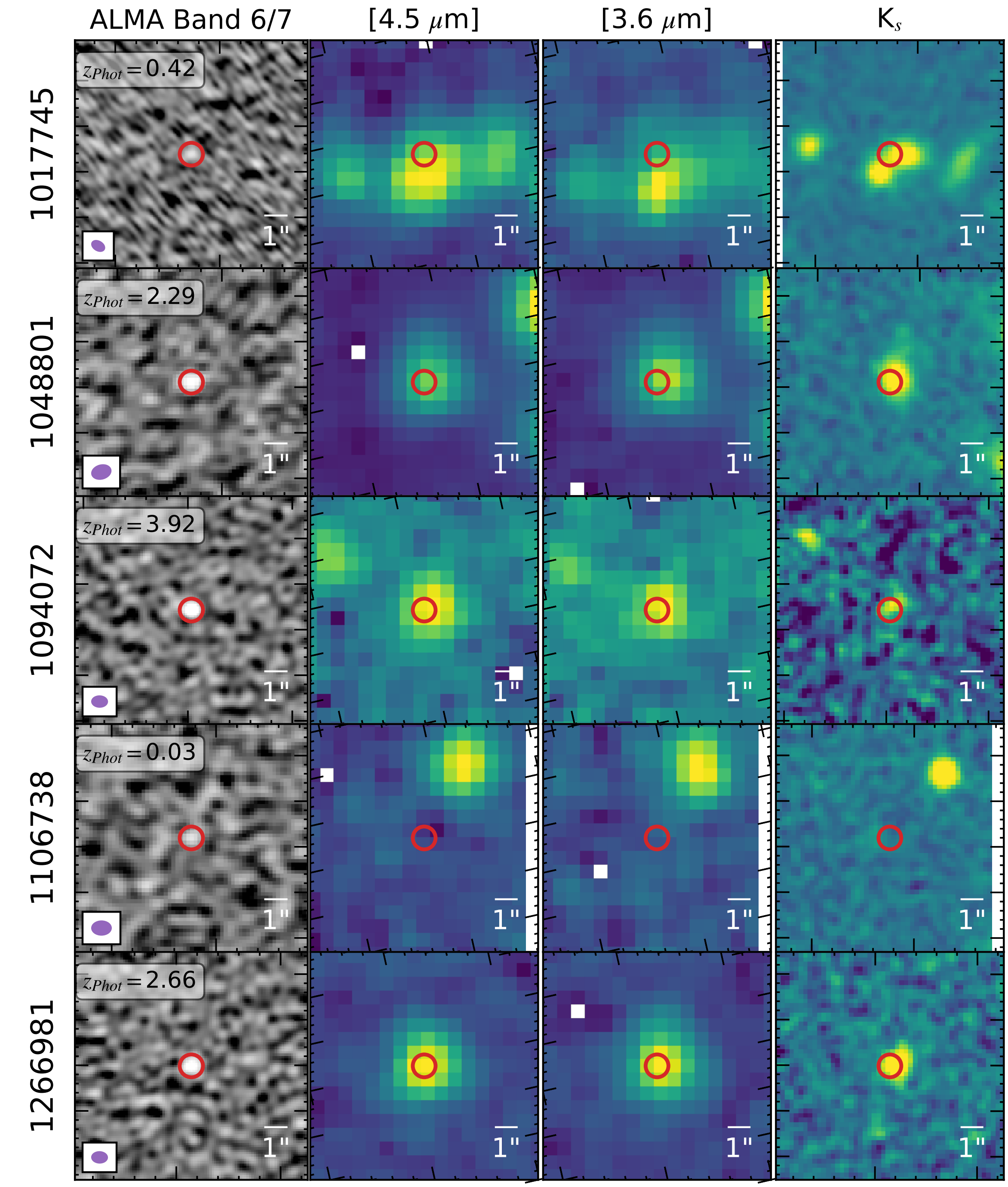

Figure 4.5: *Continued*

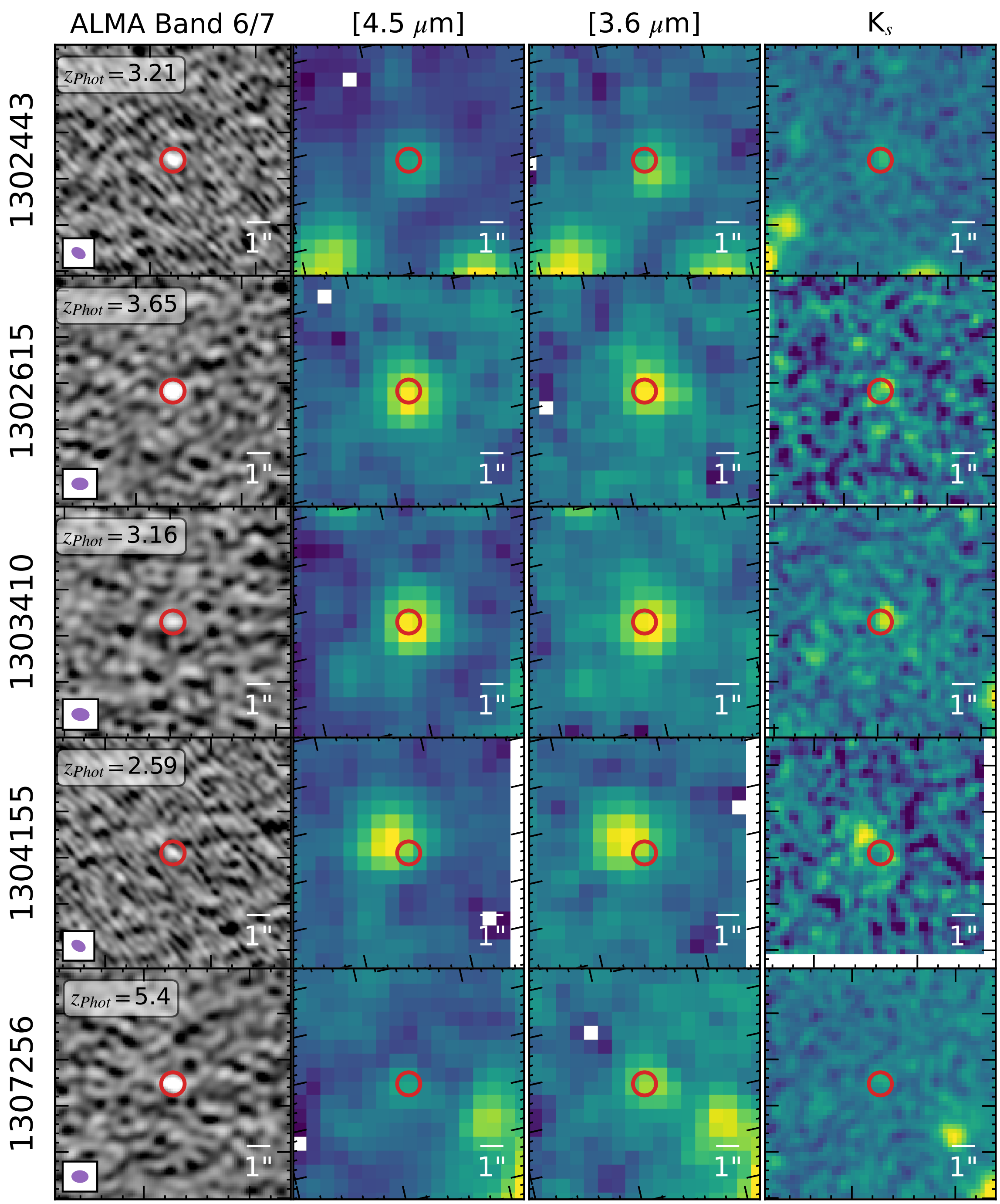

Figure 4.5: *Continued*

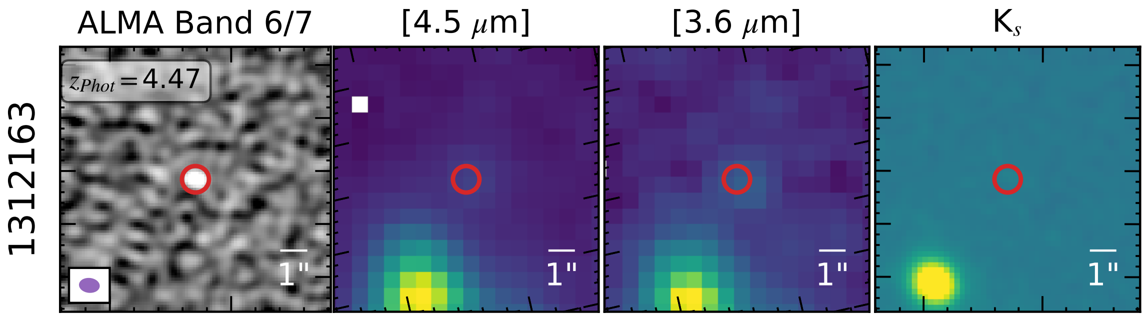

Figure 4.5: *Continued*

in the IRAC bands and utilize a large number of filters compared to the previous studies.

4.4 Discussion

4.4.1 Flux and Redshift Distribution

We show the flux distribution of our catalog in Figure 4.6. 57% of the sources have fluxes fainter than 1 mJy. The binomial uncertainty[10] for each flux density bin is shown as the red line at the center of each bin. We plot the redshift distribution of the entire sample in Figure 4.7. Two separate histograms for different frequency bands (blue for Band 6 and red for Band 7) are shown. The median redshifts for bands 6 and 7 are $\langle z \rangle = 2.72$ and 2.57, respectively. We also compare the median redshift values from our work with other ALMA surveys. Our median redshift falls within the range of redshifts from other recent studies of SMGs.

Béthermin et al. (2015) showed that the median redshift of the sample of dusty galaxies depends significantly on the depth and the observing wavelength of the infrared surveys. They concluded that the median redshift increases with increasing wavelength up to 2 mm due to the negative k-correction. However, increasing the observing depth results in the detections of the lower-redshift, fainter sources. Hence, the observed variation in median values could just be an outcome of the varying depth of the surveys. The 1σ rms level in the ~ 1.1 mm surveys by Aravena et al. (2016) and Dunlop et al. (2017) are 13 μJy beam^{-1} and 30 μJy beam^{-1}, respectively. The median redshift values of their samples are also lower compared to the other studies ($\langle z \rangle =$ 1.6 and 2.15). The survey by Brisbin et al. (2017) has a shallower depth of 150 μJy and, therefore, a higher median redshift of 2.48. Continuing the trend, Franco et al.

[10] The binomial uncertainty is defined as $\sigma_{n_i} = \sqrt{n_i(1 - n_i/N)}$ where n_i is the number of galaxies in bin i and N is the total number of galaxies.

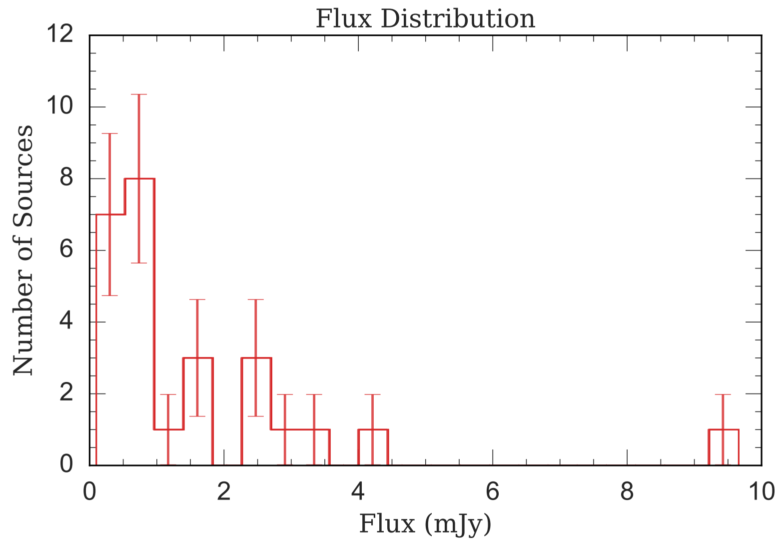

Figure 4.6: The flux distribution of our sample. The red line at the center of each bin is the binomial uncertainty. There are 15/26 galaxies (57%) with fluxes fainter than 1 mJy. Except for one very bright galaxy ($S \sim 9.5\,\mathrm{mJy}$), the rest of the bright sample has fluxes ranging from 1 to 5 mJy.

(2018) found a population at a median value of $\langle z \rangle = 2.9$ based on their survey with a sensitivity of $450\,\mu$Jy. In case of our work, the average depths for the Band 6 and 7 are $110\,\mu$Jy and $300\,\mu$Jy, respectively. As we have only five galaxies in Band 7, we exclude those galaxies from any further analysis involving the median redshift. Even though we find a slightly larger median redshift for a depth shallower than Brisbin et al. (2017), the redshifts and depths are comparable within the margin of errors. Therefore, our redshift distribution is consistent with other studies discussed in this section and the predictions by Béthermin et al. (2015).

4.4.2 Previously Identified Galaxies

As mentioned before, 11 ALMA detections in our catalog are not new. If these targets are DFSGs and unlensed, we have still included them in our catalog. With the availability of multi-wavelength observations from SERVS and our robust 13-

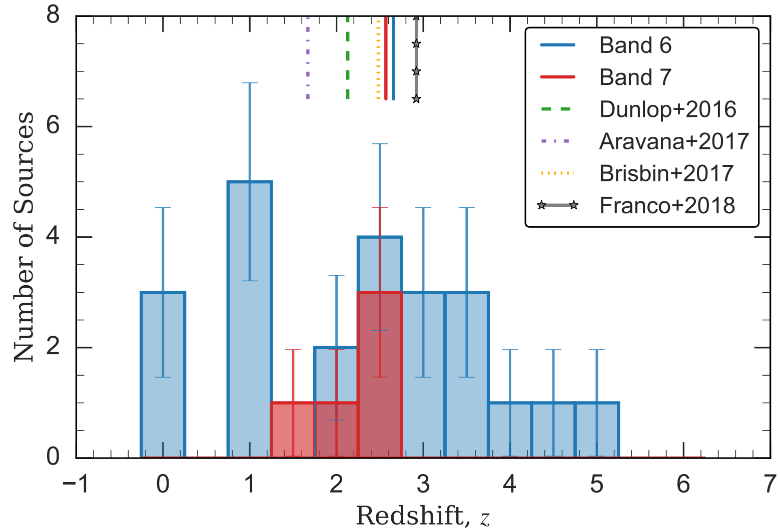

Figure 4.7: The redshift distribution of the faint SMGs. The photometric redshifts are evaluated using EAZY (Section 4.3.4). We show separate histograms for the ALMA frequency bands, 6 and 7. A line at the center of the bin shows the binomial uncertainty in each bin. The vertical lines at the top are the median redshifts for our sample as well as other faint SMG samples. Blue and red solid lines show the median values for the Band 6 and 7, respectively. Other studies included in the plot are: Aravena et al. (2016) – Purple dash-dotted line; Dunlop et al. (2017) – Green dashed line; Brisbin et al. (2017) – Yellow dotted line; Franco et al. (2018) – Gray solid line with star symbols. The average depth for our Band 6 sample is 110 μJy. The median redshift and depth of Band 6 data are consistent with the findings of Béthermin et al. (2015).

band photometry, we can better understand the nature of the previously identified galaxies and the overall population in general. We provide the references to the previous ALMA detection in Column 11 of Table 4.3. Four out of 11 galaxies were serendipitously detected in previous ALMA archival mining studies (J0216−0506, J0217−0454: Fujimoto et al. 2016; Hatsukade et al. 2015; J0217−0442: Fujimoto et al. 2016; J0217−0508: Ono et al. 2014).

Six of the 11 known galaxies are detected in the ALMA follow-up programs of the bright DFSGs. However, we still include targets in our analysis both the faint and bright SMGs belong to the same category of dusty galaxies. Also, it would be interesting to observe differences in the multi-wavelength properties of these two classes. Three of the six bright SMGs belong to a single Herschel source (J0219−0524.63, J0219−0524.77, J0219−0524.84; Bussmann et al. 2015). The Herschel source is resolved into multiple components at the ALMA resolution. The alignment and similar mid-IR colors of these three galaxies indicate an overdense region. The ALMA flux densities of these targets are larger than the rest of our sample galaxies, but we will still include them to compare the physical properties. Rest of the three galaxies (J0217−0508, J0217−0445, J0217−0504) are selected from the AzTEC survey. These dusty, $z > 3$ bright SMGs are thought to be the progenitors of low redshift massive ellipticals (Ikarashi et al., 2015). They typically host a compact starburst in their centers, and their luminosities are comparable to nearby ULIRGs.

The remaining galaxy J0226−0452 from the WMH5 field is a $z \sim 6$ UV-luminous Lyman-break galaxy (Willott et al., 2013). As some of the sources in our sample are part of the original ALMA program, that could lead to potential environmental biases in our results. However, 10 out of 11 galaxies are either faint SMGs or selected from bright SMG surveys. Only one galaxy from our sample is the primary target of the original ALMA program, and no other galaxy has the same redshift as the primary target (where the redshift of the primary target is known). Given the small amount of overlap between the ALMA primary targets and our faint SMGs, we do not believe that our sample is significantly affected by environmental biases.

Spectroscopic redshifts are available for three targets (J0226−0452, J0216−0506, J0217−0454) taken from different studies, and the references are given in the Table 4.3. Target J0216−0506 is detected in most of the studies mentioned above, and Seko et al. (2016a) have discussed the spectroscopic redshift and ISM properties of that galaxy. It is a member of the sample of $z \sim 1.4$ star-forming main sequence galaxies. CO emission studies with ALMA have indicated larger molecular gas fractions and gas-to-dust ratios than local galaxies. Banerji et al. (2011) have identified the target J0217−0454 as Submillimeter Faint Radio Galaxy (SFRG) which are similar to bright SMGs but have hotter dust temperatures. Its spectroscopic redshift ($z = 1.456$) was measured using [OII] 3727 emission line. In all the cases, the spectroscopic redshifts are well within the 95% confidence interval of our photometric redshifts.

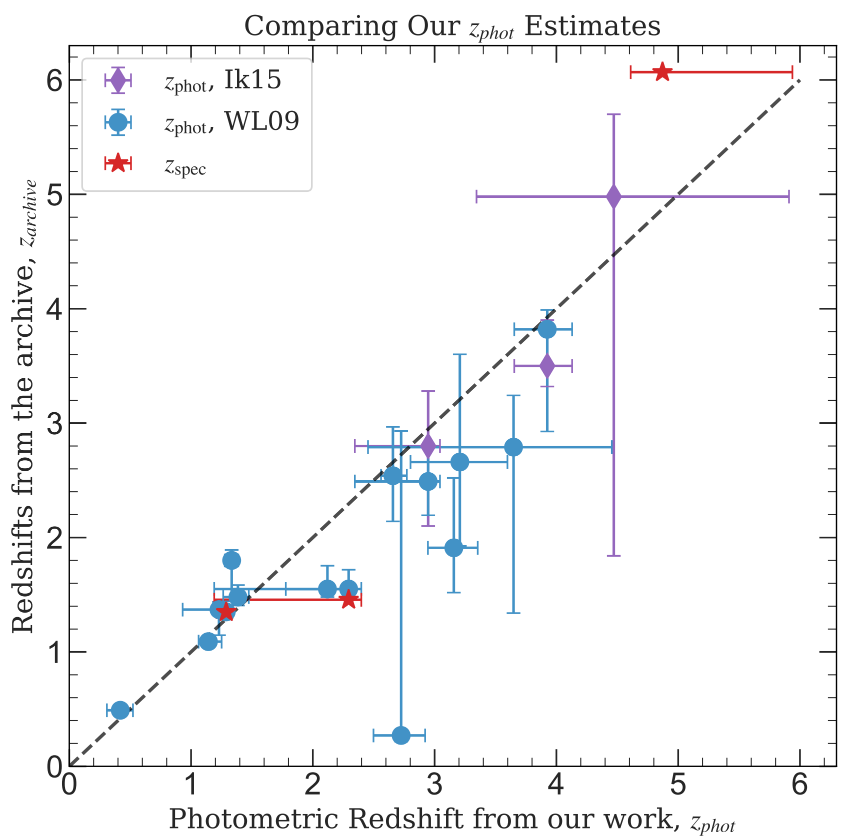

Figure 4.8: A comparison of the photometric redshifts evaluated in this work with redshift estimates from previous studies. A total of 18/26 sources have either photometric or spectroscopic redshifts available in the literature. The red stars correspond to sources with spectroscopic redshifts. The purple diamonds and blue circles have photometric redshift estimates published by Ikarashi et al. (2015) and Williams et al. (2009) , respectively. The uncertainties from our work are smaller than in previous studies, highlighting our improved photometry through the use of the *Tractor* image modeling software.

Figure 4.8 compares the performance of our redshift estimation with archival results. The purpose of this comparison is to conduct a consistency check on the forced photometry technique used in this work. The overall uncertainties on the photo-z estimates are small in most cases. The values are in very good agreement at lower redshifts, $z < 2.5$. However, at higher redshifts, we see an increased scatter in the redshift agreement. This could potentially be due to large uncertainties in the photometric measurements, differences in the filters used for the photo-z estimation, and inherent limitations of the SED templates. Our photometry includes u-band data which is lacking in the previous studies. Also, different methods of source deblending in the *Spitzer* bands could lead to differences in the photometry. This issue can be resolved using spectroscopic data.

4.4.3 Optical-NIR Triple Color Selection

Chen et al. (2016b) have devised a selection technique to identify bright as well as faint SMGs using a training dataset from the UKIDSS-UDS field. The method is called Optical-Infrared Triple Color selection (OIRTC) and uses three optical-NIR colors:$z-K_s$, $K_s-[3.6]$, and $[3.6]-[4.5]$. The color cuts are defined such that the mean SMG fraction redder than the color threshold is at least 5%. The training sample contains ALMA and 850 μm SCUBA-2 observations of bright SMGs. By combining radio and optical-NIR selection techniques, their identification is about 83% complete. Chen et al. (2016a) have utilized this technique to identify faint SMGs with expected fluxes, $S_{850\,\mu m} < 2$ mJy.

Here, we compare the optical-IR colors of our faint SMG sample with the color selection method described in Chen et al. (2016b). Figure 4.8 illustrates the OIRTC color selection, where different colored symbols represent our sample along with faint SMG samples of Fujimoto et al. (2016), Hatsukade et al. (2015), Laporte et al. (2017),

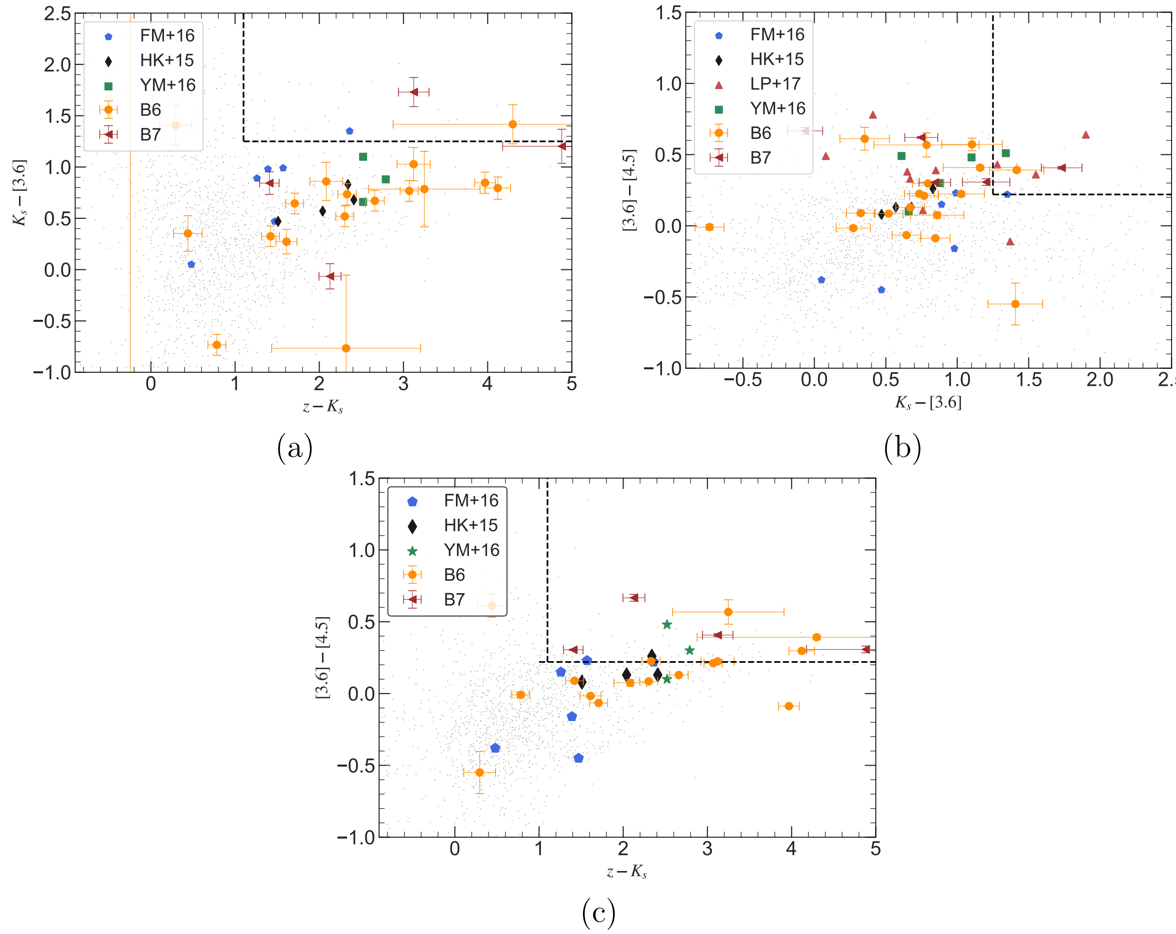

Figure 4.8: The plot shows the SMG OIRTC color selection criteria defined in Chen et al. (2016b). Each sub-figure is a color-color plot of the combination of z, K_s, [3.6], and [4.5] filters. Bright SMGs tend to occupy the reddest part of the color space due to the presence of dust. The black dotted line in each sub-figure is a color cut-off estimated by Chen et al. (2016b) using an ALMA sample of bright SMGs. The fraction of SMGs in the population redder than the color threshold is at least 5%. The yellow filled circles (B6), and brown horizontal triangles (B7) represent Band 6 and 7 sources in our sample, respectively. Other faint SMG samples are shown as follows:- YM+16 (Green stars) - Yamaguchi et al. (2016); HK+15 (Black diamonds) - Hatsukade et al. (2015); FM+16 (Blue pentagons) - Fujimoto et al. (2016); LP+17 (Red vertical triangles) - Laporte et al. (2017). The light gray symbols in the background show the field non-SMG galaxies found within all ALMA pointings. Our sample occupies a bluer color space than the OIRTC selection cut-off mainly due to the mail$Ks-[3.6]\,\mu m$ color. This shows that the optical-NIR color properties of our faint SMG population are different from the bright SMGs.

and Yamaguchi et al. (2016). A comparison with other samples will allow us to evaluate the significance of our results and also to check the consistency between different methods adopted in all of the studies. We see that almost our entire sample occupies the color space outside the selection cuts defined by the OIRTC technique. Furthermore, the galaxies from the comparison samples also lie mostly outside the OIRTC color selection. The light-grey symbols in Figure 4.8 are the non-SMG field galaxies found within the search radius of all the ALMA pointings used in our study. These field galaxies will allow us to check whether the colors of faint SMGs are systematically redder.

We observe that 75% of faint SMGs satisfy the $z - K_s$ color criterion of having redder colors than the OIRTC $z - K_s$ color criterion. Whereas only 47% and 18% of the faint SMG population satisfy the OIRTC $[3.6]\,\mu m - [4.5]\,\mu m$ and $K_s - [3.6]\,\mu m$ color criteria, respectively. Laporte et al. (2017) and Cowie et al. (2018) have also analyzed the OIRTC criteria for their sample sources. Both the studies found that majority of their samples do not satisfy the OIRTC $K_s - [3.6]\,\mu m$ cut. A few factors could be responsible for the differences. The primary extrinsic factor is the variations in the photometry techniques used to obtain colors. Laporte et al. (2017) pointed out that the disagreement of the $K_s - [3.6]$ colors between their and Chen et al. (2016b) sample was mainly due to the differences in the *Spitzer* IRAC aperture correction methods. When the OIRTC color criteria were re-calibrated for their field galaxies, the new color-cuts were 80% complete. The *Tractor* forced photometry presented in our work takes the point spread function of each band into account, thus removing the need for aperture corrections. Nevertheless, we still find a significant fraction of the sample occupying bluer Ks-[3.6] colors, which may be due to the differences in the intrinsic properties of the faint and bright SMGs. Hence, additional checks are needed before directly applying color cuts from the other studies. It would be useful to perform future studies which combine all the different faint SMGs and provide consistent photometry for all the comparison samples.

As mentioned above, the other reason could be the intrinsic differences in the SEDs of bright and faint SMGs. The OIRTC color selection method is trained using bright SMGs, and the faint population in Chen et al. (2016a) does not have confirmed interferometric detections. Hence, the technique is targeting faint galaxies having SEDs similar to the bright SMGs. To further support this, Hatsukade et al. (2015) found bluer colors for their sample of faint SMGs. Therefore, additional study is needed, including spectroscopic follow-up, in order to better understand the colors of faint SMGs.

4.4.4 The UVJ color-color plot

At higher redshifts, where it is difficult to classify galaxies based on their morphologies, classifications via rest-frame broad-band colors have proven to be useful. Star-forming and quiescent galaxies show a bi-modality in rest-frame colors up to $z \sim 2.5$ in the UVJ color-color diagram (Labbé et al., 2005; Wuyts et al., 2007; Williams et al., 2009; Whitaker et al., 2011; Brammer et al., 2011; Patel et al., 2011). The quiescent galaxies form a red clump called the "red sequence", and star-forming galaxies fall on a diagonal line. The redder galaxies on the star-forming main sequence have higher dust extinction. The $U - V$ and $V - J$ colors of the DFSGs are both reddened by dust extinction. However, in the case of quiescent galaxies, only the $U - V$ colors are reddened due to the Balmar/4000 Å break, and the $V - J$ colors are bluer as compared to the $U - V$ (Chen et al., 2016b). Therefore, the $V - J$ color is a good proxy for dust extinction, and the two colors can separate DFSGs and red sequence quiescent galaxies up to $z \sim 2.5$.

Figure 4.9 shows the rest frame UVJ color diagram for our sample. The rest frame colors are estimated using EAZY as explained in Section 4.3.4. To estimate the uncertainties in the U, V, and J bands, we find the two nearest filters for each band, and add their errors in quadrature. Then, we calculate the uncertainties of the rest-frame colors using a simple error propagation rule. Here, we consider only measurement errors and exclude the errors in the SED templates and fitting.

The quiescent galaxy color cuts are taken from Williams et al. (2009). The color selection is defined as follows:

$$U - V > 1.3 \tag{4.1}$$

$$V - J < 1.6 \tag{4.2}$$

$$U - V > 0.88 \times (V - J) + 0.49 \tag{4.3}$$

The third criterion has a small dependence on redshift, and we used the equation for the redshift bin $1 < z < 2$. Five out of 26 galaxies are located within the quiescent box, and the rest of the sample has colors similar to the star-forming galaxies. When we compare the bi-color sequence from Williams et al. (2009), we see that our star-forming sample occupies redder $U - V$ and $V - J$ colors indicating the dusty and high-redshift nature of our sample.

4.4.5 Stacking of Undetected ALMA Sources

We used stacking to investigate the nature of the faint population that was not individually detected in our photometric catalog. As the rate of contamination of the ALMA catalog by noise fluctuations is expected to be very small above 5σ, we stacked the DeepDrill IRAC data at the positions of the $> 5\sigma$ sources (60/176). We divided our sample into sources that were bright ($> 1\,\mathrm{mJy}$), or faint ($< 1\,\mathrm{mJy}$) We

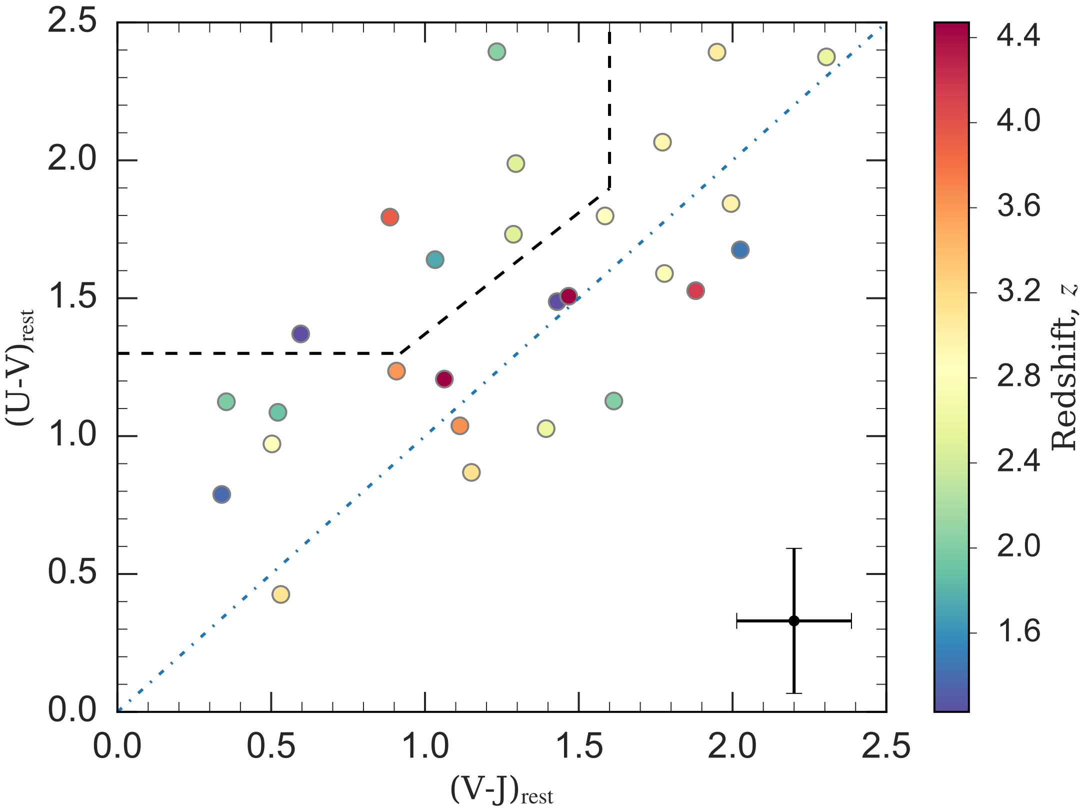

Figure 4.9: UVJ color selection diagram. The symbols are color coded based on their photometric redshifts and the color bar is shown on the right. Five out of the 26 galaxies lie in the quiescent galaxy clump. The blue dotted line is a proportionality line and is plotted to identify the diagonal track occupied by the star-forming galaxies. The black error-bar in the bottom-right corner shows the average uncertainties in the color estimation.

Table 4.1: Results of stacking $> 5\sigma$ ALMA objects that were undetected in the IRAC bands

Stack	Number	3.6μm AB mag	4.5μm AB mag
All undetected	60	>26.1	>26.1
$>$ 1mJy	44	>25.8	>25.9
$<$ 1mJy	16	>25.5	25.3

only detected $> 3\sigma$ emission in the IRAC 4.5 μm channel stack of the faint sources (Table 4.1) at the level of 0.34 μJy ($AB = 25.3$). This indicates that the majority of the undetected population is extremely faint in the IRAC bands ($AB \gtrsim 25$), and is either of low stellar mass ($\lesssim 10^{10}\, M_{\odot}$ at $z = 2$) and/or highly reddened.

4.5 Summary and Conclusions

In this paper, we have successfully demonstrated the use of archival ALMA observations to search for faint SMGs. The ALMA detections in the XMM-LSS field greater than 3.9σ were cross-matched with the deep optical-NIR observations taken from SERVS/DeepDrill, VIDEO, CFHTLS, and HSC. We identify 26 sources with NIR counterparts, 15 of which are newly-identified faint SMGs. To further investigate the nature of this cosmologically important population, we have analyzed the basic properties of our sample. Of the total 26 sources, there are 16 faint SMGs ($S_{1.1\,mm} <$ 1 mJy) with a median flux of 0.57 mJy and 10 bright SMGs with a median flux of 2.44 mJy. Robust 13-band forced photometry using the *Tractor* image modeling code is available for our entire catalog.

The resulting photometric measurements were used to estimate photometric redshifts and rest-frame colors. Our sources have redshifts in the range of $0.4 < z_{\mathrm{phot}} <$ 5.3, with a median photometric redshifts of $\langle z \rangle = 2.72$ and 2.57 for Band 6 and 7, respectively. The median redshift and the average depth of our search are in good agreement with the predictions given in Béthermin et al. (2015).

We performed an optical-NIR triple-color selection that showed that most of our sample galaxies have bluer colors than the redder bright SMGs. Different color properties of faint SMGs could indicate different physical properties compared to their brighter counterparts. Based on the rest-frame UVJ colors, we found that most of the galaxies in our sample form the star-forming diagonal track on the UVJ diagram. Their colors are consistent with star-forming main sequence galaxies.

ALMA has made the discovery of this population of DSFGs possible. We will continue mining publicly available ALMA archival observations, and expand our search to the remaining five SERVS/DeepDrill fields to find a large sample of faint SMGs. We will include robust optical-NIR photometry along with far-IR *Herschel* observations to perform SED modeling of all the targets and estimate stellar masses, star formation rates, and other physical properties. Pilot studies (including this work) are unveiling the nature of the faint SMGs that dominate the CIB. Future large-scale surveys are essential to understanding the role of these galaxies in shaping galaxy evolution.

4.6 Data Tables

Table 4.2 provides a list of continuum maps used in the search of the faint SMG population. There are 75 individual pointings used in our work, and the sky position, date of observation, project ID, central frequency of observation, clean beam size, and rms noise levels are given in the paper. Table 4.3 presents the list of 26 sources, their ALMA fluxes, and photometric redshifts estimated in this work. Table 4.4 gives the flux measurements obtained from the Tractor forced photometry (Section 4.3.2).

Table 4.2: Details of the ALMA Archival observations and Individual Pointings

Index (1)	Map (2)	RA (J2000) (3)	Dec (J2000) (4)	Date of Observation ($yyyy-mm-dd$) (5)	Project ID (6)	ν_{obs} (GHz) (7)	λ_{obs} (mm) (8)	θ_{beam} ($'' \times ''$) (9)	σ_{rms} (μJy beam^{-1}) (10)
0	CLM1	02h28m02.970s	-04d16m18.30s	2014-06-16	2013.1.00815.S	258	1.16	0.53 × 0.46	15.42
1	HiZELS-UDS-NBK-1147	02h17m37.000s	-05d09m12.00s	2014-01-27	2012.1.00934.S	222	1.35	1.64 × 0.7	58.27
2	HiZELS-UDS-NBK-1196	02h17m40.120s	-05d12m02.35s	2014-01-27	2012.1.00934.S	222	1.35	1.65 × 0.7	60.39
3	HiZELS-UDS-NBK-1348	02h17m51.470s	-05d10m36.40s	2014-01-27	2012.1.00934.S	222	1.35	1.65 × 0.7	59.21
4	HiZELS-UDS-NBK-8806	02h17m18.650s	-05d07m54.20s	2014-01-27	2012.1.00934.S	222	1.35	1.64 × 0.7	59.53
5	Himiko	02h17m57.563s	-05d08m44.45s	2012-07-15	2011.0.00115.S	259	1.16	0.71 × 0.48	19.86
6	SXDF1100.013	02h16m46.210s	-05d03m47.83s	2013-11-19	2012.1.00326.S	265	1.13	0.57 × 0.38	81.4
7	SXDF1100.019	02h17m15.920s	-05d04m03.13s	2013-11-19	2012.1.00326.S	265	1.13	0.57 × 0.38	81.23
8	SXDF1100.027	02h17m20.550s	-05d08m42.36s	2013-11-19	2012.1.00326.S	265	1.13	0.57 × 0.38	80.98
9	SXDF1100.036	02h18m00.700s	-05d07m29.69s	2013-11-19	2012.1.00326.S	265	1.13	0.57 × 0.38	81.5
10	SXDF1100.039	02h18m30.590s	-05d01m16.09s	2013-11-19	2012.1.00326.S	265	1.13	0.57 × 0.38	79.86
11	SXDF1100.045	02h18m15.350s	-04d54m03.36s	2013-11-19	2012.1.00326.S	265	1.13	0.57 × 0.38	79.46
12	SXDF1100.049	02h17m33.310s	-04d57m02.02s	2013-11-19	2012.1.00326.S	265	1.13	0.57 × 0.38	81.66
13	SXDF1100.053	02h16m48.170s	-04d58m56.66s	2013-11-19	2012.1.00326.S	265	1.13	0.57 × 0.38	82.26
14	SXDF1100.060	02h17m37.700s	-05d08m23.17s	2013-11-30	2012.1.00326.S	265	1.13	0.68 × 0.48	137.39
15	SXDF1100.063	02h17m35.990s	-04d52m18.15s	2013-11-19	2012.1.00326.S	265	1.13	0.57 × 0.38	80.8
16	SXDF1100.073	02h18m10.270s	-05d11m26.18s	2013-11-30	2012.1.00326.S	265	1.13	0.68 × 0.48	141.14
17	SXDF1100.082	02h17m58.290s	-04d59m11.16s	2013-11-30	2012.1.00326.S	265	1.13	0.69 × 0.48	141.18
18	SXDF1100.083	02h17m11.830s	-05d03m59.71s	2013-11-30	2012.1.00326.S	265	1.13	0.69 × 0.48	143.26
19	SXDF1100.090	02h17m23.660s	-04d57m24.06s	2013-11-30	2012.1.00326.S	265	1.13	0.69 × 0.48	139.67
20	SXDF1100.101	02h18m35.580s	-05d10m02.67s	2013-11-30	2012.1.00326.S	265	1.13	0.69 × 0.48	139.46
21	SXDF1100.104	02h18m04.930s	-05d08m19.32s	2013-11-30	2012.1.00326.S	265	1.13	0.68 × 0.48	141.65
22	SXDF1100.109	02h18m23.720s	-05d08m05.49s	2013-11-30	2012.1.00326.S	265	1.13	0.69 × 0.48	140.09
23	SXDF1100.110	02h17m44.200s	-05d04m08.78s	2013-11-30	2012.1.00326.S	265	1.13	0.69 × 0.48	141.69
24	SXDF1100.123	02h18m11.930s	-05d14m20.94s	2013-11-30	2012.1.00326.S	265	1.13	0.69 × 0.48	138.85
25	SXDF1100.127	02h17m33.080s	-04d48m51.89s	2013-11-30	2012.1.00326.S	265	1.13	0.64 × 0.46	65.92
26	SXDF1100.154	02h18m14.490s	-04d56m12.80s	2013-11-30	2012.1.00326.S	265	1.13	0.64 × 0.46	63.9
27	SXDF1100.174	02h18m16.350s	-05d15m28.80s	2013-11-30	2012.1.00326.S	265	1.13	0.64 × 0.46	64.95
28	SXDF1100.179	02h18m43.870s	-04d57m33.62s	2013-11-30	2012.1.00326.S	265	1.13	0.64 × 0.46	64.43
29	SXDF1100.230	02h17m58.610s	-04d45m49.13s	2013-11-30	2012.1.00326.S	265	1.13	0.64 × 0.46	64.6
30	SXDF1100.231	02h17m59.910s	-04d46m50.05s	2013-11-30	2012.1.00326.S	265	1.13	0.64 × 0.46	65.54
31	SXDF1100.233	02h18m53.030s	-04d58m14.74s	2013-11-19	2012.1.00326.S	265	1.13	0.57 × 0.38	81.82
32	SXDF1100.250	02h17m52.690s	-05d20m31.72s	2013-11-30	2012.1.00326.S	265	1.13	0.64 × 0.46	64.78
33	SXDF1100.253	02h18m26.970s	-05d14m38.61s	2013-11-30	2012.1.00326.S	265	1.13	0.64 × 0.46	64.45
34	SXDF1100.276	02h18m33.930s	-04d54m23.85s	2013-11-30	2012.1.00326.S	265	1.13	0.64 × 0.46	66.35
35	SXDF1100.277	02h17m24.090s	-05d20m21.94s	2013-11-30	2012.1.00326.S	265	1.13	0.64 × 0.46	63.16
36	SXDF.220GHZ	02h18m56.536s	-05d19m58.92s	2014-05-03	2012.1.00374.S	224	1.33	0.82 × 0.62	12.56

Table 4.2 continued

Table 4.2: Details of the ALMA Archival observations and Individual Pointings (continued)

Index (1)	Map (2)	RA (J2000) (3)	Dec (J2000) (4)	Date of Observation ($yyyy-mm-dd$) (5)	Project ID (6)	ν_{obs} (GHz) (7)	λ_{obs} (mm) (8)	θ_{beam} ($'' \times ''$) (9)	σ_{rms} (μJy beam^{-1}) (10)
37	SXDF-NB1	02h18m56.536s	-05d19m58.92s	2015-12-27	2013.A.00021.S	224	1.33	1.94 × 1.07	15.1
38	SXDS1_13015	02h17m13.617s	-05d09m39.82s	2012-08-15	2011.0.00648.S	243	1.23	0.8 × 0.58	100.87
39	SXDS1_1723	02h17m32.701s	-05d13m16.47s	2012-08-26	2011.0.00648.S	240	1.25	1.11 × 0.59	111.28
40	SXDS1_33244	02h16m47.397s	-05d03m28.09s	2012-08-26	2011.0.00648.S	240	1.25	0.95 × 0.59	77.72
41	SXDS1_35572	02h17m34.652s	-05d02m38.97s	2012-08-11	2011.0.00648.S	236	1.27	0.78 × 0.58	46.17
42	SXDS1_59863	02h17m45.877s	-04d54m37.60s	2012-08-15	2011.0.00648.S	243	1.23	0.81 × 0.58	95.02
43	SXDS1_59914	02h17m12.977s	-04d54m40.40s	2012-08-26	2011.0.00648.S	240	1.25	1.04 × 0.59	109.0
44	SXDS1_67002	02h19m02.654s	-04d49m55.83s	2012-08-15	2011.0.00648.S	243	1.23	0.83 × 0.57	97.8
45	SXDS1_68849	02h17m00.276s	-04d48m14.53s	2012-08-26	2011.0.00648.S	240	1.25	0.85 × 0.6	96.21
46	SXDS1_79518	02h18m59.059s	-04d51m24.91s	2012-08-26	2011.0.00648.S	240	1.25	0.9 × 0.6	99.08
47	SXDS1	02h17m05.789s	-04d51m25.68s	2012-08-09	2011.0.00648.S	231	1.3	0.8 × 0.67	64.28
48	SXDS2_13316	02h17m39.035s	-04d44m41.75s	2012-08-15	2011.0.00648.S	243	1.23	0.81 × 0.57	92.28
49	SXDS2_22198	02h17m53.416s	-04d42m53.42s	2012-08-11	2011.0.00648.S	236	1.27	0.81 × 0.58	44.84
50	SXDS2	02h17m24.356s	-05d00m44.85s	2012-08-09	2011.0.00648.S	231	1.3	0.8 × 0.66	63.38
51	SXDS3_101746	02h18m04.178s	-05d19m38.28s	2012-08-26	2011.0.00648.S	240	1.25	0.93 × 0.6	99.25
52	SXDS3_103139	02h16m57.652s	-05d14m34.86s	2012-08-11	2011.0.00648.S	236	1.27	0.77 × 0.58	46.08
53	SXDS3_110465	02h18m20.953s	-05d19m07.71s	2012-08-26	2011.0.00648.S	240	1.25	0.99 × 0.6	99.74
54	SXDS3	02h17m13.683s	-05d04m07.66s	2012-08-09	2011.0.00648.S	231	1.3	0.81 × 0.66	60.34
55	SXDS5_19723	02h16m24.372s	-05d09m18.05s	2012-08-11	2011.0.00648.S	236	1.27	0.77 × 0.58	45.41
56	SXDS5_28019	02h16m08.532s	-05d06m15.61s	2012-08-11	2011.0.00648.S	236	1.27	0.78 × 0.58	46.36
57	SXDS5_9364	02h16m33.807s	-05d13m44.68s	2012-08-15	2011.0.00648.S	243	1.23	0.81 × 0.57	97.7
58	UDS16	02h17m25.474s	-05d11m08.25s	2016-03-31	2015.1.01105.S	241	1.24	0.96 × 0.8	21.5
59	WMH5	02h26m27.030s	-04d52m38.30s	2014-06-16	2013.1.00815.S	262	1.14	0.5 × 0.48	18.05
60	XMMF10	02h16m31.850s	-05d53m22.20s	2012-06-17	2011.0.00539.S	343	0.87	0.51 × 0.41	220.03
61	XMMF11	02h21m35.220s	-06d26m16.97s	2012-06-17	2011.0.00539.S	343	0.87	0.51 × 0.41	261.51
62	XMMF12	02h22m50.830s	-03d24m13.81s	2012-06-17	2011.0.00539.S	342	0.87	0.49 × 0.41	212.05
63	XMMF13	02h18m41.550s	-03d50m01.90s	2012-06-17	2011.0.00539.S	343	0.87	0.51 × 0.41	227.81
64	XMMF14	02h20m29.140s	-06d48m45.89s	2012-06-17	2011.0.00539.S	343	0.87	0.51 × 0.41	236.57
65	XMMF15	02h22m05.540s	-07d07m27.20s	2012-06-17	2011.0.00539.S	343	0.87	0.51 × 0.41	212.96
66	XMMF16	02h19m42.910s	-05d24m32.54s	2012-06-17	2011.0.00539.S	343	0.87	0.51 × 0.41	224.83
67	XMMF17	02h19m18.400s	-03d10m51.30s	2012-06-17	2011.0.00539.S	343	0.87	0.51 × 0.42	259.53
68	XMMF18	02h29m44.790s	-03d41m10.17s	2012-06-17	2011.0.00539.S	343	0.87	0.52 × 0.41	300.12
69	XMMF19	02h20m21.610s	-01d53m29.12s	2012-06-17	2011.0.00539.S	343	0.87	0.52 × 0.42	277.51
70	XMMF4	02h20m16.689s	-06d01m44.38s	2012-06-17	2011.0.00539.S	343	0.87	0.51 × 0.41	262.64
71	XMMF5	02h22m01.576s	-03d33m40.60s	2012-06-17	2011.0.00539.S	343	0.87	0.52 × 0.41	233.23
72	XMMF6	02h25m48.210s	-04d17m51.10s	2012-06-17	2011.0.00539.S	343	0.87	0.51 × 0.41	254.89
73	XMMF7	02h18m53.100s	-06d33m23.70s	2012-06-17	2011.0.00539.S	343	0.87	0.51 × 0.41	219.54

Table 4.2 continued

Table 4.2: Details of the ALMA Archival observations and Individual Pointings (continued)

Index	Map	RA	Dec	Date of Observation	Project ID	ν_{obs}	λ_{obs}	θ_{beam}	σ_{rms}
		(J2000)	(J2000)	$(yyyy-mm-dd)$		(GHz)	(mm)	$(''\times'')$	(μJy beam^{-1})
(1)	(2)	(3)	(4)	(5)	(6)	(7)	(8)	(9)	(10)
74	XMMF8	02h30m05.980s	-03d41m52.70s	2012-06-17	2011.0.00539.S	343	0.87	0.52 × 0.41	254.45

Table 4.3: ALMA Source Catalog of Faint SMGs

Source	IAU ID	Field	RA (J2000)	Dec. (J2000)	λ_{obs} (mm)	$S_{\lambda_{obs}}$ (mJy)	$z_{\rm phot}$	$z_{\rm archival}$	Ref.	ALMA Ref.
(1)	(2)	(3)	(4)	(5)	(6)	(7)	(8)	(9)	(10)	(11)
191313	J0226−0452	WMH5	02h26m27.00s	−04d52m38.38s	1.14	0.18 ± 0.04	$4.87^{+1.07}_{-0.26}$	6.068†	4	a
309436	J0225−0417	XMMF6	02h25m48.03s	−04d17m48.96s	0.87	1.33 ± 0.53	$2.77^{+0.14}_{-0.25}$	...	...	...
315617	J0228−0416	CLM1	02h28m02.58s	−04d16m06.99s	1.16	0.17 ± 0.03	$0.29^{+0.26}_{-0.09}$	...	...	...
477360	J0219−0524.63	XMMF16	02h19m42.63s	−05d24m37.07s	0.87	9.66 ± 1.22	$1.75^{+0.16}_{-0.11}$	2.048	1	b
814024	J0219−0524.52	XMMF16	02h19m42.52s	−05d24m41.27s	0.87	2.61 ± 0.50	$2.49^{+0.46}_{-0.42}$	...	...	...
842544	J0219−0524.77	XMMF16	02h19m42.77s	−05d24m36.43s	0.87	2.81 ± 0.50	$2.57^{+0.22}_{-0.24}$	1.489	1	b
911805	J0219−0524.84	XMMF16	02h19m42.84s	−05d24m35.11s	0.87	2.69 ± 0.49	$2.97^{+0.12}_{-0.12}$	1.489	1	b
932297	J0217−0520	SXDF1100.277	02h17m23.50s	−05d20m08.62s	1.13	2.28 ± 0.41	$3.62^{+0.12}_{-0.12}$	...	...	...
935442	J0218−0519	SXDF.220GHZ	02h18m56.10s	−05d19m51.00s	1.33	0.10 ± 0.03	$1.38^{+0.09}_{-0.12}$	$1.48^{+0.10}_{-0.07}$	1,2	...
971686	J0217−0511	UDS16	02h17m25.72s	−05d11m03.17s	1.24	0.10 ± 0.03	$2.73^{+0.20}_{-0.23}$	$0.27^{+2.66}_{-0.05}$	2	...
978351	J0217−0510	UDS16	02h17m26.10s	−05d10m58.20s	1.24	0.95 ± 0.12	$2.12^{+0.14}_{-0.34}$	$1.55^{+0.20}_{-0.07}$	1,2	...
987090	J0217−0508	SXDF1100.027	02h17m20.95s	−05d08m37.17s	1.13	1.39 ± 0.18	$2.95^{+0.10}_{-0.60}$	$2.80^{+0.48}_{-0.70}$	1,5	c
993676	J0216−0506	SXDS5.28019	02h16m08.51s	−05d06m15.89s	1.27	0.18 ± 0.10	$1.29^{+0.05}_{-0.08}$	1.348†	1,2,6	d,e
998253	J0217−0508	HIMIKO	02h17m58.28s	−05d08m30.64s	1.16	0.59 ± 0.04	$1.14^{+0.11}_{-0.08}$	$1.09^{+0.03}_{-0.04}$	1,2	f
1002990	J0216−0503	SXDF1100.013	02h16m47.10s	−05d03m44.54s	1.13	1.46 ± 0.18	$3.03^{+0.23}_{-2.27}$	...	...	...
1017745	J0218−0501	SXDF1100.039	02h18m30.98s	−05d01m23.22s	1.13	0.49 ± 0.17	$0.42^{+0.10}_{-0.11}$	$0.49^{+0.03}_{-0.03}$	1,2	...
1048801	J0217−0454	SXDS1.59863	02h17m46.28s	−04d54m39.77s	1.23	0.69 ± 0.20	$2.29^{+0.10}_{-1.10}$	1.456†	1,2,3	d,e
1094072	J0217−0445	SXDF1100.230	02h17m59.38s	−04d45m53.13s	1.13	1.54 ± 0.14	$3.92^{+0.20}_{-0.27}$	$3.50^{+0.40}_{-0.18}$	1,2,5	c
1106738	J0217−0442	SXDS2.22198	02h17m53.17s	−04d42m39.61s	1.27	0.44 ± 0.10	$0.03^{+0.04}_{-0.02}$	...	...	d
1266981	J0217−0520	SXDF1100.277	02h17m23.95s	−05d20m28.02s	1.13	0.55 ± 0.14	$2.66^{+0.11}_{-0.10}$	$2.54^{+0.43}_{-0.40}$	1	...

Table 4.3 continued

Table 4.3: ALMA Source Catalog of Faint SMGs (continued)

Source	IAU ID	Field	RA	Dec.	λ_{obs}	$S_{\lambda_{obs}}$	$z_{\rm phot}$	$z_{\rm archival}$	Ref.	ALMA Ref.
			(J2000)	(J2000)	(mm)	(mJy)				
(1)	(2)	(3)	(4)	(5)	(6)	(7)	(8)	(9)	(10)	(11)
1302443	J0218−0501	SXDF1100.039	02h18m30.23s	−05d01m21.19s	1.13	0.84 ± 0.17	$3.21^{+0.39}_{-0.41}$	$2.66^{+0.94}_{-0.73}$	1	...
1302615	J0217−0520	SXDF1100.250	02h17m52.00s	−05d20m32.34s	1.13	0.97 ± 0.14	$3.65^{+0.81}_{-1.20}$	$2.79^{+0.45}_{-1.45}$	1	...
1303410	J0218−0508	SXDF1100.109	02h18m23.99s	−05d08m11.40s	1.13	0.79 ± 0.31	$3.16^{+0.20}_{-0.21}$	$1.91^{+0.61}_{-0.39}$	1	...
1304155	J0217−0452	SXDF1100.063	02h17m35.50s	−04d52m11.79s	1.13	0.62 ± 0.17	$2.59^{+0.44}_{-0.45}$	...	...	...
1307256	J0218−0457	SXDF1100.179	02h18m43.41s	−04d57m33.05s	1.13	0.79 ± 0.14	$5.40^{+0.56}_{-5.38}$	...	...	...
1312163	J0217−0504	SXDF1100.110	02h17m43.58s	−05d04m10.31s	1.13	2.61 ± 0.30	$4.47^{+1.44}_{-1.13}$	$4.98^{+0.72}_{-3.14}$	5	c

NOTE —

Column 1: Source name. Column 2: Source name based on the IAU convention. Column 3: Field name indicated in the ALMA archive. Columns 4-5: Source right ascension and declination. The position corresponds to the peak of the Gaussian source fitted using PyBDSF. Column 6: ALMA observing wavelength. Column 7: ALMA integrated flux. Column 8: Photometric redshift estimated using our *Tractor* forced photometry (Table 4.4). Column 9: Previously published source redshift. Values marked by the † symbol are spectroscopic redshifts; the rest are photometric redshifts. Column 10: References for literature redshifts and previous detections at all wavelengths: (1) Rowan-Robinson et al. (2013); (2) Williams et al. (2009); (3) Banerji et al. (2011); (4) Willott et al. (2013); (5) Ikarashi et al. (2015); (6) Seko et al. (2016a).
Column 11: References for previous ALMA detections: (a) Willott et al. (2015); (b) Bussmann et al. (2015); (c) Ikarashi et al. (2015); (d) Fujimoto et al. (2016); (e) Hatsukade et al. (2013); (f) Ono et al. (2014)

Table 4.4: Multi-band Tractor Photometry

Source (1)	F_{Ks} (2)	F_H (3)	F_J (4)	F_Y (5)	F_Z (6)	$F_{u'}$ (7)	F_g (8)	F_r (9)	F_i (10)	F_z (11)	F_y (12)	$F_{3.6\mu m}$ (13)	$F_{4.5\mu m}$ (14)
191313†	0.37 ± 0.06	0.62 ± 0.14	0.35 ± 0.03	0.47 ± 0.02	0.28 ± 0.01	−0.03 ± 0.01	−0.04 ± 0.01	−0.07 ± 0.01	−0.06 ± 0.02	0.54 ± 0.04	0.38 ± 0.08	1.35 ± 0.07	0.81 ± 0.10
309436†	7.43 ± 0.83	6.48 ± 0.22	2.39 ± 0.10	1.38 ± 0.07	1.05 ± 0.05	0.04 ± 0.02	0.28 ± 0.02	0.90 ± 0.03	0.84 ± 0.05	1.06 ± 0.08	1.32 ± 0.14	7.00 ± 0.14	12.92 ± 0.13
315617†	0.51 ± 0.07	0.91 ± 0.16	0.81 ± 0.04	0.78 ± 0.03	0.55 ± 0.02	...	0.01 ± 0.01	0.20 ± 0.01	0.31 ± 0.02	0.42 ± 0.04	0.54 ± 0.07	−0.20 ± 0.07	−0.92 ± 0.10
477360	6.83 ± 0.72	3.05 ± 0.12	1.23 ± 0.07	0.23 ± 0.04	−0.31 ± 0.02	−0.01 ± 0.08	−0.10 ± 0.01	−0.21 ± 0.02	−0.02 ± 0.02	−0.01 ± 0.04	0.36 ± 0.08	13.61 ± 0.06	24.10 ± 0.09
814024	1.77 ± 0.27	0.93 ± 0.06	0.21 ± 0.04	0.05 ± 0.02	0.02 ± 0.01	−0.03 ± 0.04	0.01 ± 0.01	0.03 ± 0.01	0.01 ± 0.01	0.02 ± 0.02	0.10 ± 0.04	5.37 ± 0.08	7.12 ± 0.11
842544	2.20 ± 0.29	1.68 ± 0.07	0.31 ± 0.03	0.18 ± 0.02	0.12 ± 0.01	0.01 ± 0.04	−0.01 ± 0.01	0.09 ± 0.01	0.05 ± 0.01	0.05 ± 0.02	−0.00 ± 0.04	10.84 ± 0.07	15.77 ± 0.09
911805	11.12 ± 1.12	9.23 ± 0.30	3.89 ± 0.14	3.61 ± 0.12	3.04 ± 0.10	0.34 ± 0.10	1.40 ± 0.04	1.95 ± 0.06	2.54 ± 0.08	2.94 ± 0.10	3.04 ± 0.14	24.17 ± 0.07	32.00 ± 0.09
932297	0.71 ± 0.09	0.59 ± 0.06	0.39 ± 0.05	0.51 ± 0.09	0.47 ± 0.02	0.00 ± 0.04	0.15 ± 0.01	0.46 ± 0.02	0.44 ± 0.02	0.52 ± 0.03	0.49 ± 0.04	−0.14 ± 0.07	0.17 ± 0.08
935442	16.62 ± 1.54	10.80 ± 0.33	5.54 ± 0.18	4.02 ± 0.12	1.99 ± 0.06	0.11 ± 0.06	0.31 ± 0.01	0.57 ± 0.02	1.06 ± 0.03	1.83 ± 0.06	3.06 ± 0.11	26.82 ± 0.04	29.01 ± 0.05
971686	0.44 ± 0.07	0.64 ± 0.05	0.35 ± 0.04	0.42 ± 0.07	0.29 ± 0.01	0.05 ± 0.04	0.30 ± 0.01	0.37 ± 0.01	0.31 ± 0.01	0.30 ± 0.02	0.27 ± 0.03	0.61 ± 0.03	1.07 ± 0.05
978351	19.63 ± 1.82	10.49 ± 0.33	4.96 ± 0.17	2.16 ± 0.08	1.16 ± 0.04	0.11 ± 0.09	0.18 ± 0.01	0.44 ± 0.02	0.77 ± 0.03	1.17 ± 0.05	1.86 ± 0.09	39.81 ± 0.04	48.34 ± 0.06
987090	7.04 ± 0.67	3.63 ± 0.12	0.73 ± 0.05	0.29 ± 0.02	0.18 ± 0.01	0.01 ± 0.05	−0.01 ± 0.00	0.01 ± 0.01	0.05 ± 0.01	0.13 ± 0.02	0.22 ± 0.04	15.35 ± 0.04	14.16 ± 0.06
993676	14.72 ± 1.35	11.32 ± 0.35	6.05 ± 0.19	5.67 ± 0.17	3.98 ± 0.12	0.48 ± 0.06	0.83 ± 0.03	1.36 ± 0.04	2.06 ± 0.06	3.79 ± 0.12	4.79 ± 0.15	19.85 ± 0.06	21.56 ± 0.09
998253	20.95 ± 1.93	12.57 ± 0.39	6.75 ± 0.23	5.56 ± 0.17	4.35 ± 0.14	0.48 ± 0.10	0.82 ± 0.03	1.28 ± 0.04	2.21 ± 0.07	4.30 ± 0.13	5.09 ± 0.17	37.95 ± 0.08	35.73 ± 0.08
1002990	−0.06 ± 0.06	0.19 ± 0.04	0.21 ± 0.03	0.01 ± 0.02	0.13 ± 0.03	0.02 ± 0.03	0.06 ± 0.00	0.08 ± 0.01	0.10 ± 0.01	0.15 ± 0.01	0.16 ± 0.03	0.53 ± 0.06	0.32 ± 0.09
1017745	19.10 ± 1.77	16.91 ± 0.52	11.27 ± 0.35	11.30 ± 0.34	9.29 ± 0.28	1.04 ± 0.10	2.00 ± 0.06	4.96 ± 0.15	7.11 ± 0.21	9.10 ± 0.28	0.68 ± 0.33	9.72 ± 0.12	9.64 ± 0.12
1048801	13.33 ± 1.27	7.36 ± 0.24	3.83 ± 0.14	2.19 ± 0.08	1.56 ± 0.05	0.19 ± 0.08	0.47 ± 0.02	0.68 ± 0.02	1.06 ± 0.04	1.62 ± 0.06	1.88 ± 0.08	26.22 ± 0.04	32.26 ± 0.07
1094072	1.42 ± 0.24	0.51 ± 0.05	0.22 ± 0.04	0.23 ± 0.02	0.21 ± 0.01	0.02 ± 0.04	0.02 ± 0.00	0.12 ± 0.01	0.12 ± 0.01	0.16 ± 0.02			

Table 4.4 continued

Table 4.4: Multi-band Tractor Photometry (continued)

Source (1)	F_{Ks} (2)	F_H (3)	F_J (4)	F_Y (5)	F_Z (6)	$F_{u'}$ (7)	F_g (8)	F_r (9)	F_i (10)	F_z (11)
					F_y (12)		$F_{3.6\mu\mathrm{m}}$ (13)		$F_{4.5\mu\mathrm{m}}$ (14)	
					0.17 ± 0.03		3.13 ± 0.03		3.35 ± 0.06	
1106738	0.75 ± 0.11	1.19 ± 0.25	0.86 ± 0.06	0.99 ± 0.04	0.94 ± 0.03	0.24 ± 0.06	0.68 ± 0.02	0.91 ± 0.03	0.96 ± 0.03	1.01 ± 0.04
					1.00 ± 0.07		0.00 ± 0.05		−0.08 ± 0.06	
1266981	10.22 ± 1.02	5.58 ± 0.19	0.74 ± 0.09	0.56 ± 0.04	0.23 ± 0.02	0.02 ± 0.07	0.00 ± 0.01	0.07 ± 0.01	0.14 ± 0.02	0.20 ± 0.03
					0.41 ± 0.06		21.25 ± 0.05		27.94 ± 0.06	
1302443	1.43 ± 0.27	0.57 ± 0.06	0.14 ± 0.05	−0.05 ± 0.03	−0.01 ± 0.02	−0.02 ± 0.04	0.02 ± 0.01	0.04 ± 0.01	0.03 ± 0.01	0.22 ± 0.03
					−0.01 ± 0.04		3.96 ± 0.13		6.70 ± 0.16	
1302615	1.15 ± 0.27	0.30 ± 0.05	−0.04 ± 0.05	0.05 ± 0.02	−0.11 ± 0.01	−0.01 ± 0.04	0.00 ± 0.01	0.02 ± 0.01	0.01 ± 0.01	0.04 ± 0.02
					0.06 ± 0.04		3.34 ± 0.03		4.86 ± 0.05	
1303410	1.87 ± 0.28	0.96 ± 0.06	0.31 ± 0.04	0.02 ± 0.02	0.11 ± 0.01	−0.01 ± 0.04	0.00 ± 0.00	−0.00 ± 0.01	0.01 ± 0.01	0.05 ± 0.02
					−0.02 ± 0.03		4.82 ± 0.04		5.93 ± 0.07	
1304155	1.60 ± 0.28	0.88 ± 0.07	0.16 ± 0.06	0.12 ± 0.04	0.03 ± 0.04	−0.05 ± 0.06	0.01 ± 0.01	0.04 ± 0.01	0.03 ± 0.01	0.01 ± 0.02
					0.08 ± 0.04		5.88 ± 0.07		8.44 ± 0.09	
1307256	0.61 ± 0.26	−0.14 ± 0.10	−0.23 ± 0.12	0.03 ± 0.06	0.07 ± 0.05	−0.02 ± 0.04	−0.01 ± 0.00	−0.02 ± 0.01	−0.01 ± 0.01	−0.03 ± 0.02
					−0.04 ± 0.03		0.30 ± 0.15		3.02 ± 0.11	
1312163	0.86 ± 0.28	0.10 ± 0.06	−0.01 ± 0.05	0.10 ± 0.03	0.04 ± 0.02	−0.05 ± 0.05	0.00 ± 0.01	−0.03 ± 0.01	−0.02 ± 0.01	−0.03 ± 0.02
					−0.09 ± 0.04		1.77 ± 0.12		2.99 ± 0.13	

NOTE — All fluxes and uncertainties are given in units of μJy. Column 1: Source name. Column 2: Ks-band flux from the VIDEO survey. Column 3: H-band flux from the VIDEO survey. Column 4: J-band flux from the VIDEO survey. Column 5: Y-band flux from the VIDEO survey. Column 6: Z-band flux from the VIDEO survey. Column 7: u'-band flux from the wide tier of the CFHTLS survey (CFHTLS-W1). Column 8: g-band flux from the Ultradeep tier of DR1 of the HSC survey. Column 9: r-band flux from the Ultradeep tier of DR1 of the HSC survey. Column 10: i-band flux from the Ultradeep tier of DR1 of the HSC survey. Column 11: z-band flux from the Ultradeep tier of DR1 of the HSC survey. Column 12: y-band flux from the Ultradeep tier of DR1 of the HSC survey. Column 13: 3.6μm *Spitzer* IRAC flux from the DeepDrill survey. Column 14: 4.5μm *Spitzer* IRAC flux from the DeepDrill survey.

† The CFHTLS flux is based on the deeper CFHTLS-D1 tier and the HSC flux is based on the shallower Deep tier.

Chapter 5

Ongoing and Future Work

The VLA snapshot survey of my primary sample not only revealed exciting results, but it also helped identify subsamples for further follow-up studies. In this chapter, I summarize ongoing research and early results of the projects led by me during my graduate studies.

Section 5.1 describes multi-frequency, multi-resolution imaging conducted with VLA, VLBA, and e-MERLIN. Section 5.2 presents the early results from the pilot ALMA study to investigate the thermal dust structure and the molecular gas content in three targets. Section 5.3 summarizes a pilot program conducted to understand the intrinsic AGN properties via X-ray observations. Finally, Section 5.4 discusses the prospects of next-generation Very Large Array (ngVLA) and its synergies with multi-wavelength facilities in improving our understanding of young radio AGN. This section is a chapter (Patil et al., 2018) in the published ngVLA Science Book (Murphy, 2018).

5.1 Multi-band and Multi-scale Radio Imaging with VLA, VLBA, and e-MERLIN

The initial snapshot VLA (Patil et al., 2020, Chapter 3) and VLBA (Lonsdale et al. in prep.) surveys have shown a range in physical sizes (100 pc− 50 kpc). Deep, high-resolution, multi-frequency observations are required to probe the spatial and spectral information in these sources thoroughly. Two subsamples were identified to conduct follow-up observations using multiple radio telescopes. The first sample includes 12 sources with sub-kpc-scale radio morphology. These have been followed up with multi-frequency VLA, VLBA, and e-MERLIN observations. The second sample includes 20 relatively extended sources with radio emission on scales $\sim 5 - 50$ kpc. These have been followed up with multi-frequency VLA observations. I hope to obtain high-fidelity structural and spectral information on spatial scales ranging from 300 pc to 20 kpc with these observations. The lower-resolution VLA observations will also detect diffuse radio emission in the host galaxy from a starburst and/or a larger, older, radio source. The data has already been acquired for all of the proposals submitted. Table 5.1 provides parameters for all of the follow-up observations and below I briefly summarize the status of each project and I present a few preliminary results.

5.1.1 Sources with Arcsecond-scale Structures

We identified 20 sources based on our 10 GHz snapshot survey to conduct sensitive, multi-frequency VLA follow-up observations. All of these sources have radio emission on scales of $0.5'' - 5''$. The primary goal of this follow-up study is to fully characterize their spatial structures, spectral properties, and polarimetric information, if possible. From these we will try to establish the "evolutionary stage" of each source – its age and energetics, and its development and relation to the surrounding medium.

Table 5.1: Summary of VLA, VLBA, and e-MERLIN Follow-up Observations

Telescope	Project ID	Dates	Time	N	Frequency Band Parameters				
					Band	ν	BW†	t_{int}*	σ_{th}‡
		Month dd, yyyy	hours			GHz	GHz	min	μJy beam^{-1}
(1)	(2)	(3)	(4)	(5)	(6)	(7)	(8)	(9)	(10)
VLA	16B−376	October 16, 2016− February 1, 2017	51.4	20	L	1.52	1.0	5.4	50
					C	6	4	9.6	10
					X	10	4	7.2	10
					Ku	15	6	8.8	10
					Ka	33	13.5	28.4	10
VLA	16B−353	October 2, 2016− January 24, 2017	30	12	C	6	4	9.6	10
					X	10	4	7.2	10
					Ku	15	6	8.8	10
					Ka	33	13.5	28.4	10
VLA	15A−337	July 14 − August 28, 2015	14.65	21	L	1.52	1.0	5.6	40
					Q	45	10	10	25
VLBA	BL209	July 27, 2015− January 13, 2016	72	12	L	1.6	0.256	90	30
					C1[a]	4.1	0.256	90	20
					C2[a]	7.7	0.256	90	20
					U	15	0.256	90	50
e-MERLIN	CY3229	January 10 − January 24, 2016	150	15	L	1.51	0.512	204	30
					C	5.08	0.512	156	30

Note — Column 1: Name of the radio telescope; Column 2: Proposed project ID; Column 3: The dates between which the data was observed; Column 4: Total approved observing time in hours; Column 5: Number of sources observed; Column 6−10: Technical specifications of individual frequency band; Column 6: Name of the frequency band; Column 7: Central frequency in GHz; Column 8: Total bandwidth of the observed data in GHz; Column 9: Typical source integration time in minutes; Column 10: Thermal noise in μJy Beam^{-1} estimated using observatory provided sensitivity calculator.

† We have specified the total bandwidth available. But, a part of the bandwidth may be severely affected by Radio Frequency Interference (RFI), especially at low frequencies. In case of the VLA, 40%, 15%, 15%, and 12% of the total bandwidths for L-, C-, X-, and Ku-bands could be affected by RFI.

* We provide an average value for the entire project. The total integration time for individual source may vary depending on the scheduling constraints and the elevation of the target.

‡ Thermal noise limit. We also assumed a robust weighting and a source at a median declination. The actual measured values are usually higher.

[a] C-band was split into two parts, one at 4.1 GHz and the other at 7.7 GHz. This way we avoided the lower-edge of C-band where T_{sys} is higher while having 2 well spaced bands for spectral index calculations.

Observations:

I observed 20 sources with the VLA in the A-configuration at five frequency bands: L (1.5 GHz), C (6 GHz), X (10 GHz), Ku (15 GHz), and Ka (33 GHz). The data was taken under project 16B-376 spanning a total of 51.4 hours. The WIDAR correlator was set to dual-polarization mode with 3-bit samplers (except for L-band) to make use of the maximum available bandwidth. Figure 5.1 provides a visualization of the resolution and bandwidths of the observed data. Purple-colored boxes highlight the currently discussed VLA data. I required the point-source-sensitivity to reach about $10\,\mu$Jy beam^{-1} in all bands except L-band, which had a slightly higher limit of $\sim 50\,\mu$ Jy. The data was split into 59 scheduling blocks to allow for flexibility in scheduling. Our strategy was to put different frequency bands in different scheduling blocks, and group nearby sources to reduce weather constraints that are frequency dependant. All of our data was successfully acquired between October 2016 and February 2017.

Scientific Analysis

The radio structures seen in our initial VLA X-band survey are on scales $0.5 - 5''$ which is $\sim 4 - 40$ kpc at $z \sim 2$. Deeper resolved imaging allows for the study of energetics in the radio lobes. An important use of these images is to compare with ALMA observations (Section 5.2). Taking advantage of the P-band ($\sim$ 325 MHz) commensal data from VLITE, I will construct integrated radio SEDs from 325 MHz to 33 GHz. The current observations have high S/N. They are taken almost simultaneously (many sources have multi-band data taken within a few hours to a few days) that will allows us to investigate the presence of long-term variability. These observations would therefore constitute a significant improvement on our initial SED analysis (Chapter 4).

I will also make spectral index maps in sources with well-resolved radio emission and sufficient S/N ratio. For example, a resolution matched mapping between L- and C-band ($1.5 - 6$ GHz) will create a spectral index map with a resolution of $\sim 1''$ (8 kpc) with a LAS of $\sim$ 20kpc. Similar combinations of either X- and Ku-band ($10 - 15$ GHz) with a $0.2''$ (1.6 kpc) resolution or Ku- and Ka-band ($15 - 33$ GHz) with a $0.1''$ (800 pc) resolution are also possible.

Although the primary aim of this project is to obtain continuum imaging, all of the observations recorded both the parallel- and cross-hand polarizations, which can yield polarization maps which in turn can yield maps of the magnetic field structure in the sources.

5.1.2 Compact Sources with mas-scale Structures

Lonsdale et al. (in prep) observed 90 sources of the parent sample with "quick-look" VLBA imaging at 4.8 GHz, yielding angular resolutions of $1-2$ mas ($\sim 10-20$ pc at $z \sim 2$). This subsample was selected based primarily on declination and is therefore representative of the parent sample. Of the 90 sources, 62 were successfully imaged, showing a wide range of morphologies, including unresolved point sources, clearly resolved single components on the scale of one or two mas, unequal doubles, core-jet morphologies, and complex multi-component structures. A subset of 12 sources was chosen for detailed follow-up studies. These 12 sources comprise all those with complex multi-component structure that is bright enough for multifrequency imaging. Lower resolution analyses from Chapter 2 and 3 have confirmed that all 12 sources are compact on all scales $> 0.5''$ and have peaked radio SEDs. Therefore, we believe that these sources are GPS candidates and possibly young. This subsample has been observed with VLA, VLBA, and e-MERLIN, to probe angular scales ranging from mas to arcsecond.

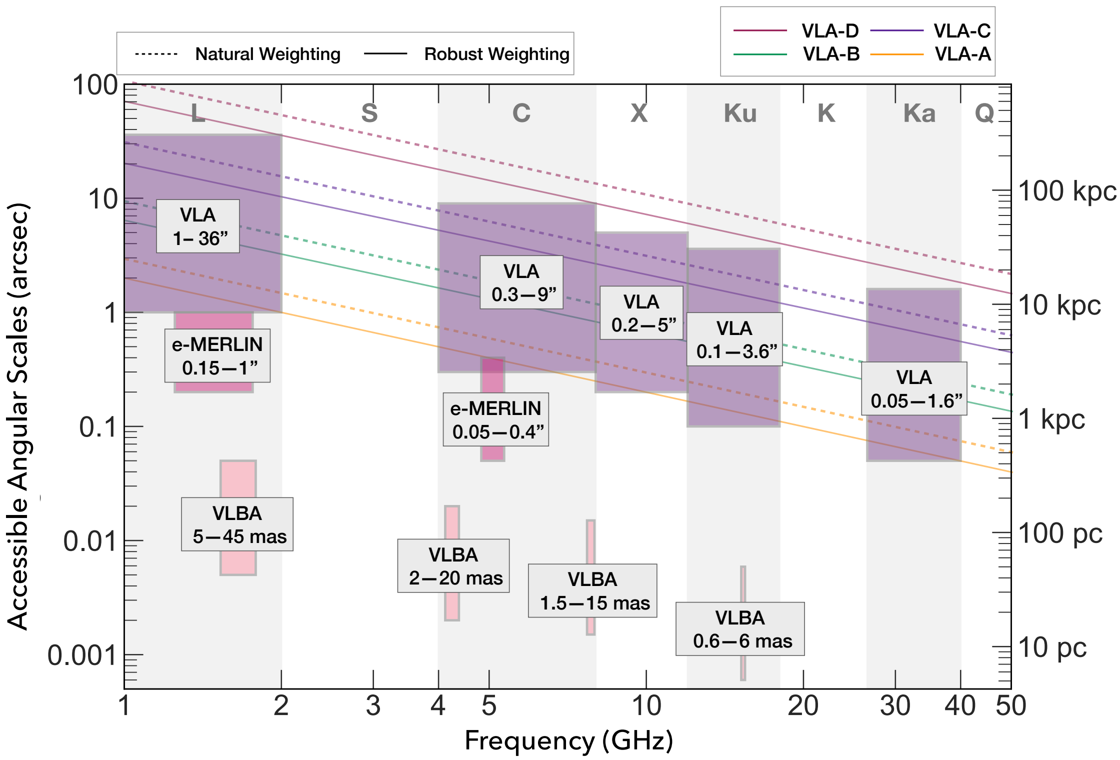

Figure 5.1: Summary of VLA, e-MERLIN, and VLBA follow-up observations (Section 5.1.1 and 5.1.2). The purple, dark-pink, and light-pink boxes represent the frequency coverage and angular scales probed by our VLA, e-MERLIN, and VLBA data, respectively. The grey and white panels in the background highlight the frequency ranges covered by the VLA, with their names shown along the top. The dashed and solid lines are the expected resolutions, λ/b_{max} (where λ is observing wavelength and b_{max} is the maximum baseline length), for the VLA assuming natural and uniform weighting, respectively. The colors of these lines correspond to different VLA configurations— A (Orange); B(Green); C(Purple), D(Maroon).

VLA

Two VLA proposals, 15A−337 and 16B−353, were submitted to obtain multi-band imaging of these 12 sources. Technical specifications for both the projects are given in Table 5.1 and Figure 5.1. Project 15A−337 observed these sources in L-band and Project 16B−353 completed the observations in C-, X-, Ku-, and Ka-band. The correlator setup was identical to the companion VLA proposal focusing on 20 sources with more extended emission. A combined total of 35 hours from these two projects were dedicated to this subsample, reaching a point source sensitivity of $10 - 40\,\mu$Jy beam^{-1}.

The primary goal of these lower resolution observations is to obtain integrated SEDs. The low-frequency (P-, L-, and C-band) images can help constrain any diffuse low surface-brightness emission originating from a previous epoch of radio activity (e.g., Shabala et al., 2020). These observations also play a role as the first epoch of multi-epoch radio SED monitoring to constrain variability (e.g., Nyland et al., 2020) and identify genuinely young sources (e.g., Tinti et al., 2005; Orienti et al., 2010).

VLBA

The VLBA snapshot survey of 90 sources showed that a significant fraction of my sample has structures on $\sim 10 - 100$s pc (Lonsdale et al. in prep). The VLBA observations were obtained under project BL−209. This was a total of 72 hours divided into three 24 hour blocks each containing four sources relatively near to each other in the sky. Four frequencies were chosen between 1.6 and 15 GHz, each with a 512 MHz bandwidth. The on-source integration time was 90 minutes per source per frequency band, which resulted in a noise level of $20 - 50\,\mu$Jy beam^{-1}. Although some targets were bright enough for self-calibration, phase referencing was used for all targets. Every observing run had targets cycled through L-, C-[1], and U-bands and

[1]The C-band was split into two frequencies centered at 4.1 and 7.7 GHz to obtain well-spaced

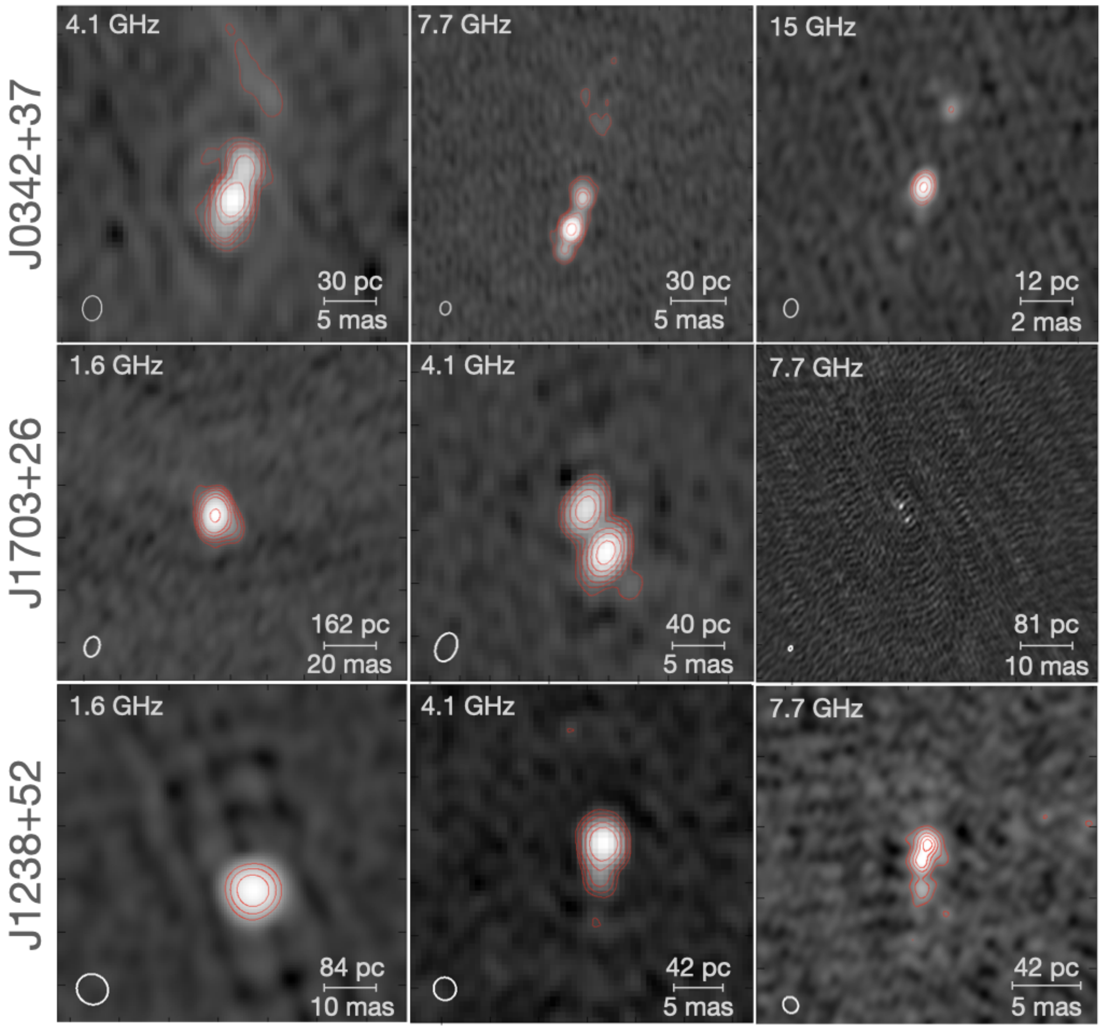

Figure 5.2: Example multi-band continuum VLBA images for J0342+37 (top), J1703+26 (middle), and J1238+52 (bottom). For each image the central frequency is given on the top left; the angular and physical scale in the lower right; and the synthesized beam in the lower left corner. The red contours starting from a lowest value of $5\,\sigma$ and increase in equal intervals.

interleaved with other target scans to maximize $uv-$coverage and observing efficiency.

The data was observed between July 2015 and January 2016 and correlated using the DiFX software correlator (Deller et al., 2011) in dual-polarization mode. I used the AIPS package to perform data editing, calibration, and imaging using the standard VLBA procedures. After the initial data editing and flagging, I used AIPS's standard VLBAPROC procedures to apply flux and phase calibration to the dataset.[2] Then individual uv datasets were split for imaging. If needed, a few rounds of self-calibration were performed to improve the image quality. I used the AIPS task IMAGR to form a continuum image. I have successfully imaged 18 out of 48 (12×4) continuum images, as shown in Figure 5.2. I plotted C1, C2, and U band images of J0342+37 and L, C1, and C2 band images of J1238+52 and J1703+26. All of these sources have spectroscopic redshifts available. The VLBA follow-up data have confirmed the complex morphological structures on scales of $10-100$ pc. I also found that very few of these sources are detected at U-band. Either they are too faint to detect at 15 GHz due to steep radio spectra, or there could still be issues with phase referencing. Support for the 15 GHz non-detections comes from the fact that this subsample has very steep ($\lesssim -1.2$) 10 GHz in-band spectral indices, measured using our lower-resolution VLA data. However, a careful look into the calibration accuracy will still be done to eliminate the possibility of instrumental effects averaging out the signal.

I plan to estimate energy densities and pressures in the synchrotron plasma for this sample, like the VLA study. These, in turn, can be used to constrain ISM densities, the rate of advance of the shock front into the medium. Simulations have shown that relativistic plasma generated in regions of jet-cloud interactions can fill the gaps in the ISM, leading to pressure-driven outflows (Wagner et al., 2016; Mukherjee et al.,

frequency coverage.

[2] I followed the step-by-step guide to perform VLBA data calibration given in the AIPS Cookbook Appendix C.

2016). This dataset is also observed in full polarization mode to enable polarimetric studies. AGN radio emission is frequently highly polarized (a few tens of percent) in the lobes of older FRI/II sources (O'Sullivan et al., 2015). Compact jets have appeared to have little polarization in some old studies due in part to observing limitations (e.g., Fanti et al., 2004; Cotton et al., 2003b; Rossetti et al., 2008). However, when observed with high resolution, the compact sources such as GPS, CSS show asymmetries in the polarization structure of the lobes likely due to interactions of the jets and lobes with the ambient medium, leading to high rotation measures (RM) (e.g., Garrington & Conway, 1991; Mantovani et al., 2002; Pasetto et al., 2016; An et al., 2017). Such high-angular resolution studies contributes to our knowledge of the nuclear environment, including the columns of thermal, ionized, gas with which the radio source is associated (e.g., Gómez et al., 2011). Given the large columns already suspected from the red MIR colors, this VLBA polarization study is an important part of our program. It will allow us to use the sub-kpc-scale radio emission to probe the central regions of these powerful transitional AGN.

e-MERLIN

e-MERLIN is a high-angular resolution interferometer consisting of seven telescopes stationed across the UK – one antenna of 76-m, one of 32-m and five of 25-m. The telescopes operate at L, C, and K-bands with a longest baseline of 217-km, which provides an angular resolution of $0.2''(0.5'')$ at 5(1.5) GHz. We proposed to observe 15 of the Northernmost sources from our primary sample (Project ID: CY3229) at L and C bands, aiming to obtain spatial and spectral information on scales between those of the VLA and VLBA. Due to geometrical constraints, only 5/12 of the most compact sources and 1/20 of the slightly larger sources (Section 5.1.1) were included in this project. Here, I will focus on the five most compact sources that were also part of the VLBA multi-frequency campaign (Section 5.2).

The total requested time of 150 hours was divided into 21 individual scheduling blocks observed over multiple days between January 1−March 7, 2016. The on-source integration time per source per frequency band was about 4 hours resulting in a 1 σ rms noise of 30 μJy beam^{-1}. The observations were kept separate for L and C-bands. The total time per target was sub-divided into shorter scans and observed over multiple days to maximize the *uv* coverage. Given our demand for *uv* coverage and substantial integration time, the 76-m Lovell telescope at Jodrell Bank was not included due to its highly restricted time. Although some sources were likely to be bright enough for self-calibration, all observations were performed in phase referencing mode to ensure accurate astrometry and as insurance against unexpectedly weak or resolved structures. The initial data processing and calibration were performed by the Jodrell Bank Observatory using a customized CASA-based pipeline. The data was then averaged down and sent to me along with the results and statistical plots of the reduction, and preliminary images of the targets and calibrators. The overall strategy of data editing and calibration is similar to VLA (e.g., Section 2.3). I used the e-MERLIN CASA Pipeline (eMCP)[3] to inspect and calibrate the data. I used CASA task IMAGR to create continuum images. I have completed 4/12 images relevant to this study.

One of the primary goals of the *e*-MERLIN observations is to obtain high-quality images on angular scales between those of the VLA and the VLBA. I will perform an analysis similar to the VLA and VLBA to obtain energy densities and pressures and search for any emission missed by the VLBA. Figure 5.3 shows the continuum *e*-MERLIN images for two targets J0342+37 and J1651+34, taken from the two subsamples. I also show VLA 10 GHz images for comparison. J0342+37 appears

[3]eMCP is a python pipeline developed using CASA to process and calibrate *e*-MERLIN data. See https://github.com/e-merlin/eMERLIN_CASA_pipelinefordocumentation.

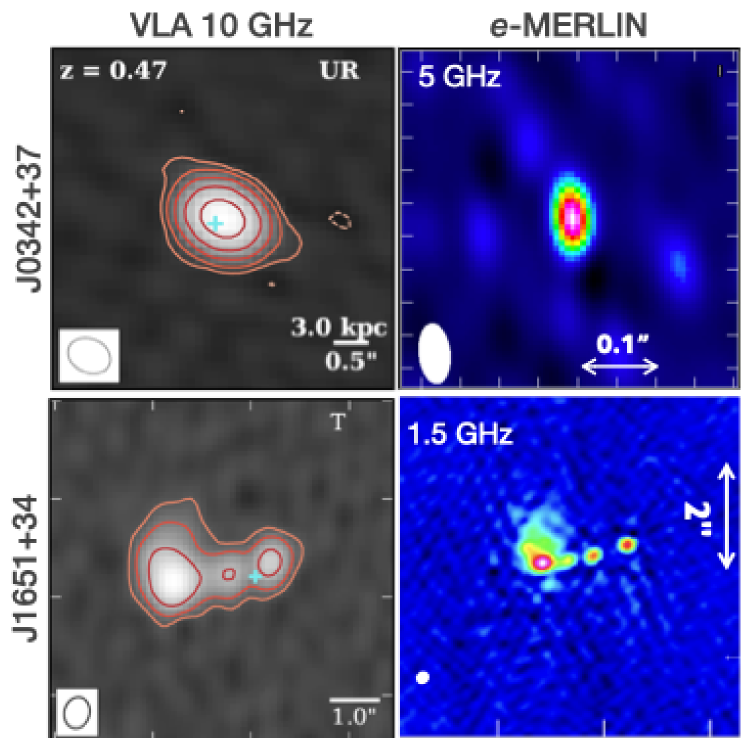

Figure 5.3: Comparison of the *e*-MERLIN continuum images with our lower resolution 10 GHz VLA 10 images. The upper panel shows the VLA X-band (left) and *e*-MERLIN C-band (right) images of J0342+37 taken from the subsample of sources with very compact radio morphology. The lower panel shows VLA X-band (left) and *e*-MERLIN L-band images of J1651+34, which belongs to the subsample of 20 more extended sources.

to be compact even on 100 mas scales confirming its extremely compact nature. J1651+34 is one of the well-extended sources and has a triple morphology. The higher resolution *e*-MERLIN image provides a detailed look into the one-sided diffuse lobe in this source. I will obtain a resolution-matched spectral index map by combining *e*-MERLIN C- and L-bands with the VLA Ku- and Ka-bands for J1651+34.

5.1.3 Summary

The sample selection and follow-up observations strongly favor a rare, luminous population of transitional objects in which AGN jets have recently switched on but not yet destroyed the dusty nuclear ISM. Strong interactions between the jets and the ISM are therefore anticipated in such objects, with strong shocks, particle acceleration, and bright, compact radio components at the interaction sites, analogous to those modeled in the simulations by Mukherjee et al. (2016).

Depending on the AGN's evolutionary state, associated radio emission can have structures ranging from sub-mas to arcseconds, and even arcminutes (An & Baan, 2012). The high sensitivity, multi-frequency images generated by the VLA, *e*-MERLIN, and VLBA will be a viable probe of the inner-most regions of these systems. These datasets can yield radio structural, spectral, and polarimetric information on parsec to kiloparsec scales when used together. This detailed analysis would also allow for internal comparisons among these sources to look for trends expected from radio source evolution (O'Dea, 1998; An & Baan, 2012); such as, high radio lobe pressures in younger or more frustrated jets, and spectral evolution in older sources.

5.2 Probing the ISM Content and Conditions using ALMA

An important aspect of my program is the study of molecular gas in the host galaxies. ALMA 870 μm imaging of 49 southern sources yielded 26 detections with bright (> 2 mJy), unresolved ($< 1 - 2''$) dust continuum emission (Lonsdale et al., 2015). One of our ALMA follow-up programs aims to obtain high-resolution imaging of a small subsample to map fluxes, gas masses, excitation, and kinematics using the CO ladder and [CII] lines, if possible. This 870 μm imaging could also be used to compare to the radio jet structure on kpc scales. With this goal, I initiated a successful pilot survey of three WISE-NVSS galaxies in ALMA Cycle-6 to spatially resolve the sub-mm emission and search for CO line emission. My strategy was to obtain 870 μm continuum observations that are resolution-matched to the VLA 10 GHz map and a frequency setup optimized to detect CO line emission.

5.2.1 Observations

J0404-24, J0612-06, J0630-21, and J0642-27 were chosen to observe in this proposal. I identified these sources such that they have detection in the cycle-0, have redshift available, show resolved radio emission on the scales of $1''$and have deep 5 (350 MHz$-$33 GHz) band imaging at VLA from the proposal (Part of VLA 16B-376 observations; Section 5.1.1). The data was observed under the project ID 2018.1.01616.S during October 2018 - April 2019. Out of 7.5 hours of total requested time (priority C), 4 hours of data was taken that included 3/4 sources (J0404-24, J0612-06, and J0630-21). The observations were carried out in Band 7 (345 GHz) with a receiver tuned to include one redshifted CO line depending on individual redshifts. A total bandwidth of 7 GHz was split into four basebands, each containing 128 channels of

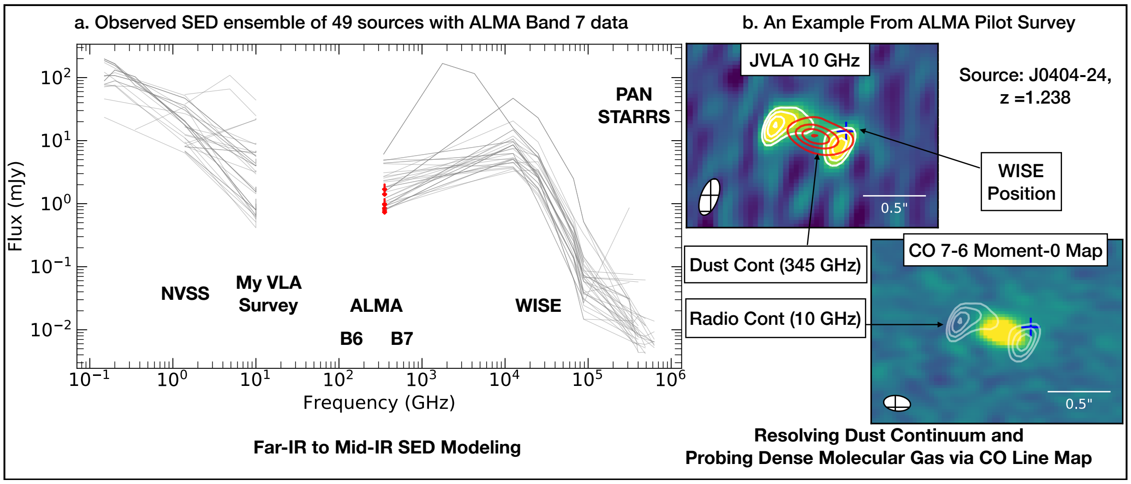

Figure 5.4: **a.** Radio to optical SEDs of 49 sources. Grey lines are SEDs in the observed frame with the red arrows indicating upper limits (for 23/49 sources). **b.** Preliminary results from my ALMA pilot survey. **Top:** The dust continuum (red) shows slight extension along the direction of radio jets (white). **Bottom:** Moment-0 CO (7-6) line map.

31-MHz resolution. The 1σ sensitivity is about 30 μJy beam^{-1}. The angular resolution achieved was between $0.1''-0.3''$to match the ALMA image with our 10 GHz VLA data. The data is currently in the processing and analysis stage. I provide a quick summary of the preliminary results.

5.2.2 Preliminary Results

Figure 5.4a shows a spectrum ensemble of the 49 sources, including observations from radio to optical. The ALMA Band 7 observations are highlighted in the blue panel. Figure 5.4b shows an example of one target, J0404-24, from the ALMA high-resolution follow-up survey. The upper image compares the radio morphology (colored image and white contours) with 345 GHz ALMA continuum observations representing the dust emission (red contours). The lower image is the moment-0 map of the detected CO (7-6) line with white contours showing radio jets' location for comparison.

Resolving the dust emission: High-resolution mapping of dust and molecular gas in these systems can provide crucial insights into the dynamics of the galactic scale interactions involved in AGN feedback. The three sources observed with ALMA show resolved morphologies on the scales of a few arcseconds, corresponding to linear sizes of a few kpc at $z \sim 2$. The comparison with radio images will allow me to resolve the submm emission, determine the source morphology and surface brightness relative to the 10 GHz sub-arcsec (sub-galaxy sized) radio jet structures, and the spatial extent of star formation in the host galaxies.

Spectral line studies: Another goal of this study is to search for CO lines to determine the distribution of molecular gas relative to the dust continuum, and hopefully identify any turbulence or outflow associated with the radio synchrotron structure. It was very gratifying to find that all three sources show a strong CO line detection! (Figure 5.4). The new CO data reveals kpc-scale molecular gas with a mass of $M_{H_2} \sim 10^{10} M_{\odot}$ and a broad spectral profile (> 500 km/s) that may be associated with an outflow (Patil et al., in prep). A preliminary assessment suggests the velocity structure includes a component of galaxy rotation along with a more extended ISM with turbulence and/or an outflow. J0612-06 has an additional serendipitous detection of the HCN line, possibly related to shocked gas. The results are in preparation and will be published soon after this dissertation. Depending on the success of this study, I plan to request additional ALMA time to study other molecular species and transitions (Izumi et al., 2016, e.g.,); for example, the CO SLED (e.g., Glenn et al., 2015), the [CII] 158 μm line (Díaz-Santos et al., 2018), the [NII] 122 μm line and the [CI] 370 μm line, and perhaps the HCO+ and HCN lines as tracers of shocks (e.g., Imanishi et al., 2018).

5.3 A NuSTAR View of the Central Engine of the Target J0612–06

5.3.1 Overview

An important way to probe intrinsic AGN power via high-energy X-rays, which can penetrate even the high columns expected in most AGN. A low X-ray optical depth and low contamination from the host makes such studies one of the most reliable ways to characterize the obscured population. Although I have obtained or planned observations at other wavelengths for at least a subset of my sample, a crucial X-ray perspective that targets the AGN is still missing.

We have found that the WISE-NVSS sample includes some of the most luminous sources in the Universe, as judged from their NIR-MIR emission (up to 10^{14} $L_{\odot}$). One of the ubiquitous properties of AGN is their X-ray emission – it seems that X-ray luminosity correlates with all other tracers of bolometric luminosity (Lansbury, 2015), and hence we expect – all things being equal – for the WISE-NVSS sources to be luminous X-ray emitters.

However, what might render these sources apparently weak in X-rays, is the possibility of very high columns to the nuclear region, as indicated by the very red MIR colors and faint optical counterparts. While only modest columns can absorb soft X-rays (e.g., $0.2-4$ keV), hard X-rays can penetrate much higher columns, and indeed hard X-ray surveys are often viewed as a gold standard at picking up an unbiased sample of AGN (Hickox & Alexander, 2018).

Our telescope of choice is the NuSTAR satellite (Nuclear Spectroscopic Telescope Array), launched in 2012, which is the first focusing observatory in the hard X-ray band, $3-79$ keV (Harrison et al., 2013). We initially focus on a small nearby subset of our sample to check the feasibility of X-ray observations. The aim of this proposal is to estimate the intrinsic AGN output and see whether the sources are Compton-thick. Whether Compton think or thin, either helps us understand the nature of near-nuclear environments in these sources.

5.3.2 Target Selection

Due to the obscured and high-redshift nature of our sample and the limited sensitivity of X-ray telescopes, it isn't feasible to a large number of sources. Therefore, our strategy is to start with a pilot study on the most promising targets and plan subsequent X-ray studies based on these first results. Therefore, I selected one promising target galaxy from the parent sample, J0612–06 ($z = 0.47$). Since it has a comparatively low redshift but a typical luminosity and radio source size, it can act as good prototype for the higher$-z$ objects that dominate the sample. Furthermore, J0612$-$06 has rich multi-wavelength observations available, including deep multi-frequency (350 MHz–33 GHz) VLA imaging (Section 5.1.1) and new 870 μm ALMA Cycle-6 continuum and spectral line observations (Section 5.2). The target shows resolved radio emission in the VLA image on scales of $\sim 1''(\sim 6$ kpc), and the radio SED fit shows a curved spectral shape, consistent with the presence of a young radio AGN. A preliminary analysis of the ALMA CO data has revealed kpc-scale molecular gas emission with a mass of $M_{H_2} \sim 1.5 \times 10^{10} M_{\odot}$) and a broad velocity profile ($\sim$500 km s^{-1}) that is possibly associated with an outflow.

The proposal to obtain a 70 ks observation of this target has been accepted with A-priority in the NuSTAR Cycle-6 program (proposal ID:6252) and will be observed in the upcoming months.

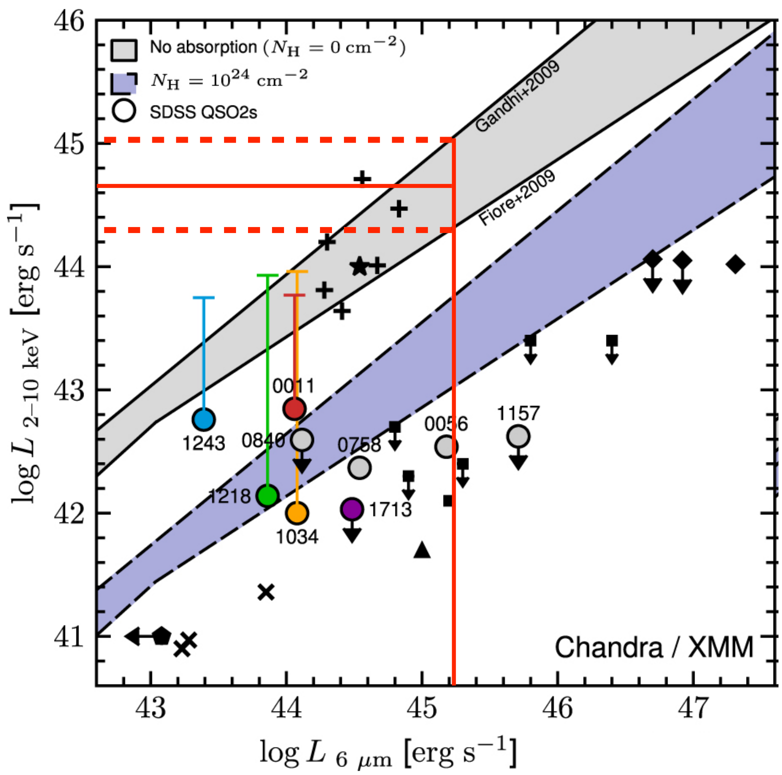

Figure 5.5: Rest-frame X-ray luminosity at 2-10 keV *vs.* 6 μm luminosity (from Lansbury 2015). The vertical red line indicates the $L_{6\,\mu m}$ luminosity of the proposed target. The horizontal red dashed lines show the expected range of intrinsic X-ray luminosity. We select the average value of $\log(L_{2-10\,\rm kev}/\rm erg\ s^{-1}) = 44.5$ (solid horizontal line) and estimate source counts for a range of column densities ($N_{\rm H} = 0.6 - 3 \times 10^{24}$ cm^{-2}).

5.3.3 Observations and Scientific Analysis

The detection of heavily obscured AGN at higher redshifts ($z \sim 2$) is now possible with NuSTAR with its unique combination of better sensitivity and wide spectral coverage that includes hard X-rays bands (e.g., Yan et al., 2019; Lansbury et al., 2017). Based on the ALMA CO data, I estimated a molecular column density of N_{H_2} $\sim 0.6 - 3 \times 10^{24}$ cm^{-2} (likely a lower limit to the total N_H in the nucleus). The large H_2 mass and column density are consistent with the high degree of obscuration inferred from the IR to submm SED given in (Lonsdale et al., 2015) and is in-line with N_H at

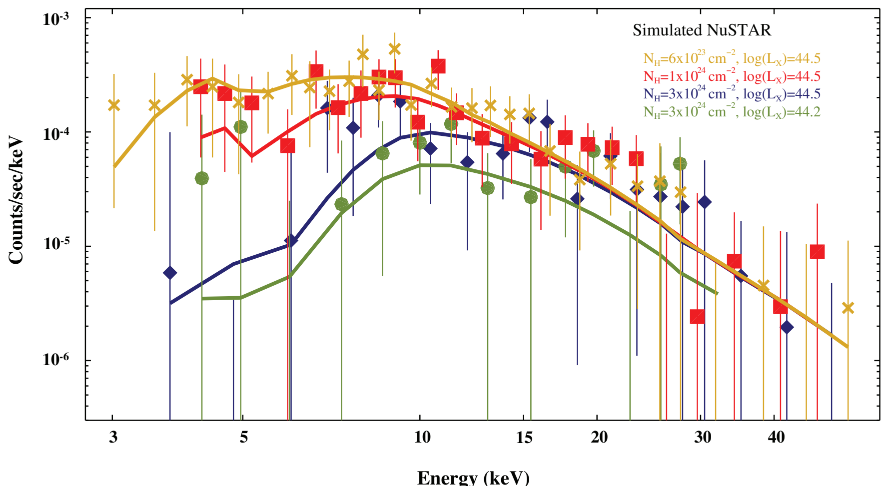

Figure 5.6: Simulated NuSTAR spectra for three different levels of obscuration, normalized with intrinsic 2–10 keV flux based on 6μm emission. Figure courtesy: Lauranne Lanz

Table 5.2: Predicted NuSTAR Counts for a 70 ks observation assuming intrinsic 2–10 kev luminosity of $\log(L_X/\text{erg s}^{-1}) = 44.5$

$N_{\rm H}$ $\rm cm^{-2}$	Total Cnt 3-79 keV	Src Cnt 3-24 keV
0.6e24	490	220
1.2e24	460	170
3e24	370	90

or near the Compton thick (CT) regime, as seen in similar source populations (e.g., Hot DOGs; Vito et al. 2018). Using the correlations of Gandhi et al. (2009) and Fiore et al. (2009), I estimate an intrinsic 2-10 keV luminosity in the rang $\log(L_X/\text{erg s}^{-1}) = 44.2 - 44.8$ for the 6 μm luminosity of $\log(\nu L_\nu/\text{erg s}^{-1}) = 45.11$. This analysis is illustrated in Figure 5.5, where we show the $L_{2-10\text{keV}} - L_{6\,\mu\text{m}}$ correlation plot taken from Lansbury (2015) along with an estimated range of $L_{2-10\text{kev}}$ for J0612–06.

The predicted $3-24$ keV source count ranges from 220 for a borderline CT source ($N_{\rm H} = 0.6 \times 10^{24}$ cm^{-2}) to ~ 90 for an extreme $N_{\rm H}$ column[4]. Table 5.2 shows the

[4]I used the `webPIMMS` calculator to estimate the source count. It is a versatile web-based sim-

source count predictions for a range of $N_{\rm H}$ columns expected for this target. In the case of a detection with NuSTAR, I can estimate the accretion luminosity via X-ray template fitting (e.g., using the MYTORUS model). The reflection component is likely to contribute to the hard X-ray emission. With enough counts, I will be able to account for the reflection component (in particular if Fe Kα line is detected) and constrain the accretion luminosity.

Spectral modeling in the NuSTAR data will also allow me to measure the circum-nuclear obscuration by the gas and its absorbing $N_{\rm H}$ column density. Based on the simulations, I will be able to constrain these parameters with $\sim 30\% - 40\%$ accuracy even for high column densities. Simulated NuSTAR spectra[5] for the three different levels of obscuration is given in Figure 5.6. In the case of a weak or no detection, upper limits on the X-ray luminosity and column density would imply the presence of either an extreme obscuration or intrinsically X-ray weak, but MIR-bright quasar, which would still be an important result.

5.4 Young Radio AGN in the ngVLA Era

5.4.1 Introduction

Young, compact radio AGNs represent an important phase in the life cycles of jetted AGN and provide direct insights into associated physical processes. An open question regarding young radio AGN is the degree to which they can affect the ISM of the host galaxy. Since their radio jets are fully contained within the host galaxy, spatially-resolved observations are necessary to assess this. A growing number of

ulation tool for X-ray astronomers, most commonly used to determine source flux or count rates. https://heasarc.gsfc.nasa.gov/cgi-bin/Tools/w3pimms/w3pimms.pl

[5]We used `sherpa` software to simulate spectra for 3 different values of $N_{\rm H}$, and an intrinsic $\Gamma = 1.9$ power-law to determine the corresponding observed flux and count rate for an unobscured luminosity of $\log(L_X/\mathrm{erg\ s^{-1}}) = 44.5$. https://cxc.cfa.harvard.edu/sherpa/

studies have detected signatures of multiphase outflows associated with young radio AGN, suggesting jet-ISM feedback (e.g.Chandola et al. 2011; Holt et al. 2011; Morganti et al. 2013), but the importance of this feedback in the context of galaxy evolution remains unclear. The ngVLA will address this issue through both continuum and spectral line observations. Broad-band continuum measurements of the turnover frequency of the radio SEDs of young radio sources will also directly constrain the density distribution of the ISM for sources at low redshift (Section 5.4.3; Bicknell et al. 1997; Jeyakumar 2016; Bicknell et al. 2018). Follow-up spectral line observations will further constrain the kinematics of the gas, which in turn constrain the energy of the jet-driven feedback.

Young radio AGNs also hold important clues about radio triggering and duty cycles, which are still poorly understood (Tadhunter, 2016). An improved understanding of MBH duty cycles and MBH accretion mechanisms will help explain the impact of MBH growth on galaxy growth and evolution (Shulevski et al., 2015). Molecular line diagnostics or HI absorption diagnostics can establish a link between fueling and different triggering mechanisms (Maccagni et al., 2014). A significant amount of dense gas is seen in young radio AGN (O'Dea, 1998), and several studies have found that HI is detected more frequently in GPS and CSS sources compared to other types of radio AGN (Geréb et al. 2014; O'Dea 1998 and references therein). Therefore, the investigation of these newborn radio AGN can give us a direct view of many transient processes and better inform simulations of galaxy formation and evolution.

5.4.2 The next-generation Very Large Array (ngVLA)

The VLA's impact on the world of radio astronomy is unparalleled, and it continues to be an essential instrument in the astronomical community. The ngVLA is a planned next-generation radio interferometer that will improve upon VLA and

VLBA to join the suites of future multi-wavelength facilities (Murphy et al., 2017). The project is being developed by National Radio Astronomy Observatory (NRAO), and is designed to provide up to ten times the sensitivity of the VLA and ALMA and an almost continuous spectral coverage from $1.2 - 116$ GHz. The present concept of the ngVLA array design consists of three subarrays: the main array of 214 18m-reflector antennas, a Short Baseline Array (SBA) of 19 6m-reflector antennas, and a Long Baseline Array (LBA) of 30 18m-reflector antennas (Figure 5.7).

5.4.3 Anticipated Results

Mapping Radio Morphology

The WISE-NVSS sources observed by the VLBA reveal jet extents of 60 to 85 pc (Figure 5.2). The VLBA or any current VLBI facility has sensitivity limitations due to the small number of antennas. The angular resolution, frequency range, and sensitivity offered by the ngVLA are optimal for efficiently resolving the structures of young radio AGN, such as the sources highlighted in Section 5.1.2, and constraining their ages through broadband continuum observations (Section 2.7.2).

Simulations of relativistic jets interacting with ISM (Mukherjee et al., 2016; Bicknell et al., 2018; Mukherjee et al., 2018) have shown that jets drive shocks in the ISM via an energy bubble. Furthermore, Mukherjee et al. (2018) have found that jet powers, inclinations, and densities affect AGN-driven outflows, thus motivating the need for high-resolution radio imaging to obtain spatially-resolved structural, spectral, and polarimetric information on the radio jets. In addition, direct measurements of flux densities and source sizes provide estimates of the energy density and pressure in the synchrotron plasma, which can then constrain ISM densities and the rate of the advancing shock front into the ambient medium. Limits on Faraday rotation measures obtained through polarimetry help constrain models of the nuclear environment.

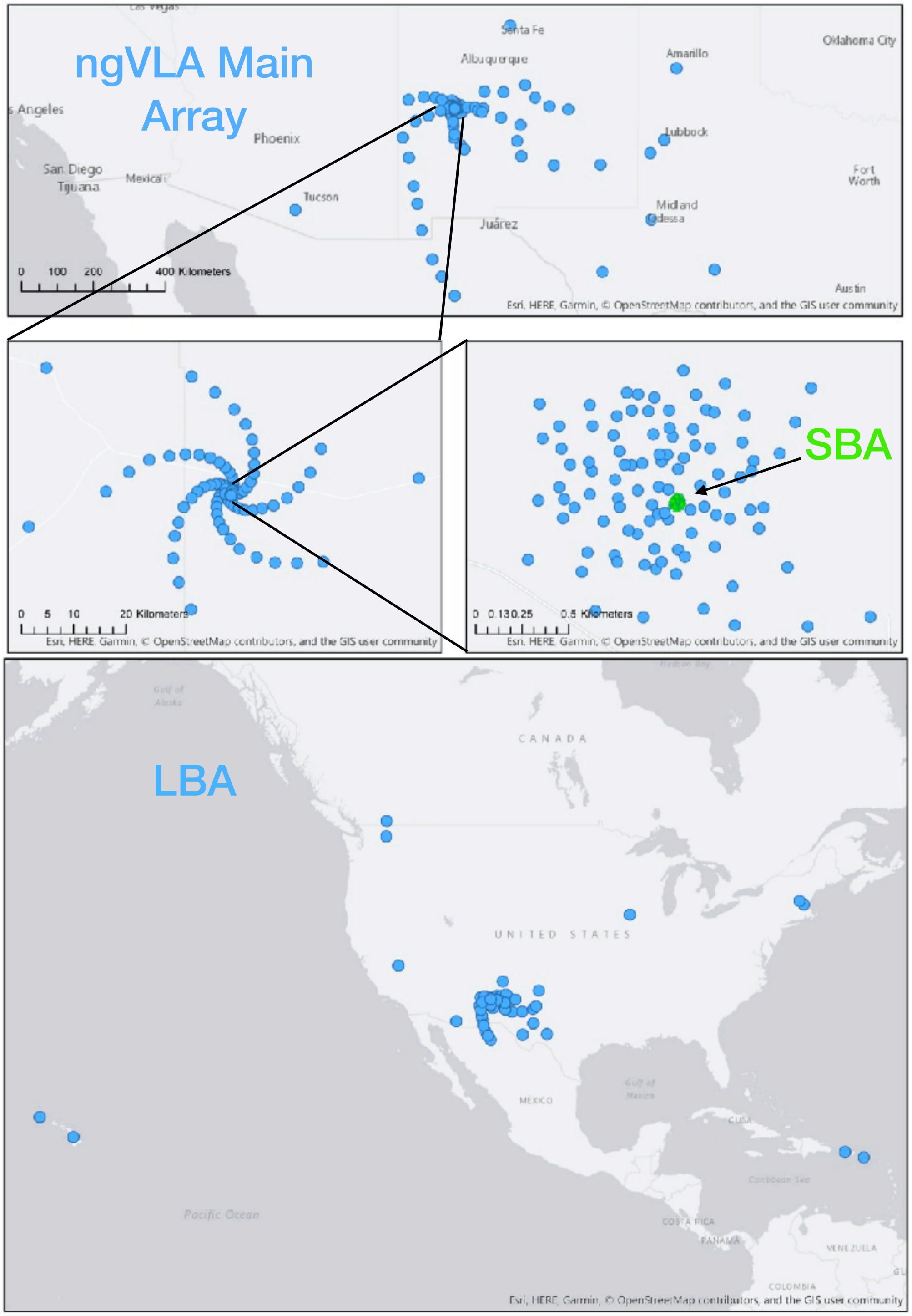

Figure 5.7: The current plan for the ngVLA configuration. The top image shows a full view of the main array consisting of 214 antennas. The middle two images show incrementally magnified views of the core. The green points in the middle right image is the SBA. The bottom image show the continental baselines along with main array which forms the LBA. Credit: NRAO

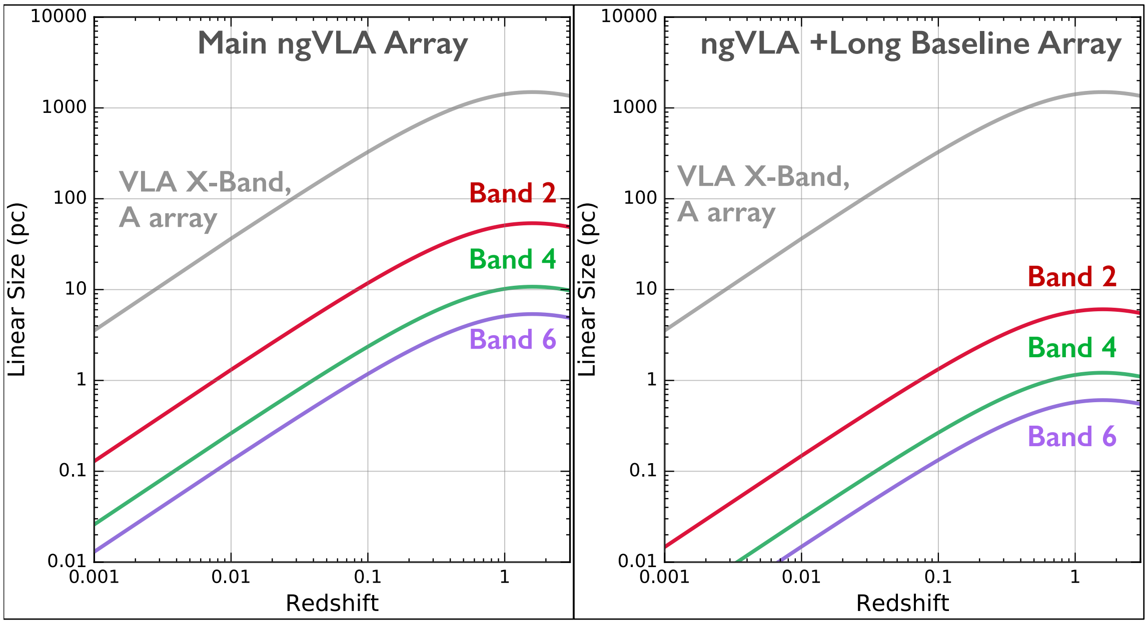

Figure 5.8: Linear sizes probed by ngVLA's frequency bands 2 (6.6 GHz; red), 4 (26.4 GHz; green), and 6 (90.1 GHz; purple) as a function of redshift. The left and right panels show the resolution capabilities for the ngVLA main array and LBA, respectively. The ngVLA main array with the addition of continental baselines will be able to resolve parsec-scale radio emission at $z \sim 2$. The gray line is the current VLA's resolution at X-band (10 GHz) in A-array. Credit: Kristina Nyland

Figure 5.8 shows the angular resolution achievable by the ngVLA's main array and LBA in three frequency bands, 2(6.6 GHz), 4(26.4 GHz), and 6(90.1 GHz), as a function of redshift. For a comparison, the VLA's resolution at X-band in A-array is shown by the gray line. The longest baselines planned for the ngVLA are ~1000 km which are required to provide the subarcsecond resolution needed to study young radio AGN. The significant increase in point-source sensitivity compared to the VLA will enable the ngVLA to detect young radio AGN over a wide redshift range (Nyland et al., 2018). An interesting point of comparison is the Legacy eMERLIN Multi-band Imaging of Nearby Galaxies survey (LeMMINGs; Baldi et al. 2018b) that targets the radio properties of nearby AGN at sub-arcsecond resolution. In the same on-source integration time used in the LeMMINGs survey (48 minutes), the ngVLA would be about 100 times more sensitive ($\sim$0.7 μJy beam^{-1}) in its Band 1 ($1.2 - 3.5$ GHz).

Characterizing Spectral Turnover

CSS, GPS, and HFP sources show an inverse correlation between the spectral peak frequency and their linear sizes (O'Dea, 1998; Orienti & Dallacasa, 2014). The origin of the peak is thought to be due to absorption by either a relativistic plasma (synchrotron self-absorption, SSA) or an external screen of ionized gas (free-free absorption, FFA). Simulations by Bicknell et al. 2018 have shown that the location of each source on the turnover-linear size relation depends on the warm ISM density, suggesting an evolutionary link between all three classes of young radio AGN. The details of the absorption model, however, remain unclear (Callingham et al., 2015). High-resolution observations at frequencies either side of the peak frequency can help identify the absorption process, while lower frequency observations in the optically-thick regime (e.g. below about 1 GHz) provide additional ways to distinguish between SSA and FFA (Kellermann, 1966). The Next Generation LOw Band Observatory (ngLOBO; Taylor et al. 2017), which is a proposed enhancement to the basic ngVLA reference design, would extend the ngVLA's frequency range below 1 GHz. The ngLOBO would enable more robust spectral aging models of the radio SEDs, particularly for slightly older (>10 Myr) and more distant ($z > 1$) sources.

Radio Spectral Ages

For a fixed magnetic field, if the initial energy distribution of a population of electrons follows a power law, given by $N(E) = N_0 E^{-\delta}$, the energy losses scale as $\tau = \frac{E}{dE/dt} \propto 1/E \propto 1/\nu^2$. This results in a preferential cooling of higher energy electrons. Assuming no other mode of particle acceleration, the resulting spectrum becomes increasingly curved over time. This behavior can be used to determine the characteristic age of a radio source (e.g., Myers & Spangler 1985; Harwood et al.

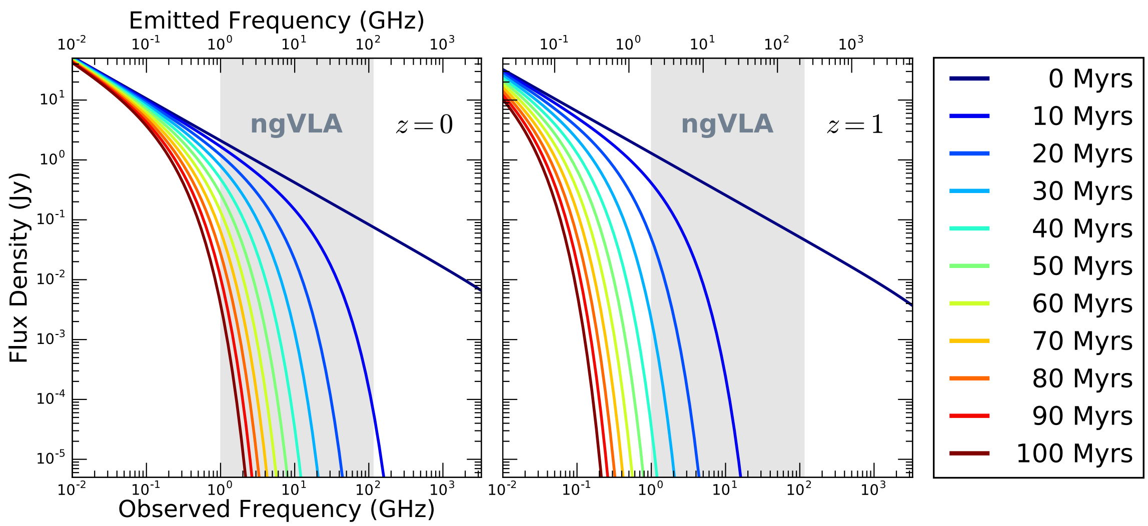

Figure 5.9: Example of JP model (Jaffe & Perola, 1973) spectral ages calculated using the BRATS software (Harwood et al., 2013) illustrating the need for ngVLA observations spanning a wide range of frequencies. The left and center panels correspond to redshifts of 0 and 1, respectively. The flux density values shown on the y-axis have been arbitrarily scaled. The combination of wide spectral coverage and high angular resolution, compared even to the SKA, make the ngVLA uniquely suited to studies of low-redshift radio AGN that are young, or higher-redshift AGN that are embedded in dense environments. Figure adapted from Nyland et al. (2018).

2013).

In Figure 5.9, we show an example of spectral ages calculated using the BRATS software[6] (Harwood et al., 2013) for an arbitrary jetted radio AGN at $z = 0$ and $z = 1$. As illustrated by the spectral age curves in the figure, the ngVLA will excel in studies of radio AGN spanning a broad range of ages at low redshift, as well as young or embedded radio AGN at higher redshifts. The results from the Australia Telescope 20 GHz (AT20G) survey (Murphy et al., 2010) indicate that continuum measurements in the tens of GHz range are needed to model the radio spectral energy distributions adequately (Sadler et al., 2006, 2008). These observations are particularly crucial for modeling the ages of young, low-redshift sources less than 10 Myrs old. Lower

[6] http://www.askanastronomer.co.uk/brats/

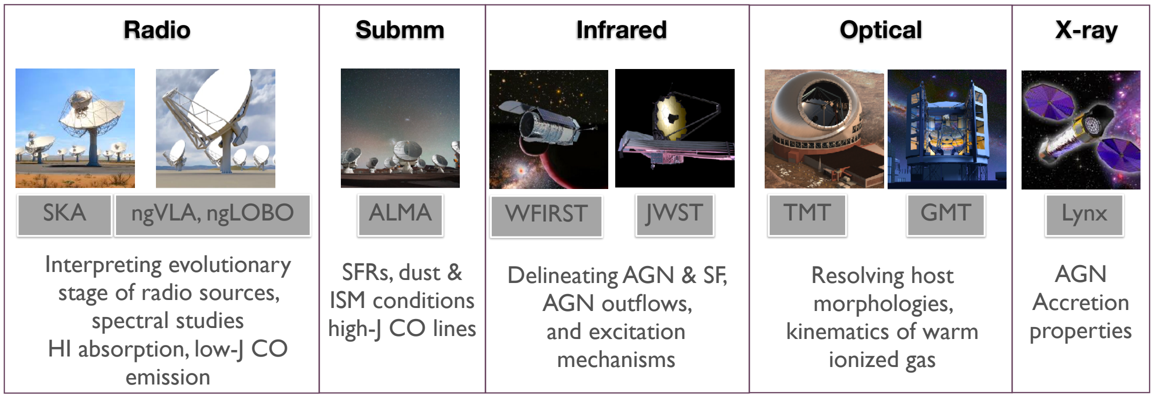

Figure 5.10: Synergies of the ngVLA with current and future multi-wavelength facilities. The key AGN science that will be enabled by each facility is given below each telescope image. A complete understanding of young radio AGN in luminous quasars at $z > 1$ will require the combination of ngVLA and ngLOBO observations with current and future instruments in the mm/submm, optical, and X-ray.

frequency radio continuum data down to tens of MHz regime (e.g., Heald et al., 2015) are important for constraining the ages of high-z sources; however, the inclusion of the lowest-frequency ngVLA bands down to $\sim$1 GHz would provide sufficient frequency coverage for measuring the ages of sources as old as 30-40 Myrs at $z \sim 1$.

5.4.4 Multiwavelength Synergy

Ultimately, a multi-waveband approach will be necessary to significantly advance our understanding of the evolution and energetics of young radio AGN, and the radio jet's influence on galaxy growth and evolution.

SKA

The ngVLA and Square Kilometre Array (SKA) will both allow broadband studies of radio SEDs. These can provide the necessary data to apply spectral aging models that help frame the evolutionary stage of the source. The SKA will be able to detect emission associated with fading radio lobes, uncovering older or prior periods of activity ("AGN archaeology"; Morganti 2017a). In Figure 5.9, we showed that the 1–116

GHz observing range of the ngVLA is well-matched to studies of low-redshift radio AGN or very young sources of intermediate redshift. Such young sources are often embedded in dense environments and are known to drive multi-phase gas outflows (e.g., Holt et al., 2008; Geréb et al., 2015). Broadband radio continuum surveys with both the ngVLA and SKA will therefore be needed to construct a complete picture of the life cycles of radio AGN and their connection to galaxy evolution.

ALMA

The frequency range of the ngVLA is well-matched to non-thermal synchrotron emission from both AGN and recent star formation. The higher frequency bands of the Atacama Large Millimeter/Submillimeter Array (ALMA) are sensitive to the dust continuum, which can be used to help determine star formation rates. The line capabilities of the ngVLA allow molecular CO gas to be detected through the low-J transitions, while ALMA will be sensitive to higher-J CO transitions as well as a wide variety of additional molecular species and transitions that characterize the ISM conditions. Thus, the ngVLA and ALMA will be important for constraining the impact of young radio AGN on the ISM and star formation on galactic scales.

Optical and Infrared Telescopes:

Next-generation optical and infrared telescopes such as the *James Webb* Space Telescope *(JWST)*, Thirty Meter Telescope (TMT), Giant Magellan Telescope (GMT), and the Wide-Field Infrared Survey Telescope *(WFIRST)* will provide a wealth of complementary information about the physical conditions of young radio AGN and the properties of their hosts. This includes resolving host morphologies, studying the kinematics of the warm ionized gas via spectroscopy, delineating star-formation and AGN via mid-infrared imaging and SED analyses, and tracing AGN-driven outflows and their excitation mechanisms.

Chapter 6

Conclusions

My main conclusions are as follows:

- In this thesis, I present radio properties of a sample selected to find heavily obscured, MIR bright, $z \sim 2$ quasars with recently turned on jets. The initial sample selection identified 155 sources over two-third of the sky with redshift $0.4 < z < 3$, suggesting these sources are rare either due to a short evolutionary phase or extreme properties of these systems.

- In Chapter 2, I present 10 GHz VLA observations for the entire sample of obscured quasars. I found that most of these sources are compact even on sub-arcsecond-scale resolution with no sign of large-scale extended emission that might have come from a prior epoch of AGN activity.

- These sources have radio luminosity ($L_{1.4\mathrm{GHz}} = 10^{25} - 10^{26}$ W Hz^{-1}), linear extents ($\lesssim 1.7$ kpc at $z \sim 2$), and lobe pressures ($\gtrsim 10^{-7} - 10^{-8}$ dyne cm^{-2}) similar to other luminous samples of compact and peaked spectrum sources such as CSS, GPS, and HFPs, that are well known to harbor young radio AGN.

- Application of a simple adiabatic lobe expansion model suggests relatively young dynamical ages ($< 10^3 - 10^6$ years), relatively high ambient ISM densities ($\sim 10^{-4} - 10$ cm^{-3}), and modest lobe expansion speeds ($\sim 0.003c - 0.1c$).

- I used the new wide-band receiver data to measure in-band spectral indices, confirming their values and uncertainties both empirically and theoretically. The distribution of 10 GHz spectral indices have a mean near -1, which is somewhat steeper than the canonical -0.7 usually found for optically thin synchrotron emission.

- I calculated the radio luminosity function using the V/V$_{max}$ method and found that our sources have considerably lower ($2-3$ dex) space densities than other classes of radio AGN. Folding together the rarity of our sources and their young dynamical age, I estimate that perhaps 20% of our AGN evolve through compact phases (such as GPS and CSS) to become large scale FR-I/II radio sources.

- In Chapter 3, I presented radio spectra of the entire sample made using flux measurements from our snapshot survey and archival radio data. The broad frequency range spanned by our data identified 46 (30% of the sample) sources with peaked spectra with turnover frequency in the range 150 MHz to 10 GHz. Additionally, 43 sources had curved spectra with a possible turnover below 150 MHz.

- The turnover or the curvature in the spectra accompanied by unresolved morphology is consistent with a self-absorbed compact source, suggesting a recently triggered young jet. An alternate possibility is an older source slowed down by an unusually dense ambient medium, and subject to free-free absorption. Clarifying the difference will require more detailed radio spectra, particularly at lower frequencies.

- Assuming the turnover is caused by synchrotron self-absorption, and that the magnetic field is also in approximate equipartition, I derived emitting region sizes of $2 - 52$ pc and magnetic fields of $6 - 400$ mG. These are consistent with young sources similar to those found in HFPs. We reapply the dynamical model from Chapter 2 using the new values of source size and magnetic field and find even younger ages. The ages of the youngest sources are now consistent with the recent discovery of a new class of compact peaked sources that turned on in the last $10 - 20$ years (Nyland et al., 2020). A more detailed investigation of such compact region sizes in our sample will be the focus of our VLBA snapshot observations with mas resolution.

- I investigated the possible origin of the steep ($\alpha_{high} \sim -1$) high-frequency spectra. While inverse Compton scattering off the CMB is unlikely, the bolometric AGN photon flux is sufficiently intense in the region of the radio source that inverse Compton scattering of these photons is likely.

- Extrapolating the synchrotron emission into the sub-mm cannot account for the ALMA fluxes detected in 26/49 of the sources. For these sources, at least, another component is present, most likely thermal emission from cold dust.

- Overall, I find these sources consistent with a population of newly triggered, young jets caught in a brief evolutionary stage in which they still reside within the dense gas reservoirs of their hosts.

- In Chapter 4, I led a survey to search for serendipitous detections of faint SMGs in the large ALMA archival database. I identified 26 sources with NIR counterparts, of which 15 were new. I also presented 13-band forced photometry using the Tractor image modeling code.

- I estimated photometric redshifts and rest-frame colors using the EAZY software package. The median redshift is 2.66, consistent with the model predictions for the SMG population by Béthermin et al. (2015).

- I found that our faint SMGs have bluer colors than bright SMGs, and the UVJ color-color plot places them on the main sequence of star-forming galaxies. These results also highlight the difficulty of finding larger samples of this important class of galaxy.

- Chapter 5 summarized ongoing projects that I led during my graduate studies. These include multi-band, multi-resolution radio imaging of a subset of obscured quasars; a pilot ALMA program to map the dense molecular gas and search for outflows via the CO emission line; and a pilot NuSTAR study to directly probe obscured AGN via hard X-ray emission.

My dissertation highlights the need for high-resolution radio observations to investigate the early stages of luminous radio AGN. My sample, however, is just a tip of an iceberg, and the life-cycles of radio AGN across a range of luminosity and environment, especially in the young phase, remain relatively unexplored due to the limitations of current instruments. With unprecedented sensitivity and high angular resolution, the next-generation facilities such as ngVLA and SKA are set to revolutionize our understanding of radio AGN and their broader connection to galaxy evolution.

References

Aihara, H., Armstrong, R., Bickerton, S., et al. 2017, ArXiv e-prints, arXiv:1702.08449

Aird, J., Coil, A. L., Georgakakis, A., et al. 2015, MNRAS, 451, 1892

Alaghband-Zadeh, S., Chapman, S. C., Swinbank, A. M., et al. 2012, MNRAS, 424, 2232

Alberts, S., Wilson, G. W., Lu, Y., et al. 2013, MNRAS, 431, 194

Alexander, D. M., & Hickox, R. C. 2012, NewAR, 56, 93

Alexander, D. M., Chary, R. R., Pope, A., et al. 2008, ApJ, 687, 835

Alexander, P. 2000, MNRAS, 319, 8

An, T., & Baan, W. A. 2012, ApJ, 760, 77

An, T., Lao, B. Q., Zhao, W., et al. 2017, MNRAS, 466, 952

An, T., Wu, F., Yang, J., et al. 2012, ApJS, 198, 5

Antonucci, R. 1993, ARA&A, 31, 473

Appleton, P. N., Fadda, D. T., Marleau, F. R., et al. 2004, ApJS, 154, 147

Aravena, M., Decarli, R., Walter, F., et al. 2016, ApJ, 833, 68

Aretxaga, I., Wilson, G. W., Aguilar, E., et al. 2011, MNRAS, 415, 3831

Artyukh, V. S., Chernikov, P. A., & Tyul'Bashev, S. A. 2008, A&A, 486, 735

Assef, R. J., Stern, D., Noirot, G., et al. 2018, ApJS, 234, 23

Assef, R. J., Stern, D., Kochanek, C. S., et al. 2013, ApJ, 772, 26

Assef, R. J., Eisenhardt, P. R. M., Stern, D., et al. 2015, ApJ, 804, 27

Athreya, R. M., & Kapahi, V. K. 1998, Journal of Astrophysics and Astronomy, 19, 63

Austermann, J. E., Dunlop, J. S., Perera, T. A., et al. 2010, MNRAS, 401, 160

Baade, W., & Minkowski, R. 1954, ApJ, 119, 215

Baldi, R. D., Capetti, A., & Giovannini, G. 2015, A&A, 576, A38

Baldi, R. D., Capetti, A., & Massaro, F. 2018a, A&A, 609, A1

Baldi, R. D., Williams, D. R. A., McHardy, I. M., et al. 2018b, MNRAS, 476, 3478

Baldwin, J. A., Phillips, M. M., & Terlevich, R. 1981, PASP, 93, 5

Banerji, M., Chapman, S. C., Smail, I., et al. 2011, MNRAS, 418, 1071

Barger, A. J., Cowie, L. L., Sanders, D. B., et al. 1998, Nature, 394, 248

Barger, A. J., Wang, W.-H., Cowie, L. L., et al. 2012, ApJ, 761, 89

Baron, D., & Ménard, B. 2019, MNRAS, 487, 3404

Becker, R. H., White, R. L., & Helfand, D. J. 1995, ApJ, 450, 559

Beckmann, R. S., Devriendt, J., Slyz, A., et al. 2017, MNRAS, 472, 949

Beckmann, V., & Shrader, C. R. 2012, Active Galactic Nuclei

Begelman, M. C. 1999, in The Most Distant Radio Galaxies, ed. H. J. A. Röttgering, P. N. Best, & M. D. Lehnert (Royal Netherlands Academy of Arts and Science (January 1999)), 173

Bertoldi, F., Carilli, C., Aravena, M., et al. 2007, ApJS, 172, 132

Best, P. N., Arts, J. N., Röttgering, H. J. A., et al. 2003, MNRAS, 346, 627

Best, P. N., & Heckman, T. M. 2012, MNRAS, 421, 1569

Best, P. N., Ker, L. M., Simpson, C., Rigby, E. E., & Sabater, J. 2014, MNRAS, 445, 955

Béthermin, M., De Breuck, C., Sargent, M., & Daddi, E. 2015, A&A, 576, L9

Bicknell, G. V., Dopita, M. A., & O'Dea, C. P. O. 1997, ApJ, 485, 112

Bicknell, G. V., Mukherjee, D., Wagner, A. Y., Sutherland, R. S., & Nesvadba, N. P. H. 2018, MNRAS, 475, 3493

Bicknell, G. V., & Sutherland, R. S. 2006, Astronomische Nachrichten, 327, 235

Biggs, A. D., Ivison, R. J., Ibar, E., et al. 2011, MNRAS, 413, 2314

Blain, A. W., Jameson, A., Smail, I., et al. 1999, MNRAS, 309, 715

Blain, A. W., Smail, I., Ivison, R. J., Kneib, J.-P., & Frayer, D. T. 2002, PhR, 369, 111

Blandford, R., Meier, D., & Readhead, A. 2019, ARA&A, 57, 467

Blandford, R. D., & Znajek, R. L. 1977, MNRAS, 179, 433

Blecha, L., Snyder, G. F., Satyapal, S., & Ellison, S. L. 2018, MNRAS, 478, 3056

Blundell, K. M., & Lacy, M. 1995, MNRAS, 274, L9

Blundell, K. M., Rawlings, S., & Willott, C. J. 1999, AJ, 117, 677

Bornancini, C. G., O'Mill, A. L., Gurovich, S., & Lambas, D. G. 2010, MNRAS, 406, 197

Böttcher, M., Reimer, A., Sweeney, K., & Prakash, A. 2013, ApJ, 768, 54

Brammer, G. B., van Dokkum, P. G., & Coppi, P. 2008, ApJ, 686, 1503

Brammer, G. B., Whitaker, K. E., van Dokkum, P. G., et al. 2011, ApJ, 739, 24

Bridge, C. R., Blain, A., Borys, C. J. K., et al. 2013, ApJ, 769, 91

Brienza, M., Godfrey, L., Morganti, R., et al. 2017, A&A, 606, A98

Brisbin, D., Miettinen, O., Aravena, M., et al. 2017, A&A, 608, A15

Buchner, J., Georgakakis, A., Nandra, K., et al. 2015, ApJ, 802, 89

Burbidge, G. R. 1956, ApJ, 124, 416

Burbidge, G. R., & Burbidge, E. M. 1969, Nature, 222, 735

Bussmann, R. S., Riechers, D., Fialkov, A., et al. 2015, ApJ, 812, 43

Buttiglione, S., Capetti, A., Celotti, A., et al. 2010, A&A, 509, A6

Callingham, J. R., Gaensler, B. M., Ekers, R. D., et al. 2015, ApJ, 809, 168

Callingham, J. R., Ekers, R. D., Gaensler, B. M., et al. 2017, ApJ, 836, 174

Capetti, A., Massaro, F., & Baldi, R. D. 2017, A&A, 601, A81

Carniani, S., Maiolino, R., De Zotti, G., et al. 2015, A&A, 584, A78

Casey, C. M., Narayanan, D., & Cooray, A. 2014, PhR, 541, 45

Casey, C. M., Chen, C.-C., Cowie, L. L., et al. 2013, MNRAS, 436, 1919

Casey, C. M., Hodge, J. A., Lacy, M., et al. 2015, ArXiv e-prints, arXiv:1510.06411

Cavagnolo, K. W., McNamara, B. R., Nulsen, P. E. J., et al. 2010, ApJ, 720, 1066

Ceraj, L., Smolčić, V., Delvecchio, I., et al. 2018, A&A, 620, A192

Chambers, K. C., Magnier, E. A., Metcalfe, N., et al. 2016, arXiv e-prints, arXiv:1612.05560

Chandola, Y., Sirothia, S. K., & Saikia, D. J. 2011, MNRAS, 418, 1787

Chapin, E. L., Chapman, S. C., Coppin, K. E., et al. 2011, MNRAS, 411, 505

Chapman, S. C., Blain, A. W., Ivison, R. J., & Smail, I. R. 2003, Nature, 422, 695

Chapman, S. C., Blain, A. W., Smail, I., & Ivison, R. J. 2005, ApJ, 622, 772

Chapman, S. C., Scott, D., Borys, C., & Fahlman, G. G. 2002, MNRAS, 330, 92

Chapman, S. C., Smail, I., Blain, A. W., & Ivison, R. J. 2004, ApJ, 614, 671

Chen, C.-C., Cowie, L. L., Barger, A. J., et al. 2013a, ApJ, 762, 81

—. 2013b, ApJ, 776, 131

Chen, C.-C., Cowie, L. L., Barger, A. J., Wang, W.-H., & Williams, J. P. 2014, ApJ, 789, 12

Chen, C.-C., Smail, I., Swinbank, A. M., et al. 2015a, ApJ, 799, 194

—. 2016a, ApJ, 831, 91

Chen, C.-C., Smail, I., Ivison, R. J., et al. 2016b, ApJ, 820, 82

Chen, C.-T. J., Hickox, R. C., Alberts, S., et al. 2015b, ApJ, 802, 50

Chhetri, R., Kimball, A., Ekers, R. D., et al. 2020, MNRAS, 494, 923

Cisternas, M., Jahnke, K., Inskip, K. J., et al. 2011, ApJ, 726, 57

Clarke, T. E., Kassim, N. E., Brisken, W., et al. 2016, Society of Photo-Optical Instrumentation Engineers (SPIE) Conference Series, Vol. 9906, Commensal low frequency observing on the NRAO VLA: VLITE status and future plans, 99065B

Collier, J. D., Banfield, J. K., Norris, R. P., et al. 2014, MNRAS, 439, 545

Collier, J. D., Tingay, S. J., Callingham, J. R., et al. 2018, MNRAS, 477, 578

Condon, J. 2015, ArXiv e-prints, arXiv:1502.05616

Condon, J., & Ransom, S. 2016, Essential Radio Astronomy, Princeton Series in Modern Observational Astronomy (Princeton University Press)

Condon, J. J. 1992, ARA&A, 30, 575

Condon, J. J., Cotton, W. D., & Broderick, J. J. 2002, AJ, 124, 675

Condon, J. J., Cotton, W. D., Greisen, E. W., et al. 1998, AJ, 115, 1693

Cooray, A. 2016, Royal Society Open Science, 3, 150555

Coppejans, R., Cseh, D., van Velzen, S., et al. 2016, MNRAS, 459, 2455

Coppin, K., Chapin, E. L., Mortier, A. M. J., et al. 2006, MNRAS, 372, 1621

Cornwell, T. J., Golap, K., & Bhatnagar, S. 2005, in Astronomical Society of the Pacific Conference Series, Vol. 347, Astronomical Data Analysis Software and Systems XIV, ed. P. Shopbell, M. Britton, & R. Ebert, 86

Cotton, W. D. 2008, PASP, 120, 439

Cotton, W. D., Dallacasa, D., Fanti, C., et al. 2003a, A&A, 406, 43

Cotton, W. D., Spencer, R. E., Saikia, D. J., & Garrington, S. 2003b, A&A, 403, 537

Cowie, L. L., Barger, A. J., & Kneib, J.-P. 2002, AJ, 123, 2197

Cowie, L. L., González-López, J., Barger, A. J., et al. 2018, ApJ, 865, 106

Croston, J. H., & Hardcastle, M. J. 2014, MNRAS, 438, 3310

Croston, J. H., Hardcastle, M. J., Birkinshaw, M., Worrall, D. M., & Laing, R. A. 2008, MNRAS, 386, 1709

Croston, J. H., Hardcastle, M. J., Harris, D. E., et al. 2005, ApJ, 626, 733

Croston, J. H., Ineson, J., & Hardcastle, M. J. 2018, MNRAS, 476, 1614

Croton, D. J., Springel, V., White, S. D. M., et al. 2006, MNRAS, 365, 11

Czerny, B., Siemiginowska, A., Janiuk, A., Nikiel-Wroczyński, B., & Stawarz, Ł. 2009, ApJ, 698, 840

Dabhade, P., Röttgering, H. J. A., Bagchi, J., et al. 2020, A&A, 635, A5

Daddi, E., Cimatti, A., Renzini, A., et al. 2004, ApJ, 617, 746

Dallacasa, D., Stanghellini, C., Centonza, M., & Fanti, R. 2000, A&A, 363, 887

de Kool, M., & Begelman, M. C. 1989, ApJ, 345, 135

de Vries, N., Snellen, I. A. G., Schilizzi, R. T., & Mack, K. H. 2009, Astronomische Nachrichten, 330, 214

Deller, A. T., Brisken, W. F., Phillips, C. J., et al. 2011, DiFX2: A more flexible, efficient, robust and powerful software correlator, , , ascl:1102.024

Dey, A., Soifer, B. T., Desai, V., et al. 2008, ApJ, 677, 943

Di Matteo, T., Springel, V., & Hernquist, L. 2005, Nature, 433, 604

Díaz-Santos, T., Assef, R. J., Blain, A. W., et al. 2016, ApJ, 816, L6

—. 2018, Science, 362, 1034

Dole, H., Lagache, G., Puget, J.-L., et al. 2006, A&A, 451, 417

Donley, J. L., Koekemoer, A. M., Brusa, M., et al. 2012, ApJ, 748, 142

Donley, J. L., Kartaltepe, J., Kocevski, D., et al. 2018, ApJ, 853, 63

D'Onofrio, M., Marziani, P., & Sulentic, J. W. 2012, Fifty Years of Quasars, Vol. 386, doi:10.1007/978-3-642-27564-7

Douglas, J. N., Bash, F. N., Bozyan, F. A., Torrence, G. W., & Wolfe, C. 1996, AJ, 111, 1945

Dubois, Y., Peirani, S., Pichon, C., et al. 2016, MNRAS, 463, 3948

Duffy, P., & Blundell, K. M. 2012, MNRAS, 421, 108

Dunlop, J. S., McLure, R. J., Yamada, T., et al. 2004, MNRAS, 350, 769

Dunlop, J. S., McLure, R. J., Biggs, A. D., et al. 2017, MNRAS, 466, 861

Eisenhardt, P. R. M., Wu, J., Tsai, C.-W., et al. 2012, ApJ, 755, 173

Engel, H., Tacconi, L. J., Davies, R. I., et al. 2010, ApJ, 724, 233

Esquej, P., Alonso-Herrero, A., González-Martín, O., et al. 2014, ApJ, 780, 86

Ezawa, H., Kawabe, R., Kohno, K., & Yamamoto, S. 2004, in Proc. SPIE, Vol. 5489, Ground-based Telescopes, ed. J. M. Oschmann, Jr., 763–772

Fabian, A. C. 1999, MNRAS, 308, L39

—. 2012, ARA&A, 50, 455

Falcke, H., Körding, E., & Markoff, S. 2004, A&A, 414, 895

Falkendal, T., De Breuck, C., Lehnert, M. D., et al. 2019, A&A, 621, A27

Falle, S. A. E. G. 1991, MNRAS, 250, 581

Fan, L., Han, Y., Fang, G., et al. 2016, ApJL, 822, L32

Fanaroff, B. L., & Riley, J. M. 1974, MNRAS, 167, 31P

Fanti, C. 2009, Astronomische Nachrichten, 330, 120

Fanti, C., Fanti, R., Dallacasa, D., et al. 1995, A&A, 302, 317

Fanti, C., Pozzi, F., Dallacasa, D., et al. 2001, A&A, 369, 380

Fanti, C., Branchesi, M., Cotton, W. D., et al. 2004, A&A, 427, 465

Fanti, R., Fanti, C., Schilizzi, R. T., et al. 1990, A&A, 231, 333

Farrah, D., Petty, S., Connolly, B., et al. 2017, ApJ, 844, 106

Fiore, F., Puccetti, S., Brusa, M., et al. 2009, ApJ, 693, 447

Förster Schreiber, N. M., & Wuyts, S. 2020, arXiv e-prints, arXiv:2010.10171

Franceschini, A., Toffolatti, L., Mazzei, P., Danese, L., & de Zotti, G. 1991, A&AS, 89, 285

Franco, M., Elbaz, D., Béthermin, M., et al. 2018, ArXiv e-prints, arXiv:1803.00157

Fritz, J., Franceschini, A., & Hatziminaoglou, E. 2006, MNRAS, 366, 767

Fu, H., Cooray, A., Feruglio, C., et al. 2013, Nature, 498, 338

Fujimoto, S., Ouchi, M., Ono, Y., et al. 2016, ApJS, 222, 1

Furusawa, H., Kosugi, G., Akiyama, M., et al. 2008, ApJS, 176, 1

Gandhi, P., Horst, H., Smette, A., et al. 2009, A&A, 502, 457

Garrington, S. T., & Conway, R. G. 1991, MNRAS, 250, 198

Geach, J. E., Chapin, E. L., Coppin, K. E. K., et al. 2013, MNRAS, 432, 53

Geach, J. E., Dunlop, J. S., Halpern, M., et al. 2017, MNRAS, 465, 1789

Gebhardt, K., Bender, R., Bower, G., et al. 2000, ApJL, 539, L13

Gendre, M. A., Best, P. N., Wall, J. V., & Ker, L. M. 2013, MNRAS, 430, 3086

George, I. M., & Fabian, A. C. 1991, MNRAS, 249, 352

Geréb, K., Maccagni, F. M., Morganti, R., & Oosterloo, T. A. 2015, A&A, 575, A44

Geréb, K., Morganti, R., & Oosterloo, T. A. 2014, A&A, 569, A35

Ghez, A. M., Salim, S., Weinberg, N. N., et al. 2008, ApJ, 689, 1044

Ghisellini, G. 2016, Galaxies, 4, 36

Giommi, P., Padovani, P., & Polenta, G. 2013, MNRAS, 431, 1914

Glenn, J., Rangwala, N., Maloney, P. R., & Kamenetzky, J. R. 2015, ApJ, 800, 105

Godfrey, L. E. H., & Shabala, S. S. 2016, MNRAS, 456, 1172

Gómez, J. L., Roca-Sogorb, M., Agudo, I., Marscher, A. P., & Jorstad, S. G. 2011, ApJ, 733, 11

González-López, J., Bauer, F. E., Romero-Cañizales, C., et al. 2017, A&A, 597, A41

González-López, J., Novak, M., Decarli, R., et al. 2020, ApJ, 897, 91

Goulding, A. D., Greene, J. E., Bezanson, R., et al. 2018, PASJ, 70, S37

Gregory, P. C., Scott, W. K., Douglas, K., & Condon, J. J. 1996, ApJS, 103, 427

Greve, T. R., Ivison, R. J., Bertoldi, F., et al. 2004, MNRAS, 354, 779

Gugliucci, N. E., Taylor, G. B., Peck, A. B., & Giroletti, M. 2005, ApJ, 622, 136

Gültekin, K., Cackett, E. M., Miller, J. M., et al. 2009, ApJ, 706, 404

Güsten, R., Nyman, L. Å., Schilke, P., et al. 2006, A&A, 454, L13

Gwyn, S. D. J. 2012, AJ, 143, 38

Hardcastle, M. J. 2018, MNRAS, 475, 2768

Hardcastle, M. J., & Croston, J. H. 2020, NewAR, 88, 101539

Harrison, C. 2014, PhD thesis, Durham University

Harrison, C. M. 2017, Nature Astronomy, 1, 0165

Harrison, F. A., Craig, W. W., Christensen, F. E., et al. 2013, ApJ, 770, 103

Harwood, J. J. 2017, MNRAS, 466, 2888

Harwood, J. J., Hardcastle, M. J., Croston, J. H., & Goodger, J. L. 2013, MNRAS, 435, 3353

Harwood, J. J., Croston, J. H., Intema, H. T., et al. 2016, MNRAS, 458, 4443

Hatsukade, B., Ohta, K., Seko, A., Yabe, K., & Akiyama, M. 2013, ApJL, 769, L27

Hatsukade, B., Ohta, K., Yabe, K., et al. 2015, ApJ, 810, 91

Hatsukade, B., Kohno, K., Aretxaga, I., et al. 2011, MNRAS, 411, 102

Hatziminaoglou, E., Pérez-Fournon, I., Polletta, M., et al. 2005, AJ, 129, 1198

Hauser, M. G., Arendt, R. G., Kelsall, T., et al. 1998, ApJ, 508, 25

Heald, G. H., Pizzo, R. F., Orrú, E., et al. 2015, A&A, 582, A123

Heckman, T. M., & Best, P. N. 2014, ARA&A, 52, 589

Helfand, D. J., White, R. L., & Becker, R. H. 2015, ApJ, 801, 26

Herzog, A., Middelberg, E., Norris, R. P., et al. 2014, A&A, 567, A104

Herzog, A., Norris, R. P., Middelberg, E., et al. 2016, A&A, 593, A130

Hickox, R. C., & Alexander, D. M. 2018, ARA&A, 56, 625

Hodge, J. A., & da Cunha, E. 2020, arXiv e-prints, arXiv:2004.00934

Holt, J., Tadhunter, C. N., & Morganti, R. 2008, MNRAS, 387, 639

Holt, J., Tadhunter, C. N., Morganti, R., & Emonts, B. H. C. 2011, MNRAS, 410, 1527

Hopkins, A. M., Whiting, M. T., Seymour, N., et al. 2015, PASA, 32, e037

Hopkins, P. F., & Hernquist, L. 2006, ApJS, 166, 1

Hopkins, P. F., Hernquist, L., Cox, T. J., & Kereš, D. 2008, ApJS, 175, 356

Hopkins, P. F., & Quataert, E. 2010, MNRAS, 407, 1529

Hsu, L.-Y., Cowie, L. L., Chen, C.-C., Barger, A. J., & Wang, W.-H. 2016, ApJ, 829, 25

Hubble, E. 1929, Proceedings of the National Academy of Science, 15, 168

Hughes, D. H., Serjeant, S., Dunlop, J., et al. 1998, Nature, 394, 241

Hurley-Walker, N., Callingham, J. R., Hancock, P. J., et al. 2017, MNRAS, 464, 1146

Huynh, M. T., Norris, R. P., Siana, B., & Middelberg, E. 2010, ApJ, 710, 698

Ibar, E., Cirasuolo, M., Ivison, R., et al. 2008, MNRAS, 386, 953

Ikarashi, S., Ivison, R. J., Caputi, K. I., et al. 2015, ApJ, 810, 133

Imanishi, M., Nakanishi, K., & Izumi, T. 2018, ApJ, 856, 143

Ineson, J., Croston, J. H., Hardcastle, M. J., & Mingo, B. 2017, MNRAS, 467, 1586

Inoue, A. K., Tamura, Y., Matsuo, H., et al. 2016, Science, 352, 1559

Intema, H. T., Jagannathan, P., Mooley, K. P., & Frail, D. A. 2017, A&A, 598, A78

Isobe, T., Feigelson, E. D., & Nelson, P. I. 1986, ApJ, 306, 490

Ivison, R. J., Smail, I., Le Borgne, J.-F., et al. 1998, MNRAS, 298, 583

Ivison, R. J., Greve, T. R., Smail, I., et al. 2002, MNRAS, 337, 1

Ivison, R. J., Greve, T. R., Dunlop, J. S., et al. 2007, MNRAS, 380, 199

Ivison, R. J., Smail, I., Amblard, A., et al. 2012, MNRAS, 425, 1320

Izumi, T., Kohno, K., Aalto, S., et al. 2016, ApJ, 818, 42

Jaffe, W. J., & Perola, G. C. 1973, A&A, 26, 423

Jansky, K. G. 1933, Nature, 132, 66

Jarvis, M. E., Harrison, C. M., Thomson, A. P., et al. 2019, MNRAS, 485, 2710

Jarvis, M. J., Bonfield, D. G., Bruce, V. A., et al. 2013, MNRAS, 428, 1281

Jennison, R. C., & Das Gupta, M. K. 1953, Nature, 172, 996

Jeyakumar, S. 2016, MNRAS, 458, 3786

Johansson, D., Sigurdarson, H., & Horellou, C. 2011, A&A, 527, A117

Jones, S. F., Blain, A. W., Stern, D., et al. 2014, MNRAS, 443, 146

Jones, S. F., Blain, A. W., Lonsdale, C., et al. 2015, MNRAS, 448, 3325

Jun, H. D., Assef, R. J., Bauer, F. E., et al. 2020, ApJ, 888, 110

Jurlin, N., Morganti, R., Brienza, M., et al. 2020, A&A, 638, A34

Kaiser, C. R., & Alexander, P. 1997, MNRAS, 286, 215

Kaiser, C. R., & Best, P. N. 2007, MNRAS, 381, 1548

Kardashev, N. S. 1962, Soviet Ast., 6, 317

Kauffmann, G., & Haehnelt, M. 2000, MNRAS, 311, 576

Kaviraj, S., Laigle, C., Kimm, T., et al. 2017, MNRAS, 467, 4739

Keim, M. A., Callingham, J. R., & Röttgering, H. J. A. 2019, A&A, 628, A56

Kellermann, K. I. 1966, Australian Journal of Physics, 19, 195

Kellermann, K. I. 2015, in IAU Symposium, Vol. 313, Extragalactic Jets from Every Angle, ed. F. Massaro, C. C. Cheung, E. Lopez, & A. Siemiginowska, 190–195

Kellermann, K. I., Bouton, E. N., & Brandy, S. S. 2020, Open Skies: The National Radio Astronomy Observatory and Its Impact on US Radio Astronomy, doi:10.1007/978-3-030-32345-5

Kellermann, K. I., Condon, J. J., Kimball, A. E., Perley, R. A., & Ivezić, Ž. 2016, ApJ, 831, 168

Kellermann, K. I., & Pauliny-Toth, I. I. K. 1981, ARA&A, 19, 373

Ker, L. M., Best, P. N., Rigby, E. E., Röttgering, H. J. A., & Gendre, M. A. 2012, MNRAS, 420, 2644

Kerr, R. P. 1963, PhRvL, 11, 237

Kewley, L. J., Groves, B., Kauffmann, G., & Heckman, T. 2006, MNRAS, 372, 961

Kim, M., Ho, L. C., Lonsdale, C. J., et al. 2013, ApJL, 768, L9

Kim, S., Wardlow, J. L., Cooray, A., et al. 2012, ApJ, 756, 28

Kimball, A. E., Kellermann, K. I., Condon, J. J., Ivezić, Ž., & Perley, R. A. 2011, ApJL, 739, L29

King, A., & Pounds, K. 2015, Annual Review of Astronomy and Astrophysics, 53, 115

Klamer, I. J., Ekers, R. D., Bryant, J. J., et al. 2006, MNRAS, 371, 852

Kleinmann, D. E., & Low, F. J. 1970, ApJL, 159, L165

Knudsen, K. K., van der Werf, P. P., & Kneib, J.-P. 2008, MNRAS, 384, 1611

Kocevski, D. D., Brightman, M., Nandra, K., et al. 2015, ApJ, 814, 104

Kohno, K., Yamaguchi, Y., Tamura, Y., et al. 2016, in IAU Symposium, Vol. 319, Galaxies at High Redshift and Their Evolution Over Cosmic Time, ed. S. Kaviraj, 92–95

Kormendy, J., & Ho, L. C. 2013, ARA&A, 51, 511

Koss, M., Mushotzky, R., Veilleux, S., & Winter, L. 2010, ApJL, 716, L125

Krolik, J. H., & Chen, W. 1991, AJ, 102, 1659

Kunert-Bajraszewska, M., Gawroński, M. P., Labiano, A., & Siemiginowska, A. 2010, MNRAS, 408, 2261

Labbé, I., Huang, J., Franx, M., et al. 2005, ApJL, 624, L81

Lacy, M., Petric, A. O., Sajina, A., et al. 2007, AJ, 133, 186

Lacy, M., & Sajina, A. 2020, Nature Astronomy, 4, 352

Lacy, M., Storrie-Lombardi, L. J., Sajina, A., et al. 2004, The Astrophysical Journal Supplement Series, 154, 166

Lacy, M., Ridgway, S. E., Gates, E. L., et al. 2013, The Astrophysical Journal Supplement Series, 208, 24

Lacy, M., Myers, S. T., Chandler, C. J., et al. 2019, VLASS Project Memo #13: Pilot and Epoch 1 Quick Look Data Release,

Lacy, M., Baum, S. A., Chandler, C. J., et al. 2020, PASP, 132, 035001

Lagache, G., Puget, J.-L., & Dole, H. 2005, ARA&A, 43, 727

Laing, R. A., Jenkins, C. R., Wall, J. V., & Unger, S. W. 1994, in Astronomical Society of the Pacific Conference Series, Vol. 54, The Physics of Active Galaxies, ed. G. V. Bicknell, M. A. Dopita, & P. J. Quinn, 201

Laing, R. A., Riley, J. M., & Longair, M. S. 1983, MNRAS, 204, 151

Lane, W. M., Cotton, W. D., van Velzen, S., et al. 2014, MNRAS, 440, 327

Lang, D., Hogg, D. W., & Schlegel, D. J. 2016, AJ, 151, 36

Lansbury, G. B. 2015, ApJ, 809, 115

Lansbury, G. B., Alexander, D. M., Aird, J., et al. 2017, ApJ, 846, 20

Laporte, N., Bauer, F. E., Troncoso-Iribarren, P., et al. 2017, A&A, 604, A132

Laurent, G. T., Aguirre, J. E., Glenn, J., et al. 2005, ApJ, 623, 742

Lawrence, A., Warren, S. J., Almaini, O., et al. 2007, MNRAS, 379, 1599

Ledlow, M. J., & Owen, F. N. 1995, AJ, 109, 853

Liu, D., Lang, P., Magnelli, B., et al. 2019, ApJS, 244, 40

Longair, M. S. 2011, High Energy Astrophysics

Longair, M. S., & Seldner, M. 1979, MNRAS, 189, 433

Lonsdale, C., Polletta, M. d. C., Surace, J., et al. 2004, ApJS, 154, 54

Lonsdale, C. J., Lacy, M., Kimball, A. E., et al. 2015, ApJ, 813, 45

Luo, B., Brandt, W. N., Xue, Y. Q., et al. 2017, ApJS, 228, 2

Lutz, D. 2014, ARA&A, 52, 373

Lynden-Bell, D. 1969, Nature, 223, 690

Maccagni, F. M., Morganti, R., Oosterloo, T. A., & Mahony, E. K. 2014, A&A, 571, A67

Maciel, T., & Alexander, P. 2014, MNRAS, 442, 3469

Madau, P., & Dickinson, M. 2014, ARA&A, 52, 415

Mahatma, V. H., Hardcastle, M. J., Williams, W. L., et al. 2019, A&A, 622, A13

Maini, A., Prandoni, I., Norris, R. P., et al. 2016, A&A, 596, A80

Mantovani, F., Junor, W., Ricci, R., et al. 2002, A&A, 389, 58

Mantovani, F., Rossetti, A., Junor, W., Saikia, D. J., & Salter, C. J. 2013, A&A, 555, A4

Maraschi, L., Ghisellini, G., & Celotti, A. 1992, ApJL, 397, L5

Marr, J. M., Perry, T. M., Read, J., Taylor, G. B., & Morris, A. O. 2014, ApJ, 780, 178

Mateos, S., Alonso-Herrero, A., Carrera, F. J., et al. 2013, MNRAS, 434, 941

—. 2012, MNRAS, 426, 3271

Mauch, T., Murphy, T., Buttery, H. J., et al. 2003, MNRAS, 342, 1117

Mauduit, J.-C., Lacy, M., Farrah, D., et al. 2012, PASP, 124, 714

McConnell, N. J., & Ma, C.-P. 2013, ApJ, 764, 184

McLure, R. J., & Dunlop, J. S. 2002, MNRAS, 331, 795

McMullin, J. P., Waters, B., Schiebel, D., Young, W., & Golap, K. 2007, in Astronomical Society of the Pacific Conference Series, Vol. 376, Astronomical Data Analysis Software and Systems XVI, ed. R. A. Shaw, F. Hill, & D. J. Bell, 127

McNamara, B. R., & Nulsen, P. E. J. 2007, ARA&A, 45, 117

—. 2012, New Journal of Physics, 14, 055023

Merloni, A., Bongiorno, A., Brusa, M., et al. 2014, MNRAS, 437, 3550

Mhaskey, M., Gopal-Krishna, Paul, S., et al. 2019, MNRAS, 489, 3506

Michałowski, M., Hjorth, J., & Watson, D. 2010, A&A, 514, A67

Michałowski, M. J., Dunlop, J. S., Koprowski, M. P., et al. 2017, MNRAS, 469, 492

Middelberg, E., Norris, R. P., Hales, C. A., et al. 2011, A&A, 526, A8

Middelberg, E., Norris, R. P., Tingay, S., et al. 2008, A&A, 491, 435

Miettinen, O., Novak, M., Smolčić, V., et al. 2015, A&A, 584, A32

Miley, G. 1980, ARA&A, 18, 165

Miley, G., & De Breuck, C. 2008, A&A Rv, 15, 67

Mingo, B., Hardcastle, M. J., Croston, J. H., et al. 2014, MNRAS, 440, 269

Mingo, B., Croston, J. H., Hardcastle, M. J., et al. 2019, MNRAS, 488, 2701

Minkowski, R. 1960, ApJ, 132, 908

Miraghaei, H., & Best, P. N. 2017, in Journal of Physics Conference Series, Vol. 869, Journal of Physics Conference Series, 012078

Miyoshi, M., Moran, J., Herrnstein, J., et al. 1995, Nature, 373, 127

Moffet, A. T. 1975, Strong Nonthermal Radio Emission from Galaxies (the University of Chicago Press), 211

Mohan, N., & Rafferty, D. 2015, PyBDSF: Python Blob Detection and Source Finder, , , ascl:1502.007

Mooley, K. P., Hallinan, G., Bourke, S., et al. 2016, ApJ, 818, 105

Morabito, L. K., & Harwood, J. J. 2018, MNRAS, 480, 2726

Morganti, R. 2017a, Nature Astronomy, 1, 596

—. 2017b, Frontiers in Astronomy and Space Sciences, 4, 42

Morganti, R., Frieswijk, W., Oonk, R. J. B., Oosterloo, T., & Tadhunter, C. 2013, A&A, 552, L4

Mortlock, D. J., Warren, S. J., Venemans, B. P., et al. 2011, Nature, 474, 616

Mukherjee, D., Bicknell, G. V., Sutherland, R., & Wagner, A. 2016, MNRAS, 461, 967

Mukherjee, D., Bicknell, G. V., Wagner, A. e. Y., Sutherland, R. S., & Silk, J. 2018, MNRAS, 479, 5544

Murgia, M., Fanti, C., Fanti, R., et al. 1999, A&A, 345, 769

Murgia, M., Parma, P., Mack, K. H., et al. 2011, A&A, 526, A148

Murphy, E., ed. 2018, Astronomical Society of the Pacific Conference Series, Vol. 517, Science with a Next Generation Very Large Array

Murphy, E. J., Momjian, E., Condon, J. J., et al. 2017, ApJ, 839, 35

Murphy, T., Sadler, E. M., Ekers, R. D., et al. 2010, MNRAS, 402, 2403

Mutel, R. L., Hodges, M. W., & Phillips, R. B. 1985, ApJ, 290, 86

Myers, S. T., & Spangler, S. R. 1985, ApJ, 291, 52

Narayan, R., & McClintock, J. E. 2012, MNRAS, 419, L69

Narayan, R., & Yi, I. 1995, ApJ, 444, 231

Narayanan, D., Turk, M., Feldmann, R., et al. 2015, Nature, 525, 496

Netzer, H. 2015, ARA&A, 53, 365

Norris, R. P., Afonso, J., Bacon, D., et al. 2013, PASA, 30, e020

Nyland, K., Alatalo, K., Wrobel, J. M., et al. 2013, ApJ, 779, 173

Nyland, K., Young, L. M., Wrobel, J. M., et al. 2016, MNRAS, 458, 2221

Nyland, K., Davis, T. A., Nguyen, D. D., et al. 2017, ApJ, 845, 50

Nyland, K., Harwood, J. J., Mukherjee, D., et al. 2018, ApJ, 859, 23

Nyland, K., Dong, D. Z., Patil, P., et al. 2020, arXiv e-prints, arXiv:2011.08872

O'Dea, C. P. 1998, PASP, 110, 493

O'Dea, C. P., & Baum, S. A. 1997, AJ, 113, 148

O'Dea, C. P., Baum, S. A., & Stanghellini, C. 1991, ApJ, 380, 66

O'Dea, C. P., & Saikia, D. J. 2020, arXiv e-prints, arXiv:2009.02750

Ono, Y., Ouchi, M., Kurono, Y., & Momose, R. 2014, ApJ, 795, 5

Orenstein, B. J., Collier, J. D., & Norris, R. P. 2019, MNRAS, 484, 1021

Orienti, M. 2016, Astronomische Nachrichten, 337, 9

Orienti, M., & Dallacasa, D. 2008a, A&A, 487, 885

—. 2008b, A&A, 477, 807

—. 2014, MNRAS, 438, 463

Orienti, M., Dallacasa, D., & Stanghellini, C. 2010, MNRAS, 408, 1075

O'Sullivan, S. P., Gaensler, B. M., Lara-López, M. A., et al. 2015, ApJ, 806, 83

Oteo, I., Zwaan, M. A., Ivison, R. J., Smail, I., & Biggs, A. D. 2016, ApJ, 822, 36

Ouchi, M., Ellis, R., Ono, Y., et al. 2013, ApJ, 778, 102

Owen, F. N. 2018, ApJS, 235, 34

Oyabu, S., Ishihara, D., Malkan, M., et al. 2011, A&A, 529, A122

Pacholczyk, A. G. 1970, Radio astrophysics. Nonthermal processes in galactic and extragalactic sources

Padovani, P. 2016, A&A Rv, 24, 13

Padovani, P., Alexander, D. M., Assef, R. J., et al. 2017, A&A Rv, 25, 2

Parma, P., Murgia, M., de Ruiter, H. R., et al. 2007, A&A, 470, 875

Pasetto, A., Kraus, A., Mack, K. H., Bruni, G., & Carrasco-González, C. 2016, Astronomische Nachrichten, 337, 91

Patel, S. G., Kelson, D. D., Holden, B. P., Franx, M., & Illingworth, G. D. 2011, ApJ, 735, 53

Patil, P., Nyland, K., Harwood, J. J., Kimball, A., & Mukherjee, D. 2018, in Astronomical Society of the Pacific Conference Series, Vol. 517, Science with a Next Generation Very Large Array, ed. E. Murphy, 595

Patil, P., Nyland, K., Lacy, M., et al. 2019, ApJ, 871, 109

Patil, P., Nyland, K., Whittle, M., et al. 2020, ApJ, 896, 18

Peacock, J. A., Miller, L., & Longair, M. S. 1986, MNRAS, 218, 265

Peacock, J. A., & Wall, J. V. 1982, MNRAS, 198, 843

Pentericci, L., Carniani, S., Castellano, M., et al. 2016, ApJL, 829, L11

Perera, T. A., Chapin, E. L., Austermann, J. E., et al. 2008, MNRAS, 391, 1227

Perley, R. A., & Butler, B. J. 2013, ApJS, 204, 19

Perucho, M. 2018, in International Conference on Black Holes as Cosmic Batteries: UHECRs and Multimessenger Astronomy. 12-15 September 2018. Foz do Iguaçu, 17

Phillips, R. B., & Mutel, R. L. 1982, A&A, 106, 21

Pier, E. A., & Krolik, J. H. 1992, ApJ, 401, 99

Planck Collaboration, Ade, P. A. R., Aghanim, N., et al. 2016, A&A, 594, A13

Polatidis, A. G., & Conway, J. E. 2003, PASA, 20, 69

Polisensky, E., Lane, W. M., Hyman, S. D., et al. 2016, ApJ, 832, 60

Polletta, M., Omont, A., Berta, S., et al. 2008, A&A, 492, 81

Pope, A., Scott, D., Dickinson, M., et al. 2006, MNRAS, 370, 1185

Pracy, M. B., Ching, J. H. Y., Sadler, E. M., et al. 2016, MNRAS, 460, 2

Pringle, J. E. 1981, ARA&A, 19, 137

Ramos Almeida, C., & Ricci, C. 2017, Nature Astronomy, 1, 679

Rastello, S., Dallacasa, D., & Orienti, M. 2016, Astronomische Nachrichten, 337, 42

Rau, U., & Cornwell, T. J. 2011, A&A, 532, A71

Readhead, A. C. S. 1994, ApJ, 426, 51

Readhead, A. C. S., Taylor, G. B., Xu, W., et al. 1996, ApJ, 460, 612

Rengelink, R. B., Tang, Y., de Bruyn, A. G., et al. 1997, A&AS, 124, 259

Ricci, C., Bauer, F. E., Treister, E., et al. 2017a, MNRAS, 468, 1273

Ricci, C., Assef, R. J., Stern, D., et al. 2017b, ApJ, 835, 105

Richards, G. T., Fan, X., Schneider, D. P., et al. 2001, AJ, 121, 2308

Robson, I., Holland, W. S., & Friberg, P. 2017, Royal Society Open Science, 4, 170754

Rossetti, A., Dallacasa, D., Fanti, C., Fanti, R., & Mack, K. H. 2008, A&A, 487, 865

Rossetti, A., Fanti, C., Fanti, R., Dallacasa, D., & Stanghellini, C. 2006, A&A, 449, 49

Rowan-Robinson, M., Gonzalez-Solares, E., Vaccari, M., & Marchetti, L. 2013, MNRAS, 428, 1958

Rowan-Robinson, M., Babbedge, T., Oliver, S., et al. 2008, MNRAS, 386, 697

Rybicki, G. B., & Lightman, A. P. 1986, Radiative Processes in Astrophysics

Ryle, M. 1962, Nature, 194, 517

Sabater, J., Best, P. N., Hardcastle, M. J., et al. 2019, A&A, 622, A17

Sadler, E. M., Ekers, R. D., Mahony, E. K., Mauch, T., & Murphy, T. 2014, MNRAS, 438, 796

Sadler, E. M., Ricci, R., Ekers, R. D., et al. 2008, MNRAS, 385, 1656

—. 2006, MNRAS, 371, 898

Saikia, D. J., & Jamrozy, M. 2009, Bulletin of the Astronomical Society of India, 37, 63

Sajina, A., Yan, L., Fadda, D., Dasyra, K., & Huynh, M. 2012, ApJ, 757, 13

Salpeter, E. E. 1964, ApJ, 140, 796

Sanders, D. B., Soifer, B. T., Elias, J. H., et al. 1988, ApJ, 325, 74

Sanghera, H. S., Saikia, D. J., Luedke, E., et al. 1995, A&A, 295, 629

Satyapal, S., Ellison, S. L., McAlpine, W., et al. 2014, MNRAS, 441, 1297

Schmidt, M. 1963, Nature, 197, 1040

—. 1968, ApJ, 151, 393

—. 1970, ApJ, 162, 371

Scott, K. S., Yun, M. S., Wilson, G. W., et al. 2010, MNRAS, 405, 2260

Scott, K. S., Wilson, G. W., Aretxaga, I., et al. 2012, MNRAS, 423, 575

Sekiguchi, K., & SXDS Team. 2004, in Bulletin of the American Astronomical Society, Vol. 36, American Astronomical Society Meeting Abstracts, 1478

Seko, A., Ohta, K., Yabe, K., et al. 2016a, ApJ, 819, 82

—. 2016b, ApJ, 833, 53

Seyfert, C. K. 1943, ApJ, 97, 28

Shabala, S. S. 2018, MNRAS, 478, 5074

Shabala, S. S., Jurlin, N., Morganti, R., et al. 2020, MNRAS, 496, 1706

Shakura, N. I. 1972, AZh, 49, 921

—. 1973, Soviet Ast., 16, 756

Shang, Z., Brotherton, M. S., Wills, B. J., et al. 2011, ApJS, 196, 2

Shankar, F., Weinberg, D. H., & Miralda-Escudé, J. 2009, ApJ, 690, 20

Shen, Y., Richards, G. T., Strauss, M. A., et al. 2011, ApJS, 194, 45

Shields, G. A. 1999, PASP, 111, 661

Shimwell, T. W., Röttgering, H. J. A., Best, P. N., et al. 2017, A&A, 598, A104

Shulevski, A., Morganti, R., Barthel, P. D., et al. 2015, A&A, 583, A89

Sijacki, D., Vogelsberger, M., Genel, S., et al. 2015, MNRAS, 452, 575

Simpson, J. M., Swinbank, A. M., Smail, I., et al. 2014, ApJ, 788, 125

Simpson, J. M., Smail, I., Swinbank, A. M., et al. 2017, ApJ, 839, 58

Singh, V., Beelen, A., Wadadekar, Y., et al. 2014, A&A, 569, A52

Siringo, G., Kreysa, E., Kovács, A., et al. 2009, A&A, 497, 945

Slish, V. I. 1963, Nature, 199, 682

Smail, I., Ivison, R. J., & Blain, A. W. 1997, ApJL, 490, L5

Smail, I., Ivison, R. J., Blain, A. W., & Kneib, J.-P. 2002, MNRAS, 331, 495

Smith, D. J. B., Dunne, L., Maddox, S. J., et al. 2011, MNRAS, 416, 857

Smolcic, V. 2016, arXiv e-prints, arXiv:1603.05687

Snellen, I. A. G., Schilizzi, R. T., de Bruyn, A. G., et al. 1998, Astronomy and Astrophysics Supplement Series, 131, 435

Snellen, I. A. G., Schilizzi, R. T., Miley, G. K., et al. 2000, MNRAS, 319, 445

Speagle, J. S., Steinhardt, C. L., Capak, P. L., & Silverman, J. D. 2014, ApJS, 214, 15

Spencer, R. E., McDowell, J. C., Charlesworth, M., et al. 1989, MNRAS, 240, 657

Spinoglio, L., & Malkan, M. A. 1989, ApJ, 342, 83

Stanghellini, C., Dallacasa, D., & Orienti, M. 2009, Astronomische Nachrichten, 330, 223

Steidel, C. C., Giavalisco, M., Pettini, M., Dickinson, M., & Adelberger, K. L. 1996, ApJL, 462, L17

Stern, D., Eisenhardt, P., Gorjian, V., et al. 2005, ApJ, 631, 163

Stern, D., Assef, R. J., Benford, D. J., et al. 2012, ApJ, 753, 30

Stern, D., Lansbury, G. B., Assef, R. J., et al. 2014, ApJ, 794, 102

Swinbank, A. M., Simpson, J. M., Smail, I., et al. 2014, MNRAS, 438, 1267

Tadhunter, C. 2016, A&A Rv, 24, 10

Taylor, G., Dowell, J., Malins, J., et al. 2017, ArXiv e-prints, arXiv:1708.00090

Tingay, S. J., & de Kool, M. 2003, AJ, 126, 723

Tingay, S. J., Macquart, J. P., Collier, J. D., et al. 2015, AJ, 149, 74

Tinti, S., Dallacasa, D., de Zotti, G., Celotti, A., & Stanghellini, C. 2005, A&A, 432, 31

Tokunaga, A. T., Simons, D. A., & Vacca, W. D. 2002, PASP, 114, 180

Torniainen, I., Tornikoski, M., Lähteenmäki, A., et al. 2007, A&A, 469, 451

Treister, E., Schawinski, K., Urry, C. M., & Simmons, B. D. 2012, ApJL, 758, L39

Treister, E., Cardamone, C. N., Schawinski, K., et al. 2009, ApJ, 706, 535

Tristram, K. R. W., Meisenheimer, K., Jaffe, W., et al. 2007, A&A, 474, 837

Tsai, C.-W., Eisenhardt, P. R. M., Wu, J., et al. 2015, ApJ, 805, 90

Tsai, C.-W., Eisenhardt, P. R. M., Jun, H. D., et al. 2018, ApJ, 868, 15

Turner, R. J., & Shabala, S. S. 2015, ApJ, 806, 59

Ueda, Y., Akiyama, M., Hasinger, G., Miyaji, T., & Watson, M. G. 2014, ApJ, 786, 104

Urry, C. M., & Padovani, P. 1995, PASP, 107, 803

Vaddi, S., Kharb, P., Daly, R. A., et al. 2019, MNRAS, 484, 385

van Breugel, W., Miley, G., & Heckman, T. 1984, AJ, 89, 5

Viero, M. P., Moncelsi, L., Quadri, R. F., et al. 2013, ApJ, 779, 32

Villar Martín, M., Emonts, B., Humphrey, A., Cabrera Lavers, A., & Binette, L. 2014, MNRAS, 440, 3202

Villforth, C., Hamilton, T., Pawlik, M. M., et al. 2017a, in Galaxy Evolution Across Time, 9

Villforth, C., Hamilton, T., Pawlik, M. M., et al. 2017b, MNRAS, 466, 812

Virtanen, P., Gommers, R., Oliphant, T. E., et al. 2020, Nature Methods

Vito, F., Brandt, W. N., Stern, D., et al. 2018, MNRAS, 474, 4528

Wagner, A. Y., Bicknell, G. V., & Umemura, M. 2012, ApJ, 757, 136

Wagner, A. Y., Bicknell, G. V., Umemura, M., Sutherland, R. S., & Silk, J. 2016, Astronomische Nachrichten, 337, 167

Wang, F., Fan, X., Yang, J., et al. 2017, ApJ, 839, 27

Wardlow, J. L., Smail, I., Coppin, K. E. K., et al. 2011, MNRAS, 415, 1479

Weaver, R., McCray, R., Castor, J., Shapiro, P., & Moore, R. 1977, ApJ, 218, 377

Weiß, A., Kovács, A., Coppin, K., et al. 2009, ApJ, 707, 1201

Weston, M. E., McIntosh, D. H., Brodwin, M., et al. 2017, MNRAS, 464, 3882

Whitaker, K. E., Labbé, I., van Dokkum, P. G., et al. 2011, ApJ, 735, 86

White, R. L., Becker, R. H., Helfand, D. J., & Gregg, M. D. 1997, ApJ, 475, 479

Williams, R. J., Quadri, R. F., Franx, M., van Dokkum, P., & Labbé, I. 2009, ApJ, 691, 1879

Willott, C. J., Carilli, C. L., Wagg, J., & Wang, R. 2015, ApJ, 807, 180

Willott, C. J., Rawlings, S., Blundell, K. M., & Lacy, M. 1999, MNRAS, 309, 1017

Willott, C. J., McLure, R. J., Hibon, P., et al. 2013, AJ, 145, 4

Wołowska, A., Kunert-Bajraszewska, M., Mooley, K., & Hallinan, G. 2017, Frontiers in Astronomy and Space Sciences, 4, 38

Wolstencroft, R. D., Parker, Q. A., Lonsdale, C. J., & Scarrott, S. M. 2000, MNRAS, 311, 541

Woo, J.-H., Bae, H.-J., Son, D., & Karouzos, M. 2016, ApJ, 817, 108

Worrall, D. M., & Birkinshaw, M. 2000, ApJ, 530, 719

Wright, E. L., Eisenhardt, P. R. M., Mainzer, A. K., et al. 2010, AJ, 140, 1868

Wu, J., Tsai, C.-W., Sayers, J., et al. 2012a, ApJ, 756, 96

Wu, J., Jun, H. D., Assef, R. J., et al. 2018, ApJ, 852, 96

Wu, X.-B., Hao, G., Jia, Z., Zhang, Y., & Peng, N. 2012b, AJ, 144, 49

Wuyts, S., Labbé, I., Franx, M., et al. 2007, ApJ, 655, 51

Yamaguchi, Y., Tamura, Y., Kohno, K., et al. 2016, PASJ, 68, 82

Yamaguchi, Y., Kohno, K., Hatsukade, B., et al. 2019, ApJ, 878, 73

Yan, W., Hickox, R. C., Hainline, K. N., et al. 2019, ApJ, 870, 33

York, D. G., Adelman, J., Anderson, Jr., J. E., et al. 2000, AJ, 120, 1579

Yuan, F., & Narayan, R. 2014, ARA&A, 52, 529

Zavala, J. A., Casey, C. M., da Cunha, E., et al. 2018, ApJ, 869, 71

Zinn, P. C., Middelberg, E., & Ibar, E. 2011, A&A, 531, A14